SCUOLA DI DOTTORATO
UNIVERSITÀ DEGLI STUDI DI MILANO-BICOCCA

Dipartimento di / Department of

Physics “G.Occhialini”

Dottorato di Ricerca/PhD program: Physics and Astronomy Ciclo/Cycle: XXXVIII

Curriculum in Plasma Physics and Biophysics (D)

Study of Gamma-Ray Diagnostics Based on Cerium-Activated Lanthanum Bromide Detectors in Tokamaks

Cognome / Surname: Fugazza Nome / Name: Simone Lorenzo

Matricola / Registration number 858839

Tutore / Tutor: Dr. Marco Tardocchi

Supervisor: Prof. Massimo Nocente

Coordinatore / Coordinator: Prof. Stefano Ragazzi

ANNO ACCADEMICO / ACADEMIC YEAR 2024/2025

Scuola di dottorato
Università degli studi di Milano–Bicocca

Department of Physics G. Occhialini
PhD program in Physics and Astronomy – XXXVIII cycle

Study of Gamma-Ray Diagnostics Based on Cerium-Activated Lanthanum Bromide Detectors in Tokamaks

Simone Lorenzo Fugazza
Registration number 858839

Supervisor: Prof. **Massimo Nocente**
Tutor: Dr. **Marco Tardocchi**

Coordinator: Prof. Stefano Ragazzi

Academic year
2024/2025

Summary

Magnetic confinement fusion devices operate in environments with intense particle emissions, which can be measured by dedicated diagnostics to gather information about the state of the plasma. Diagnostics will play a crucial role in the success of future tokamaks for commercial fusion power generation.
This thesis explores the use of gamma-ray diagnostics in tokamaks for multiple applications. The Cerium-activated Lanthanum Bromide ($LaBr_3$:Ce) scintillator has been selected as the reference detector, as it represents the state of the art in gamma-ray diagnostics thanks to its high performance and robustness in harsh radiative conditions.

The primary study investigates the feasibility of using a $LaBr_3$:Ce-based gamma-ray measurement system to evaluate fusion power at SPARC, a tokamak designed to achieve fusion gains of Q>1 with Deuterium–Tritium (DT) plasmas for the first time in a magnetic confinement fusion device. In present tokamaks, fusion power is typically determined by measuring neutron yields through flux monitors cross-calibrated with activation foils. Here, the possibility of performing analogous measurements using gamma-rays from the rarer DT branch T(D, γ)^{5}He is assessed. The analysis builds on the experience gained at JET, where DT gamma-ray emission was recently observed and used to estimate fusion power for the first time in a tokamak. The study aims to define the fusion power range in which such DT gamma-ray measurements could be effectively performed at SPARC.

The second application concerns the use of gamma-ray spectroscopy to study fast ions in Deuterium–Helium-3 (D–^{3}He) plasmas from Three-Ion Scheme experiments at JET. In these scenarios, a fast deuteron population is injected by Neutral Beam Injection and further accelerated via Ion Cyclotron Resonance Heating. Using the Gamma Camera Upgrade system equipped with $LaBr_3$:Ce detectors, gamma-ray data can be collected and, through tomographic reconstructions, spatial emissivity profiles can be obtained. The D–^{3}He reaction predominantly produces an alpha particle and a proton, but a rarer branch emits a ~16 MeV gamma-ray that can be detected by the Gamma Camera, allowing the reconstruction of the alpha particle birth profile. The aim of this work is to validate TRANSP code simulations performed at JET for these plasmas by comparing experimental results with synthetic profiles generated from the simulations.

The last study investigates the use of multiple gamma-ray diagnostics to detect Bremsstrahlung radiation from runaway electron (RE) events. The goal is to demonstrate that detectors observing the plasma along multiple lines of sight can collect qualitatively distinct Bremsstrahlung spectra only if the RE pitch-angle distribution is not fully co-passing (i.e., not all electrons have pitch angles equal to zero), as it

has been assumed in algorithms aimed at infering the RE energy distribution from hard x-ray spectra using deconvolution methods. This hypothesis derives from experimental observations at JET, where different $LaBr_3$:Ce detectors observe distinct spectral features during RE events. These findings suggest that employing multiple lines of sight may provide the opportunity to study the RE pitch-angle distribution in tokamaks, while also offering a more complete understanding of RE behaviour and emission mechanisms.

List of Publications

First author:

[1] S. L. Fugazza et al. «Feasibility Study of Gamma-Ray Spectroscopy for the Determination of the Fusion Power at the SPARC Tokamak». In: *Fusion Engineering and Design* 222 (Jan. 2026), p. 115403. ISSN: 0920-3796. DOI: 10.1016/j.fusengdes.2025.115403.

[2] S. L. Fugazza et al. «Validation of TRANSP simulations of the fast deuterium beam distribution in D^3He plasmas from (D)-(D_{NBI})-(^3He) three-ions scheme experiments at JET». In: *Plasma Physics and Controlled Fusion* (expected 2026). Submitted.

As a co-author:

[1] B. Eriksson et al. «First Measurement in a Magnetic Confinement Fusion Experiment of the $^3H + ^3H \rightarrow ^5He + n$ Intermediate Two-Body Resonant Reaction». In: *Physical Review C* 109.5 (May 2024), p. 054620. DOI: 10.1103/PhysRevC.109.054620.

[2] G. Marcer et al. «Absolute measurement of the deuterium-tritium reaction gamma-ray emission in magnetic confinement fusion plasmas». In: *Nuclear Fusion* (2025). ISSN: 0029-5515. DOI: 10.1088/1741-4326/adeea7.

[3] M. Nocente et al. «COSMONAUT: A COmpact Spectrometer for Measurements of Neutrons at the ASDEX Upgrade Tokamak». In: *Review of Scientific Instruments* 95.8 (Aug. 2024), p. 083501. ISSN: 0034-6748. DOI: 10.1063/5.0218178.

[4] A. Valentini et al. «Orbit-Space Sensitivity of Two-Step Reaction Gamma-Ray Spectroscopy». In: *Nuclear Fusion* (2025). ISSN: 0029-5515. DOI: 10.1088/1741-4326/ae013d.

Contents

Chapter 1

Introduction

In this chapter, the fundamental aspects of the nuclear fusion and the magnetic confinement reactor are introduced [1, 2]. Subsequently, gamma-ray detection is briefly discussed, focusing on the Cerium-activated Lanthanum Bromide ($LaBr_3$:Ce) scintillator, representing the state of the art of the gamma ray diagnostics in tokamaks. This spectrometer can investigate multiple aspects about particles in a tokamak, providing an all-in-one solution for gamma diagnostics. In this thesis, three different applications of a $LaBr_3$:Ce-based detector are proposed, regarding fusion power measurements (Chapter 2), alpha birth profile reconstruction (Chapter 3) and Bremsstrahlung emission detection from Runaway Electrons (Chapter 4).

1.1 Basic concepts of fusion reactors

1.1.1 Nuclear fusion

To understand how the fusion reaction works and how energy can be obtained from this process, it is first necessary to introduce the concept of *binding energy*. The binding energy B of a nucleus ${}^{\mathrm{A}}_{\mathrm{Z}}\mathrm{X}_{\mathrm{N}}$ (Z: number of protons; N: number of neutrons, $A = Z + N$: mass number) is the difference in mass (expressed in energy by the relation $E = mc^2$) between the nucleus itself and its single nucleons:

$$B = \{Zm_p + Nm_n - m(X)\}\, c^2 \tag{1.1}$$

where m_p and m_n are the proton and neutron mass, respectively, $m(X)$ is the mass of the nucleus and c is the speed of light.
In the liquid drop model of the atomic nucleus, it is possible to define a relationship between binding energy and atomic mass:

$$B = a_v\, A - a_s\, A^{2/3} - a_c\, Z(Z-1)A^{-1/3} - a_{sym}\, \frac{(A-2Z)^2}{A} + \delta \tag{1.2}$$

The first term is called the *volume term*, the second the *surface term*, the third the *Coulomb term*, the fourth the *symmetry term* and finally δ denotes the *pairing term*. Dividing the binding energy by A, we obtain the binding energy per nucleon B/A (see Figure 1.1). In Figure 1.1, one can distinguish a region at $A \sim 60$ with approximately

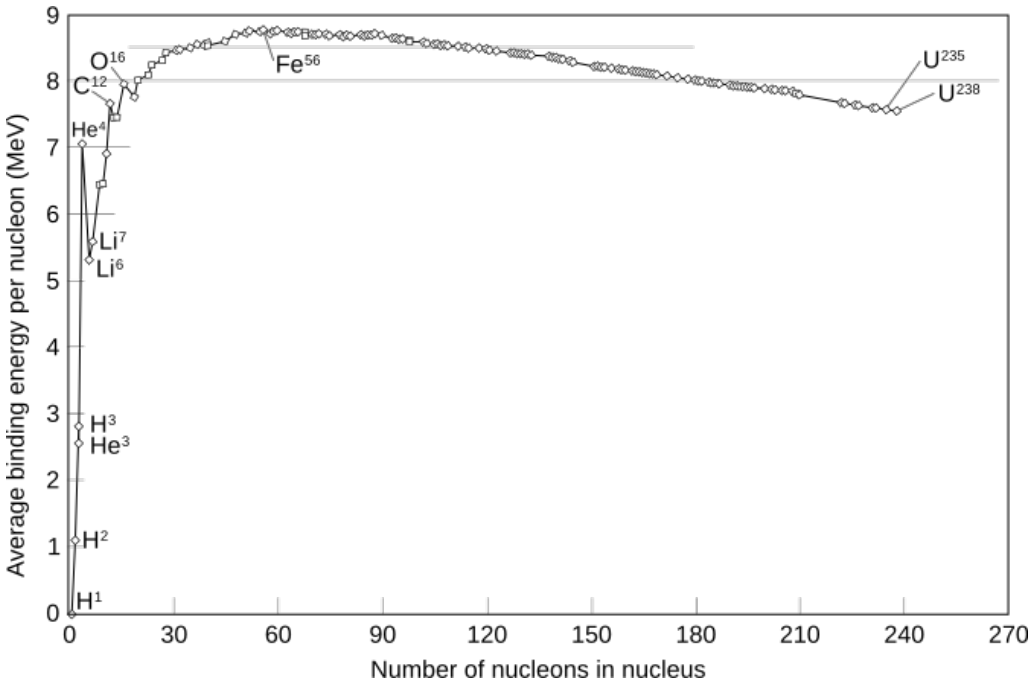

Figure 1.1: Binding energy per nucleon as a trend of the mass number.[3]

constant B/A, a region at low A (A≪60) where B/A increases suddenly, and a region at high A (A≫60) where B/A decreases slowly. It can be deduced that by dividing a heavy nucleus (high A region) into two lighter nuclei, it is possible to release energy, since a reaction of this type, called *fission*, is exoenergetic. On the contrary, if two light nuclei (low A region) are merged together to produce a nucleus with a higher A, it is possible to release energy. This process is called **fusion**.

The fusion reaction is based on the strong nuclear interaction, a short-range force (with characteristic length on the order of the diameter of a nucleus), much more intense than the repulsive Coulomb interaction between 2 positive nuclei at these distances. By merging light nuclei we increase the binding energy between the initial and final states.
Considering a generic nuclear reaction:

$$\alpha + \beta \longrightarrow 1 + 2 + ... + \mathrm{n} + \mathrm{Q} \tag{1.3}$$

the released energy Q will be given by:

$$Q = \left[m_\alpha + m_\beta - m_1 - m_2 - ... - m_n\right] c^2 \tag{1.4}$$

where α and β are the two reactants; 1,2,...,n are the products; m_α and m_β are the reactant masses; m_1 ... m_n are the product masses. Usually Q can reach up to 10-100 MeV for nuclear reactions.

The sun is a typical example of a self-sustaining fusion "reactor". Indeed, the fusion reactions that occur in the core of this star are responsible for its luminosity, and consequently for the presence of life on Earth. The most significant reaction involves protons in the proton-proton cycle, where the net production is constituted

by a helium-4 nucleus starting from four protons:

$$4\,{}^{1}\mathrm{H} \longrightarrow {}^{4}\mathrm{He} + 2\,\mathrm{e}^{+} + 2\,\nu + 26.7\ \mathrm{MeV} \tag{1.5}$$

Deuterium (D) and Tritium (T), hydrogen isotopes, are the most interesting "fuels" for controlled fusion on Earth. The reaction between them (DT reaction) is considered the most promising for the production of electric energy:

$$\mathrm{D} + \mathrm{T} \longrightarrow {}^{4}\mathrm{He} + \mathrm{n} + 17.59\ \mathrm{MeV} \tag{1.6}$$

The Q factor of the reaction is approximately equal to 17.6 MeV. This energy is released as kinetic energy of the fusion products, where the neutron obtain about four-fifths (≈ 14.1 MeV) of the total released energy while the alpha particle obtain about one-fifth (≈ 3.5 MeV). Deuterium consists of the 0.0153% of the total hydrogen in nature, which is still abundant enough for fusion purposes. This means that there is one deuterium nucleus for every ≈ 6500 hydrogen nuclei. The amounts of deuterium in nature is enough to satisfy the world's energy needs. It is expected to last for millions of years, based on current consumption [4]. In contrast, tritium cannot be found in sufficient quantities in nature, as it is radioactive and has a half-life of about 12 years. It can be produced from lithium through the following reactions:

$$\begin{aligned} \mathrm{n} + {}^{6}\mathrm{Li} &\longrightarrow {}^{4}\mathrm{He} + \mathrm{T} + 4.78\,\mathrm{MeV} \\ \mathrm{n} + {}^{7}\mathrm{Li} &\longrightarrow {}^{4}\mathrm{He} + \mathrm{T} + \mathrm{n} - 2.57\,\mathrm{MeV} \end{aligned} \tag{1.7}$$

If all fusion-born neutrons contribute to the reaction with lithium-6, this would guarantee the generation of a tritium nucleus for each incident neutron. In practice, neutron losses (i.e., neutrons that don't react with lithium) are always present, so neutron multiplication is necessary. This solution consists of using the incident fusion-born neutron to produce multiple neutrons coming from a fission blanket.
The natural reserves of lithium on Earth are quite large, approximately for a few tens of thousands of years (based on current world energy consumption). Lithium from sea water could represent another longer source of this element (up to millions of years) [5]. The DT reaction has some disadvantages related to tritium hazard, as tritium is radioactive. In addition, neutrons can make the reactor walls radioactive through activation [6].

Another of the most studied fusion reactions is that involving a deuterium and a helium-3 ($\mathrm{D}^{3}\mathrm{He}$) nucleus:

$$\mathrm{D} + {}^{3}\mathrm{He} \longrightarrow {}^{4}\mathrm{He} + \mathrm{p} + 18.3\,\mathrm{MeV} \tag{1.8}$$

Helium is rare on Earth, so this reaction is not considered among the most promising ones. Furthermore, compared to the DT reaction, higher temperatures are needed to obtain comparable performances. The advantage is that, since this reaction doesn't produce neutrons, risks of damage and activation of the walls of the machine are reduced. Anyway, deuterium is present and deuterium-deuterium (DD) reaction, producing neutrons, can occur.

The DD reaction involves two deuterium nuclei. This reaction has two main channels:

$$\begin{aligned} \mathrm{D} + \mathrm{D} &\longrightarrow {}^{3}\mathrm{He} + \mathrm{n} + 3.27\ \mathrm{MeV} \\ \mathrm{D} + \mathrm{D} &\longrightarrow \mathrm{T} + \mathrm{p} + 4.03\ \mathrm{MeV} \end{aligned} \tag{1.9}$$

The DD reaction produces both helium-3 and tritium. These can undergo fusion reaction with the deuterium already present in the machine through the D^{3}He and DT reaction, respectively, establishing the catalyzed DD reaction:

$$6\,\mathrm{D} \longrightarrow 2\,\mathrm{H} + 2\,\mathrm{n} + 2\,{}^{4}\mathrm{He} + 43.2\ \mathrm{MeV} \tag{1.10}$$

Using this reaction, the necessity to produce tritium from lithium disappears, but higher temperatures are needed and lower power densities than the DT reaction are obtained.

To trigger the fusion reaction, the charged reactants must collide and overcome the strong Coulomb potential barrier. Based on the relative energy between them, there is a finite probability of overcoming the barrier and undergoing fusion. The fusion cross section describes and quantifies the phenomenon. Observing Figure 1.2,

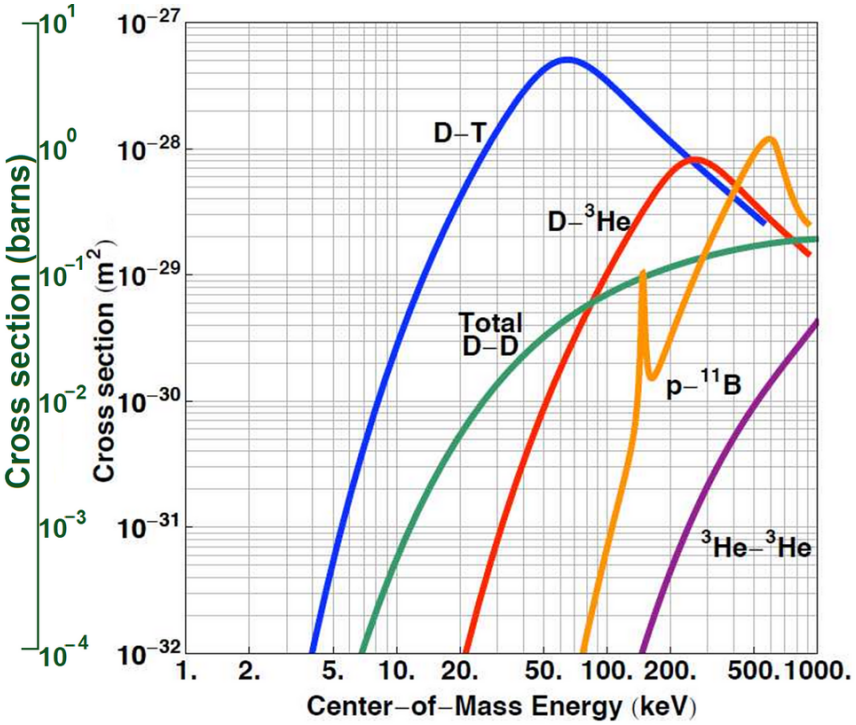

Figure 1.2: Cross section for different types of fusion reactions, as a trend of the collision energy in the centre of mass frame. [7]

the reasons behind the choice of a machine exploiting deuterium and tritium becomes clear. It is found that at 20 keV the DT cross section is about 100 times the DD cross section. Therefore, for the DD reaction a more advanced technology is needed, suggesting that the first fusion production milestone will be likely reached through the DT reaction.

1.1.2 Plasma

The fusion reaction is in competition with other ones, which can significantly lower the efficiency of a reactor. For instance, these can derive from Coulomb collisions between charged particles, or from atomic collisions between charged and neutral particles. If this type of collisions are inelastic, they can excite or ionise atoms. Moreover, the typical cross sections are much larger than the fusion cross sections (10^{-16} cm^2 compared to the fusion cross sections 10^{-24} cm^2).

For example, a beam of deuterium ($\sim 10 - 50$ keV) can impinge on a fixed target (solid, liquid or gas) of tritiated water T_2O, in order to produce energy. By directing a beam against a neutral target, it happens that most of the reactions that take place are ionization reactions rather than fusion reactions. Most of the collisions are related to atomic processes that dissipate most of the beam energy. Given the average time to have a fusion reaction $\tau_f = (\sigma_f v_{b-t} n_t)^{-1}$ and given the average time for an atomic collision $\tau_a = (\sigma_a v_{b-t} n_t)^{-1}$, one can notice that

$$\frac{\tau_f}{\tau_a} = \frac{\sigma_a}{\sigma_f} \sim 10^8 \tag{1.11}$$

that is, for each fusion reaction, about 10^8 atomic processes occur. Here, v_{b-t} is the relative velocity between the beam and the target particles, while n_t is the density of the target. The quantities σ_f and σ_a are the fusion and atomic reaction cross section, with characteristic values of 10^{-24} cm^2 and 10^{-16} cm^2, respectively. Therefore, neutral targets are not energetically convenient for fusion reactor purposes.

Already ionised fuels could represent a better choice, like a **plasma**:

"A plasma is a quasi-neutral gas of charged and neutral particles exhibiting collective behaviours." [8]

A plasma is a state of matter (the fourth, after solid, liquid and gas) composed of a multitude of ions, electrons, atoms or molecules, interacting with each other. The force responsible for the collective behaviours is the Coulomb force. To obtain a plasma it is necessary that a gas is supplied with a sufficient amount of energy to start the ionization process. Atoms or molecules lose electrons as a result of ionization processes due to the high kinetic energies of other particles, when the latter reach a sufficient energy threshold. It is possible to do this state-transition through photoionization, or through an electric discharge into the plasma. In the first case, the gas particles absorb photons with energy greater than or equal to the ionization potential of the particle itself. The excess energy is transformed into kinetic energy that is exchanged in the new-born electron-ion pair. Instead, for electric discharges an electric field applied in the gas region is used. Free electrons are accelerated to the point where they acquire enough energy to ionise neutral particles in the gas. Typically, electrons are released from the ionization process with a higher kinetic energy than ions. As a result, the electron population usually has a higher temperature than the ions, and the transfer of energy through collisions of electrons with much heavier particles is very slow.
In the tokamak core, fusion plasmas have the characteristic of being completely

ionised and having ionic and electronic temperatures approximately equal, both around 1-10 keV. They are subjected to large magnetic fields (a few Tesla), and have typical densities around $10^{19} - 10^{21}$ particles per cubic meter.
The cause of collective behaviour is due to the fact that the plasma consists of charged particles. Therefore, when these move, they can generate local concentrations of positive and negative charges, producing electric fields. In addition, electric currents or magnetic fields can be generated. These fields can influence the motion of other more distant charged particles.

To obtain fusion reactions, one can take a target plasma and collide the ionised particles in it (beam-target). Even if in this case the ionization reactions are not present, there will be competition with Coulomb collisions. In this case, the beam would lose much of its energy by transferring it to the plasma particles instead of incurring fusion reactions. However, this process could serve as a heating mechanism. It is possible to use two beams of ions that are brought to collide (beam-beam), but the typical density of the beams is much lower than that of the plasmas. Consequently, the fusion power produced would be very low. It is more convenient to use exclusively the plasma itself at high temperature, where the target particles and incident ones coincide (target-target).

1.1.3 Magnetic confinement and tokamaks

The magnetic confinement of plasmas is considered the most promising method for exploiting fusion energy. Closed geometries are preferred for confinement systems, where the magnetic field lines are enclosed in toroidal volumes.

Consider a vacuum chamber in the shape of an infinitely long cylinder, in which a plasma is generated. If no magnetic field were applied, the plasma particles would suddenly reach the walls and would be lost. Instead, if a strong magnetic field were turned on, directed along the axis of the cylinder, the free motion of the particles would be interrupted, and helical trajectories would be observed. Therefore, a magnetic field is capable of confining ions and electrons in the direction transverse to the axis of the cylinder. The motion of charged particles is influenced by the Lorentz force:

$$m\frac{d\vec{v}}{dt} = q\vec{E} + q\left(\vec{v} \wedge \vec{B}\right) \tag{1.12}$$

where m is the mass of the particle, q its charge, $\vec{v}$ its velocity, $\vec{E}$ and $\vec{B}$ are the electric and the magnetic fields, respectively.
Then, the circular motion around the field line is produced by the Lorentz force, with a pulsation given by:

$$\omega_c = \frac{qB}{m} \tag{1.13}$$

called cyclotron or Larmor pulsation. Instead, the Larmor radius of the circular rotation motion, is given by

$$r_L = \frac{v_\perp}{\omega_c} = \frac{mv_\perp}{qB} \tag{1.14}$$

Therefore, r_L increases with increasing transverse velocity to the magnetic field, $v_\perp$, and decreases with increasing magnetic field intensity, B.

Since the velocity scales as the square root of the kinetic energy, if the energy is related to the thermal motion of the particles then, in the case of deuterium:

$$r_L\ (cm) \simeq \frac{\sqrt{T\ (keV)}}{2B\ (T)} \tag{1.15}$$

In practice, taking a 10 keV plasma immersed in a magnetic field of 5 T, then $r_L \sim$ 0.3 cm for deuterium, and this length is much smaller than the typical dimensions of the chamber ($\sim$ 1 m). For electrons, r_L is even smaller. The gyration of ions and electrons around the guiding centre is a phenomenon comparable to that of small coils carrying current. Indeed, similarly to currents in coils, charged particles produce a dipole moment when immersed in a magnetic field. A small field is generated that is opposite to the external magnetic field, thus reducing the latter. This behaviour is called plasma diamagnetism.

So far, an ideal configuration of an infinite cylinder has been considered. However, into a real scenario the size of the device is finite. Throughout years, several kind of geometries for plasma confinement have been studied. The toroidal geometry has proved to be the most promising. Essentially, a torus consists of a finite cylinder, bended so that the two ends are joint, resulting in a closed geometry. However, The ideal confinement conditions begin to break down in the case of the toroid. The confinement technique loses effectiveness, due to the arising of magnetic field inhomogeneities.
The plasma particles, when immersed in non-uniform magnetic fields, will experience velocity drifts. In this treatment, collisions between plasma particles and particle-waves interaction are ignored, and only interactions with external forces are considered. The arising of drifts is studied in toroidal configurations, leading the particles to escape from the machine.
Assuming that we have a magnetic field parallel to the axis of the torus, if there were no external forces $\vec{F} = 0$, then the trajectory of ions and electrons would be helical. If instead $\vec{F} \neq 0$ (due, for example, to inhomogeneities in the magnetic field), in addition to the circular motion in the plane orthogonal to the magnetic field, a drift velocity is established, in the same plane on which the circular motion occurs. This trajectory is called cycloid. The velocity of a particle in this case can be expressed as follows:

$$\vec{v} = \vec{v}_{\parallel} + \vec{v}_{rot} + \vec{v}_d \tag{1.16}$$

where

$$\vec{v}_d = \frac{\vec{F} \wedge \vec{B}}{qB^2} \tag{1.17}$$

is the drift velocity, which is always perpendicular to the direction of the magnetic field and to the external force acting on the particle [9]. Then, the particle motion will have a component parallel to the field B ($\vec{v}_{\parallel}$, possibly accelerated by an external force F_z), a rotational motion around the magnetic field line ($\vec{v}_{rot}$), and a drift of the Larmor centre of rotation ($\vec{v}_d$).
This approach, called the *guiding centre* approximation, is applicable to both ions and electrons and is valid under some conditions: the typical dimensions of the plasma must be much larger than the Larmor radius of the ions; collisions are not

considered; the temporal and spatial variations of the external forces and the magnetic field must be small on the spatial and temporal scales of the gyration motion.

The токамáк is a device for studying nuclear fusion, confining plasmas in a closed geometry through magnetic fields (a schematic is shown in Figure 1.3). It consists in a toroidal chamber wrapped by coils used to generate a magnetic field along the axis of the torus.

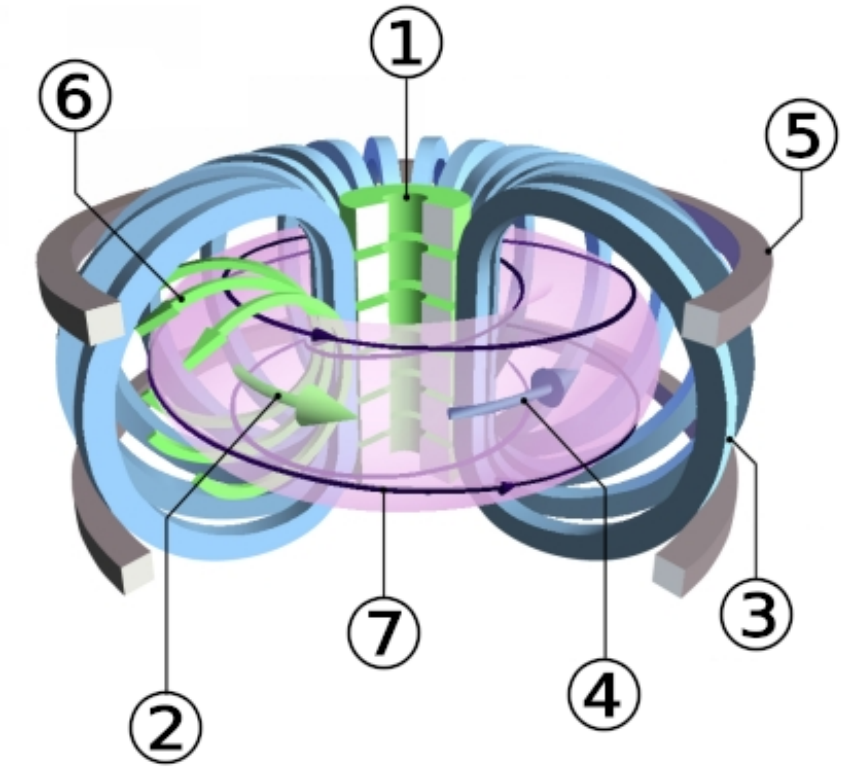

Figure 1.3: Schematic of a tokamak device and its fields. (1) Central solenoid for the production of the toroidal current (and poloidal magnetic field). (2) Toroidal magnetic field. (3) Toroidal field coils. (4) Toroidal current. (5) Poloidal Field Coil for plasma shaping and control. (6) Poloidal Field. (7) Resulting magnetic field lines. [10]

The inhomogeneities that arise in this type of closed field line configuration can be derived. Let I be the current flowing in the coils. This is linked with each circumference on which the magnetic field lies inside the torus. By the Ampere's circuitation theorem:

$$\oint \vec{B} \cdot d\vec{l} = 2\pi RB = \mu_0 I \tag{1.18}$$

therefore

$$B \propto \frac{1}{R} \tag{1.19}$$

where R is the radius of the device in cylindrical coordinates.
Ultimately, the Tokamak has an inhomogeneous magnetic field, due to the curvature

of the field lines but also due to its gradient: in fact, the field is greater closer to the centre of the torus. Therefore

$$\vec{v}_d = \vec{v}_\nabla + \vec{v}_{curv} \tag{1.20}$$

It can be shown that the drifts due to curvature and field gradient are given by the following relations

$$\vec{v}_\nabla = -\mu \frac{\nabla B \wedge \vec{B}}{qB^2} \tag{1.21}$$

$$\vec{v}_{curv} = -\frac{mv_\parallel^2}{R_C^2} \frac{\vec{R}_C \wedge \vec{B}}{qB^2} \tag{1.22}$$

where μ is the magnetic dipole moment of the particle, $v_\parallel$ is the velocity parallel to the magnetic field, R_C is the distance from the central axis of the torus (the radius of curvature related to the curvature of the field lines) [9]. Both effects, in the toroidal configuration, induce a drift of the particles in the vertical direction. Furthermore, the presence of the charge q in Eq. 1.21 and 1.22 leads to an opposite drift in the case of electrons and ions, establishing a net current with consequent separation of the charges which produces an electric field E. The drift due to the electric force $\vec{F} = q\vec{E}$ is given by

$$\vec{v}_E = \frac{\vec{E} \wedge \vec{B}}{B^2} \tag{1.23}$$

which is independent of the charge. This fact will lead to a translation of the entire plasma. In the case of the toroid, this drift is directed outwards, that is, towards the direction of $\vec{R}$.
As a result, given a high-temperature plasma, there would be a rapid loss of particles, resulting in damage to the chamber walls and contamination of the plasma. This fact shows that it is not possible to use a purely toroidal field for plasma confinement in a Tokamak.
To solve the problem, the idea is to add a poloidal magnetic field that modifies the field lines. To produce the poloidal field, a toroidal current is used in the plasma. The latter is established using a current-carrying solenoid placed on the internal vertical axis of the torus, which acts as the primary circuit of a transformer, while the plasma itself acts as the secondary circuit.
The resulting magnetic lines are helical, and wrapped around toroidal surfaces. A particle, following the field line, will repeatedly find itself above or below the surface, and the vertical drift will cause the particle to move outside and inside that surface, alternately. In this way the two effects compensate each other and the particle's orbit remains in a limited spatial region around the toroidal surface.
These surfaces are called magnetic surfaces. In the toroid both the poloidal component B_P and the toroidal component B_T of the magnetic field can be found. The force lines of the total field $\vec{B} = \vec{B}_P + \vec{B}_T$ are helices that wind on toroidal surfaces.

In toroidal magnetic confinement devices, the *safety factor* q is a fundamental parameter that characterises the winding of magnetic field lines around the torus. It is defined as the number of toroidal revolutions a field line makes for each poloidal

revolution:

$$q = \frac{\text{toroidal turns}}{\text{poloidal turns}} = \frac{r}{R}\frac{B_T}{B_P}, \tag{1.24}$$

where R is the major radius, r the minor radius, B_T the toroidal magnetic field, and B_P the poloidal magnetic field. Equivalently, the rotational transform i is the poloidal angle advanced per toroidal turn, with $q = 2\pi/i$.

Magnetic surfaces can be classified as *rational* or *irrational* depending on the ratio $i/2\pi$. On rational surfaces, $i/2\pi = n/m$ is a rational number, meaning the field line reconnects after a finite number of turns. On irrational surfaces, $i/2\pi$ is irrational, and the field line densely covers the surface in an ergodic fashion [2].

The safety factor q is crucial for plasma stability: low or very high values of q are associated with the onset of magnetohydrodynamic (MHD) instabilities, such as kink or tearing modes. Typical tokamak operation aims to maintain q within a safe interval, often $q \gtrsim 1$ at the plasma center, to avoid such instabilities and ensure effective confinement.

1.1.4 Energetic balance of a tokamak

In this section, the conditions under which a fusion reactor should operate to reach ignition are discussed. The plasma should be able to sustain the fusion reaction continuously, without the need for external heating.
Different tokamak operation regimes will be considered: ignition in the ideal case (without energy losses due to transport); ignition in non-ideal cases; and the externally driven regime, i.e., the case in which the plasma is sustained by external energy input, without reaching ignition.

First, two important parameters are introduced: the reaction rate and the reactivity.
The reaction rate represents the number of fusion reactions occurring per unit time and per unit volume, at a specific location within the plasma. For two interacting species with given distribution functions, the reaction rate R is given by

$$R = \iint d^3\vec{v}_1 d^3\vec{v}_2 \, \sigma(v_{rel}) \, v_{rel} \, f_1(\vec{v}_1) f_2(\vec{v}_2) \tag{1.25}$$

where the integral is taken over all possible velocities of reactants 1 and 2 ($\vec{v}_1$ and $\vec{v}_2$, respectively). v_{rel} is the relative velocity between $\vec{v}_1$ and $\vec{v}_2$, while f_1 and f_2 are the distribution functions of the two reactant species.
Typically, in tokamak thermonuclear plasmas, the velocity distributions of the reactants are assumed to be Maxwellian:

$$f_j(v_j) = n_j \left(\frac{m_j}{2\pi T_j}\right)^{3/2} \exp\left(-\frac{m_j v_j^2}{2T_j}\right) \tag{1.26}$$

where n_j is the density of reactant j, m_j its mass, and T_j its temperature. The distribution function may vary significantly if different heating schemes are applied. For a homogeneous plasma with constant n_j, the reaction rate can be rewritten as:

$$R = n_1 n_2 \langle \sigma v \rangle \tag{1.27}$$

where $\langle \sigma v \rangle$ is called the *reactivity*. Figure 1.4 shows reactivity curves as a function of temperature for Maxwellian distributions in various reactions.

The fusion power density P_f is described by:

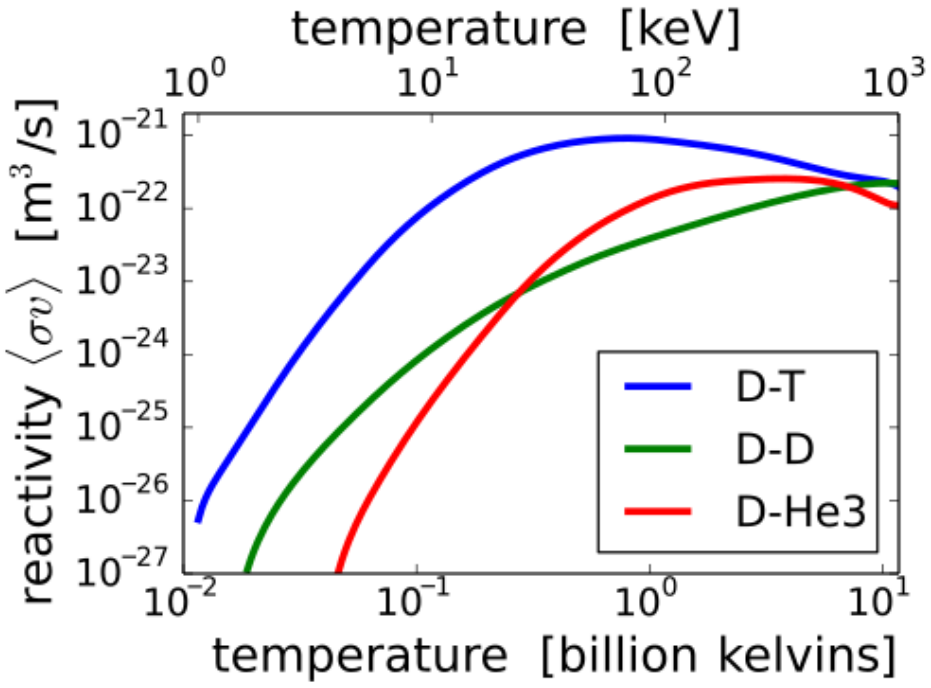

Figure 1.4: Reactivity as a function of plasma temperature (expressed in keV and GK) assuming Maxwellian distributions, for DT, DD, and D^3He reactions [11].

$$P_f = R\,\epsilon_f = n_1 n_2 \langle \sigma v \rangle \epsilon_f \tag{1.28}$$

where ϵ_f is the energy released by a single fusion reaction. For the DT reaction, the power densities corresponding to the specific reaction products are:

$$\begin{aligned} P_\alpha &= n_D n_T \langle \sigma v \rangle \epsilon_\alpha \\ P_n &= n_D n_T \langle \sigma v \rangle \epsilon_n \end{aligned} \tag{1.29}$$

with $\epsilon_\alpha \simeq \epsilon_f/5$ and $\epsilon_n \simeq 4\epsilon_f/5$. One can note that $\epsilon_f = \epsilon_\alpha + \epsilon_n$, so

$$P_f = P_\alpha + P_n \tag{1.30}$$

The power density depends on the total energy released per reaction and on the reactivity. Assuming pure Maxwellian reactants, Figure 1.4 shows that the DT reaction provides the highest fusion power density compared to DD and D^3He reactions. For simplicity and to maximize fusion power, the case $n/2 = n_D = n_T$ is considered.

Ignition

For a plasma with Maxwellian reactants, achieving ignition requires exceeding a characteristic temperature such that the power generated by fusion surpasses the

power lost by the plasma. This temperature is approximately 4 keV for DT and 40 keV for DD. However, energy losses also arise from other mechanisms. An *effective ignition temperature* is defined, at which the charged products balance all energy losses.

The power loss density is given by:

$$P_L = \frac{W}{\tau_E} \tag{1.31}$$

where τ_E is the energy confinement time, and W is the total plasma energy density:

$$W = \frac{1}{V} \int 3nTd^3\vec{x} \tag{1.32}$$

This loss is compensated by auxiliary heating, with power density

$$P_H = P_L \tag{1.33}$$

The energy confinement time can be calculated from experimentally measurable quantities:

$$\tau_E = \frac{W}{P_H} \tag{1.34}$$

Fusion reactions produce charged particles (e.g., alpha particles in DT plasmas) that transfer energy to the plasma via Coulomb collisions. For DT, the total fusion power is:

$$P_f = P_\alpha + P_n \simeq 5P_\alpha \tag{1.35}$$

The associated alpha power density (Equation 1.29) is:

$$P_\alpha = \frac{1}{4} n^2 \langle \sigma v \rangle \epsilon_\alpha \tag{1.36}$$

and Equation 1.33 becomes:

$$P_L = P_H = P_H^{ext} + P_\alpha \tag{1.37}$$

Assuming uniform (in terms of temperature and density) plasma (Equation 1.32), this can be rewritten as:

$$P_H^{ext} + \frac{1}{4} n^2 \langle \sigma v \rangle \epsilon_\alpha = \frac{3nT}{\tau_E} \tag{1.38}$$

The ignition condition occurs when auxiliary heating is not required ($P_H^{ext} = 0$) and the plasma is self-sustaining. Assuming uniform density and temperature, Equation 1.38 reduces to:

$$(n\tau_E)_i > \frac{12}{\langle \sigma v \rangle} \frac{T}{\epsilon_\alpha} \tag{1.39}$$

For Maxwellian distributions, the right-hand side of Equation 1.39 is minimized at $T \simeq 30$ keV. In practice, τ_E also depends on temperature, shifting the optimal range to 10–20 keV, where the reactivity scales approximately with T^2. The *Lawson criterion* for ignition is thus:

$$(nT\tau_E)_i > 3 \cdot 10^{21} \frac{keV \cdot s}{m^3} \tag{1.40}$$

For parabolic profiles of n and T (varying with distance from the plasma centre), the criterion becomes $5 \cdot 10^{21}$ keV s m^{-3}.

Breakeven

Breakeven occurs when $P_f = P_L$, i.e., the fusion power equals the power lost:

$$P_L = P_\alpha + P_n \tag{1.41}$$

Similarly to ignition, the breakeven criterion is:

$$(n\tau_E)_b \geq \frac{12}{\epsilon_f}\frac{T}{\langle\sigma v\rangle} = \frac{1}{5}(n\tau_E)_i \tag{1.42}$$

Hence, the $n\tau_E$ required for breakeven is five times smaller than that for ignition.

The Fusion gain factor

The gain factor Q of a tokamak is defined as:

$$Q = \frac{\text{thermal power output}}{\text{heating power input}} = \frac{P_{out}}{P_{in}} = \frac{P_f}{P_H^{ext}} \tag{1.43}$$

Q ranges from 0 to ∞. $Q = 0$ indicates no energy production ($P_f = 0$), while $Q = \infty$ corresponds to ignition ($P_{in} = 0$). For $Q = 1$, the fusion power equals the auxiliary heating power. Experimental reactors like ITER or SPARC aim for $Q \sim 10$, while future energy-producing reactors target $Q \sim 30$–40. These conditions correspond to the *externally driven regime*.

Externally driven regime

In the externally driven regime, $P_H^{ext} \neq 0$. Denoting f_α as the fraction of alpha particle power retained in the plasma, energy balance requires:

$$P_H^{ext} + f_\alpha P_\alpha \geq P_L \tag{1.44}$$

where P_L accounts for all energy losses, including Bremsstrahlung and turbulence. For the DT reaction, assuming an efficiency η for recovering energy leaving the plasma, the auxiliary heating can be expressed as:

$$P_H^{ext} = \eta[(1 - f_\alpha)P_\alpha + P_n + P_L] \simeq \eta\left[(5 - f_\alpha)\,P_\alpha + P_L\right] \tag{1.45}$$

where $P_n \simeq 5P_\alpha$. The fraction $(1 - f_\alpha)$ of alpha particle power leaving the plasma can be recovered and reused for heating.
The Lawson criterion for the externally driven regime becomes:

$$(n\tau_E)_{ext} \geq \gamma\frac{12}{\epsilon_\alpha}\frac{T}{<\sigma v>} = \gamma(n\tau_E)_i \tag{1.46}$$

with

$$\gamma = \frac{1-\eta}{f_\alpha + \eta\,(5 - f_\alpha)} \tag{1.47}$$

The ignition criterion corresponds to $\gamma = 1$. If $\gamma \leq 1$, ignition could in principle be easier to achieve. In practice, however, achieving $\gamma < 1$ is difficult due to the typically low value of η ($\lesssim 0.3$). Note that in this analysis, total neutron power compensates for losses; if neutron energy were to be used productively, η would decrease further.

1.2 Gamma-ray detection

Tokamak plasmas emit various kinds of particles and radiation. In particular, these particles carry valuable information about the plasma conditions.
In this thesis, the role of gamma-ray diagnostics in tokamaks is discussed, and practical applications of gamma-ray measurements are investigated. This section provides a brief introduction to gamma-ray spectroscopy, focusing in particular on scintillator detectors, taking Cerium-activated Lanthanum Bromide ($LaBr_3$:Ce) as a reference. A detailed description of gamma-ray detection can be found in Ref. [12].

1.2.1 Interaction of gamma-rays with matter

In a medium, radiation loses energy through different interaction mechanisms, which depend on the type of particle or photon:

- **Heavy charged particles** (e.g., protons, alpha particles, and ionised nuclei) primarily lose energy via *Coulomb interactions* with the electrons of the medium. At high energies, additional processes such as *Bremsstrahlung* can contribute.

- **Fast electrons** (e.g., beta particles) also interact predominantly through Coulomb collisions. They can additionally radiate energy via *Bremsstrahlung* when accelerated in the electric fields of nuclei.

- **Photons** (X-rays and gamma rays) interact through discrete processes: the *photoelectric effect*, *Compton scattering*, and *pair production* at high energies. These interactions transfer energy to electrons or, in pair production, create electron-positron pairs, which subsequently deposit energy in the medium similarly to fast electrons.

- **Neutrons** interact with nuclei of the medium in discrete collisions, often transferring a significant fraction of their energy in each event.

This classification clarifies how different radiation types deposit energy, and it provides the basis for understanding the operation of detectors: in all cases, the measurable signal arises from the energy ultimately transferred to electrons or nuclei in the medium.

Fast electrons lose energy along a scattered, non-linear path within the material. Their mean free path is generally larger than that of heavy charged particles, and large deviations from the initial trajectory occur because the mass of the fast particle is comparable to that of the medium's electrons. Consequently, a larger fraction of energy can be lost in each interaction.
Bethe derived an expression describing the energy loss of an electron through colli-

sions (referred as stopping power):

$$-\left(\frac{dE}{dx}\right)_{\text{coll}} = \frac{2\pi e^4 ZN}{m_e v^2}\left[\ln\left(\frac{m_e v^2 E}{2I^2(1-\beta^2)}\right)\right.$$
$$\left. - (\ln 2)\left(2\sqrt{1-\beta^2} - 1 + \beta^2\right) + (1-\beta^2) + \frac{1}{8}\left(1-\sqrt{1-\beta^2}\right)^2\right] \quad (1.48)$$

where Z is the atomic number of the medium, N is the number of atoms per unit volume, m_e is the electron mass, v is the velocity of the incoming electron, $\beta = v/c$, E is the energy of the incoming electron, and I is the mean ionisation potential of the medium [13].
There are also radiative processes, mainly due to Bremsstrahlung emission, through which fast electrons lose energy in the material. These processes are usually less efficient but become more relevant for materials with high Z and at high electron energies. From theory, any accelerated charged particle emits radiation, and the acceleration corresponds to a deflection of its trajectory. The radiative energy loss can be expressed as:

$$-\left(\frac{dE}{dx}\right)_{\text{rad}} = \frac{NEZ(Z+1)e^4}{137 m_e^2 c^4}\left[4\ln\left(\frac{2E}{m_e c^2}\right) - \frac{4}{3}\right] \quad (1.49)$$

The total energy loss rate is given by the sum of Equations 1.48 and 1.49.
Roughly, the range of fast electrons in materials is of the order of a few millimetres per MeV, depending on the material's density. The typical attenuation curve of fast electrons is empirically approximated as:

$$I = I_0 e^{-nt} \quad (1.50)$$

where I_0 is the initial intensity of the electron beam, I is the intensity after passing through a thickness t (g/cm^2) of material, and n is the absorption coefficient.
Fast electrons have been discussed because gamma rays interact with matter primarily by transferring their energy to the medium's electrons. The main gamma–electron interaction mechanisms are: photoelectric absorption, Compton scattering, and pair production. As previously mentioned, gamma rays interact through one or a few discrete events with electrons, whereas the latter gradually transfer their energy to atoms.

Photoelectric effect

Photoelectric absorption is characterised by the complete transfer of the gamma-ray energy to an atomic electron in the medium. In this process, the photon disappears, giving all its energy to the ejected photoelectron. Typically, for sufficiently energetic gamma rays, the photoelectron originates from the a K-shell of the atom, the most tightly bound shells. The photoelectron gains an energy given by:

$$E_e = E_\gamma - E_B \quad (1.51)$$

where E_γ is the energy of the incoming gamma ray, and E_B is the electron binding energy. For photons with energies of a few hundred keV or more, the photoelectron acquires almost all the photon's energy.
A vacancy is left in the atom, which can be filled by a free electron or by an electron transition from an upper shell, producing a characteristic X-ray or, alternatively, an Auger electron.
The photoelectric effect is the most probable interaction for gamma rays in the X-ray and soft gamma-ray energy range, and it is enhanced in materials with high atomic number Z. The photoelectric probability scales approximately as:

$$\tau \propto \frac{Z^n}{E_\gamma^{3.5}} \tag{1.52}$$

where n varies between 4 and 5, depending on the gamma-ray energy range. This strong dependence on Z explains why high-Z materials such as tungsten and lead are effective gamma-ray shields.

Compton scattering

During Compton scattering, an incident gamma-ray photon interacts with an electron of the material. Both are scattered, and the photon transfers part of its energy to the electron as kinetic energy. In this process, all scattering angles are possible, and the transferred energy varies from nearly zero up to a significant fraction of the initial photon energy. The energy of the scattered photon, E'_γ, is given by:

$$E'_\gamma = \frac{E_\gamma}{1 + \frac{E_\gamma}{m_e c^2}(1 - \cos\theta)} \tag{1.53}$$

where E_γ is the energy of the incoming photon, m_e is the electron mass, c is the speed of light, and θ is the photon scattering angle relative to its initial direction.
As indicated by Equation 1.53, the energy transferred to the electron is negligible for $\theta \approx 0$, while it becomes maximal for $\theta \approx \pi$, even though the photon is not completely absorbed.
The angular distribution of the scattered gamma rays is given by the Klein–Nishina formula, defining the scattering cross section as:

$$\frac{d\sigma}{d\Omega} = Z r_0^2 \left(\frac{1}{1+\alpha(1-\cos\theta)}\right)^2 \left(\frac{1+\cos^2\theta}{2}\right)\left(1 + \frac{\alpha^2(1-\cos\theta)^2}{(1+\cos^2\theta)[1+\alpha(1-\cos\theta)]}\right) \tag{1.54}$$

where r_0 is the classical electron radius, $\alpha = E_\gamma/(m_e c^2)$, and Z is the atomic number of the medium. The cross section is proportional to Z, as the probability of Compton scattering per atom depends on the total number of available electrons. An example is shown in Figure 1.5 for different photon energies.

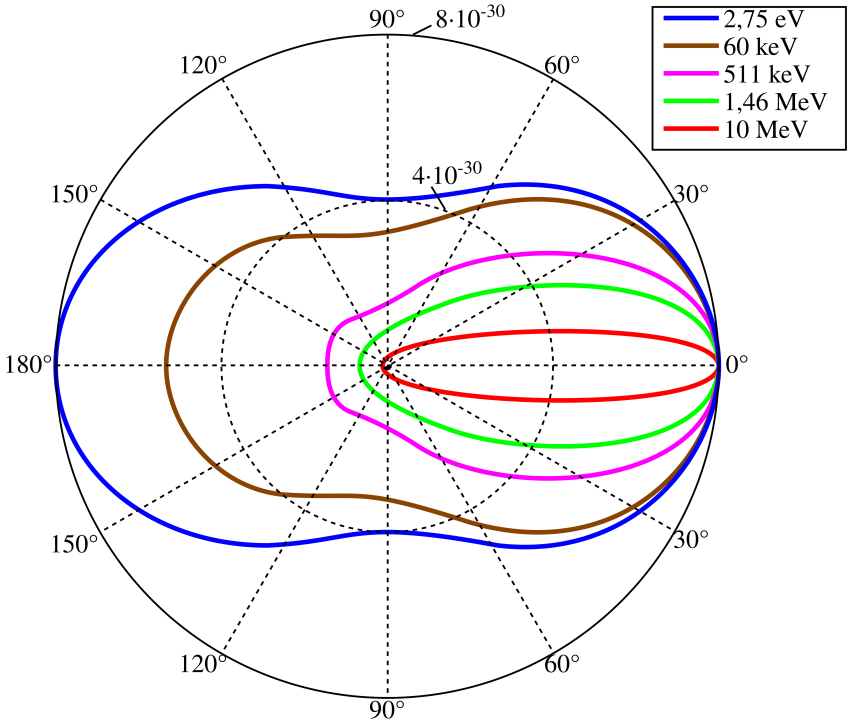

Figure 1.5: Polar plot of the Klein–Nishina angular distribution [14].

Pair production

When the incoming gamma ray has energy greater than twice the electron rest mass (1.02 MeV), another process becomes energetically possible: pair production. This mechanism becomes dominant when the gamma-ray energy exceeds a few MeV. It occurs when the photon interacts with the electromagnetic field of a nucleus in the absorber, producing an electron–positron pair while the photon disappears. The excess energy above 1.02 MeV is shared as kinetic energy between the two particles. The positron, after slowing down, annihilates with an electron in the medium, producing two 0.511 MeV gamma rays emitted in opposite directions. These secondary photons may subsequently interact via photoelectric absorption or Compton scattering.
There is no simple analytical expression for the probability of pair production per atom, but the cross section scales approximately with the square of the absorber's atomic number Z.

Figure 1.6 shows the absorption coefficients for the three main gamma–electron interactions as a function of photon energy, for lead ($Z = 82$).
In summary, the photoelectric effect dominates at low energies (up to a few hundred keV) and for high-Z materials; pair production dominates at high energies (above a few MeV) and for high Z; while Compton scattering is dominant at intermediate energies or in low-Z materials. Figure 1.7 summarises the dependence on both Z and photon energy.

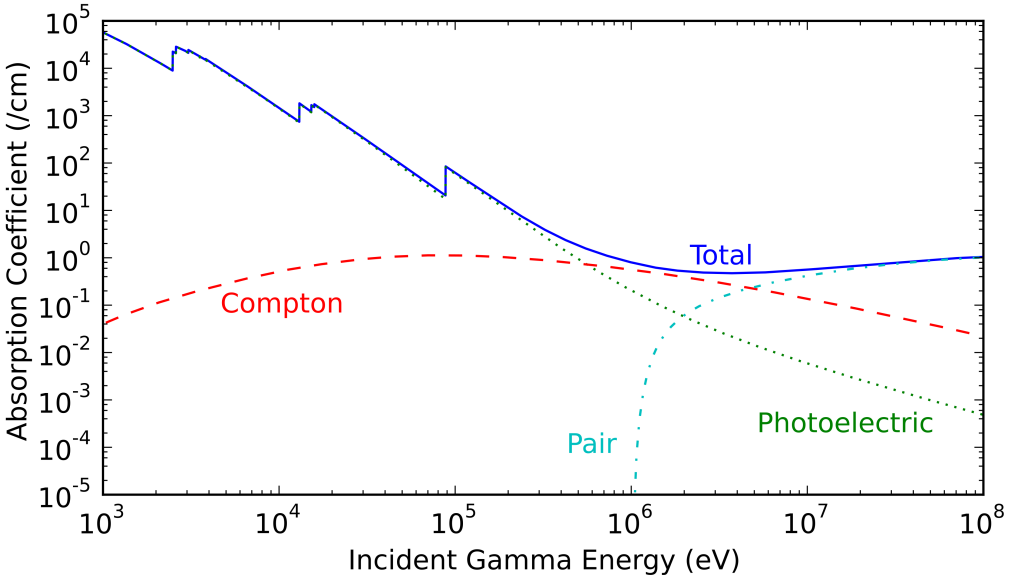

Figure 1.6: Absorption coefficients for gamma rays incident on lead ($Z = 82$). The three main components are shown, as well as the total attenuation coefficient [15].

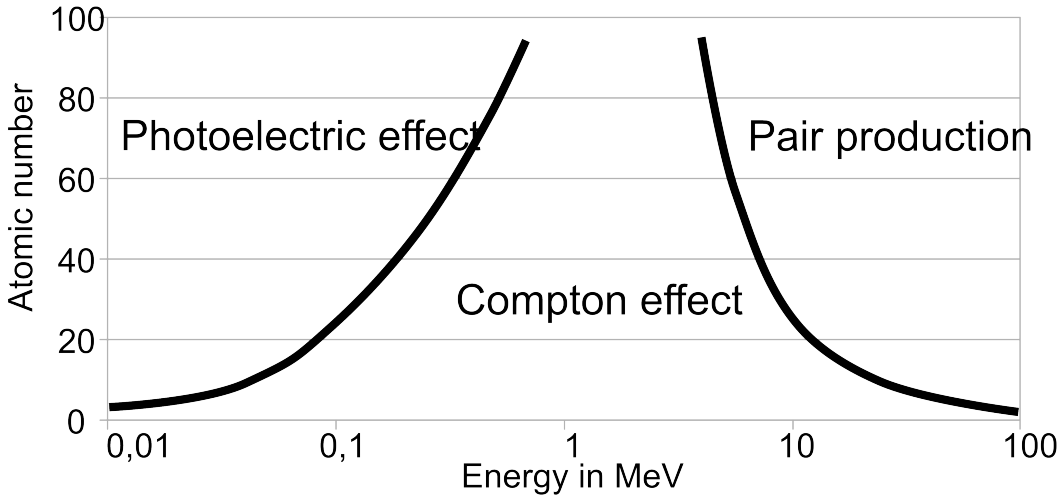

Figure 1.7: Schematic showing the dominant attenuation mechanisms of gamma rays as a function of photon energy and absorber atomic number Z [16].

Attenuation

A gamma-ray beam passing through an absorber is attenuated either by absorption or by deflection from its original direction. The attenuation per unit path length is described by the linear attenuation coefficient, μ:

$$\mu = \tau_{\text{photoelectric}} + \sigma_{\text{Compton}} + \kappa_{\text{pair production}} \tag{1.55}$$

which determines the beam attenuation as:

$$I(x) = I_0 e^{-\mu t} \tag{1.56}$$

The mean free path, defined as $\lambda = 1/\mu$, represents the average distance a gamma ray travels before being absorbed or scattered. Typical values in solids range from a few millimetres to several centimetres.
It is often convenient to introduce the mass attenuation coefficient $\left(\frac{\mu}{\rho}\right)$, where ρ is the absorber density. Equation 1.56 then becomes:

$$I(x) = I_0 e^{-\left(\frac{\mu}{\rho}\right)\rho t} \tag{1.57}$$

Finally, for compounds or mixtures:

$$\left(\frac{\mu}{\rho}\right)_c = \sum_i w_i \left(\frac{\mu}{\rho}\right)_i \tag{1.58}$$

where i denotes the i-th element of the compound and w_i is its weight fraction.

1.2.2 Inorganic scintillator crystals

In the crystal lattice of insulators or semiconductors, electrons can only occupy discrete energy bands. The lower energy band is commonly called the *valence band*, while the upper one is the *conduction band*. In the former, electrons are bound to their lattice sites, whereas in the latter, they have sufficient energy to move between lattice sites. Between these two bands lies the *forbidden band*, an energy gap that electrons cannot access in a pure crystal.
When energy is absorbed by an electron, it can be promoted from the valence band to the conduction band, leaving behind a vacancy (hole). The electron may subsequently return to the valence band, but this process is usually inefficient, and the emitted photon typically lies above the visible range.

In inorganic scintillators, the energy deposited by a gamma ray is converted into visible light. To enhance visible photon emission during de-excitation, the crystal is doped with small amounts of impurities known as *activators*. These introduce additional energy levels within the forbidden band, known as *recombination centres*. The promoted electron can then de-excite through these intermediate levels, emitting photons of lower energy, typically in the visible range.
When a charged particle passes through the scintillator, a large number of electron–hole pairs are generated. The holes tend to occupy activator sites, ionising them, while the excited electrons migrate through the lattice until they recombine at these

sites. The resulting de-excitation produces visible photons. Moreover, this mechanism leads to materials that are transparent to scintillation light, since the emitted wavelengths are longer than those required to create new electron–hole pairs. Other competing processes may occur, such as *phosphorescence* (caused by thermal excitation), which contributes to background light. One can refer to [12] for a more detailed discussion on scintillators.

An ideal scintillator should exhibit the following properties:

- Efficient conversion of electron kinetic energy into visible photons, with most emission occurring via prompt fluorescence.
- A light yield that is linear with the deposited energy.
- Transparency to the visible light produced by prompt fluorescence.
- A short decay time of prompt fluorescence, allowing for fast signal pulses.
- A sufficiently large volume to stop the incoming radiation.
- A refractive index close to that of glass (~1.5) to ensure efficient optical coupling between the scintillator and the light sensor (e.g. a photomultiplier tube).

In practice, a compromise between these properties must be found, as no real material satisfies all of them simultaneously. Inorganic scintillators generally provide good light output and linearity, but have relatively slow decay times. Nevertheless, for gamma-ray spectroscopy, they are well suited due to the high atomic number and density of their constituents.

The state of the art in gamma-ray spectroscopy for tokamak applications is represented by Cerium-activated Lanthanum Bromide ($LaBr_3$:Ce) crystals. In general, Cerium activation provides a high light yield—a key parameter for inorganic scintillators. Consequently, these materials exhibit excellent energy resolution, around 3% at 662 keV for $LaBr_3$:Ce. This makes Cerium-activated scintillators among the most widely used for gamma-ray spectroscopy.
The deposited energy is transferred to the Cerium activator sites, where a transition occurs between the 5d and 4f levels of Ce, resulting in the emission of visible photons. Depending on the host crystal, the luminescence decay time of Cerium ranges from about 20 to 80 ns. This places Cerium-activated scintillators between traditional inorganic and organic scintillators, the latter being faster, with decay times of only a few nanoseconds.
The most effective host crystals for Cerium are rare-earth halides (such as $LaBr_3$:Ce and $LaCl_3$:Ce) and certain rare-earth oxides. Lanthanum, being a rare-earth element, forms crystals with a high effective atomic number and density, both favourable for the photoelectric effect. This is the preferred interaction, as the entire photon energy is absorbed without significant losses.
Some drawbacks of $LaBr_3$:Ce include its strong hygroscopicity (which may damage the crystal), anisotropic thermal expansion (which can induce internal stress),

and intrinsic radioactivity due to the presence of ^{138}La and ^{227}Ac isotopes, which contribute to background radiation. However, this intrinsic activity can also be exploited for convenient energy calibration and efficiency evaluation [17]. Despite these limitations, $LaBr_3$:Ce exhibits a relatively stable light yield over a wide temperature range and remarkable radiation robustness. These properties make $LaBr_3$:Ce an excellent candidate for gamma-ray spectroscopy in harsh environments such as fusion reactors. A more detailed discussion is provided in Subsection 1.2.5.

1.2.3 The photomultiplier tube

After the conversion of the incoming gamma-ray energy into visible light within the scintillator crystal, the light signal must be converted into a corresponding electrical signal to be collected and measured. This task is commonly performed using the *photomultiplier tube* (PMT).
A PMT is capable of converting a light signal consisting of as few as a few hundred photons into a measurable current pulse, without introducing significant noise. This technology remains one of the most widely used devices for converting light into an electrical signal.

A PMT consists of a glass envelope that serves as a pressure boundary to maintain a vacuum inside, which is necessary to allow the generated electrons to be efficiently accelerated. One of the major components of the PMT is the *photocathode*, which converts incoming visible photons into low-energy electrons via the photoelectric effect. This process involves three main stages: the absorption of the incident photon and the transfer of energy to an electron within the photocathode material; the migration of the electron inside the photocathode; and the escape of the electron from the inner surface of the photocathode.
In the first step, a typical blue-light photon has an energy of approximately 3 eV, representing the energy available for transfer to the electron. During migration to the surface, the photoelectron loses energy primarily through collisions with other electrons in the material. Upon exiting the surface, the photoelectron must have sufficient energy to overcome the potential barrier at the interface between the photocathode and vacuum. For PMTs, the photocathode material is chosen to have a low barrier (1.5–2 eV), allowing the photoelectron to escape. This implies an energy cut-off, typically in the red or near-infrared range. To maximise the total number of electrons available for amplification, the energy loss within the photocathode must be minimised. Indeed, most photoelectrons are generated within a very thin layer near the inner surface (from a few nanometres up to 25 nm, depending on the material). Photocathodes of this thickness are semi-transparent, so fewer than half of the incident photons are converted. The *quantum efficiency* is used to quantify the photocathode's efficiency in converting photons into electrons, defined as the number of photoelectrons emitted per incident photon.

The resulting electron pulse mirrors the temporal profile of the scintillation light reaching the photocathode. However, the charge produced by the photocathode is too small to constitute a convenient electrical signal. Therefore, the PMT incorporates a multiplier section, where the electron signal is collected and amplified. In practice, a typical scintillation pulse generates 10^7–10^8 electrons at the PMT output,

providing a measurable current signal. PMTs generally produce an output signal that is linear with respect to the number of incident photons. The duration of the resulting current pulse typically ranges from 20 to 50 ns.
Electrons from the photocathode are first accelerated towards an electrode called the *dynode*. The dynode material is selected so that each impinging electron releases multiple secondary electrons. To produce more secondary electrons, the incident electron typically requires more energy than it has immediately after leaving the photocathode (about 1 eV). The dynode material requires energy on the order of 2–3 eV (comparable to its band gap) to emit secondary electrons. Therefore, the production of secondary electrons is sensitive to the incoming electron's energy. If the electron energy is too high, secondary electrons may be generated too far from the dynode surface, reducing the number that escape. Thus, an optimum electron energy must be chosen. The multiplication factor δ is defined as the number of secondary electrons produced per incident electron and should be maximised to enhance amplification.
This process is repeated over several stages to achieve electron gains of the order of 10^6. At the first stage, each photoelectron produces δ secondary electrons, which are then accelerated to the second dynode, producing δ^2 electrons, and so on. After n stages, the overall gain G is given by:

$$G = \alpha\, \delta^n \tag{1.59}$$

where α is the fraction of photoelectrons collected by the multiplier section. Typically, conventional dynodes have $\delta \sim 5$, and ten stages produce a gain of 10^7 electrons, assuming $\alpha \sim 1$.

Identical repeated events do not yield exactly the same signal amplitude because the process is statistical. The factor δ fluctuates around a mean value at each stage and for each event. The production of electrons at a dynode can be approximated as a Poisson process, with mean δ, standard deviation $\sqrt{\delta}$, and relative variance $(\sigma/\delta)^2 = 1/\delta$. For n identical stages, the mean number of electrons collected at the anode is δ^n, while the overall relative variance is:

$$\left(\frac{\sigma}{\delta}\right)^2 = \frac{1}{\delta} + \frac{1}{\delta^2} + \frac{1}{\delta^3} + \cdots + \frac{1}{\delta^n} \approxeq \frac{1}{\delta - 1}. \tag{1.60}$$

For $\delta \gg 1$, the spread in the output pulse is dominated by fluctuations in the first dynode, where the number of electrons is lowest.
These fluctuations, particularly when the number of photoelectrons is low, can interfere with the detector's ability to discriminate signal from noise. Therefore, the higher the value of δ, the better the signal-to-noise discrimination.

Finally, Figure 1.8 shows a schematic of a gamma-ray detection system using a scintillator coupled to a PMT.

1.2.4 Gamma-ray spectroscopy

To perform gamma-ray spectroscopy, a scintillator must fulfil two key requirements. The first is the capability to convert as much of the incoming gamma-ray energy as possible into a detectable signal. The second is the ability to discriminate between

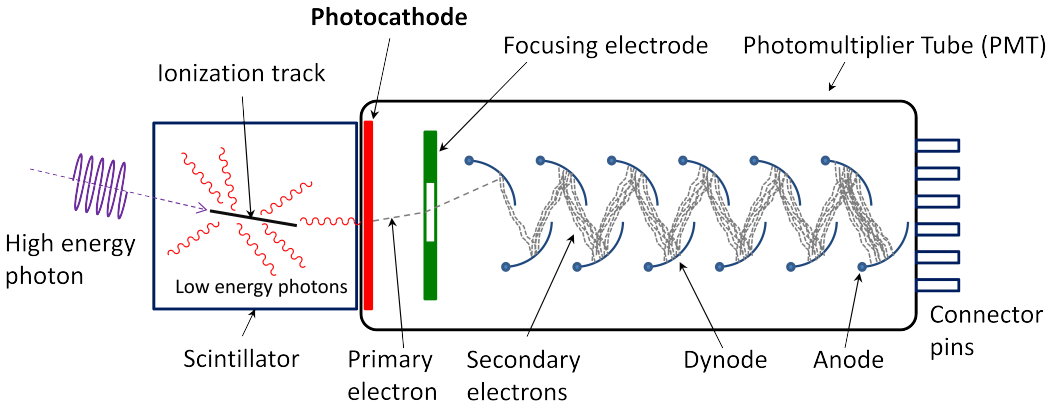

Figure 1.8: Schematic of a scintillator crystal with applied a photomultiplier tube. [18]

different gamma-ray energies.
In this treatment, it is assumed that the secondary electrons produced by fast electrons following gamma-electron interactions are completely absorbed by the scintillator without losses. In practice, only a small fraction is effectively lost, primarily if large scintillators (with minimum dimensions of at least 1 cm) are used.
In Subsection 1.2.1, the three main gamma-electron interaction mechanisms were described. Here, it is discussed how these three processes affect measurements when using a scintillator detector.

During photoelectric absorption, the original gamma-ray disappears while a single fast electron is emitted, with energy $E_\gamma - E_B$, where E_γ and E_B are the gamma-ray energy and the K-shell binding energy, respectively. Assuming $E_\gamma \gtrsim 1$ MeV, E_B represents a negligible fraction of the total gamma-ray energy, usually ranging from a few keV to a few tens of keV, so that almost all the incoming photon energy is absorbed by the scintillator. The vacancy created in the atom can then be filled by an electron from an upper shell, producing a characteristic X-ray or an Auger electron can be generated. The X-ray may interact via the photoelectric effect, releasing the remaining energy. If no losses occur, the photoelectric effect represents the ideal interaction for gamma-ray spectroscopy, as the entire incoming energy is converted into a detectable signal. The resulting energy spectrum would be a delta function centred at E_γ, called the *full energy peak* or, if the photoelectric effect dominates, the *photopeak*.

Compton interactions, in contrast, produce a scattered gamma-ray and a fast electron, with energies depending on the scattering angle. The scattered gamma-ray can escape from the scintillator without further interactions, resulting in partial energy deposition. The energy deposited in the scintillator can vary from zero (for $\theta \simeq 0$) up to a maximum value, the *Compton edge*, corresponding to backscattering ($\theta = \pi$). The energy gap between the original gamma-ray energy E_γ and the Compton edge energy $E_e(\theta = \pi)$ is given by:

$$E_{gap} = E_\gamma - E_e(\theta = \pi) = \frac{E_\gamma}{1 + 2E_\gamma / m_e c^2} \tag{1.61}$$

The resulting energy spectrum forms a continuum from zero up to the Compton edge, with a sharp drop at this energy. If the secondary gamma-ray is absorbed by the scintillator, a full energy peak also appears. If the secondary gamma-ray escapes after interacting and losing part of its energy, the gap between the full energy peak and the Compton edge is partially filled.

Finally, in pair production, an electron and a positron are generated. The electron deposits all its energy in the scintillator, while the positron annihilates with an electron of the medium after slowing down, producing two gamma-rays of 0.511 MeV each. One or both of these gamma-rays may escape from the scintillator without further interactions, resulting in partial energy deposition (*single escape* and *double escape*, respectively). The energy gaps between the full energy peak and the single escape peak or the double escape peak are 0.511 MeV and 1.022 MeV, respectively. The resulting energy spectrum thus features three peaks: the full energy peak, the single escape peak, and the double escape peak.

We now consider the response function of a scintillator detector irradiated with monoenergetic gamma-rays for three idealised cases: small, large, and medium detectors.

For a detector with "small" dimensions (with characteristic length of 1–2 cm) compared with the mean free path of secondary gamma radiation produced by Compton scattering or pair production (several cm), all secondary radiation escapes the absorber, while the full absorption of energy carried by electrons is assumed. The resulting energy spectrum exhibits the features described for the three interaction mechanisms, but some details may not be visible: the photopeak includes only events where the photoelectric effect occurred; for Compton scattering, full energy absorption is no longer visible and only the Compton continuum appears; for pair production, only the double escape peak is visible, while the single escape and full energy peaks are absent.

For "large" detectors (many tens of cm), all secondary radiation is absorbed within the scintillator. Here, the full energy peak encompasses all events in which the entire gamma-ray energy is absorbed, regardless of the interaction mechanism. The Compton continuum is no more visible, as all scattered gamma-rays are absorbed. Both single and double escape peaks are absent, since all secondary gamma-rays from positron annihilation are absorbed. Although such a detector seems ideal for gamma-ray spectroscopy, it is impractical due to self-absorption of scintillation light.

A compromise is to select an optimally sized detector. For a "medium"-sized detector (a few cm), all the features described above are visible in the energy spectrum, providing a good balance between efficiency and resolution. An example of gamma-ray spectrum collected using a scintillator is shown in Figure 1.9, where the features previously described are visible.

As noted earlier, the actual response function depends on the energy of the gamma-ray emission. At low energies (up to a few hundred keV), the photoelectric effect dominates, while Compton scattering and pair production are negligible. As the energy increases, features from Compton scattering and pair production appears, while the photoelectric effect becomes less significant. The effective Z of the material also influences the relative contributions of each mechanism (see Figure 1.7).

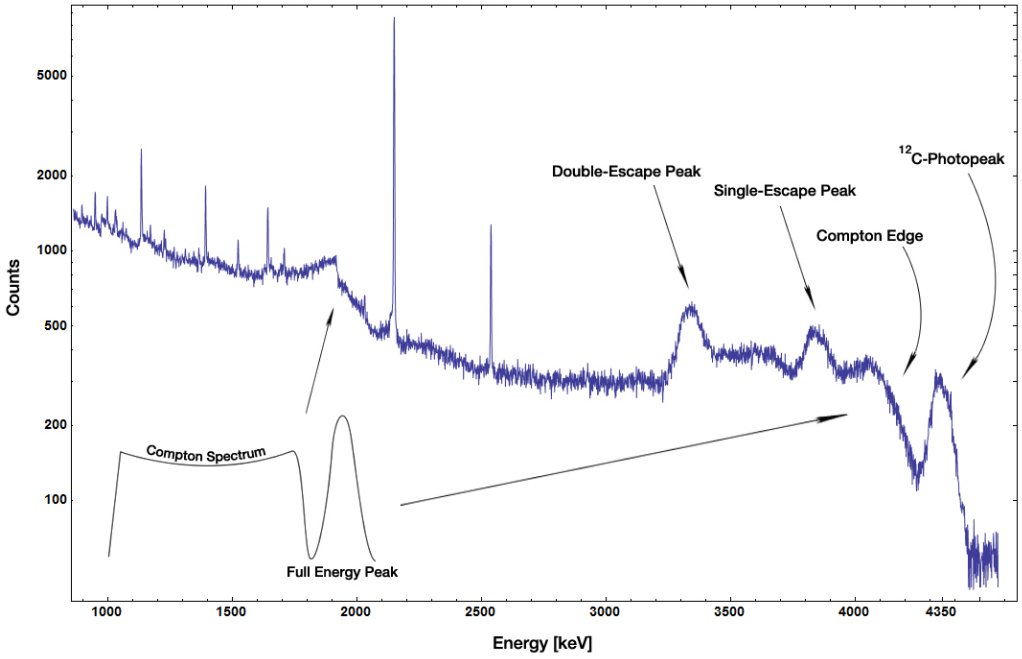

Figure 1.9: Gamma-ray spectrum resulting from neutron capture in an Am–Be source, recorded using a scintillator. [19]

Therefore, the actual response function depends on the size, shape, and composition of the scintillator, as well as the energy of the incoming radiation. Its evaluation is complex and is usually performed using MonteCarlo simulations.

Finally, an important parameter for a spectrometer is the *energy resolution*. For a spectral peak, it is commonly defined as:

$$R = \frac{FWHM}{H_0} \tag{1.62}$$

where FWHM is the "full width at half maximum" of the full energy peak, and H_0 is the height of the peak.
The main source of resolution loss is statistical fluctuations in the PMT gain. As discussed earlier, the most significant contribution arises from the stage with the fewest information carriers.
Considering only statistical broadening of the peak, the FWHM can be expressed as $FWHM \propto \sqrt{E_\gamma}$, while $H_0 \propto E_\gamma$. Thus, the energy resolution can be written as:

$$R = \frac{FWHM}{H_0} = K\frac{\sqrt{E_\gamma}}{E_\gamma} = \frac{K}{\sqrt{E_\gamma}} \tag{1.63}$$

where K is a constant of proportionality. Taking the logarithm of both sides of Relation 1.63:

$$\ln R = \ln K - \frac{1}{2}\ln E_\gamma \tag{1.64}$$

A plot of $\ln R$ against $\ln E_\gamma$ yields a linear relation with a slope of $-1/2$. In practice, the slope is less steep than predicted, due to additional sources of non-statistical

broadening.

1.2.5 $LaBr_3$:Ce Scintillator Detectors for Gamma-Ray Diagnostics in Tokamaks

The spectrometers based on $LaBr_3$:Ce scintillators currently represent the state of the art in gamma-ray spectroscopy for tokamak applications. Over the past few years, the majority of gamma-ray diagnostics in magnetic confinement fusion devices have progressively adopted this technology, mainly due to its good performance in harsh fusion environments and its capability to operate reliably under high particle flux conditions. The key advantages of $LaBr_3$:Ce scintillators include their robustness against neutron-induced damage and their ability to sustain very high counting rates when coupled with appropriate hardware and signal-processing techniques. These features are particularly relevant for the advanced operational scenarios expected in next-generation tokamaks [20, 21].

$LaBr_3$:Ce scintillators also exhibit good linearity up to energies of 10–20 MeV, a high light yield (approximately 63 photons/keV), and a relatively high detection efficiency up to about 10 MeV. In addition, their short scintillation decay time (about 16 ns) enables operation at counting rates of several MHz, provided that efficient pile-up recovery algorithms are implemented. Owing to the high photon yield, $LaBr_3$:Ce detectors achieve good energy resolution (approximately 3.2% at 662 keV), allowing the acquisition of high-quality spectra, particularly at photon energies below 5 MeV. As a result of these characteristics, $LaBr_3$:Ce-based detectors have become a primary choice in a wide range of applications, including space science, radioactive isotope identification, medical gamma-ray imaging, and, notably, diagnostics for magnetic confinement fusion reactors [22, 23].

In tokamak experiments, $LaBr_3$:Ce scintillators are mainly employed for indirect measurements of fast ions through the detection of gamma-ray emission originating from the de-excitation of nuclei produced in fusion reactions, or from secondary reactions involving energetic ions and plasma impurities. Among the most extensively studied species are fusion-born alpha particles generated in DT and D^3He reactions, as well as suprathermal ions such as fast deuterons injected into the plasma or accelerated by radio-frequency heating schemes.

At the Joint European Torus (JET) in Culham (UK), several gamma-ray diagnostics based on $LaBr_3$:Ce scintillators were installed. These included the upgraded gamma camera, which consists of multiple lines of sight intersecting the plasma to provide spatially resolved measurements. Each channel is equipped with a $LaBr_3$:Ce detector, enabling gamma-ray spectroscopy along distinct lines of sight. Through the application of dedicated deconvolution algorithms, spatial profiles of energetic particle populations can be inferred. This diagnostic has been employed to investigate a variety of MeV-range particles, including fast ions and runaway electrons. For instance, alpha-particle birth profiles have been reconstructed in D^3He plasmas by observing the gamma-ray emission associated with secondary reaction channels of the D^3He fusion process [24].

In addition to the gamma camera, two single-line-of-sight gamma-ray spectrometers based on $LaBr_3$:Ce scintillators are installed at JET. The first one, referred to as the vertical gamma-ray spectrometer (VGRS), is positioned to observe the plasma from above, providing a vertical line of sight. The second system, the tangential gamma-ray spectrometer (TGRS), is arranged such that its line of sight intercepts the inner first wall and lies in the equatorial plane of the torus, approximately 30 cm below the plasma centre. Both diagnostics have been extensively used for fast-ion studies through the observation of characteristic gamma-ray emissions. A notable example is the 4.44 MeV gamma-ray line from the $^{9}\mathrm{Be}(\alpha, \gamma n)^{12}\mathrm{C}$ reaction, which has been widely exploited to study alpha particles and to extract information on their velocity distribution. For fast deuterons, prominent gamma-ray lines originate from the $^{9}\mathrm{Be}(\mathrm{D}, n\gamma)^{10}\mathrm{B}$ and $^{9}\mathrm{Be}(\mathrm{D}, p\gamma)^{10}\mathrm{Be}$ reactions, typically in the energy range between 1 and 5 MeV [25].

$LaBr_3$:Ce scintillators have also been extensively employed in runaway electron studies at several tokamaks, particularly during dedicated experiments involving artificially induced disruptions, for example through rapid argon injection into the plasma. During runaway electron events, intense Bremsstrahlung emission is produced as a consequence of Coulomb interactions between relativistic electrons and plasma ions. This radiation is usually concentrated in the hard X-ray energy range, but photon energies extending up to several tens of MeV can be reached in tokamak plasmas, corresponding to the gamma-ray domain. Such events are typically associated with extremely high counting rates at the detector location, which can reach values of the order of 10^7 Hz. These demanding experimental conditions make $LaBr_3$:Ce scintillators particularly well suited for the detection and study of Bremsstrahlung emission from runaway electrons. A prominent example is the REGARDS diagnostic installed at the ASDEX Upgrade tokamak in Garching (Germany), which is based on $LaBr_3$:Ce detectors and has been specifically developed to observe runaway-electron-induced Bremsstrahlung radiation. By applying suitable deconvolution techniques, it has been possible to reconstruct the one-dimensional energy distribution of runaway electrons from experimental hard X-ray spectra, as well as to estimate the time-resolved maximum runaway electron energy [26].

A characteristic feature of $LaBr_3$:Ce scintillators is the presence of an intrinsic background arising from the natural radioactivity of some constituent isotopes, most notably ^{138}La and ^{227}Ac. The decay of ^{138}La produces a distinctive peak at approximately 1470 keV, mainly due to electron capture followed by gamma-ray emission. Given its extremely long half-life (of the order of 10^{11} years), the associated activity can be considered constant over experimental timescales. The decay chain of ^{227}Ac gives rise to a broader spectral structure extending roughly from 1.5 to 3 MeV, primarily due to alpha decays. While this intrinsic background may limit measurements at very low counting rates, especially at low photon energies, tokamak experiments are typically characterised by intense gamma-ray emission from the plasma. Under such conditions, the intrinsic background of $LaBr_3$:Ce scintillators can be advantageously exploited as an internal reference for low-energy auto-calibration, performed on a discharge-by-discharge basis throughout an experimental campaign [17].

$LaBr_3$:Ce scintillators are also sensitive to neutrons, which interact with the de-

tector material mainly through inelastic scattering and nuclear reactions involving ^{79}Br, ^{81}Br, and ^{139}La. During tokamak operation, intense neutron fluxes are generated, primarily from DD and DT fusion reactions, producing neutrons with energies of approximately 2.5 and 14 MeV, respectively. Consequently, $LaBr_3$:Ce detectors must be operated in conjunction with appropriate neutron attenuators when installed in fusion environments. The intrinsic detection efficiency of $LaBr_3$:Ce scintillators is approximately 76% for 2.5 MeV neutrons and about 43% for 14 MeV neutrons [27, 28].

In recent years, a novel diagnostic approach has been investigated for fusion power measurements in tokamaks based on gamma-ray detection. In particular, $LaBr_3$:Ce scintillators have been employed to measure the gamma-ray emission associated with secondary channels of the DT fusion reaction and to determine the corresponding gamma-per-neutron branching ratio for the first time in a magnetic confinement fusion reactor. This has enabled absolute measurements of the gamma-ray yield at JET during DT operations. A similar approach can also be applied to D^{3}He plasmas, providing a unique method for assessing fusion power through gamma-ray diagnostics [29, 30, 31].

Chapter 2

Fusion Power Measurements:

A gamma-ray detector for the SPARC tokamak

2.1 A novel technique to measure fusion power

2.1.1 Neutron–based diagnostics for fusion power measurements

The strong magnetic field applied in a tokamak effectively confines charged particles. As a result, fusion-born charged products remain trapped within the plasma. Neutral particles, such as neutrons, on the other hand, are unaffected by magnetic fields and can escape. In particular, DT and DD fusion reactions produce neutrons with energies of approximately 14 MeV and 2.5 MeV, respectively. These neutrons carry valuable information about the plasma and can be exploited for diagnostic purposes.
Neutron diagnostics are used for evaluating ion temperature, plasma ion composition, spatial plasma profiles, reactant distributions, and, crucially, fusion power. In tokamaks, dedicated systems are used to measure the total neutron rate, which is directly related to the fusion power. [32] At JET, this has traditionally been achieved using neutron flux monitors cross-calibrated with activation foils. To date, this remains the only well-established method for determining fusion power in tokamaks.

Accurate neutron yield measurements have been fundamental for machines such as JET, JT-60U, and TFTR, and will be equally important for future devices like SPARC, BEST, ITER, and DEMO [33]. These diagnostics support both plasma physics studies and machine control and protection [34]. Time-resolved and time-integrated neutron measurements provide, respectively, the instantaneous fusion power and the total fusion energy released per discharge, enabling the calculation of the fusion gain factor Q [34].

Tokamaks such as JET, TFTR, and JT-60U have employed a variety of neutron diagnostics, with fission chambers being the most widely used solution for neutron flux monitoring [35, 36, 37]. These detectors operate by exploiting fission reactions in materials such as ^{235}U and ^{238}U. At JET, the neutron monitoring system was designed to operate over a wide dynamic range, spanning from 10^8 n/s in hydrogen

or deuterium ohmic plasmas up to 10^{19} n/s in DT plasmas [34]. For DT operation, the detectors were calibrated using a 14 MeV neutron generator positioned inside the vessel via the remote handling system [38]. Three pairs of fission chambers were installed in moderator assemblies at the midplane, close to the transformer limbs [34]. However, a major limitation of fission chambers is their inability to discriminate between DD and DT neutrons.

Activation foils represent another important class of neutron diagnostics and play a complementary role to neutron flux monitors by providing reliable measurements of the time-integrated neutron yield over the full duration of a discharge [39, 40]. Enclosed in polyethylene capsules, the foils are pneumatically transferred to predefined irradiation ends near the vacuum vessel before each plasma pulse and retrieved after the discharge for off-line analysis [40]. Each foil consists of a metallic disk, typically 18 mm in diameter, with thickness and mass selected according to the expected neutron spectrum.

The analysis is based on the detection of gamma radiation emitted by neutron-activated nuclei in the foil, usually employing high-purity germanium (HPGe) detectors or sodium iodide (NaI) scintillators [39]. From the measured gamma-ray activity, the number of activated atoms is inferred and converted into a total neutron yield. Accurate neutron transport calculations are required to relate the local neutron fluence at the foil position to the global neutron production rate [40]. Different foil materials are selected depending on the neutron energy range of interest: for DT neutrons, high-threshold materials such as ^{56}Fe, ^{27}Al, ^{93}Nb, and ^{28}Si are commonly used, while ^{115}In is particularly suitable for DD neutrons [40].

Both neutron flux monitors and activation systems require careful calibration using well-characterized neutron sources. This is typically achieved by scanning a calibrated source throughout the vessel using remote handling systems, thereby simulating the spatial distribution of plasma neutron emission [41]. At JET, extensive calibration campaigns have been carried out at both 2.5 MeV and 14.1 MeV using ^{252}Cf sources and neutron generators [41, 38, 42].

Despite their proven effectiveness, these methodologies rely heavily on detailed Monte Carlo simulations of neutron transport through the entire machine and on extensive in situ calibration campaigns [34]. Furthermore, fission chambers are sensitive to both direct and scattered neutrons, including contributions from unintended angles or from DD reactions, which complicates the interpretation of the measured signals [35]. For these reasons, activation systems are routinely used in conjunction with neutron flux monitors. In addition, major calibration campaigns must be repeated whenever the tokamak configuration is modified.

An alternative approach to fusion power measurements in DT plasmas consists in combining neutron spectroscopy with neutron camera measurements. This method, experimentally tested at JET using the Magnetic proton Recoil (MPR) spectrometer and the neutron camera, significantly reduces the dependence on detailed neutron transport modeling and removes the need for absolute calibration campaigns [43].

2.1.2 Gamma-ray–based diagnostics for fusion power measurements

Gamma-ray emission from the DT reaction

As previously discussed, fusion power can be inferred from measurements of the fusion reaction yield during experimental campaigns. In deuterium–tritium (DT) plasmas, the main observable product is the 14.1 MeV neutron originating from the D(T,α)n reaction channel. However, this is not the sole branch through which the DT fusion reaction can proceed. A less probable channel, characterised by the emission of a gamma-ray, has been observed: D(T,^{5}He)γ. In principle, detecting gamma-rays from this reaction can offer a neutron-independent estimation of fusion power in DT plasmas, provided that the branching ratio associated with the gamma emission channel is known with sufficient accuracy, in order to obtain a precise evaluation of the more dominant neutron yield.

The so-called "gamma-per-neutron branching ratio" ($BR_{\gamma/n}$) — namely, the number of reactions with gamma-ray emission for each reaction with neutron emission — has been investigated across a range of experimental contexts, including beam–target configurations and inertial confinement fusion devices. These studies have reported results spanning approximately one order of magnitude, with typical values in the range of 10^{-5} to 10^{-4} γ/n [4, 44, 45].

The first observation of the DT gamma-ray spectrum in a magnetic confinement fusion device was reported by Rebai et al. in Ref. [30] during the DTE2 experimental campaign at JET. Building on that work, Dal Molin et al. subsequently provided, for the first time in a tokamak, an estimation of the $BR_{\gamma/n}$ associated with the DT reaction. Their publication in Ref. [29] includes a schematic overview of historical $BR_{\gamma/n}$ measurements and reports the value obtained at JET during DTE2, resulting in $2.4 \cdot 10^{-5}$ γ/n.

In this rare reaction channel, a gamma-ray is emitted, with its energy determined by the specific nuclear level transition in the excited ^{5}He nucleus:

$$\mathrm{D} + \mathrm{T} \rightarrow {}^5\mathrm{He}^{2\mathrm{nd}} \rightarrow {}^5\mathrm{He}^{\mathrm{gs}} + \gamma_0 \tag{2.1}$$

$$\mathrm{D} + \mathrm{T} \rightarrow {}^5\mathrm{He}^{2\mathrm{nd}} \rightarrow {}^5\mathrm{He}^{1\mathrm{st}} + \gamma_1 \tag{2.2}$$

At energies typical of tokamak plasmas, the most probable gamma-ray emissions occur around 16.7 MeV and ~ 14 MeV, referred to as γ_0 and γ_1, respectively. [46, 47] During the DT reaction, the ^{5}He nucleus is initially produced in its second excited state, characterised by a total angular momentum of $J^\pi = 3/2^+$. As illustrated in Figure 2.1, this isotope typically undergoes immediate disintegration into a neutron and an alpha particle, with energy distributed between the two as kinetic energy. However, a radiative transition to either the first excited state ($J^\pi = 1/2^-$) or the ground state ($J^\pi = 3/2^-$) can occur, accompanied by the emission of γ_1 and γ_0, respectively. The resulting ^{5}He nucleus then undergoes disintegration into a neutron and an alpha particle, although in this case, a significant fraction of the total energy is carried away by the photon. Rebai et al. in Ref. [30] also provided an evaluation of the relative yield between γ_1 and γ_0 emissions based on DTE2 measurements,

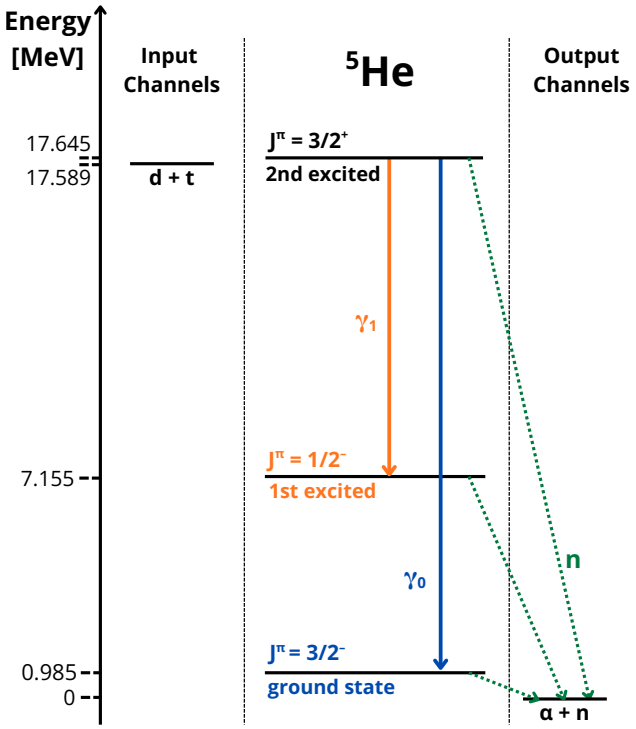

Figure 2.1: Schematic of the ^{5}He decay processes during the DT reaction.

resulting in $\gamma_1/\gamma_0 = 1.09 \pm 0.25$. The total gamma-per-neutron branching ratio is computed as follows:

$$BR_{\gamma/n} = \frac{Y_\gamma}{Y_n} = \frac{Y_{\gamma_0} + Y_{\gamma_1}}{Y_n} \tag{2.3}$$

where each Y_i denotes the measured yield of the corresponding ith-particle.

The DT gamma emission spectrum, shown in Figure 2.2, can be predicted using the R-matrix formalism [48], which is derived from a semi-empirical nuclear model. The resulting spectrum exhibits a broad distribution rather than distinct monoenergetic peaks. Specifically, the superposition of the γ_0 and γ_1 components results in a wide spectral feature spanning from approximately 10 MeV to 17 MeV.

A novel idea

Unlike charged particles, gamma-rays are unaffected by the tokamak magnetic field and can be detected externally using dedicated diagnostics. Provided that the branching ratio of the DT gamma-ray emission has been characterised in tokamak conditions, it becomes reasonable to estimate fusion power based on gamma-ray yield, independently of neutron diagnostics. This would represent a fundamentally distinct and complementary measurement technique. In scenarios where neutron-based fusion power diagnostics cannot be exploited, the gamma-ray method could provide the only available solution of assessing fusion power. For example, in the context of aneutronic fusion reactions such as D^{3}He or p^{11}B, gamma-ray diagnostics may even constitute the only viable approach to determining fusion power. Moreover, it offers the possibility of cross-validating neutron-based measurements.

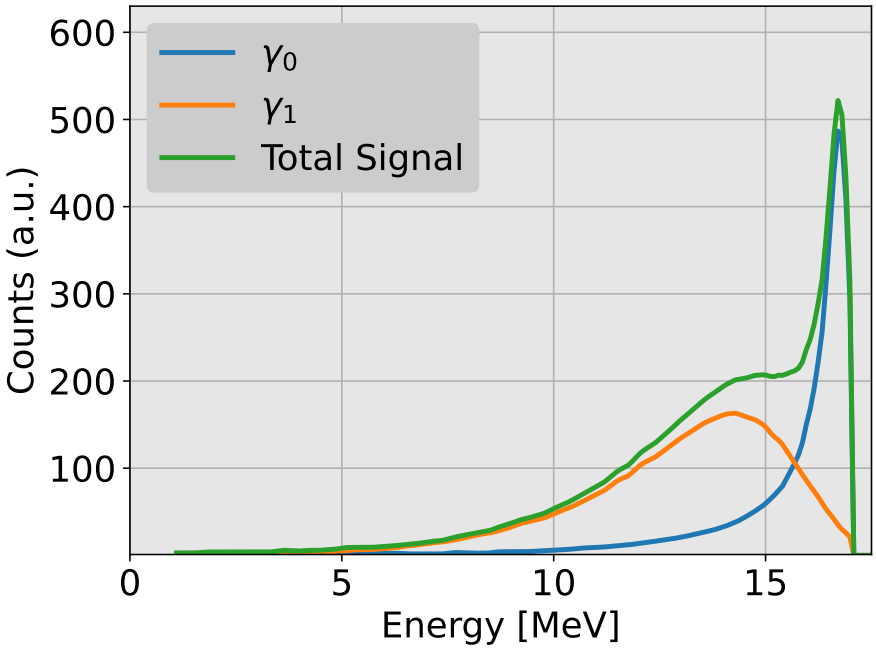

Figure 2.2: γ_0 and γ_1 emission spectra (blue and orange, respectively). The sum of the two components is shown in green, weighted by their respective yields.

Gamma-ray diagnostics for fusion power estimation present several advantages over their neutron-based counterparts. They generally do not require extensive calibration campaigns or detailed Monte Carlo simulations of the reactor geometry, owing to the relative simplicity of gamma-ray transport modelling compared to neutrons. However, several significant challenges must be addressed.
First, it is fundamental to have a precise determination of the $\mathrm{BR}_{\gamma/n}$ for the DT reaction at tokamak relevant energies. Second, one must account for the gamma-ray background, which can substantially affect the measurement accuracy. In particular, interactions of fusion neutrons with the tokamak's structural materials give rise to high-energy gamma rays, typically spanning up to 10–12 MeV, depending on the energy of the incident neutrons (e.g., 14 MeV from DT, 2.5 MeV from DD, or thermalised neutrons). This emission constitutes a significant component of the total gamma flux observed in tokamaks [49], and may pose operational challenges for gamma-ray diagnostics, especially if background count rates lead to detector saturation. Even if such background radiation does not significantly overlap the energy window of DT gamma-ray emissions, a detailed characterization of its spectral shape and total yield is crucial. Monte Carlo simulations (e.g., via MCNP), validated against data from existing facilities such as JET, will be necessary to quantify the background in the 10–17 MeV range. Without a clear and accurate understanding of these background contributions, fusion power estimates derived from gamma-ray measurements may not reach the same accuracy level of neutron based measurements, i.e., ≈ 10 %.

The experience from JET

At JET, a pre-existing gamma-ray diagnostic was used to observe the DT gamma-ray component [30, 31]. This diagnostic featured a 3" × 6" $LaBr_3$:Ce scintillator, representing the state of the art of gamma-ray measurement in tokamak environments [25, 50]. The detector was aligned along a line of sight lying on the horizontal midplane and tangential to the inner wall of the vacuum vessel. This configuration allowed the system to observe the plasma core twice along its optical path. To mitigate the intense neutron flux entering through the same line of sight, a cylindrical Lithium Hydride (LiH) attenuator, 0.8 meters in length, was installed [51].
The acquisition system included a photomultiplier tube (PMT) coupled to the scintillator, equipped with an active voltage divider to accommodate high-energy and high-count-rate conditions, reaching up to 1 Mcps. Nevertheless, based on direct experience, 500 kHz has been identified as the upper limit of the count rate for fusion power measurements, due to pile up effects that start hinder accurate signal reconstruction, and due to the resulting high current distorting the waveforms. The signal was digitized using a National Instruments NI5772 analog-to-digital converter operating at 200 MHz, with continuous data streaming capability, thereby eliminating dead time and enabling pile up correction. A dedicated control and monitoring system was also employed: two LED pulses were injected directly into the photocathode of the PMT to track and correct gain drifts associated with high count rates.
This system, known as the Tangential Gamma Ray Spectrometer (TGRS), successfully observed the DT gamma-ray emission and enabled the first estimation of the $BR_{\gamma/n}$ in a magnetic confinement fusion device. The measured branching ratio was determined to be $(2.4 \pm 0.5) \times 10^{-5}$ γ/n [29].

To derive the total DT gamma-ray yield from the entire plasma, the integrated counts recorded by the TGRS along its line of sight must be corrected using the detector response function and the gamma-ray transport factor. The total yield is given by:

$$Y_\gamma = \sum_{\gamma_0,\gamma_1} \frac{\int_{E_{min}}^{E_{max}} C_{\gamma_i}(E)\, dE}{\Omega \int_{E_{min}}^{E_{max}} S_{\gamma_i}(E) \cdot T(E) \cdot R(E)\, dE} \tag{2.4}$$

Here, Ω denotes the solid angle fraction of the detector, including geometrical and optical transport effects. $R(E)$ is the energy-dependent response function of the detector, $T(E)$ represents the energy-dependent transmittance factor (including the effect of attenuators), and $S_{\gamma_i}(E)$ is the normalized spectral shape of the respective ith-gamma emission, as obtained via R-matrix calculations. Finally, $C_{\gamma_i}(E)$ refers to the experimentally measured count rate as a function of energy. The integration is carried out over the relevant energy range $[E_{min}, E_{max}]$ usually set to $E_{min} \approx 12$ MeV and $E_{max} \approx 17$ MeV, after background subtraction.

The design and implementation of a new gamma-ray diagnostic system for future tokamaks may benefit from the experience gained with the TGRS at JET, offering a viable alternative to neutron-based fusion power measurements.

2.2 A first feasibility study: the case of SPARC

2.2.1 The SPARC tokamak

One of the main challenge that tokamaks will face during the next decades is the achievement of a fusion gain factor Q>1. This means that the tokamak is able to produce a certain amount of energy directly from fusion reactions that overcome the energy injected in the plasma to maintain it sufficiently hot to "burn" nuclei. This goal is crucial for upcoming tokamaks that aim to demonstrate the feasibility to use fusion as a source of commercially available energy. To obtain an estimation of the Q factor, fusion power measurements are necessary.

SPARC is a tokamak currently under construction in Devens (MA, USA) by Commonwealth Fusion Systems (CFS) [52, 53], designed in collaboration with the MIT Plasma Science and Fusion Center. Its goal is to be the first magnetic confinement fusion device to achieve a fusion gain factor $Q > 1$. SPARC is a medium-sized machine, with a major radius R = 1.85 m, a minor radius a = 0.57 m, and a high magnetic field $B_0 \sim 12$ T, capable of operating in deuterium-tritium (DT) mixtures. This represents an alternative approach compared to other devices under construction, such as ITER, which will achieve similar performance with lower magnetic fields but significantly larger plasma volumes. This has been made possible by using high-temperature superconductors (HTS), specifically REBCO (Rare Earth Barium Copper Oxide), for the magnetic coils. These materials can operate at higher temperatures than low-temperature superconductors (LTS), such as Nb_3Sn, which is planned for use in ITER. In principle, this leads to significantly reduced construction time and cost, as well as lower technological complexity.

SPARC will follow the "high-field path to fusion energy". According to the Lawson criterion, achieving high fusion performance requires increasing the "triple product". This can be done in three main ways: (i) increasing the plasma β, i.e., the ratio between the kinetic and magnetic pressures (attempted in spherical tokamaks, such as the STEP project in the UK), (ii) increasing the machine size (e.g., ITER) and, hence, the energy confinement time, or (iii) increasing the magnetic field (e.g., SPARC). In the latter case, the use of superconducting magnets is essential. Ohmic heating of traditional copper coils would be prohibitively high to allow for economically viable operations, as the duration of the discharge would have to be too short. In principle, SPARC relies on the same physics and technologies as previous tokamaks, with the key differences being its significantly smaller volume (about 2% of ITER's volume) and the use of REBCO magnets. Plasma heating will be provided primarily via Ion Cyclotron Resonance Heating (ICRH), with a power of up to 24 MW, targeting minority species such as Hydrogen and Helium-3.

SPARC will be equipped with several neutron diagnostics [54], including Neutron Flux Monitors (NFM), an activation foil system (FOIL), a radial Neutron Camera (NCAM), and a core Neutron Spectrometer (NSPC). During its first experimental campaigns, both DD and DT plasmas are planned, which will produce intense neutron emission. Campaign 1 is expected to reach up to 12 MW of fusion power, with $Q > 1$. Campaign 2 will focus on DD plasmas, while Campaign 3 aims to reach 140 MW of fusion power ($Q > 11$) in DT plasmas. The experiment with the highest

expected fusion power is referred to as the "primary reference discharge", with a neutron rate of $4.97 \cdot 10^{19}$ n/s. Over SPARC's operational lifetime, the neutron rate is expected to span over four orders of magnitude.
The neutron diagnostics in SPARC serve several key purposes. The NFM system is designed to measure the total neutron rate and will include 15 detectors of different types, based on neutron absorption in ^{10}B and fission chambers using ^{238}U. This configuration will allow accurate measurements over the full expected range of neutron rates across all campaigns, with a time resolution of $\Delta t < 10$ ms. This is essential both for determining fusion power and for ensuring machine safety.
To measure the neutron yield, the FOIL system will be used. It consists of two independent foil packs and provides pulse-by-pulse measurements. Its main function is to benchmark the time-integrated neutron rate measurements from the NFMs for each pulse, as well as to estimate the total fusion energy per pulse.
The NCAM will measure neutron emission with energy resolution and will include at least 7 channels, each with a radial line of sight through the plasma. Tomographic reconstructions, based on the magnetic equilibrium, will be used to derive spatial profiles of the neutron emissivity from line-integrated measurements. Integration of these profiles allows for independent estimation of the total neutron rate and fusion power. Each channel will be equipped with spectrometers capable of measuring the ion temperature profile (with an estimated uncertainty of $\sim 25\%$ and time resolution $\Delta t < 250$ ms). Chemical vapor deposition (CVD) single-crystal diamond detectors are foreseen, operating as intrinsic semiconductors and offering high energy resolution. Their low sensitivity makes them attractive for harsh environments like that of SPARC.
The NSPC will be a Magnetic Proton Recoil (MPR) spectrometer. [55, 56] It uses three electromagnets to bend the trajectories of recoil protons produced by neutron scattering on a CH_2 foil. The system is collimated to observe the plasma core along a horizontal line of sight. The energy-separated protons are then detected on an array of proton detectors. The spectrometer is designed to achieve energy resolution better than 1% and time resolution < 250 ms. The NSPC will enable multiple measurements, including core ion temperature and density, the core neutron spectrum, and the detection of suprathermal components (from ICRH heating, alpha knock-on, and triton burn-up). The ratio of thermal to non-thermal neutrons can be assessed, providing insights into fusion quality and fuel ion composition. An independent estimate of the fusion power can also be obtained by combining NSPC and NCAM data using appropriate calibration techniques.

As noted earlier, SPARC will rely on several neutron diagnostics to determine the fusion power. The primary method will involve neutron flux monitors, as done at JET, cross-calibrated with activation foils. In this thesis, the implementation of a gamma-ray detector for fusion power measurements is proposed, based on the experience gained at JET. The following sections present the first feasibility study of such a detector for integration into the SPARC tokamak.

Table 2.1: Summary of SPARC neutron diagnostics [54].

Diagnostic / Technology	Measured quantity	Resolution	Notes / Applications
NFM: ^{10}B, ^{238}U fission chambers	Total neutron rate	Time: < 10 ms	15 detectors; real-time fusion power and safety
FOIL: Activation foils + γ spectroscopy	Integrated neutron yield	Pulse-integrated	Benchmarks NFM; total energy per pulse; cross-calibration
NCAM: CVD diamond detectors; radial collimated lines; tomography	Neutron emissivity for each channel; ion temperature profile	Energy: 4% (DD) – 1.7% (DT); Time: < 250 ms	Spatial profiles; low sensitivity; independent fusion power estimate
NSPC: MPR; CH_2 foil; proton array	Core neutron spectrum; ion temp.; density; suprathermal neutrons	Energy: < 1%; Time: < 250 ms	Thermal vs non-thermal neutrons; fusion power estimate combined with NCAM
Combined: Cross-calibration (NFM+FOIL+NCAM+NSPC)	Fusion power	System-dependent	Primary SPARC method; inspired by JET

2.2.2 The gamma-ray detector

The proposed gamma ray detector is based on a $LaBr_3$:Ce scintillator spectrometer, able to observe the DT-gamma signal separated from the background. Some attractive features of this instrument are: its short decay time (30 ns) enabling gamma-ray measurements at MHz counting rates [22, 57]; the high photon yield (61/keV) [23]; the energy resolution (3.8% at 662 keV) [20, 58].

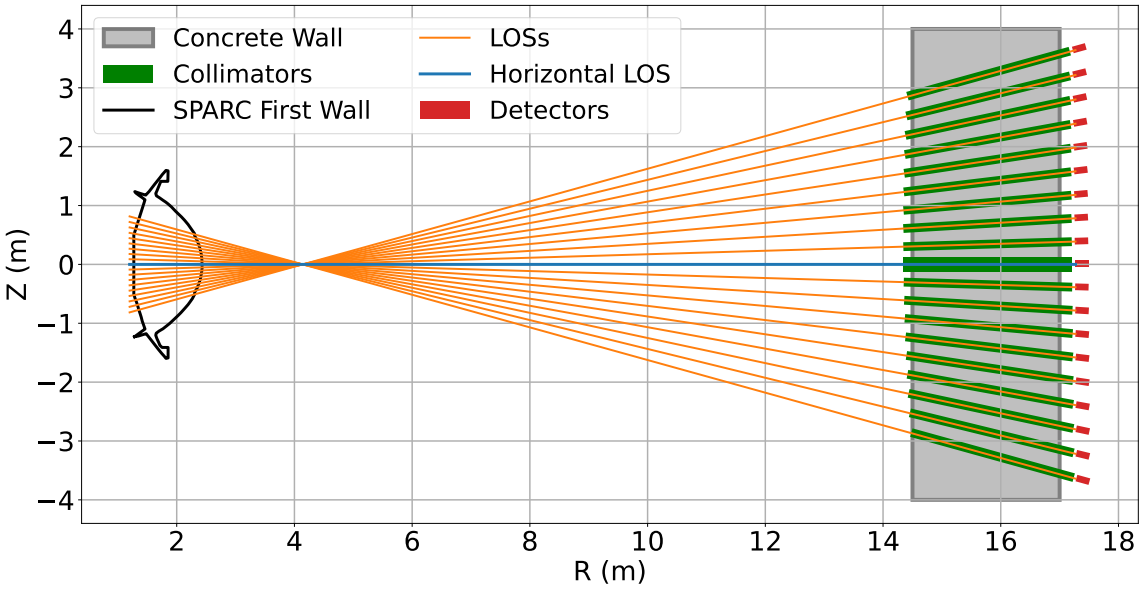

Figure 2.3: A schematic of the SPARC neutron camera. A 2.4 m thick wall separates the Diagnostic Hall from the Tokamak Hall. 19 lines of sight (labelled "LOS" in the figure and numbered 1–19 from bottom to top) observe the plasma from a radial field of view. R and Z are the radial and vertical cylindrical coordinates, respectively, with the origin at the torus centre.

The idea is to place it in a dedicated room for nuclear diagnostics, called "Diagnostic Hall", separated from the "Tokamak Hall" by a thick wall of 2.4 m [54]. In this study, the NCAM design (see Figure 2.3) consists of 19 lines of sight observing the plasma from the radial point of view, vertically scanning from outer part of the

plasma to the core. The distance of the lines of sight from each other is roughly 7 cm near the tokamak major radius.
Placing the detector along the horizontal channel of the NCAM has the advantage of observing the centre of the SPARC plasma. Indeed, it is preferable to detect the highest amount of DT-gamma signal. The main problem will be the neutron spectrometer expected along this channel, so, the gamma detector will be probably located behind the neutron spectrometer along the same line. Issues related to space availability could force to shift the detector along a contiguous line of sight (e.g., the 9th). Moreover, the Horizontal channel is preferable for its larger collimator. 3 cm of diameter will be used for the central one, while 1 cm for the others [54]. This fact increases the signal rate of a factor ~ 9, considering only collimation effects, but even greater if the detector is properly placed. The choice of selecting 3 cm to the central channel has been made because it is desirable to receive the largest possible amount of signal from the plasma, observing the centre, the most emitting part of it. In this way, the neutron spectrometer, key for the tokamak diagnostics, will receive more counts, which means a greater count statistics. Anyway, regarding gamma-rays, selecting a larger collimator will also increase the background, and choosing the 9th channel may represent a good compromise between signal and background levels.
The resulting line of sight can be considered "well collimated"; indeed, the diagnostic hall is at a distance from the torus centre of $R > 17\ m$, providing quasi-cylindrical line of sight inside the plasma and reduced observed wall section, that is an important source of background, as discussed later. Placing the diagnostics in the diagnostic hall would protect them from stray magnetic field lines and reduce background from scattered neutrons and gamma-rays.

2.2.3 Signal evaluation

To perform the feasibility study, the first step is to evaluate the total gamma-ray signal from Deuterium-Tritium reaction reaching the front face of the detector. To do so, the Monte Carlo code GENESIS [59] is employed. It was specifically developed to perform numerical calculations of nuclear radiation emission in tokamak plasmas. The code can compute various types of spectra, including neutrons, gamma-rays, Bremsstrahlung, and charged particles, and can simulate a wide range of reactions involving different particle species. Beyond its spectra simulation capabilities, GENESIS can calculate reaction reactivity and total reaction rates. Another feature of the code is the ability to simulate emissivity along a given "Line of Sight" (LoS), corresponding to a file containing information on a discretised portion of the plasma. To start a simulation, the reactant distribution functions must be specified. Some, such as Maxwellian, are already implemented, while customised distributions can also be imported to account for specific reactant populations calculated using external codes.
The code can compute the slowing-down distribution for high-energy charged particles decelerating in the plasma and includes nuclear scattering (useful for evaluating the neutron knock-on component) as well as Coulomb scattering interactions. It also calculates emission spectra of charged reaction products, such as fusion-born alpha particles. Finally, Bremsstrahlung emission, primarily implemented to simu-

late hard X-ray emission from runaway electron discharges, can also be calculated. This relies on a semi-analytical approach, cross-validated with MCNP simulations [60].

To construct the LoS file to be used in GENESIS, the MonteCarlo code REVOLT [61] is employed. This code has been specifically developed to build LoS files in tokamak environments. Its approach consists of calculating the region of plasma visible to a detector and discretising it into smaller volumes, called "voxels". For each voxel, several parameters are computed, including its position in Cartesian and cylindrical coordinates, the optical transport factor, the volume, and the vector connecting the voxel to the centre of the detector's front face.
First, the tokamak geometry is constructed: a meshgrid in terms of R, Z, and ϕ (the cylindrical radius, the vertical axis and the toroidal angle, respectively) is generated to define the voxel grid. Then, detector characteristics such as size, shape, position, and observation angle are specified, along with the tokamak first wall geometry and the inner cylinder representing the plasma boundary.
Next, objects defining and modelling the geometry of the LoS must be included. These are represented either as collimator objects to be included in the calculation, or as irregular polygons representing obstacles or other structures affecting the LoS.
Finally, the LoS is constructed, retaining only voxels with a non-zero optical transport factor T. The T parameter is calculated according to the following equation:

$$T = \frac{S\ \hat{n} \cdot \hat{u}_{los}}{4\pi d^2} H \tag{2.5}$$

where S is the surface area of the detector's front face, $\hat{n} \cdot \hat{u}_{los}$ is the dot product between the unit vector normal to the surface and the unit vector along the LoS, respectively, and d is the distance from the voxel to the detector front-face centre. Therefore, T represents the solid angle fraction $\Delta\Omega/4\pi$ subtended by the detector surface S on a sphere of radius d centred at the voxel position, multiplied by the factor H. The latter is calculated using a MonteCarlo approach and represents the fraction of the voxel volume that is actually visible to the detector.
An example of a reconstructed LoS is shown in Figure 2.4, corresponding to Channel #10 of the SPARC NCAM.

Coming back to the signal evaluation in SPARC, GENESIS needs the following input parameters: the reaction type (and the selected output particle); the reactant distributions (along with temperature and density profile if the Maxwellian distribution is selected); the magnetic equilibria (flux surfaces geometry); a REVOLT-like LoS file. The reaction type used is the classical D(T,α)n reaction, and through the evaluation of the DT gamma-per-neutron BR obtained in Ref. [29], the DT-gamma yield can directly be obtained. The reactant distributions are considered purely Maxwellian, and plasma profiles of temperature and density are taken from the SPARC GitHub open repository in Ref. [62], calculated via the TRANSP code (for more information about TRANSP, see Chapter 3). From the same repository, magnetic equilibria are retrieved, calculated via the Freegs Grad-Shafranov solver. [63] In Figure 2.5 the kinetic profile and magnetic equilibria used in these calculations are shown. For each channel of the expected NCAM in Figure 2.3, a LoS file is produced via REVOLT.

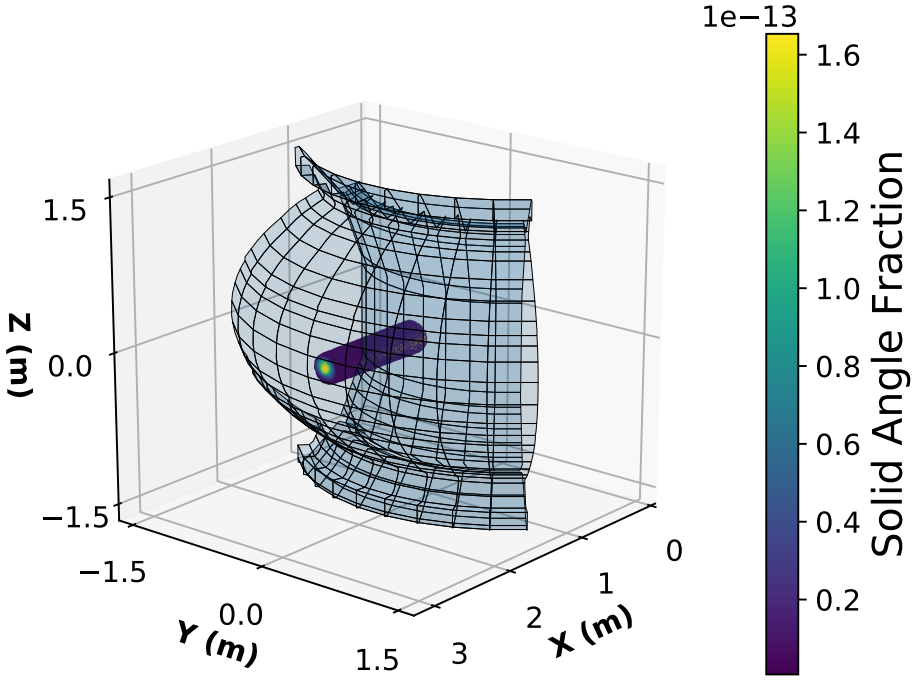

Figure 2.4: REVOLT reconstructed LoS of the Channel #10 of the SPARC NCAM, observing the plasma at the core. The colormap is relative to the solid angle fraction of each voxel of the LoS.

Plasma profiles and magnetic equilibria retrieved from the open repository are calculated in a specific SPARC scenario, called Primary Reference Discharge (PRD), in which the maximum fusion performances are expected, with 140 MW of fusion power and Q>11. From now on, this scenario will be taken as default for performing calculations. All plasma parameters corresponding to the PRD scenario are shown in Table 2.2 [52, 64]. The results of the DT-gamma calculation is shown in Figure 2.6.

Parameter	**Value**	**Units**
Toroidal field B_t	12.2	T
Plasma current I_p	8.7	MA
Major radius R_0	1.85	m
Minor radius a	0.57	m
Elongation κ	1.97	–
Triangularity δ	0.54	–
Safety factor q_{95}	3.05	–
β	0.012	–
Greenwald fraction f_G	0.37	–
External heating P_{ICRF}	11	MW
Fusion power P_{fus}	140	MW
Fusion gain Q	11	–
$<T_e>$	7.3	keV
$<n_e>$	$3 \cdot 10^{20}$	m^{-3}

Table 2.2: Plasma parameters relative to the SPARC Primary Reference Discharge.

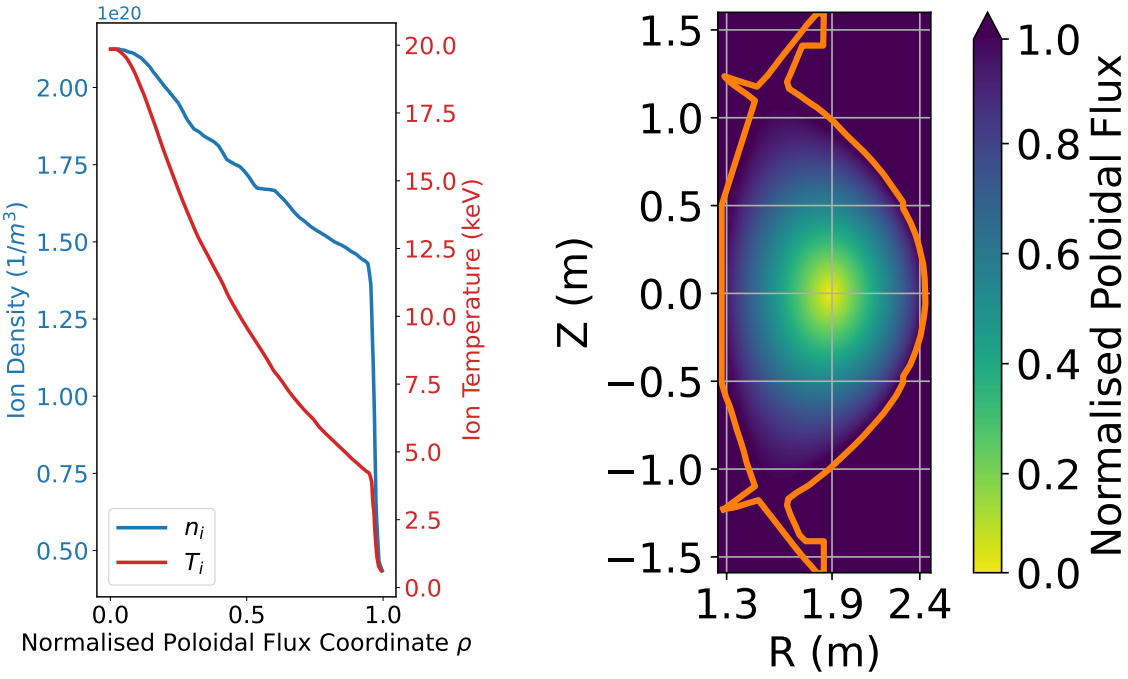

Figure 2.5: **(a)** Ion density (light blue) and ion temperature (red) simulated via TRANSP at SPARC, during the $P_{fus} = 140$ MW scenario, as a trend of the normalised poloidal flux coordinate ρ. Deuterium and Tritium kinetic profiles are considered equal ($T_d = T_t$; $n_d = n_t = n_e/2$). **(b)** Magnetic Equilibrium calculated during the $P_{fus} = 140$ MW scenario with the FreeGS code. The colorbar represents the normalised poloidal flux coordinate ρ, for each point of the 2D map.

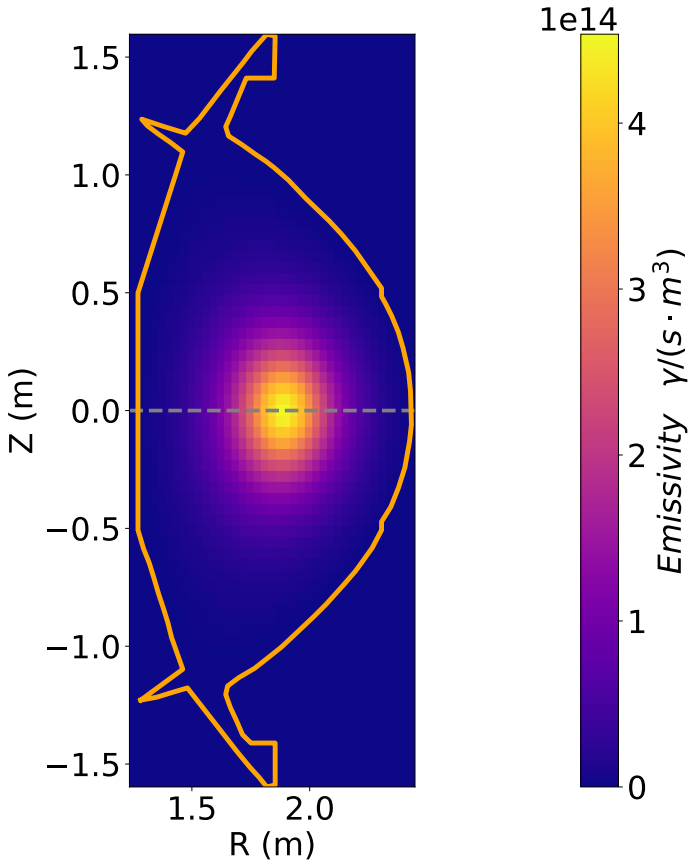

Figure 2.6: DT-gamma emissivity matrix at SPARC, during the PRD scenario, numerically calculated using GENESIS. The dashed grey line represent the observation line of Channel #10, intersecting the plasma core.

To benchmark the MonteCarlo calculation, a parallel approach has been taken. A semi-analytical code, Linalytic [65], was employed to obtain DT neutron and gamma-ray rates at the front face of the detector, for each channel (see Figure 2.7).

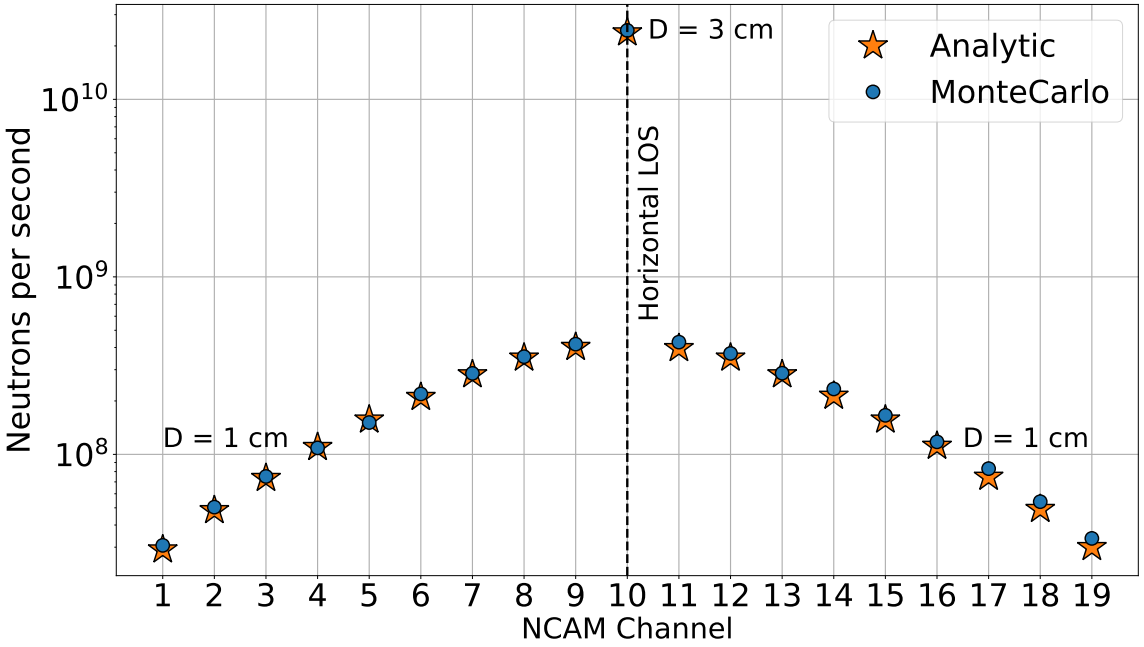

Figure 2.7: MonteCarlo (GENESIS+REVOLT) and Analytic results (Lynalitic) of the expected DT direct neutron rate for each NCAM detector. Notice that the highest rates are observed along the central horizontal channel (Channel #10), which interesects the plasma core and is equipped with a larger collimator: Channels from #1 to #19 have a collimator diameter D = 1 cm, except for Channel #10 with D = 3 cm. The detector diameter is set to 1", while the detector location is set at R = 17.2 m from the tokamak centre.

Figure 2.7 shows results of the neutron rate at the front face of the detector (set to 1" of diameter), positioned at R = 17.2 m from the tokamak centre, very close to the collimator back-end. Every channel has a collimator diameter of 1 cm but 3 cm for the horizontal one. As one can see in the figure, the central channel observes higher rates and this is mainly due to the bigger collimator diameter. Indeed, the collimator can dramatically change the particle yield at the detector, because a small change of its diameter length can strongly vary the volume of the field of view inside the plasma. To give an idea, one can consider the following relation (from Ref. [60]):

$$R = \epsilon \frac{\pi}{64} \left(\frac{d_C \, d_D}{L} \right)^2 \int_{\lambda} y(s) \, ds \tag{2.6}$$

where R is the counting rate; y is the local emissivity inside the plasma [particles/(s m^3)]; λ is the linear LoS, considered narrow; d_C and d_D are the collimator and detector diameter, respectively; L is the length of the collimator and ϵ is the intrinsic efficiency. Therefore, pairing the diameter of the collimator with that of the detector, the scaling depends with 4th power of the diameter.
The MonteCarlo and the semi-analytical methods agree within 5% for the most

peripheral channels and better than 1% for the central channel, which provides confidence on the validity of the signal calculations.

Table 2.3: DT neutrons and DT gamma-rays per second at the detector front surface (1" diameter, positioned at R = 17.2 m) calculated via GENESIS for SPARC NCAM Channel #9 (D = 1 cm) and #10 (D = 3 cm).

NCAM Channel	DT–Neutrons (Hz)	DT–Gammas (Hz)
Channel #9	$4.2\ 10^8$	$1.0\ 10^4$
Channel #10	$2.4\ 10^{10}$	$5.8\ 10^5$

Using the $BR_{\gamma/n}$, we obtain the DT gamma-ray rate. In Table 2.3 results are shown for Channels #9 and #10 (i.e. the first one before the horizontal and the horizontal itself, respectively). In principle, the preferable option for detecting the signal is the channel for which gamma rates are higher. Indeed, errors related to counting measurements are governed by the Poisson statistics, where the error is given by the standard deviation of the Poisson distribution with mean $\mu = N$, where N is the counting measurement itself. So, if the standard deviation is $\sigma = \sqrt{N}$, the relative error U is given by

$$U = \sigma/\mu = \sqrt{N}/N = 1/\sqrt{N} \tag{2.7}$$

Therefore, the higher is N, the better is the relative error associated to the measurement. Generally speaking, we prefer conditions where the signal counting rate is as high as possible, and for this reason, the horizontal channel is preferable. Nevertheless, as mentioned before, the background should be considered, and other channels could still represent a good compromise.
Nominally, our target is to reach a measurement uncertainty U = 1 %, and at least U = 10% is required. From Equation 2.7 and considering the count rate C = N/ΔT, with ΔT the integration time of the measurement, it is possible to obtain the following relation:

$$U = 1/\sqrt{\Delta T \cdot C} \tag{2.8}$$

Fixing the time resolution ΔT = 1 s, if one desires a uncertainty of 1%, C=10 kHz is needed, while for U = 10%, C = 100 Hz.
From Table 2.3 one can notice that both Channels #9 and #10 achieve the desired conditions. Nevertheless, if sources of signal reduction (like attenuators, detector efficiency, background sources, lower fusion power performances) arise, this achievement will be lowered, suggesting that Channel #10 is the preferable option to insert the detector if no source of background are considered.

2.2.4 Neutron background

In DT plasmas expected in SPARC, the direct DT neutron emission will certainly represent the main contribution to the background. As one can see in Figure 2.7, during the 140 MW fusion power scenario, the neutron rate at the NCAM detectors will range from 10^7 to 10^{10}. At JET, DT-gamma measurements with the $LaBr_3$:Ce-based detector were possible when the total counting rate did not overcome $\sim 5 \cdot 10^5$

Hz, over which pile up effects become unmanageable and the detector saturates [29]. $LaBr_3$:Ce observes DT neutron emission with a substantial intrinsic efficiency $\epsilon \sim 0.43$ and ~ 0.76 for DT and DD neutron, respectively [28, 27]. Considering the expected neutron rate to each NCAM channel, the detector will saturate and DT-gamma measurements cannot be performed. One can establish that the intense direct neutron component must be attenuated.

At JET, for the TGRS diagnostics, a Lithium-Hydride (LiH) neutron attenuator was used. The effectiveness of the LiH has been benchmarked by tests on accelerators and from the experience of JET [66, 51]. From MCNP numerical calculations (see Ref. [60]), a cylindrical LiH sample matching the collimator diameter and 1.2 m in length would attenuate DT neutrons by a factor of 10^6, and DT gamma rays by a factor of 10 in the energy range relevant for fusion power measurements. Assuming these values, Table 2.4 shows the DT gamma-ray and DT neutron yields obtained when a 1.2 m LiH attenuator is applied, for Channels #9 and #10.

Table 2.4: Intensities at the detector front surface (1" diameter, positioned at R = 17.2 m) for direct DT neutrons and DT gamma-rays with and without 1.2 m of LiH, calculated along Channels #9 and #10, during the PRD scenario. In the "Comment" columns, intensities are marked as "Not Acceptable" when in excess of 500 kHz; "Desired" when they lead to a statistical uncertainty better than 1%; "Acceptable" when leading to an uncertainty between 1% and 10%.

Particle and Attenuator	Yield/s at Ch#9	Comment (Ch#9)	Yield/s at Ch#10	Comment (Ch#10)
DT Neutron (no LiH)	$4.2\ 10^8$	Not Acceptable	$2.4\ 10^{10}$	Not Acceptable
DT Gamma (no LiH)	$1.0\ 10^4$	Desired	$5.8\ 10^5$	Not Acceptable
DT Neutron + LiH	$4.2\ 10^2$	Acceptable	$2.4\ 10^4$	Acceptable
DT Gamma + LiH	$1.0\ 10^3$	Acceptable	$5.8\ 10^4$	Desired

From Table 2.4 one can deduce that only Channel #10 still satisfy the condition of U ~ 1 % for DT-gamma measurements, while neutron rate is attenuated enough to not saturate the detector.

Finally, scattered neutrons could also affect the measurements, posing a risk of saturation. This background source originates from directions different from the dedicated LoS and is related to the interaction of fusion-born neutrons with facility structures. Similarly, gamma rays can impinge on the detector from directions outside the dedicated field of view. Nevertheless, based on the JET experience, a well-collimated line of sight should ensure a reduced scattered contribution at the detector. In the case of SPARC, the detector will be installed at $R > 17$ m in a dedicated hall for nuclear diagnostics. When required, a shielding will be applied to the detector to mitigate the scattered component, the shielding can be made by tungsten (W) for gamma ray attenuation and boron carbide (B_4C) for neutron attenuation. The only drawback associated with the shielding may concern spatial

or weight constraints, and an accurate evaluation should be carried out.

2.2.5 Neutron-induced gamma-ray background

Once the direct and scattered neutron backgrounds are controlled, another important source of background must be evaluated. Indeed, the LoS of the gamma diagnostic will intercept the tokamak inner wall at the end of the footprint. The tokamak wall, during operations, is constantly irradiated by neutrons coming from the burning plasma and these will interact with the vessel nuclei via inelastic scattering or neutron absorption. The result is the emission of a large amount of prompt gamma-rays that is intercepted by the detector (see Figure 2.8). This phenomenon has been observed at the JET tokamak, and MCNP (see Ref. [67]) simulations at JET have been conducted to study it. [49, 68] To properly know the measurement conditions of the detector, this neutron-induced gamma ray component must be taken in account and evaluated for the SPARC case.

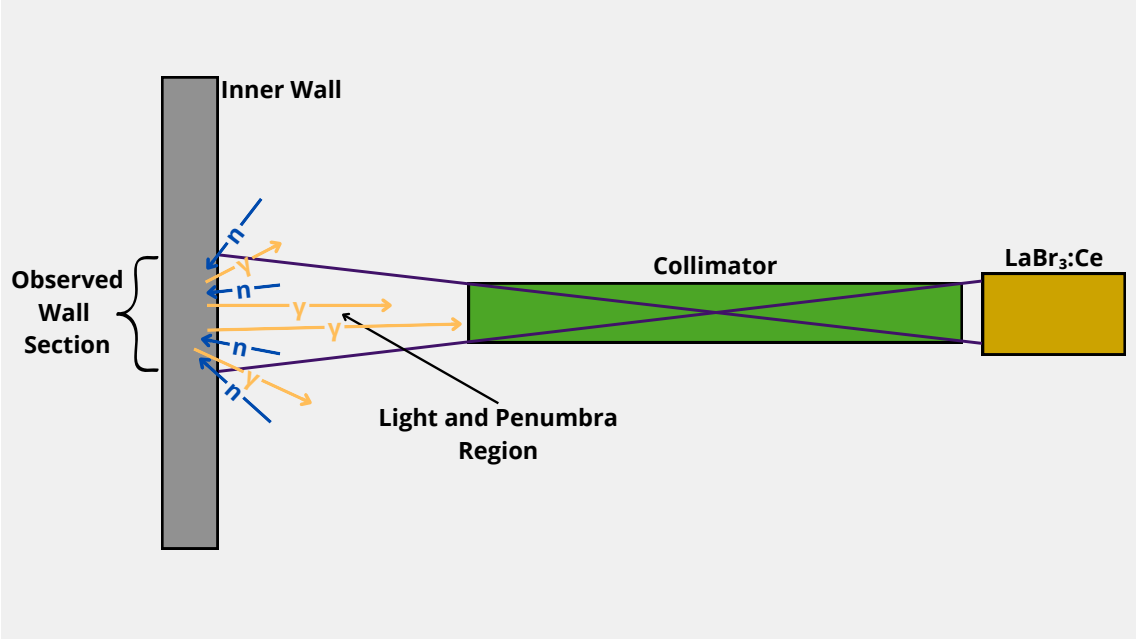

Figure 2.8: Schematic of the generation and observation process of the neutron-induced gamma-ray background. Proportions are exaggerated for graphic reasons.

For the SPARC tokamak, MCNP simulations of this component are not yet available, and measurements can be performed only after the start of operations. An empirical method to estimate it is largely described in Ref. [65], valid for all tokamaks and based on the JET data.
Suppose to know the neutron flux entering the first wall F_n^{in} at the specific location, obtained from numerical calculations. The desired quantity to be evaluated is F_γ^{out}, the neutron induced gamma flux exiting from the wall. These two quantities are connected via the probability of gamma-ray emission P

$$P = F_\gamma^{out} / F_n^{in} \tag{2.9}$$

Reasonably, it is assumed that P is dependent only from the tokamak vessel components and materials, without dependence from the neutron source intensity.
Therefore, after calculating F_n^{in} in the precise first wall location, during a selected experimental scenario, one can obtain F_γ^{out} by knowing the value of P. P can be estimated from JET experimental data where DT campaigns have already been conducted. For the SPARC case, JET-like materials and wall composition will be assumed.
At JET, from the analysis of 96 discharges from the DTE2 campaign the value of P has been extracted, resulting in P = 4.7 %. [65] This study has been performed exploiting the TGRS diagnostic. [25, 69]
In particular, the typical spectrum observed with TGRS is a background structure ranging from 1 up to 10 MeV (see Figure 2.9). The primary source is due to the gamma emission from wall, and a few percent of counts are due to nuclear reaction into the plasma core. Counting the total gamma emission, and calculating the specific neutron flux entering the observed wall, it was possible to estimate the value of P.

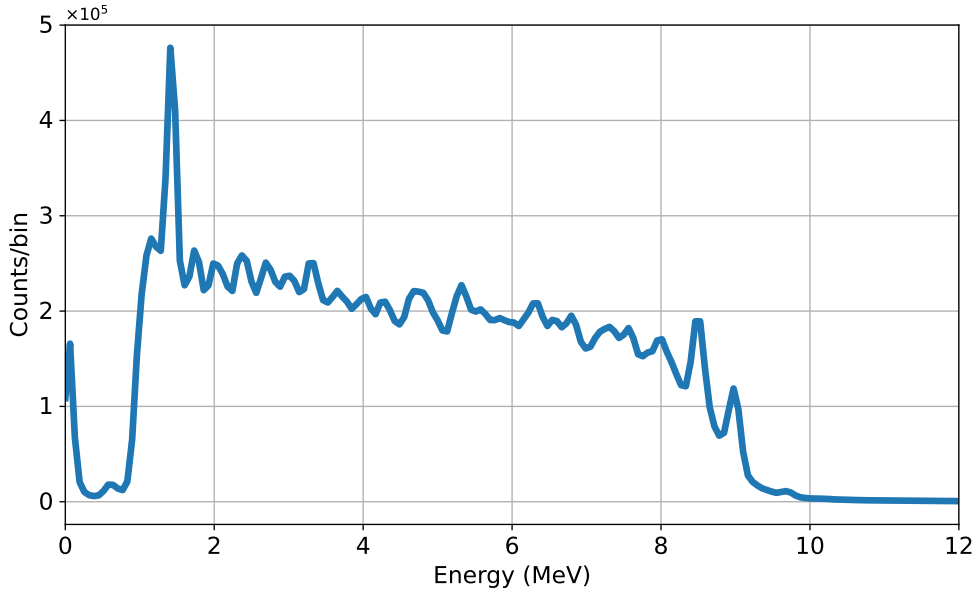

Figure 2.9: Spectrum obtained integrating data from 96 DTE2 discharges at JET, using the TGRS diagnostic.

2.2.6 The spectrometer operational range

Finally, the evaluation of the gamma-ray background in the case of SPARC, based on the experience from JET can be performed.

First, the actual section of the SPARC wall seen by the proposed detector (both for Channel #9 and #10) is calculated via REVOLT, in order to obtain the size and the transport factor of the observed 2D wall portion.
First, consider Channel #10. To obtain the LoS file, the position of the detector is shifted at R = 18.5 m and, similarly at the TGRS at JET, a detector diameter of 3" is considered. The effective detector diameter is set to 3 cm (for instance, by

the using of a 3 cm diameter plug). This is done to take in account the neutron spectrometer placed along the same LoS. It was found that, even if the detector were farther from the source, this change would not affect largely the signal reaching the detector due to the larger effective detector area. At the same time, the first wall area observed by the diagnostic is diminished, as well as the gamma background, due to the improved collimation.
In Figure 2.10 one can notice the inner wall section observed by the proposed diagnostic. The brightness corresponds to the optical transport factor of each pixel calculated via REVOLT.

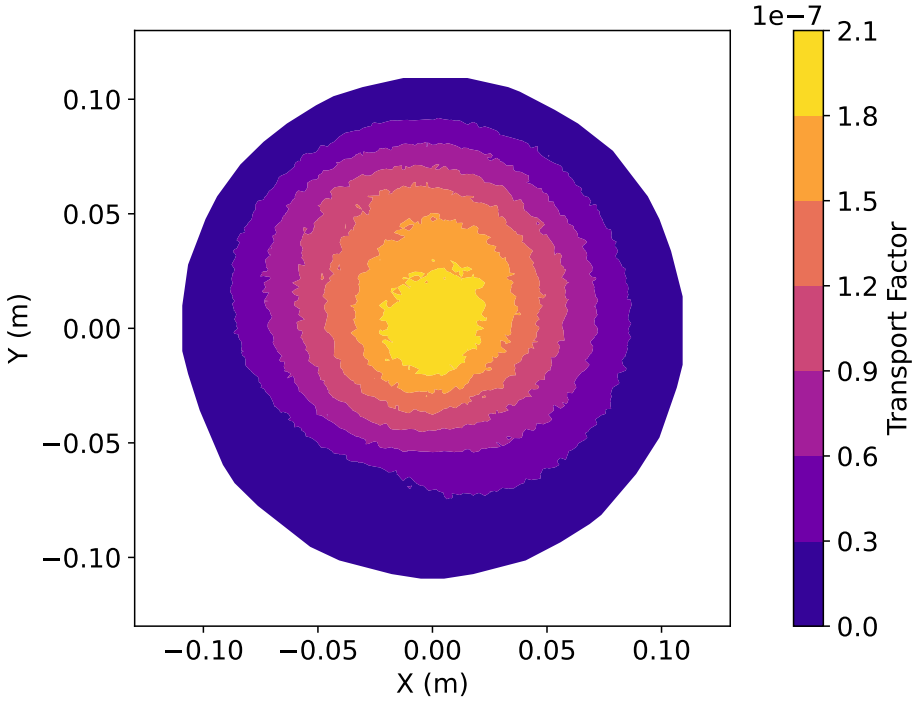

Figure 2.10: Contour plot of the SPARC inner wall section observed frontally by the detector along the Channel #10 horizontal LoS (R = 18.5 m, effective diameter of 3 cm) The brightness corresponds to the transport factor of each pixel.

Subsequently, the neutron flux entering the observed wall area is calculated via a MonteCarlo approach. This takes in consideration the thermal emissivity profile during the PRD discharge at Q>11, and the geometry of the SPARC tokamak. Results show that there is an anisotropic absorption of neutrons by the wall in terms of different poloidal angle θ of the SPARC poloidal section.
Finally, the gamma flux exiting the wall can be calculated with Relation 2.9, and using the wall portion 2D LoS of Figure 2.10, the total count to the detector of the gamma-ray background can be obtained.

Moreover, the signal and background yields are rescaled linearly down for fusion power less than 140 MW. In this way, we can obtain the operational range of the detector. The limits are determined by:

- Upper limit: The maximum sustainable total-counts/s to the front face of the detector, posed equal to 500 kHz.

- Lower limit: the minimum signal measurement requirements so that the uncertainty U<10%.

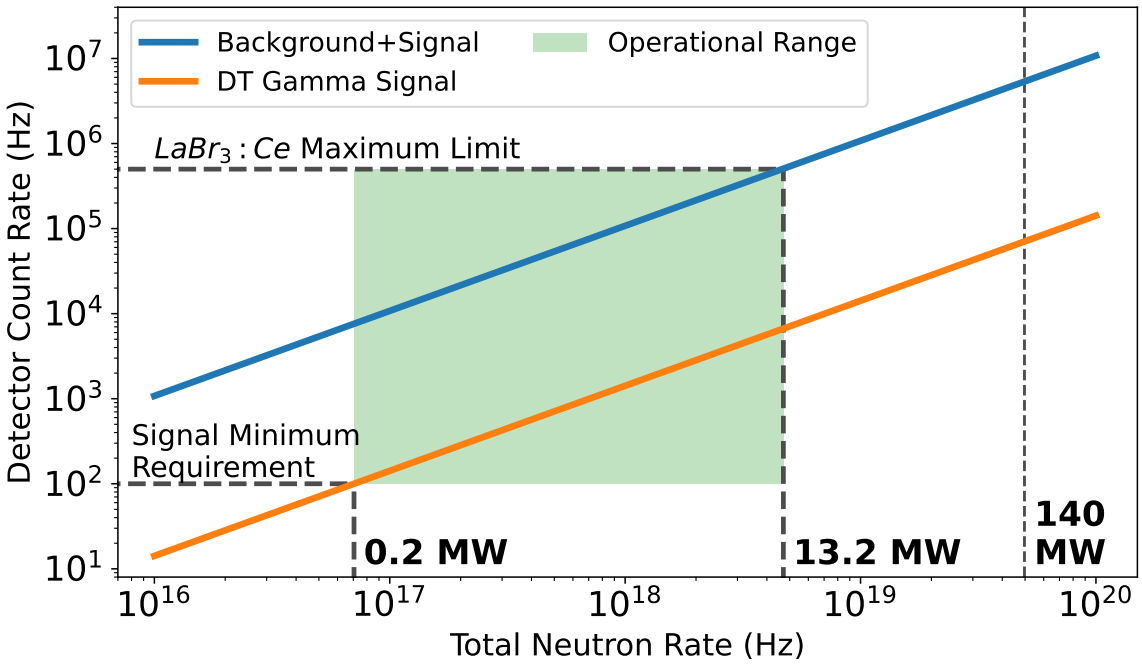

Figure 2.11: Expected count rate at the $LaBr_3$:Ce detector (with a 1.2 m LiH attenuator) when placed along Channel #10 of the SPARC-NCAM at R =18.5 m. The horizontal lines indicate the requirements for performing acceptable measurements, namely that the signal counting rate is at least 100 Hz and the overall counting rate does not exceed 500 kHz. The operational range for fusion power measurements is indicated by the green shaded area.

Figure 2.11 shows the resulting operational range of the proposed detector, considering attenuation effects and detection efficiency. It ranges from 0.2 to 13.2 MW of fusion power scenarios where measurements are possible. One can establish that measurements during high performance experiments are not possible. A tentative strategy to enable operation at higher fusion powers is to apply a gamma-ray attenuator. Tungsten (W) is relatively cheap, and it is a high-Z material, providing major effectiveness to attenuate gamma-ray fluxes. Based on the Lambert-Beer law, the gamma-ray intensity is attenuated according to

$$I(x) = I_0 \exp(-\mu x) \tag{2.10}$$

where $I(x)$ is the intensity attenuated after the gamma beam travelled a distance x inside the material, I_0 is the initial intensity, μ is the attenuation coefficient depending on the material and the gamma-ray energy itself.

Figure 2.12 shows the μ coefficient as a trend of the photon energy taken from the NIST database (see Ref. [70]). One can notice that at the typical energies of the signal (E > 10 MeV), the values of the coefficient are slightly higher than those of the background energy region (E < 10 MeV). Therefore, photons from the signal region will be attenuated more than those of the background. This effect will reduce the width of the operational range.

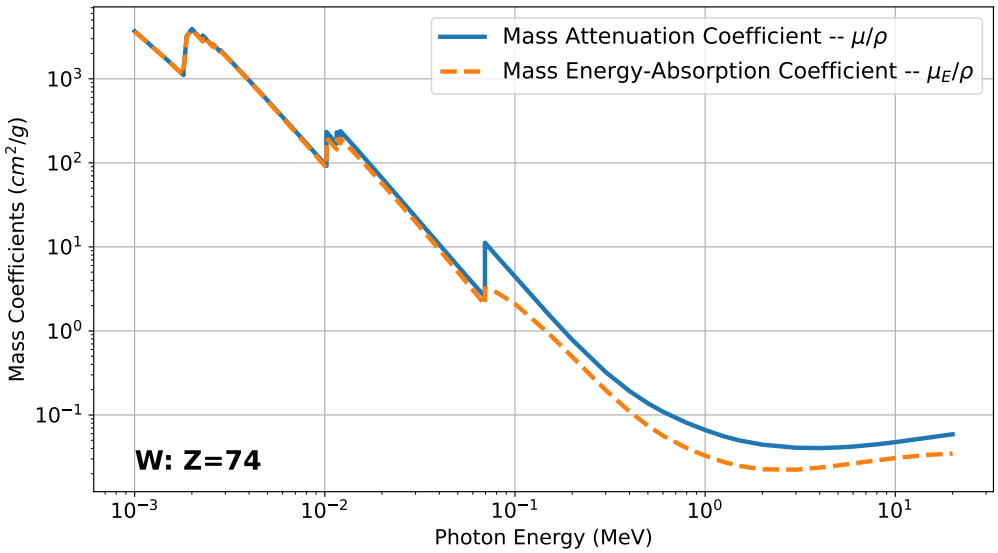

Figure 2.12: Mass attenuation coefficient and mass energy-absorption coefficient of Tungsten as a trend of the photon energy, reported as μ/ρ, where ρ is the W density.

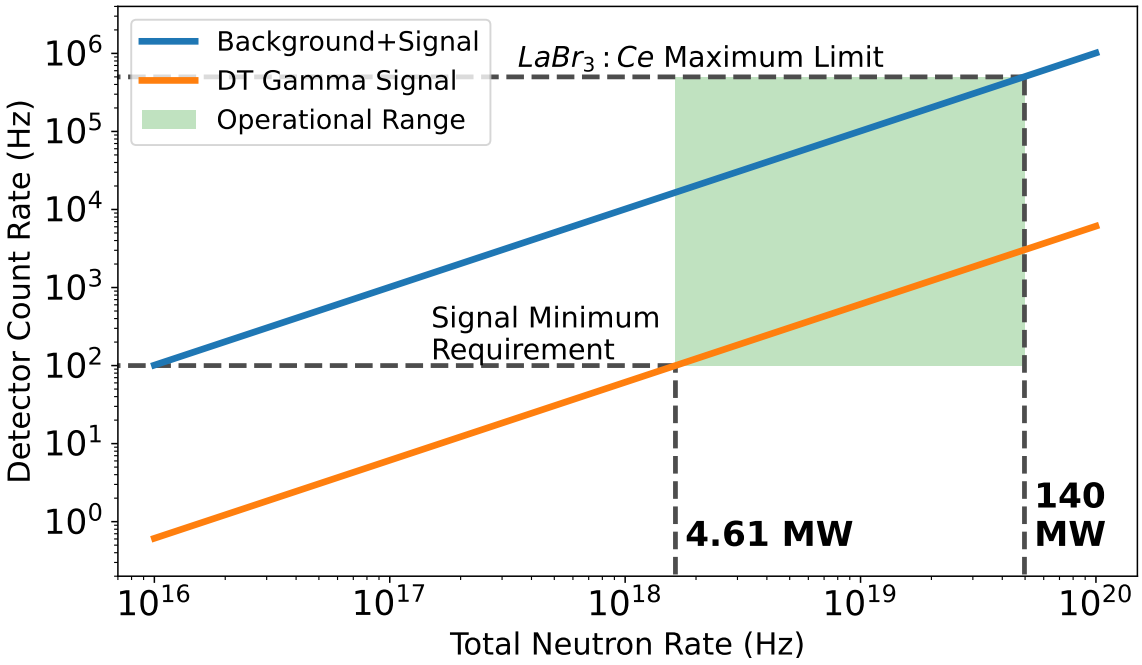

Figure 2.13: Expected count rate at the $LaBr_3$:Ce detector (with a 1.2 m LiH neutron attenuator and a 3.0 cm tungsten attenuator) when placed along Channel #10 of the SPARC-NCAM at R =18.5 m. The horizontal lines indicate the requirements for acceptable measurements, namely that the signal counting rate is at least 100 Hz and the overall counting rate does not exceed 500 kHz. The operational range for fusion power measurements is indicated by the green shaded area.

In Figure 2.13 the previous operational range but with a tungsten attenuator added is shown, ranging from ~ 5 up to 140 MW. The attenuator diameter pairs that of the effective detector area, while the selected length is l = 3.0 cm. This choice is made using the data retrieved from the NIST database, in such a way that, during the PRD, measurements are possible, with the least possible length of the attenuator. The resulting signal counting rate is ~ 3 kHz at 140 MW, corresponding of a statistical uncertainty of ~ 1.8 %. Moreover, selecting different attenuator lengths between $0 < l < 3$ cm, it is possible to shift the measurement range to the fusion power interval of interest. By chosing a W attenuator with a suitable length in the range 0 to 3 cm, the overall operational range spans from 0.2 to 140 MW, covering three orders of magnitude in terms of fusion power.

Now, consider Channel #9, where a 3"-diameter $LaBr_3$:Ce detector is placed at R = 17.2 m. The corresponding operational range is shown in Figure 2.14, where only the 1.2 m LiH attenuator is used.
The resulting operational range lies well above the maximum fusion power expected at 140 MW. At the same time, it is not null, and fusion power measurements can still be performed in high-performance scenarios, such as those foreseen for SPARC Campaign 3, where experiments with fusion powers up to 140 MW are planned.
The difference with Channel #10 is due not only to the reduced amount of signal reaching the detector, but also to the reduced gamma-ray background, which enables measurements in high-performance scenarios, from Q ~ 1 up to Q > 11. This configuration could represent an alternative solution if it is not possible to install the proposed detector along Channel #10. Moreover, without the need for a tungsten attenuator, the statistical uncertainty at 140 MW is of 2.6 %.

2.2.7 Discussions and outlooks

The results shown in this chapter suggest that there is scope for the investigation of a gamma ray diagnostic to perform fusion power measurement at SPARC. The result are based on the JET experience, including the $LaBr_3$:Ce scintillator already used for the first gamma-ray fusion power measurement in a tokamak. Anyway, before the actual implementation, some additional design aspects should be addressed. The primary assumption made is related to the gamma background. In this study, a JET-like background has been considered, but SPARC may be particularly different in terms of materials and structure. This fact might affect the resulting operational range. For this reason, comprehensive MCNP simulations related to the neutron interaction with materials in SPARC are required (benchmarked with existing experiments, like JET) in order to investigate the background into the signal region and the overall associated counting rate.
Another important factor is the choice of the neutron attenuator. LiH, despite being effective at mitigating the neutron background, presents some safety concerns in a facility. LiH is a hazardous material which undergoes violent exothermic reactions with water, even in the form of moist air. Additionally, even if properly sealed, it can release hydrogen at high temperature, leading to detonation. For this reason, alternatives are under investigation, providing similar performance in neutron

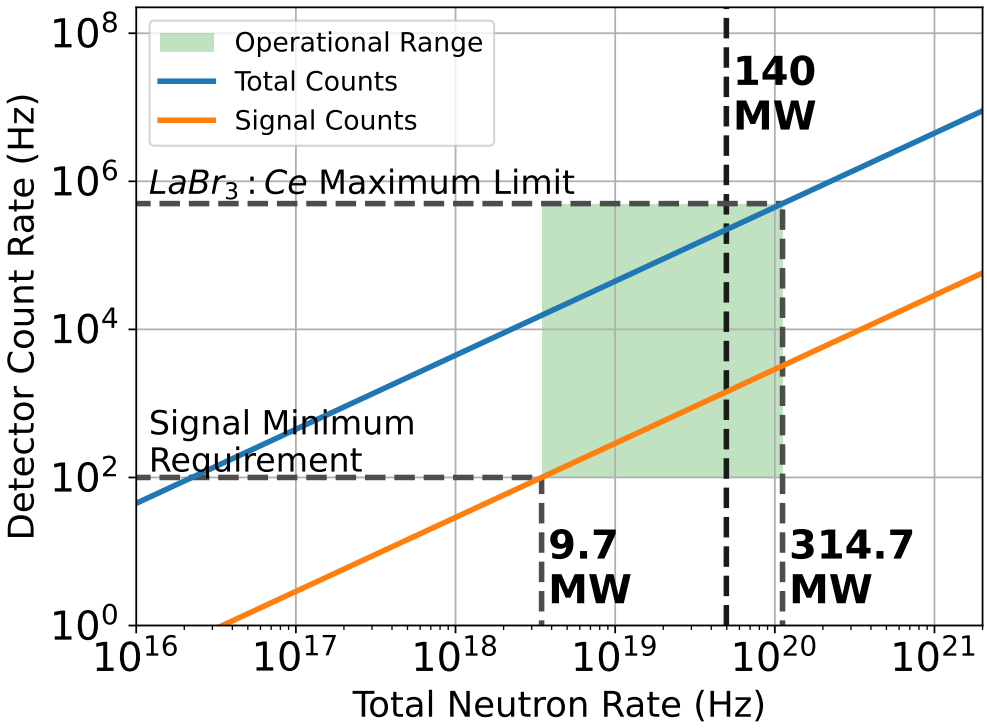

Figure 2.14: Expected count rate at the $LaBr_3$:Ce detector (with a 1.2 m LiH neutron attenuator) when placed along Channel #9 of the SPARC-NCAM at R =17.2 m. The horizontal lines indicate the requirements for acceptable measurements, namely that the signal counting rate is at least 100 Hz and the overall counting rate does not exceed 500 kHz. The operational range for fusion power measurements is indicated by the green shaded area.

reduction.

Regarding the gamma-ray attenuator, W is cheap and does not require large amount of space. It is effective at reducing the gamma ray flux to the detector, but the preferable option is an attenuator capable of mitigating better gamma rays with energy E $<$ 10 MeV compared to those of the signal region E $>$ 10 MeV. Indeed, in Figure 2.13 one can notice a reduction of the width of the operational range of a factor 2.5 with respect to that in Figure 2.13.
Finally, design factors, like the presence of ports and collimators or, more in general, constraints related to allocation of the detector and location of objects obstructing the LoS could affect the operational range, and a detailed design is needed in order to perform a precise scoping study.

2.2.8 Alpha-Boron studies

With the same detector as the one previously described, other kinds of studies can be performed [71]. At JET, investigation of alpha particle, thanks to the $LaBr_3$:Ce scintillator, have been performed [22, 72], as well as runaway electrons study [57, 73]. In particular, experiments involving the observation of gamma-ray emission from the ^{9}Be(α,nγ)^{12}C reaction have been conducted, allowing the study of the alpha particle distribution. In SPARC, ^{9}Be impurities are not expected due to the composition of the first wall, that will be made primarily by Tungsten [74, 53], differently from JET. At the same time, the process of "boronization" will be likely, where the first wall of the machine is conditioned with Boron, exploited to control the Tungsten impurities inside the tokamak [75, 76]. Boron can interact with alphas via the $^{10}\mathrm{B}(\alpha, \mathrm{p}\gamma)^{13}\mathrm{C}$ reaction, producing gamma rays at energies 3.09, 3.68 and 3.85 MeV. This might represent an alternative way for investigating the alpha particle distribution using the gamma ray spectroscopy in SPARC. At ITER, the use of the RGRS gamma-ray diagnostic is foreseen [77] to study this emission for alpha-particle investigations. In principle, this technique could also be applied to different tokamaks and mixtures, such as JT-60SA operating in D–^{3}He plasmas, where alpha particles in the MeV energy range are produced [78].

The aim is to determine if there is scope to investigate alpha particles using the same detector for the fusion power measurement in SPARC. First, we expect the signal spectrum to lie in the spectral region between 2 and 4 MeV, the same of the background. This means that the primary concern will be the signal to background ratio.
Another fact to be taken in account is the resulting spectral shape of the three peaks. Detailed cross section value of the $^{10}\mathrm{B}(\alpha, \mathrm{p}\gamma)^{13}\mathrm{C}$ reaction for each emission channel must be well known, as well other parameters like the boron impurity concentration in the plasma.

To obtain the shape and intensity of the $^{10}\mathrm{B}(\alpha, \mathrm{p}\gamma)^{13}\mathrm{C}$ emission, GENESIS has been used, where the three different channels were implemented. Cross sections of each channel where available in Ref. [79] (see Figure 2.15). Boron was assumed to be Maxwellian, with the same temperature and density profiles as the other ion species. This assumption is supported by the fact that light-impurity transport is dominated

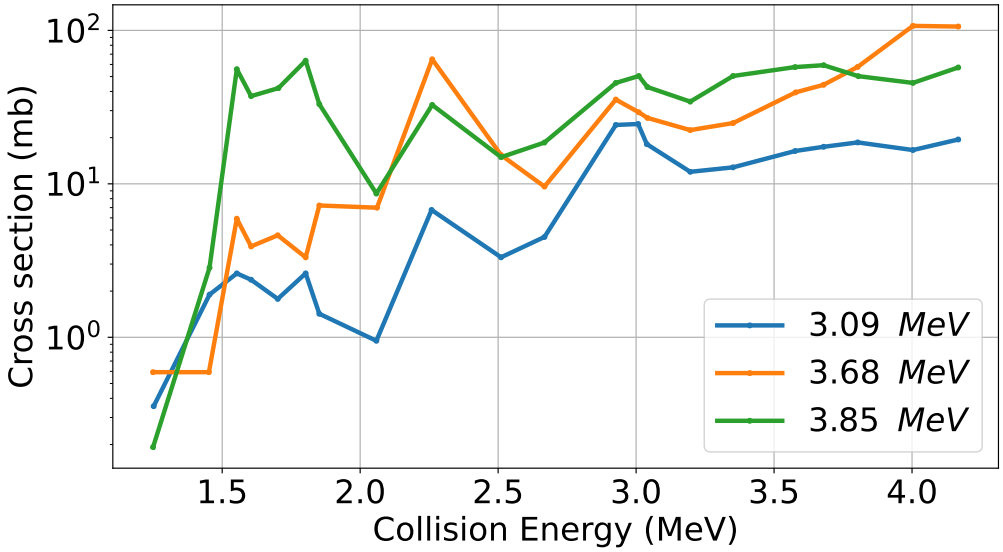

Figure 2.15: Cross section of the three emission channel of the $^{10}\mathrm{B}(\alpha, \mathrm{p}\gamma)^{13}\mathrm{C}$ reaction.

by turbulence [80]. A nominal constant Boron concentration of 1% with respect to the electron density was assumed, chosen as a representative value (i.e., the typical concentration of ^{9}Be impurity measured at JET). Of this, ^{10}B represents about 20%. Alpha particles were modeled as it follows: the typical energy distribution of DT-born alpha particle (a thermal distribution around 3.5 MeV) is generated and then "slowed-down" using an analytical method from the Fokker–Planck theory, implemented in GENESIS. The result is a broader distribution centred at lower energies (see an example in Figure 2.16).

Using the same line of sight of the proposed detector, considering the application of neutron and gamma attenuators and convoluting with the $LaBr_3$:Ce response function, the signal shape can be finally obtained along with the intensity expected during the maximum performance scenario (see Figure 2.17).

Moreover, assuming a JET-like background, it is possible to calculate the expected signal-to-background ratio (StB), resulting in $StB = 2 \cdot 10^{-3}$. It means that, to detect alpha particle features in the spectrum during the DT 140 MW scenario in SPARC, at least 6 minutes of integration time are required and longer integration times will be needed for lower performance scenarios. This result suggests that it may be difficult to perform alpha distribution studies in DT fusion plasmas at high performances at SPARC based on the $^{10}\mathrm{B}(\alpha, \mathrm{p}\gamma)^{13}\mathrm{C}$ reaction. To reach a time resolution of a few seconds, the Boron concentration would need to be increased by a factor of 30 compared to the previously considered value, but this is incompatible with plasma operation. Nevertheless, in scenarios characterised by reduced or absent neutron emission, the signal-to-background ratio should be higher, and thus there is a chance to observe the signal structure over the background. In SPARC, if a D–^{3}He plasma scenario featuring a strong alpha-particle source were to be considered, a scoping study of alpha-particle measurements via gamma-ray emission from the $^{10}\mathrm{B}(\alpha, \mathrm{p}\gamma)^{13}\mathrm{C}$ reaction could be performed.

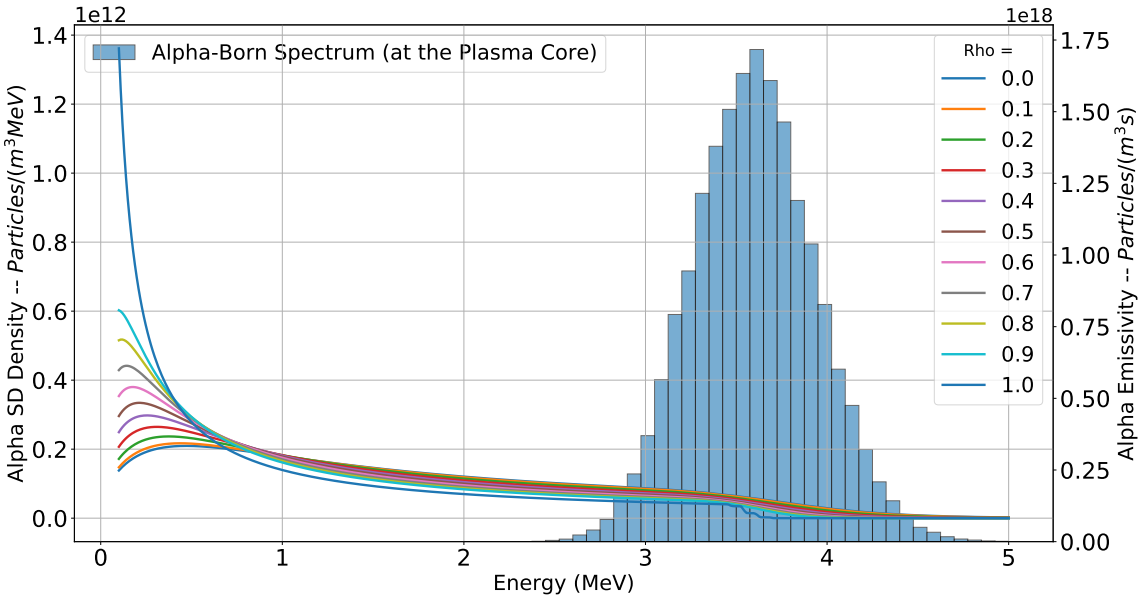

Figure 2.16: Example of a DT-born alpha particle spectrum (light blue histogram, right axis) and its related slowed down distribution at different location inside the plasma (left axis), scanning with the ρ coordinate

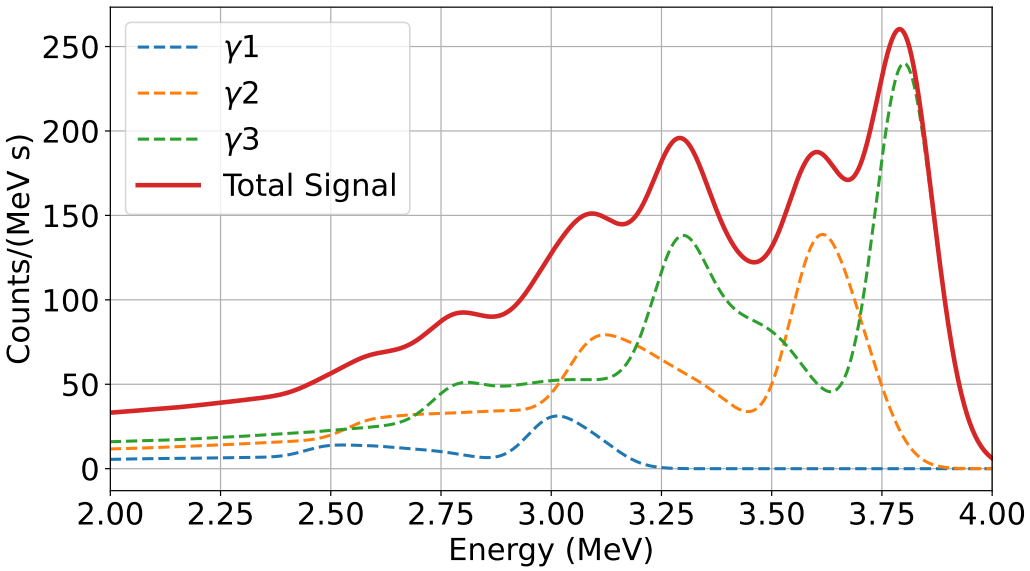

Figure 2.17: Convoluted signal from the three channels of the $^{10}B(\alpha, p\gamma)^{13}C$ reaction, along with their summation. Spectrum obtained with the same diagnostics and configuration of the proposed detector for fusion power measurements.

Chapter 3

Alpha Birth Profile Reconstruction:

Validation of TRANSP simulations in D–^{3}He plasmas from Three–Ion Scheme experiments at JET

As mentioned in the previous chapter, gamma-ray spectroscopy can be used in tokamak for diagnostics of different particle populations. Previously, the novel technique related to fusion power measurements was discussed in the case of SPARC, along with the opportunity to investigate alpha particle distribution observing the gamma ray emission from the Alpha-Boron reaction.

In this chapter, the focus will be oriented to the study of the spatial emissivity profile of alpha particles in dedicated JET experiments. The Gamma Camera Upgrade (GCU) is a gamma diagnostic system observing a poloidal profile of the JET plasma and, after collecting experimental data, through a tomographic reconstruction, a 2D gamma-ray emissivity map can be obtained.
The following chapter describes the validation of simulations performed with the TRANSP code, used to simulate particle and energy transport in tokamak plasmas. This work investigates experiments conducted in Deuterium-Helium-3 (D–^{3}He) plasmas at JET, using the "Three-Ion Scheme", where three ion species are present: thermal deuterium; thermal Helium-3 and a fast Deuterium population.
The aim is to understand if TRANSP simulations can effectively predict the fast deuterium distribution in this kind of plasmas and the profile of the corresponding alpha particle generation by the D–^{3}He fusion reaction. The task is performed leveraging on TOFOR, a neutron spectrometer installed at JET and primarily sensitive to 2.5 MeV neutrons from DD fusion reactions, and GCU data analysis and using tomographic reconstructions of the Alpha Birth Profile.

3.1 Three-Ion Scheme experiments and diagnostics at JET

3.1.1 Three-Ion Scheme discharges

Studying alpha particles is one of the most demanding tasks in tokamak diagnostics [81]. Among the various fusion reactions, the Deuterium-Tritium (DT) reaction is considered the most promising for energy generation, as it produces not only a neutron but also an alpha particle, which plays a key role in sustaining plasma heating. Because alpha particles have a positive charge, they are primarily confined within the plasma by strong magnetic fields, making their detection and analysis particularly difficult. Moreover, in DT plasmas, alpha diagnostics are further complicated by the intense neutron background and by the limited availability of facilities currently operating with tritium. These limitations highlight the need to explore alternative sources for investigating alpha particles.

A significant source of alphas has been generated at JET using D–^{3}He plasmas during experiments called "Three-Ion Scheme" (TIS) [82, 83, 72, 84]. In this kind of discharges, the plasma is made of thermal Deuterium (D) and Helium-3 (^{3}He), while a fast Deuterium (fast-D) population is introduced through Neutral Beam Injection (NBI) which absorbs the power injected by Ion Cyclotron Resonance Heating (ICRH), when the wave frequency resonates with the Doppler-shifted ion cyclotron frequency of the deuterium beam ions in the plasma core [83, 85].
Under these conditions, a strong emission of both alpha particles and neutrons is observed, produced by the reactions $^3\mathrm{He}(\mathrm{D},\mathrm{p})\alpha$ and $\mathrm{D}(\mathrm{D},\mathrm{n})^3\mathrm{He}$ respectively, with neutron production rates in the range of $\sim 1 \cdot 10^{16}$ n/s. This emission is expected to be concentrated in the core of the plasma, with little to no emission in the peripheral regions [86]. The presence of this localised and intense alpha particle source offers a valuable opportunity for testing alpha diagnostic techniques and validating fast ion simulations.

Table 3.1: Main plasma parameters of the JET discharges in D–^{3}He mixtures in Three Ion Scheme experiments analysed in this work. Helium-3 concentration data are taken from Real-Time Experiment Central Control (RTCC) system [87].

Parameter	**Value**
Plasma current	2.5 MA
Magnetic field (plasma core)	−3.7 T
Electron density (plasma core)	$\sim 1 \times 10^{20}$ m^{-3}
Helium-3 concentration	18–28% of the total ion density
Electron temperature	1–10 keV
NBI power	3.1–18.6 MW
ICRH power	2.1–6.1 MW
NBI-to-ICRH power ratio	2–3 (except discharges 95673 and 95684)
Total neutron rate	$\mathcal{O}(10^{15})$ up to $\sim 1 \cdot 10^{16}$ n/s

In this work, seven discharges at JET were analysed: 95671, 95672, 95673, 95679,

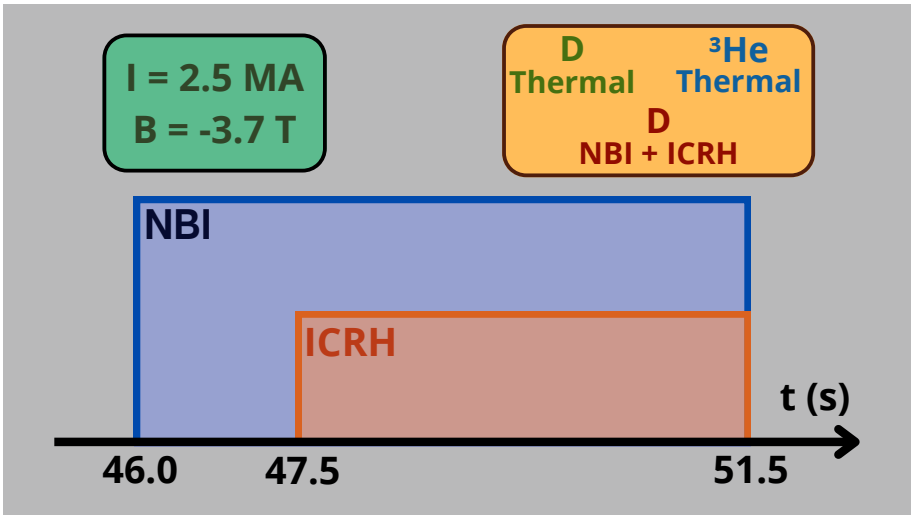

Figure 3.1: Schematic of the heating process in a typical TIS discharge.

95680, 95683, 95684. The operations were performed in the experimental conditions summarised in Table 3.1. A schematic overview of the TIS experiments is shown in Figure 3.1. The fast Deuterium is injected starting at 46 s. In this phase, only a reduced neutron emission from (D,n)^{3}He reaction is observed, along with a gamma ray emission detected by the GCU, primarily due to the prompt gamma rays emitted by the first wall nuclei, intercepting the GCU detectors. This represents a source of background, not indicating the trigger of the ^{3}He(D,p)α reaction. At 7.5 s the ICRH heating is turned on, heating the NBI-deuterons up to 1-2 MeV and resulting in an alpha emission from ^{3}He(D,p)α reactions. In Figure 3.2 one can see an example of the actual time traces of plasma parameters for Discharge #95671.

3.1.2 The TOFOR neutron spectrometer at JET

Data from two diagnostics installed at JET have been leveraged to carry out the TRANSP validation. These are the TOFOR neutron diagnostic and the Gamma Camera Upgrade, installed at JET in proximity of the 8th and 1st octants, respectively.

The TOFOR diagnostic is a neutron spectrometer based on the Time-of-Flight (ToF) technique, which is fundamental to investigate fast deuterium distribution features. In this technique, the time taken by a neutron to cross a known distance inside the instrument is measured, allowing the neutron energy to be inferred [88, 89, 90, 91].
The neutron is intercepted by two different detectors (called S1 and S2), providing the start and stop timestamps of the flight path. In S1, a neutron can undergo elastic scattering with a proton inside the scintillator material. The recoiling proton can be detected by S1 itself, providing the start timestamp. The scattered neutron is then detected by S2, which provides the stop timestamp.

S2 is positioned at a known distance $L \simeq 1221$ mm from S1, on the sphere of constant ToF with radius $R \simeq 705$ mm, and at an angle α of about 30° with respect

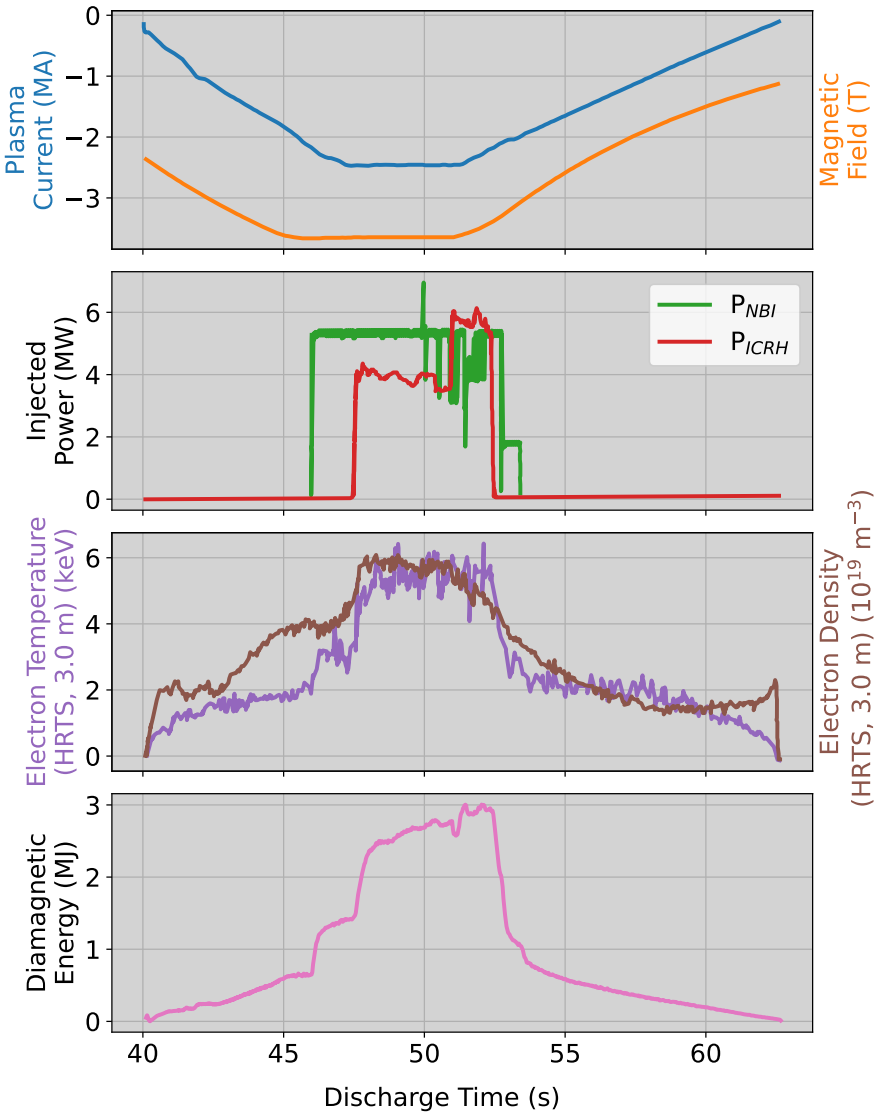

Figure 3.2: Time traces of various plasma parameters measured at the plasma core for Discharge #95671, showing: plasma current and magnetic field; NBI and ICRH power; electron temperature (High Resolution Thomson Scattering (HRTS), 3.0 m) and density (HRTS, 3.0 m); diamagnetic energy.

to the incident beam direction. This configuration avoids the detection of neutrons that have not undergone elastic scattering in S1, while limiting excessive energy loss of the scattered neutron. In fact, for elastic scattering of a neutron (n) with a proton, the energy of the scattered neutron (n') is given by:

$$E_{n'} = E_n \cos^2(\alpha), \tag{3.1}$$

where E_n and $E_{n'}$ are the energies of n and n', respectively.

Considering the geometry of the system (see Figure 3.3), it is possible to derive a relation between L and R:

$$L^2 = 2R^2[1 - \cos(\pi - 2\alpha)] = 4R^2 \cos^2(\alpha), \tag{3.2}$$

leading to the following expression for the scattered neutron energy:

$$E_{n'} = \frac{1}{2} m_n v_{n'}^2 = \frac{1}{2} m_n \left(\frac{L}{ToF}\right)^2, \tag{3.3}$$

where $v_{n'} = L/ToF$. Combining equations 3.2 and 3.3, a relationship between the energy of the incident neutron and the measured ToF is obtained:

$$E_n = \frac{2 m_n R^2}{ToF^2}, \tag{3.4}$$

which provides a useful approximation for estimating the neutron energy. For instance, a 2.5 MeV neutron corresponds to a ToF of approximately 65 ns. Longer ToF values correspond to lower neutron energies, and vice versa. In practice, the TOFOR response function is more complex [92].

S1 and S2 are plastic scintillators. S1 is placed in front of the collimated neutron beam and consists of five layers of circular detectors (40 mm diameter and 5 mm thickness per layer). The neutron flux is guided to S1 through a 1.90 m-long collimator with a diameter of 40.7 mm.
S2 covers an angular range from $\alpha - 6.98°$ to $\alpha + 7.87°$, leading to an energy spread between 1.53 and 2.08 MeV for 2.5 MeV neutrons. The scintillator is rotated by a small tilt angle $\theta = 5°$ to compensate for differences in light propagation time within the scintillator material. In total, 32 S2 detectors are arranged along the constant ToF sphere at $\alpha = 30°$.
S1 and S2 provide the start and stop timestamps t_1 and t_2. For each stop signal, start signals are searched within a predefined time window. This procedure yields both real and random coincidence pairs. Negative ToF values, where no physical signal is expected, allow an accurate estimation of the background due to random coincidences, which is subsequently subtracted from the spectrum [90].

The installation and first operations of TOFOR at the JET tokamak began in 2005. The diagnostic was developed and optimized to operate primarily in deuterium plasmas and to study the 2.5 MeV neutron component originating from the D(D,n)^{3}He fusion reaction, typically over an energy range between 1 and 5 MeV. TOFOR is positioned above the machine and observes the plasma along a vertical line of sight.

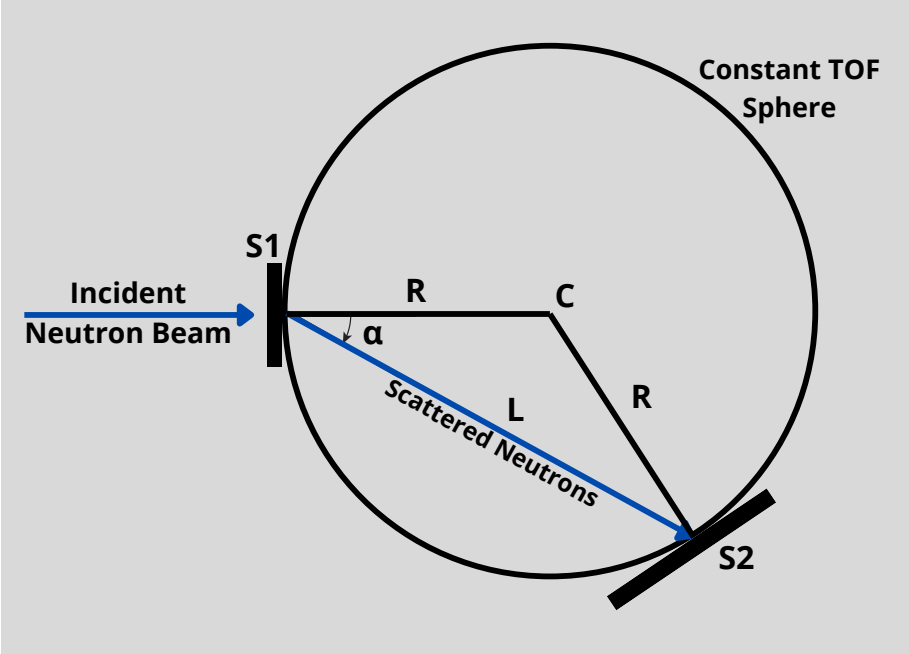

Figure 3.3: Schematic of the TOFOR diagnostic. The incident neutron beam is collimated toward S1. The scattered neutrons are detected on S2, positioned at an angle α with respect to the incident beam direction.

The diagnostic is primarily designed to operate in deuterium plasmas with total neutron rates ranging from 10^{12} to 10^{17} n/s. It was designed to achieve an optimal compromise among key performance parameters for DD neutron measurements, including an energy resolution of $\Delta E_n/E_n = 5.8\%$, a geometrical efficiency $\epsilon \simeq 0.12$ cm^2, and a maximum count rate of about 300 kHz.

The TOFOR diagnostic is particularly relevant for the analysis of Three-Ion Scheme (TIS) plasmas. In these scenarios, a significant amount of deuterium is present, leading to intense neutron emission dominated by the D(D,n)^{3}He reaction. The resulting neutron spectrum around 2.5 MeV exhibits a broad and non-trivial shape, strongly influenced by the presence of fast deuterium components. Due to their higher energies, fast deuterons increase the fusion cross section and, consequently, the neutron production rate.

During the studied TIS discharges, TOFOR operated within its optimal neutron rate range, with neutron yields not exceeding 10^{16} n/s. For good statistical accuracy, neutron yields above 10^{15} n/s are preferred.

Figure 3.4 shows representative TOFOR spectra. When neutron emission is dominated by NBI-heated deuterium reactants with energies of approximately 100 keV (as is the case for most JET discharges) the spectrum exhibits a broad peak around 65 ns. The presence of faster reactant components, for instance induced by ICRH, instead results in a significantly broader spectral structure, reflecting the underlying fast-deuterium distribution.

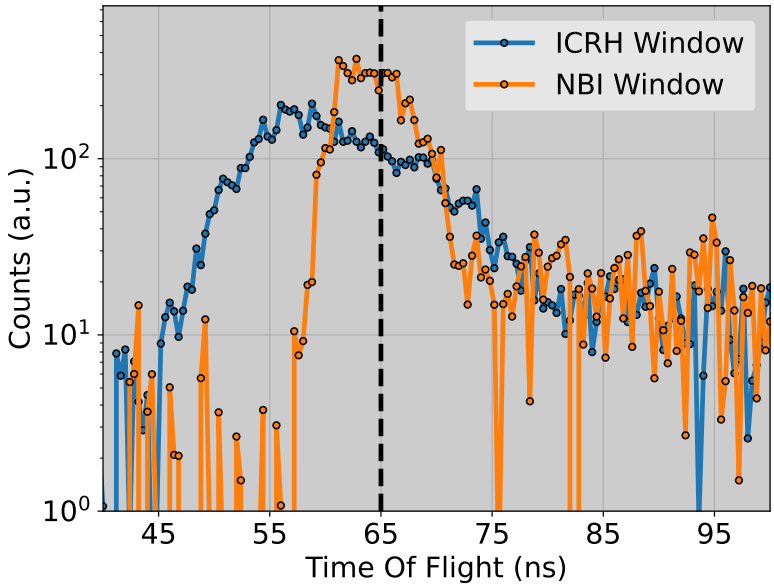

Figure 3.4: Normalised experimental spectra obtained with the TOFOR diagnostic from Three-Ion Scheme experiments. The orange curve corresponds to a discharge phase with only NBI heating applied at $E \sim 100$ keV. The blue curve corresponds to a phase where NBI deuterium is further heated by ICRH, reaching energies up to 1–2 MeV.

3.1.3 Gamma Camera Upgrade at JET

The Gamma Camera Upgrade (GCU) is a diagnostic system consisting in 19 channels, observing a poloidal section of the tokamak JET, in proximity of the 1st octant (see Figure 3.5). Its channels, 10 horizontal and 9 vertical, are divided so that they can intersect each others in the 2D section. For each channel, a 1" × 2/3" $LaBr_3$:Ce-based detector [25, 20, 22] is mounted, providing spectroscopic capabilities of gamma rays [93, 21, 71, 86, 24, 58, 94].
Silicon Photomultipliers, with dimension 12 x 12 mm, are mounted for each detector. These are chosen primarily for their very compact size and insensitivity to the magnetic field.

In 2017, the Gamma Camera has been upgraded, where the $LaBr_3$:Ce scintillator has substituted the previous CsI. CsI had limited spectroscopic capabilities, and it was characterised by a slow decay time ($0.5 - 4\ \mu s$). The upgrade was made in preparation to the higher performance discharges predicted at JET for Deuterium and Deuterium-Tritium campaigns, where high neutron yields were expected, up to $5 \cdot 10^{17}$ n/s. Energy resolution and counting rate capabilities has improved significantly with the upgrade, reaching values better than 5% at 1.1 MeV and exceeding 1 MCounts/s, respectively. Major values for counting rate can be achieved, but pile up effects start to become too harsh to be handled.

The Upgrade allows studying fast ions and runaway electrons inside the JET plasma. Indeed, these kinds of populations can react with impurities (like ^{12}C and ^{9}Be) or fusion reactants, respectively, producing gamma-rays. One of the most studied gamma-ray emissions at JET comes from the $^{9}Be(\alpha,n\gamma)^{12}C$ reaction, emitting

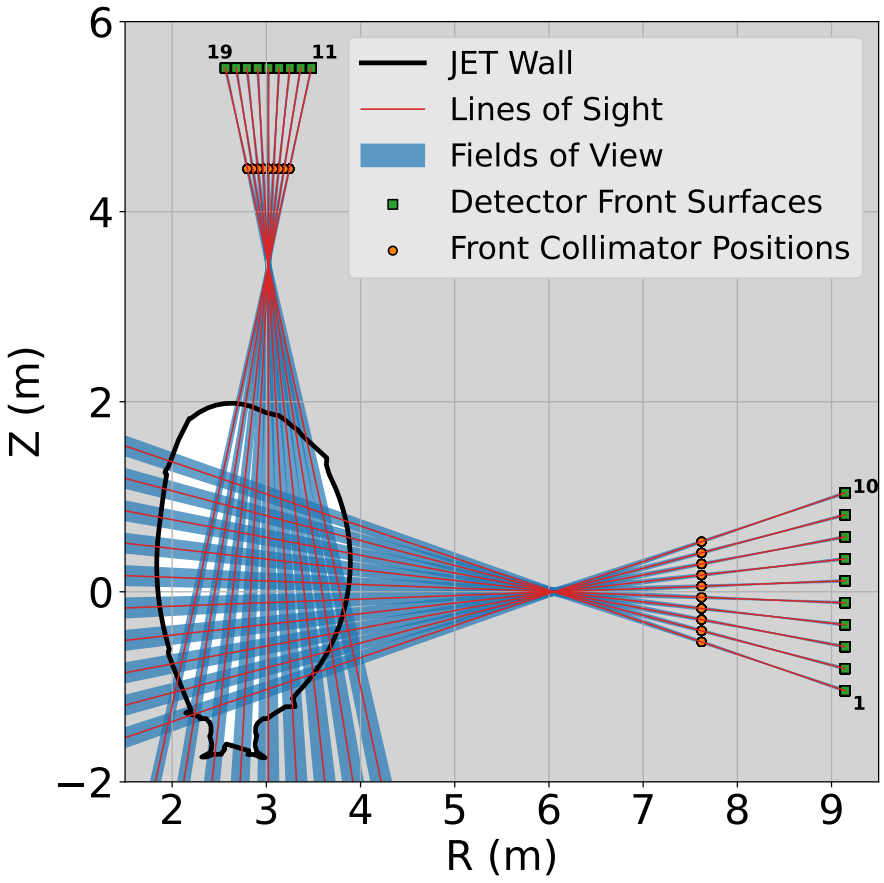

Figure 3.5: Schematic of the Gamma Camera Upgrade at JET.

at 4.44 MeV [22].
The GCU combines spectroscopic and tomographic capabilities. By analysing the spectra measured by the individual GCU channels, specific energy ranges can be selected and integrated to obtain a count profile consisting of 19 entries.
Another important factor is the intrinsic radioactivity of the $LaBr_3$:Ce scintillator. This doesn't interfere with measurements due to the very low emissivity, but it provides at the same time a way to calibrate the detectors, or for monitoring the stability of the detector between different discharges [17].

The GCU can be used to observe the gamma ray emission from the $^3He(d,\gamma)^5Li$ reaction, characterised by a broad energy spectrum at ~ 16.4 MeV [95]. This is a rarer branch of the more common $^3He(D,p)^4He$ reaction, with a relative branching ratio in the order of ~ 10^{-5} γ/α [46]. The two reaction channels have the same reactants, and this means that observing the D–^{3}He gamma ray emission would allow to infer the D–^{3}He fusion-born alpha particle 2D profile.
In Figure 3.6 a count-profile obtained using the GCU is shown. For each channel, a gamma count value is associated. This example refers to a GCU profile obtained during a TIS experiment at JET, where gamma rays from the gamma-branch of the D–^{3}He reaction were observed.

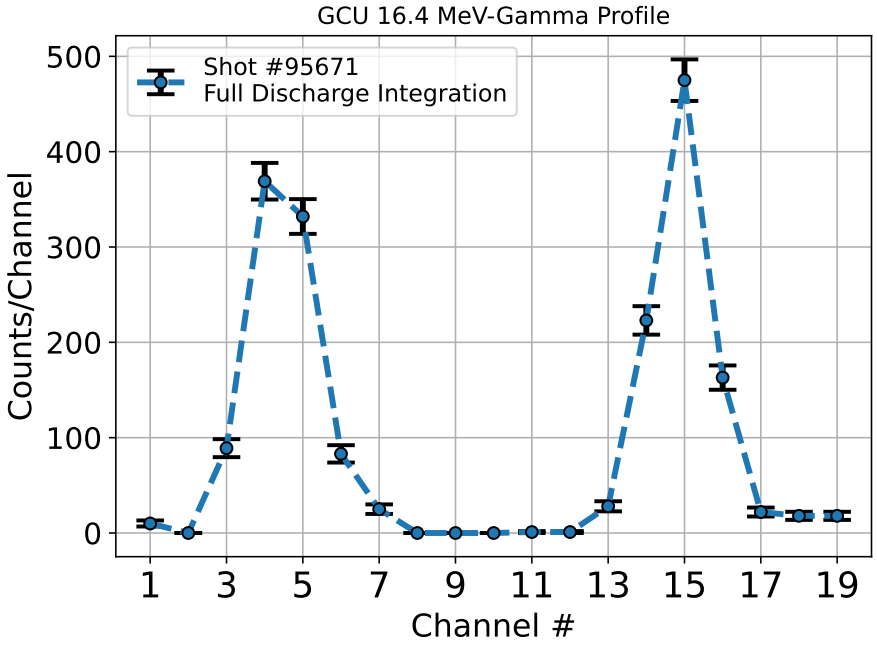

Figure 3.6: An example of Gamma Camera profile obtained at JET, during a Three-Ion Scheme experiment, observing the gamma emission from the gamma-branch of the D–^{3}He reaction, integrated over the full discharge period.

3.1.4 Tomographic reconstruction at JET

The Gamma Camera Upgrade (GCU) is capable of obtaining line-integrated data of gamma counts in a 2D poloidal profile of JET plasmas. GCU data, however,

does not represent a spatial emission profile and, more in general, doesn't provide a physical quantity easy to visualise or intuitively understand. Therefore, a software able to elaborate GCU data is needed, in order to obtain a 2D map of the emissive plasma, based on experimental data.

TREVISO [96, 86] is a python-based code developed to perform tomographic reconstruction of spatial emission profiles (mainly used to study fast ions and runaway electrons) in the JET tokamak poloidal section, starting from GCU experimental data. The code divides the plasma poloidal 2D region of JET in many smaller pixels where, for each of them, its emissivity value is determined during the reconstruction. Each pixel is a 9 x 9 mm square arranged in a 40 x 70 image (2800 pixels in total).

Consider the measured quantity y, and $S(y)$ its probability density function (pdf), both expressed as a continuous function. Consider $F(x)$ the pdf of the quantity x that needs to be reconstructed. $W(y, x)$ is defined as conditional probabilty, here introduced as a continuous function. The equation connecting S with F is given by

$$S(y) = \int_{-\infty}^{+\infty} W(y, x) F(x)\, dx \tag{3.5}$$

In the case of discretised quantity, Equation 3.5 becomes

$$\overline{S} = \overline{\overline{W}} \cdot \overline{F} \tag{3.6}$$

where $\overline{S}$ is a 19 entries vector, representing the total counts obtained from each GCU channel. $\overline{F}$ consists in a vector with 2800 entries, that represent the emissivity of each pixel of the 2D image. $\overline{\overline{W}}$ is a 19×2800 matrix, called transfer matrix, that connects the GCU count profile to the emissivity profile. The transfer matrix elements are calculated considering the combination between the overlap of the lines of sight area with the pixel area, and the solid angle subtended by the detector as seen from the pixel centre. Each element represents the probability that the radiation emitted in the j-th pixel will be detected by the i-th channel of the camera.

If $\overline{\overline{W}}$ is known, a possibility to solve the problem is to find the best estimation of $\overline{F}$ that gives the best match between the measured $\overline{S}$ and the one from Equation 3.6. Anyway, this method may need long computational time, with lower efficiency. Alternatively, inverting $\overline{\overline{W}}$, it's possible to obtain $\overline{F}$ by a measure of $\overline{S}$. The inversion of experimental data $\overline{S}$ can be performed routinely, and this process is called tomography. Tomographic techniques based on the inversion of line-integrated measurements are widely used in fusion plasma diagnostics to reconstruct local emissivity profiles, for instance in soft X-ray, bolometric and neutron diagnostics [97]. Similar approaches are also commonly applied to fast-ion diagnostics, where tomography plays a key role in inferring two-dimensional spatial or velocity-space distributions from limited experimental views [98, 84].
The iterative method used in this code is called Maximum Likelihood using Expectation Maximization (MLEM). This iterative algorithm, derived by the Bayesian statistic, is currently used to perform PET [99, 100]. The aforementioned method has been chosen for use in TREVISO due to its superior performance, as demonstrated in comparison with other methods such as Singular Value Decomposition,

Poisson regularisation, and Tikhonov regularisation [96]. The idea of the MLEM is to use a first estimate of $\overline{F}$ to compute $\overline{\overline{W}}^{-1}$, and then use $\overline{\overline{W}}^{-1}$ to recompute $\overline{F}$, to iteratively update the estimate of F (see Ref. [96] for more information). Several initial guesses for F were tested (for example, $F_i^0 = 1$ for all i), but no significant differences in the final reconstruction were observed. Finally, the method can be described by a single formula:

$$F_i^{n+1} = \frac{F_i^n}{\sum_j^{Nc} W_{ji}} \cdot \sum_j^{Nc} \left(W_{ji} \frac{S_j}{\sum_k^{Np} (W_{jk} F_k^n)} \right) \tag{3.7}$$

where N_p is the number of pixels (2800) and N_c is the number of channels (19). i indicates the pixel index, while j the channel index. n represents the iteration index.

The method converges if

$$\frac{S_j}{\sum_k^{Np} W_{jk} F_k^n} \xrightarrow[n\to\infty]{} 1 \tag{3.8}$$

In practice, to decide the maximum number of iterations, a subset of the measured data with lower statistics is used to evaluate the goodness of the reconstruction via the Pearson χ^2 statistic. The iterative algorithm is stopped when χ^2 on this independent subset stops decreasing or begins to increase, indicating that further iterations would not improve the reconstruction and could lead to overfitting.

After a custom number of iterations, a smoothing operation is performed. Indeed, noise can affect the measurements, and this factor should be considered into the reconstruction. The noise sources have zero-mean, suggesting that their effects can be reduced at the final reconstruction by means of a smoothing operator, implemented in the code. This operator "smooths" the values of nearest-neighbour pixels located on the same flux surface. Therefore, TREVISO also requires the magnetic equilibrium data as input (which can be taken directly from the TRANSP output) to perform the smoothing along flux surfaces.

An example of application of the code to data of Discharge #95671 is shown in Figure 3.7 and 3.8.

3.2 Validation of TRANSP simulations

3.2.1 The TRANSP code

TRANSP [101, 102, 103, 104] is an interpretative transport code, developed at Princeton Plasma Physics Laboratory. It is used to simulate the evolution of particle and energy transport in tokamak plasmas. It resolves the particle and energy balance equations, using experimental data as constraints. It determines the transport coefficients (thermal conductivity, diffusivity, etc.) and provides many diagnostic and modelling physics quantities, helpful for the interpretation of tokamak experiments.

The code is defined as "1.5D" dimensional, because, albeit the magnetic equilibrium is considered 2D (calculated in the poloidal section), every physics quantities are considered constant along the toroidal flux surfaces. It takes as input some

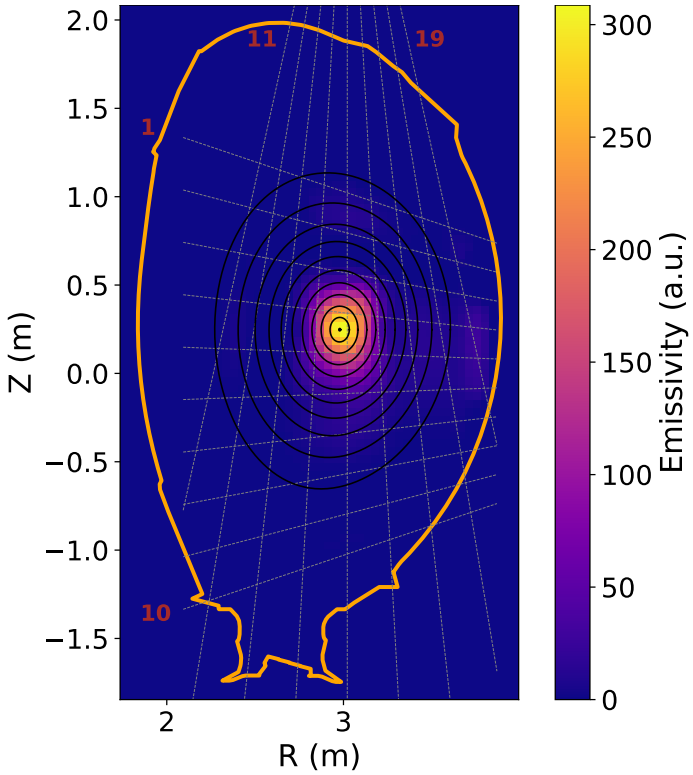

Figure 3.7: 2D emissivity matrix obtained trough a tomographic reconstruction of a Gamma Camera profile using TREVISO. Black curves: magnetic flux surfaces; white dashed lines: Gamma Camera lines of sight. Shot #95671, timestamp: 50.0 s, integration time: 1.0 s.

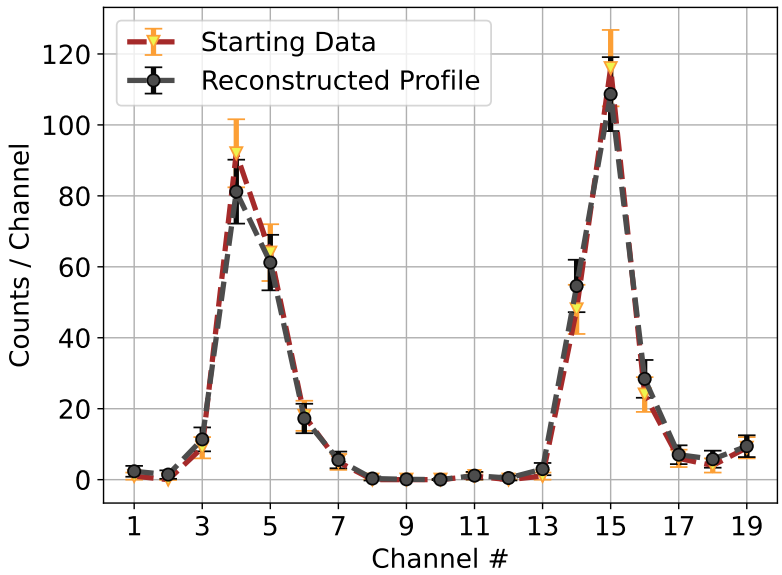

Figure 3.8: Comparison between the experimental Gamma Camera profile (yellow triangles) and the reconstructed profile via TREVISO (black rhombuses).
Shot #95671, timestamp: 50.0 s, integration time: 1.0 s.

physical quantity from diagnostics, like: electron temperature and density, for example from the High Resolution Thomson Scattering (HRTS); ion temperature from Charge Exchange Recombination Spectroscopy; radiated power from Bolometry; total plasma current; the q-profile from EFIT and the effective ion charge number Z_{eff}. The ion density, instead, is inferred from the electron density and Z_{eff}, considering plasma quasi-neutrality.

First, TRANSP resolves the Grad-Shafranov equation for each time step using the TEQ module. Using as constraints some experimental parameters, it gives the magnetic field profiles. Subsequently, it resolves the particle balance equation, for each plasma species. Particle source are calculated using the NUBEAM and FRANTIC module, for fast particle and neutrals, respectively. It then solves the ion energetic balance equation, using NUBEAM and TORIC modules, related to the NBI and ICRH auxiliary heating, respectively. The ion thermal conductivity is obtained if the ion temperature is known, otherwise it is calculated from models. Similarly, the electron energetic balance equation is resolved, and the electron thermal conductivity is obtained.
TRANSP works with fixed time steps, not dynamically evolving input profiles, with the only exception of the q-profile. At every step, auxiliary quantities are calculated, like: current and field profiles, heating profiles, heat fluxes and momenta, diffusivity and conductivity.
TRANSP, through the "namelist", can set the module that will be used during the calculation. These can be selectively activated and deactivated, based on the specific request.

As stated before, TRANSP returns a variety of auxiliary diagnostic quantities, from which analysis can be performed. In this work the TRANSP estimates of the total neutron rate time evolution during the discharge, along with the Fast Deuterium Distribution (FDD) are analysed. The aim was to perform a validation of the TRANSP output, with a comparison with experimental data, in order to test the accuracy of the prediction of the code.

The TRANSP analyses were conducted iteratively. First, plasma experimental parameters were used, including magnetic equilibria together with density, temperature, effective ion charge, and bolometric profiles. Subsequently, NBI and ICRH heating schemes were included into simulations. To model the radio-frequency power absorption, the TORIC code was used within TRANSP, while a "kick operator" was used to describe the transfer of energy from the wave to the injected deuterium beam and its consequent acceleration to higher energies [105]. Since the impurity composition at JET (mainly attributed to Beryllium and Nickel) is not precisely known as well as the ^{3}He concentration in these plasmas (which is roughly estimated at around 20% from RTCC), these quantities were varied in successive iterations until the computed plasma stored energy and neutron rate matched experimental observations.

For the discharges considered in this study, the neutron yield contains contributions from three distinct channels: reactions between bulk thermal ions (thermonucelar), interactions of fast beam ions with the thermal population (beam-target), and collisions exclusively among fast ions (beam-beam).

Table 3.2: Discharges and associated TRANSP simulations, together with the selected timestamps for Fast Deuterium Distribution analysis.

Shot #	95671	95672	95673	95679	95680	95683	95684
Simulation ID	A25	A25	A26	V36	V07	V07	A24
Time (s)	50.0	52.0	51.0	49.95	49.95	49.2	49.0

In Table 3.2 the selected TRANSP simulations relative to the studied discharges are indicated. The simulations were selected based on the accuracy in predicting the experimental data from the JET fission chambers (i.e., the time evolution of the total neutron rate). Indeed, a high neutron emission is present in Three-Ion Scheme experiments, due to the D(D,n)^{3}He reaction. An example is shown in Figure 3.9.

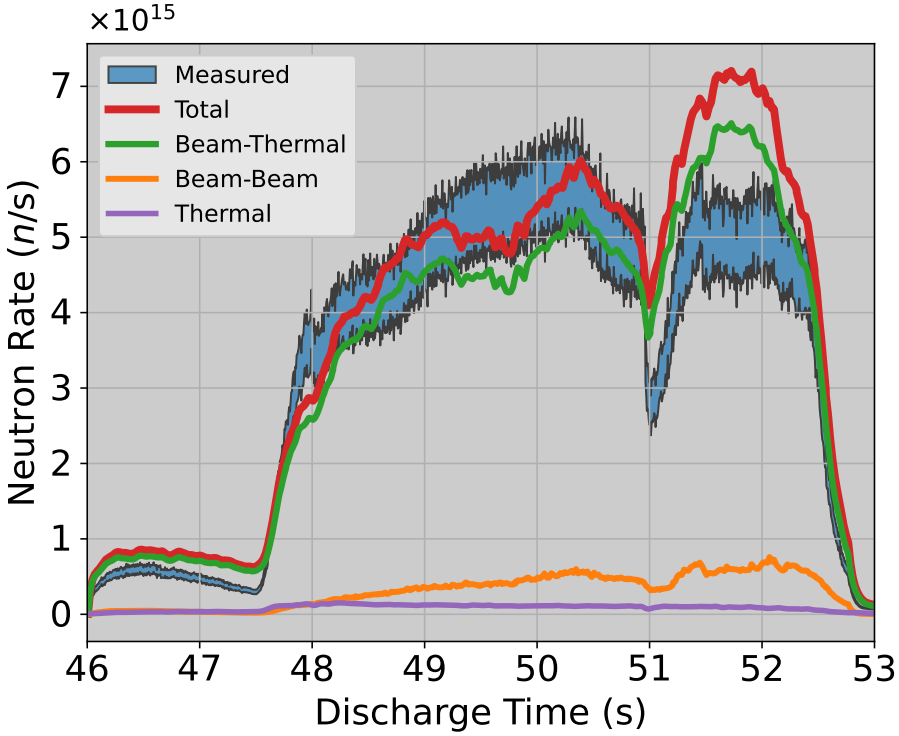

Figure 3.9: Comparison between the TRANSP-simulated and experimentally measured total neutron rate for Discharge #95671 at JET. Blue: experimental measurement from fission chambers (error bounds). Red: TRANSP-predicted total neutron rate. Green: D-beam–thermal-D contribution. Orange: beam–beam contribution. Purple: thermal–thermal contribution. Simulation ID: "A25".

This comparison is made as a first validation step for each simulations. The TRANSP calculated neutron rate in Figure 3.9 exhibits a reasonable agreement with experimental data, corresponding to Simulation 95671-A25, mostly into the phase preceding the big sawtooth crash at ~ 51 s. It is not expected that the simulated and measured data perfectly match after certain plasma events, such as sawtooth crashes, which eject fast ions in a velocity-space selective pattern [98].

More generally, discrepancies between TRANSP predictions and measurements can arise in the presence of anomalous fast-ion transport due to MHD activity or other plasma instabilities. In this work, no sawtooth crash or additional MHD activity was modelled explicitly; therefore, the comparison between simulations and nuclear diagnostic data is limited to time intervals preceding such events, where the simulated plasma is assumed to follow the measured trends most closely.
Results indicate that the primary component to the neutron production is due to the interaction between the fast deuterium (NBI+ICRH) and the thermal deuterium, highlighting the importance to accurately describe the fast-D component.
In summary, the results indicate that TRANSP simulations are capable, if properly configured, of describing quantitatively and qualitatively the neutron rate during the discharge with reasonable accuracy, but in itervals before the crash.
The time points where the best agreement between the simulation the experimental data is achieved, were selected, and the corresponding Fast D dsitribution (FDD) is extracted (see Table 3.2).

TRANSP computes the FDD resolved in space, energy and pitch (where the latter represents the cosine of the angle between the deuterium gyrocentre direction and the magnetic axis), calculated in different discharge times. An example is shown in Figure 3.10: Panel 3.10a presents the spatial density of FDD (integrated over energy and pitch), while Panel 3.10b shows the energy-pitch distribution (integrated over space). One can notice that a high-energy tail is visible in the positive pitch area, extending from 100 keV to 1-2 MeV. The FDD is concentrated in the centre of the plasma, reflecting the ICRH heating mechanism.

3.2.2 TOFOR spectra comparison

Subsequently, the Fast D Distribution (FDD) is extracted at each timestamp, for each discharge, as shown in Table 3.2. The second validation step was to compare the TOFOR experimental spectra with synthetic ones produced via the GENESIS code [59] using the TRANSP-FDD.

The experimental spectra were extracted using integration time window of 0.8 s, centred at the selected timestamps. To perform a comparison, first it is necessary to numerically calculate the neutron energy spectra and then to perform a convolution with the TOFOR response function.
To simulate spectra, GENESIS needs the TOFOR line of sight file, the magnetic equilibria for each timestamp and the Deuterium kinetic profiles (i.e., the trend of the temperature and density as a function of the normalised poloidal flux coordinate), as well as the FDD. The TOFOR line of sight was generated using the LINE2.1 code [106], from which the REVOLT code is derived. The other inputs were taken directly from the TRANSP output, as well as the FDD, taken at the selected timestamp for each discharge.

To obtain an accurate neutron spectrum, all relevant contributions to the neutron production must be assessed. Reaction involving the fast-D are expected to be more relevant in terms of neutron emissivity, due to the higher energy and, thus, the higher cross section values involved. Indeed, the DD cross section is monotonic increasing

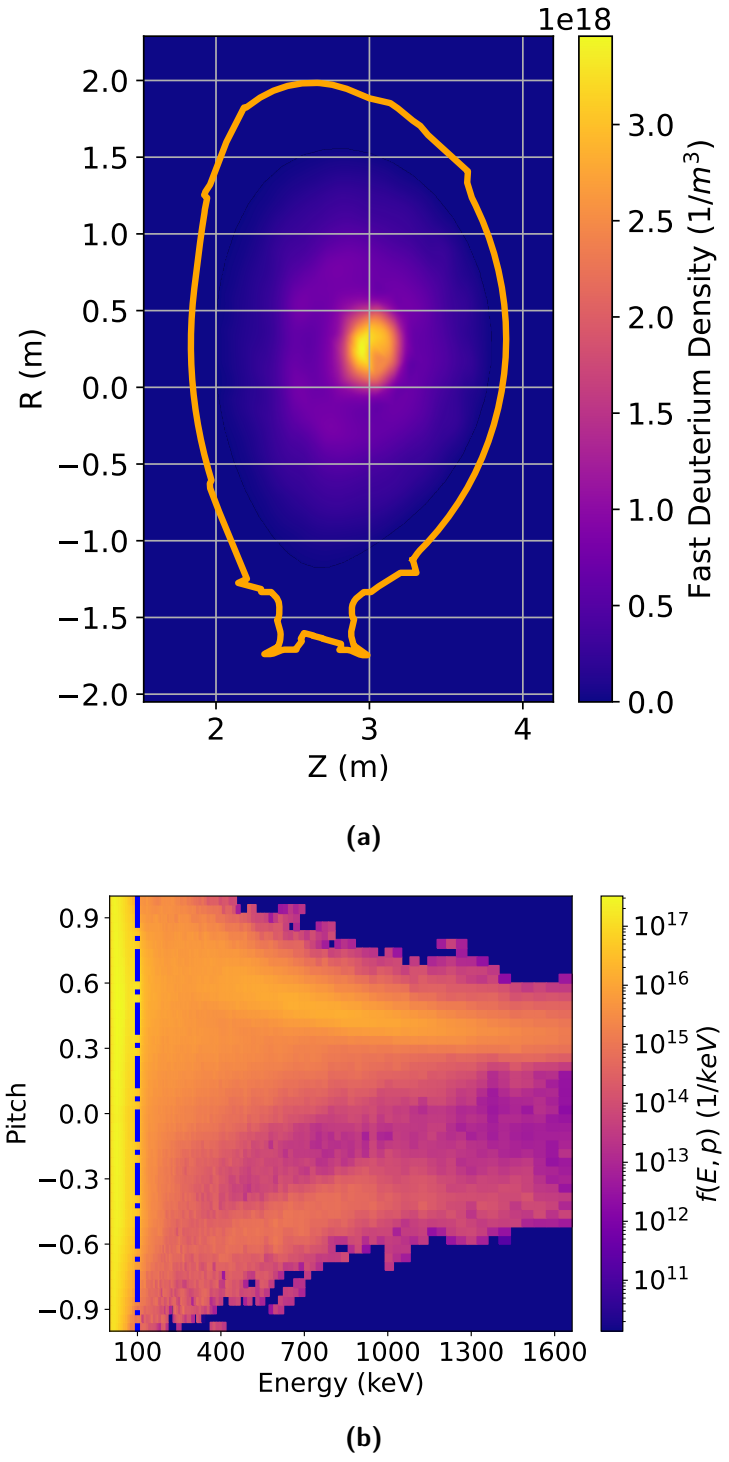

Figure 3.10: **(a)**: Fast deuterium density poloidal profile obtained from TRANSP. Shot #95671, sim. ID A25, time = 50.0 s. **(b)**: Full space-integrated energy-pitch distribution for the same case as in (a). The blue vertical dashed line at 100 keV indicates the NBI injection energy. This threshold is used to split the original fast-ion distribution into two components, corresponding to high-energy (Hfast) and low-energy (Lfast) populations.

in the typical energy ranges of Three-Ion Scheme experiment (see Figure 1.2, for DD reaction in the 1-1000 keV energy range).
The FDD was divided in two parts: one at energies less than 100 keV, and the other one with energies major than 100 keV (see the blue vertical dashed line in Panel 3.10b). The first part is interpreted as mainly due to the NBI Deuterium, not effectively heated by ICRH. Indeed, NBI at JET is usually injected at $\approx$ 100 keV. The second part is interpreted as due to the NBI deuterium effectively heated by ICRH, reaching energies up to 1-2 MeV. From now on, these two components will be called "Lfast" and "Hfast", respectively. Therefore, three deuterium species will be considered (Thermal, Lfast, Hfast) and, as a consequence, six different components to the neutron spectrum arise:

- Thermal–Thermal (Th–Th)
- Lfast–Thermal (Lf–Th)
- Hfast–Thermal (Hf–Th)
- Lfast–Lfast (Lf–Lf)
- Hfast–Lfast (Hf–Lf)
- Hfast–Hfast (Hf–Hf)

The TRANSP code is able to calculate and track the particle orbits considering either the gyrocentre or the actual position. For time performance, simulations are performed recording only the gyrocentre: this choice is a good approximation when the particle Larmor radius is little enough so that Finite Larmor Radius (FLR) effects can be neglected [107].
In case of Three-Ion Scheme (TIS) experiments, the Larmor radius can reach up to several centimetres for the fast-D. In such case, FLR effects become significant and must be considered into calculations.
Precisely, the TOFOR neutron spectrometer observes a vertical field of view inside the plasma. During TIS experiments, and considering the specific established magnetic equilibrium, some fast deuterons perform a large gyromotion, not fully encompassed by the TOFOR line of sight. In particular, when the fast-D is moving upwards, toward the detector, the movement is performed inside the field of view of the TOFOR line of sight, contrarily to the opposite case when the fast-D is moving downward, away from the detector. This means that, if the fast-D undergoes a D(D,n)^{3}He reaction, there is a chance that the neutron is observed in the first half of the gyromotion, while it cannot be observed during the second half. The consequence is that TOFOR will detect mainly neutrons produced during reaction characterised by the fast-D moving toward the detector, and for the conservation of energy and momentum, their energies will be higher (blue-shift). At the same time, TOFOR will lose those neutrons characterised by the fast-D moving away from the detector, which experience a lowered energy (red-shift).
Considering the TOFOR spectra, the final effect is a depletion of counts in the low-energy/high-ToF part. To suppress FLR effects, the orbit correction must be included in calculations.

The correction, first introduced in Ref. [107], can be implemented in a relatively simple manner. In this framework, only the toroidal component of the magnetic field is taken into account. The magnetic field experienced by each fast-deuteron gyrocentre is evaluated according to

$$B = B_0 \frac{R_0}{R}, \tag{3.9}$$

where B_0 denotes the magnetic field strength at the magnetic axis, R_0 the radial position of the magnetic axis, and R the radial position of the gyrocentre.
Once the local magnetic field is determined, the associated Larmor radius r_L is calculated as

$$r_L = \frac{m_D v_\perp}{eB}, \tag{3.10}$$

with $v_\perp$ representing the velocity component perpendicular to the magnetic field, e the proton charge, and m_D the deuteron mass. The resulting Larmor radius is then used to reconstruct the particle position in the R–Z plane by randomly sampling the gyroangle, assuming a uniform distribution.

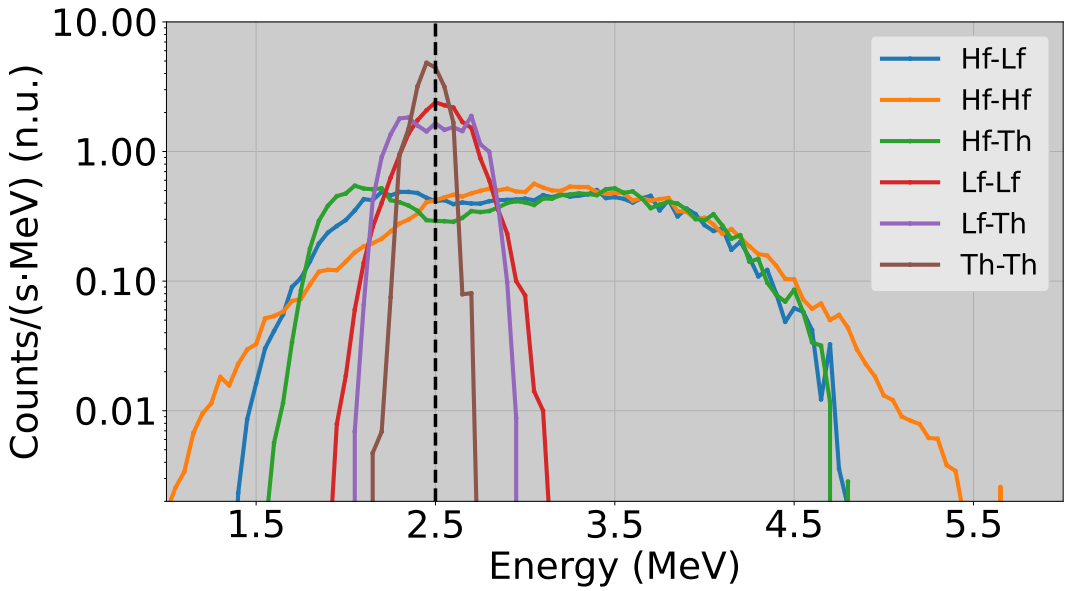

Figure 3.11: Normalised neutron spectral components from orbit-corrected simulations (TOFOR diagnostic, energy-resolved). One can notice that Hfast-related interactions dominate the spectral features at low ($E_n \lesssim 2$ MeV) and high ($E_n \gtrsim 3$ MeV) energies. Shot #95671, simulation ID A25, time = 50 s.

In Figure 3.11 a simulation of the spectral contributions observed along the TOFOR line of sight is shown, when the orbit correction is applied. One can notice that components involving only "slow" deuterium produce a spectrum centred at $\approx$ 2.5 MeV. Hfast-related components show a different behaviour, where a broad energy range, from $\sim$ 1 up to 5.5 MeV, is observed. This is mainly due to the blue and red shifts, enhancing (or weakening) the energy of the neutrons produced after the reaction. Finally, an example is shown in Figure 3.12 where one can see a

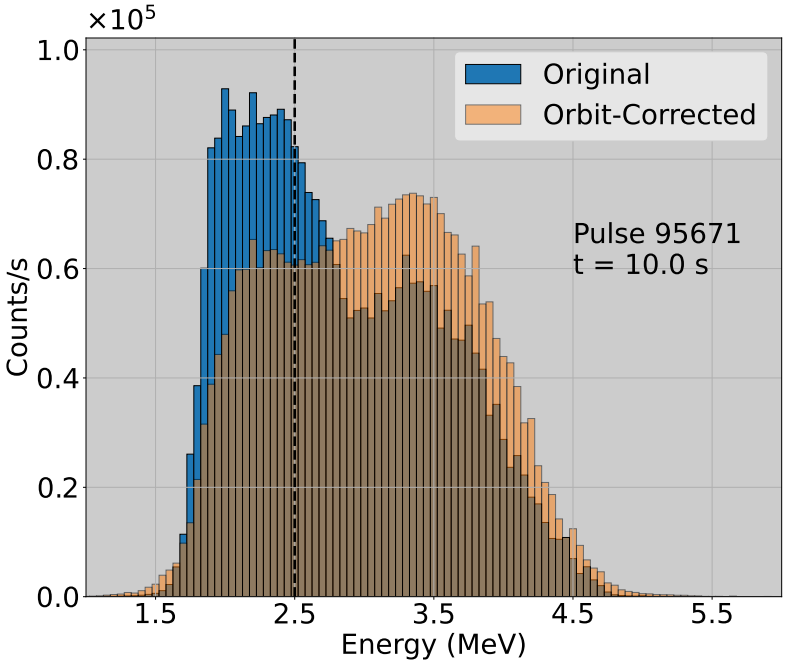

Figure 3.12: Energy spectra obtained from simulations performed with (orange) and without (blue) inclusion of FLR effects. Shot #95671, simulation ID A25, time = 50 s.

comparison between the spectrum without orbit-correction and the orbit-corrected one.

Figure 3.13 shows the final results of the comparison. In Panel 3.13a the calculations performed without considering the FLR effects are shown. One can observe that in the higher energy part (i.e., the low ToF part) the two spectral shapes are similar once superimposed. As mentioned before, neutrons in the low-ToF region are primarily generated by the fast D moving toward the detector (so that, the resulting neutron is blu-shifted), and are about-fully seen by the detector. Conversely, in the low-energy/high-ToF part, the neutron yield is largely overestimated, due to the fact that the fast deuterons moving away from the detector (and so, red-shifted) are not observed.
Panel 3.13b shows the results of calculations performed taking in account the FLR effects, where a good agreement in the full spectral range is assessed. Comparable performances are observed across the full set of discharges, supporting the validity of the FDD from the selected TRANSP simulations in terms of spatial localization, energy distribution, and pitch-angle dependence.

3.2.3 Alpha Birth Profiles comparison

In the final part of this work related to TIS experiments at JET, the aim is to reconstruct the Alpha Birth Profile (ABP) from experimental data of the Gamma Camera (GCU), and to compare it with synthetic profiles calculated using the TRANSP Fast D distribution (FDD).

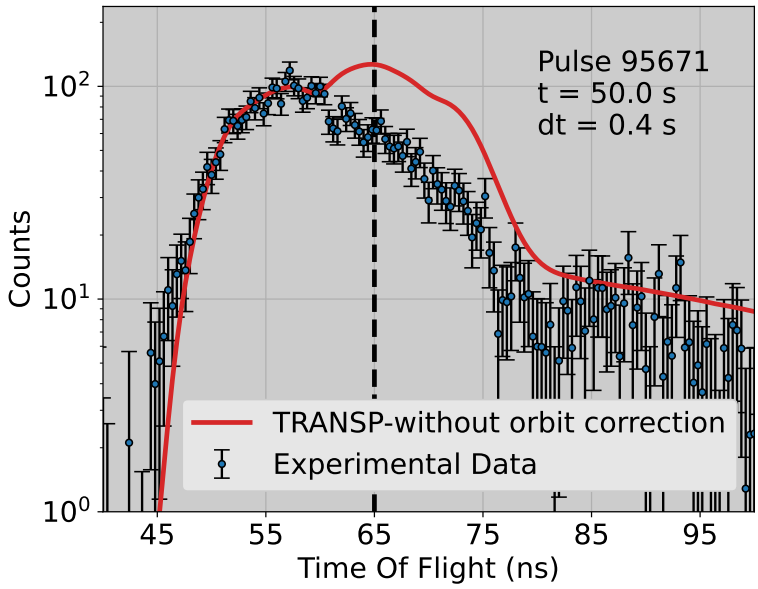

(a)

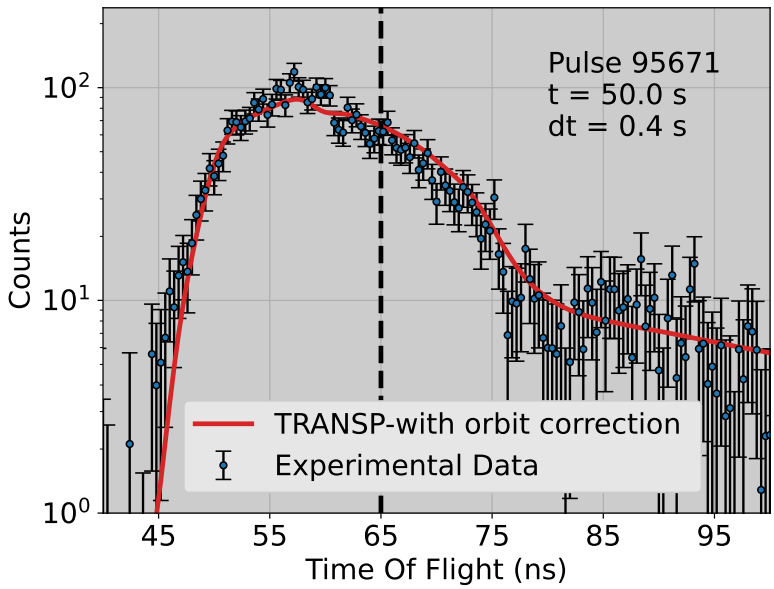

(b)

Figure 3.13: Comparison between experimental and synthetic TOFOR spectra for Discharge #95671, simulation ID "A25", at t = 50 s. **(a)**: Spectrum computed without orbit correction. **(b)**: Spectrum computed with orbit correction applied.

Plasmas from Three-Ion Scheme (TIS) experiments at JET are characterised by the intense emission of alpha particles due to the presence of Deuterium and Helium-3. The two species undergo the ^{3}He(D, p)α reaction, where an enhanced rate is observed due to the combination of both NBI and ICRH heating schemes, reaching high collision energies. Anyway, the majority of alpha particles can't escape plasma like neutrons. To measure the alpha spatial profiles, the gamma emission at ~ 16.4 MeV (characterised by a broad spectral shape, similar to the DT-gamma emission in Chapter 2) from the ^{3}He(D, γ)^{5}Li reaction [46, 47] can be exploited. The Branching Ratio (BR) of the gamma-channel of the D^{3}He reaction is much lower compared to the alpha-channel (BR ~ 10^{-5} γ/α). Nevertheless, observations of this gamma component has been assessed, and can be used to indirectly infer the ABP. [72, 86] Using the scintillator detectors mounted on the gamma camera at JET, the emission from the gamma-branch can be observed, separating the signal from the background. Indeed, gamma background lies in the E $<$ 10 MeV region, while the signal is expected at E$>$10 MeV.

GCU data consist of a collection of digitised waveforms, each associated with a corresponding time stamp. Every time a gamma-ray is recorded, its pulse is converted into a waveform, and the precise detection time is stored in the accompanying time stamp. By applying the software GetAGRaSp (Get A Gamma-Ray Spectrum), described in Ref. [108, 71], to these individual waveforms, it is possible to reconstruct the energy spectrum deposited in the crystal over any chosen time interval. In the discharges examined in this study, the capability of the code to account for overlapped pulses was crucial for properly reconstructing the spectrum in the high-energy region, which is of particular interest for alpha particle investigations. To address this, a pile up recovery procedure has recently been implemented into the code, which was also employed to analyse the dataset presented here.
An example of waveforms recorded by Channel-11 and analysed by GetAGRaSp for Discharge #95671 is shown in Figure 3.14.

The background is mainly due to the DD neutrons interacting with vessel nuclei and producing prompt gamma rays, detected by GCU channels [68, 49]. Although typical background events lay below ~ 10 MeV, the typical signal spectral shape is partially affected. To remove the background, gamma ray spectra were obtained either during the NBI-only or NBI+ICRH phases (see Figure 3.1). During NBI-only heating, the D^{3}He emission is about null compared to the ICRH-window, where higher cross sections are reached. Nevertheless, neutrons from DD reactions are present, producing a non-negligible gamma background. These data can be used to evaluate the background, to be subtracted to the total spectrum of the ICRH-phase. For each channel, the NBI gamma background is determined by integrating the gamma counts over the entire NBI-only phase and then averaging across all the studied discharges (see Figure 3.15).

Then, after performing an energy calibration (using the peaks due to the interaction of neutron with ^{56}Ni nuclei present in the collimation system material) the resulting NBI background is normalised to the total neutron yield of the selected discharge phase during ICRH heating (with an integration time of 1 s around the

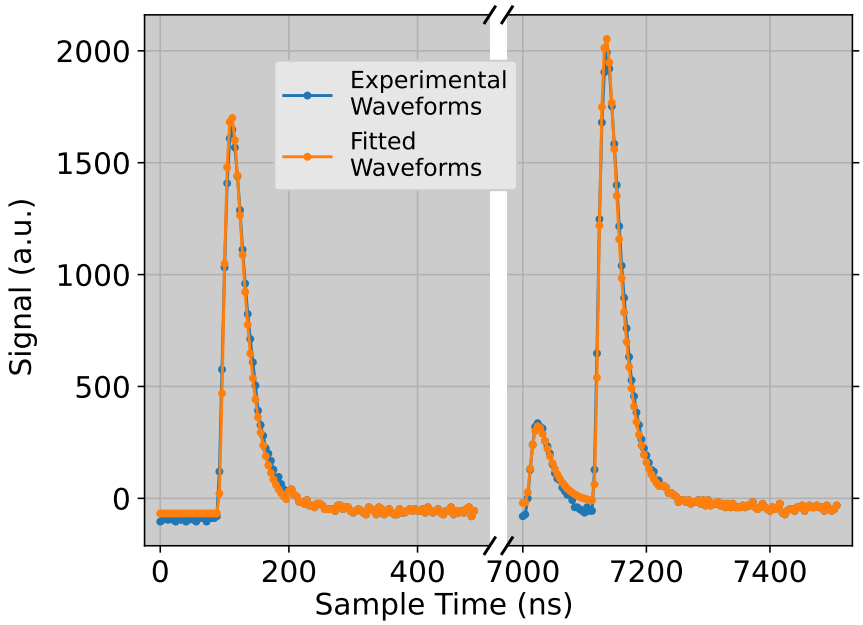

Figure 3.14: Example of recorded waveforms from Discharge #95671, Channel-11. The experimental waveforms (blue) are compared with the fitted ones (orange), obtained using the GetAGRaSp software [108]. A pile-up event, corresponding to the right part of the figure, is detected by the software.

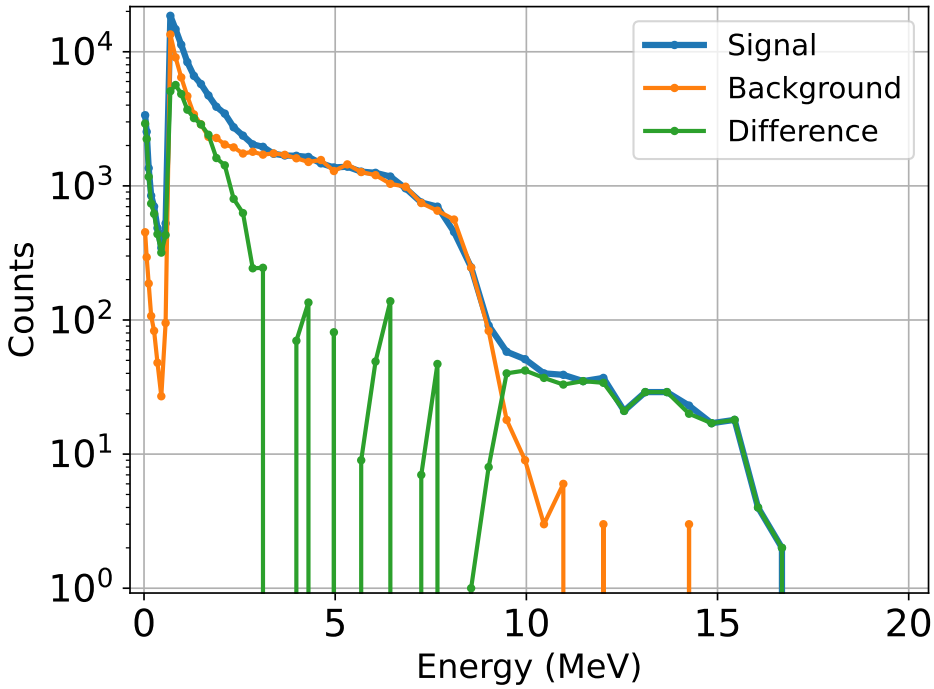

Figure 3.15: Difference (green line) between the signal spectrum (blue) and the background spectrum (orange). Shot #95671, full discharge integration, Channel-4 of the Gamma Camera.

studied timestamp, for each discharge). After subtraction, a structure is observed in the range from 9 to 17 MeV, and all events with energy exceeding a threshold of 9 MeV are counted. Performing this task for each channel, a GCU profile, for each discharge, is obtained (see an example in Figure 3.6).

Regarding synthetic spectra, GENESIS is used to calculate, for each discharge, the total counts to each channel. To do so, some input parameters are used. GCU line of sight files, calculated with LINE2.1 were used. The FDD was retrieved directly from TRANSP, along with magnetic equilibria and ion kinetic profiles. In Figure 3.16 an example of the comparison between synthetic and experimental GCU profile is shown. Across the selected discharge and timestamp, a reasonable agreement between the two profiles is observed, showing an intense emissivity along channels observing the plasma in the proximity of the magnetic axis (3–6 and 14–16). Experimental profiles generally show higher counts in channels related to the outer plasma, probably due to other sources of background (like gamma emission from walls intercepted by the line of sight, not fully subtracted, or components not fully removed during processing).

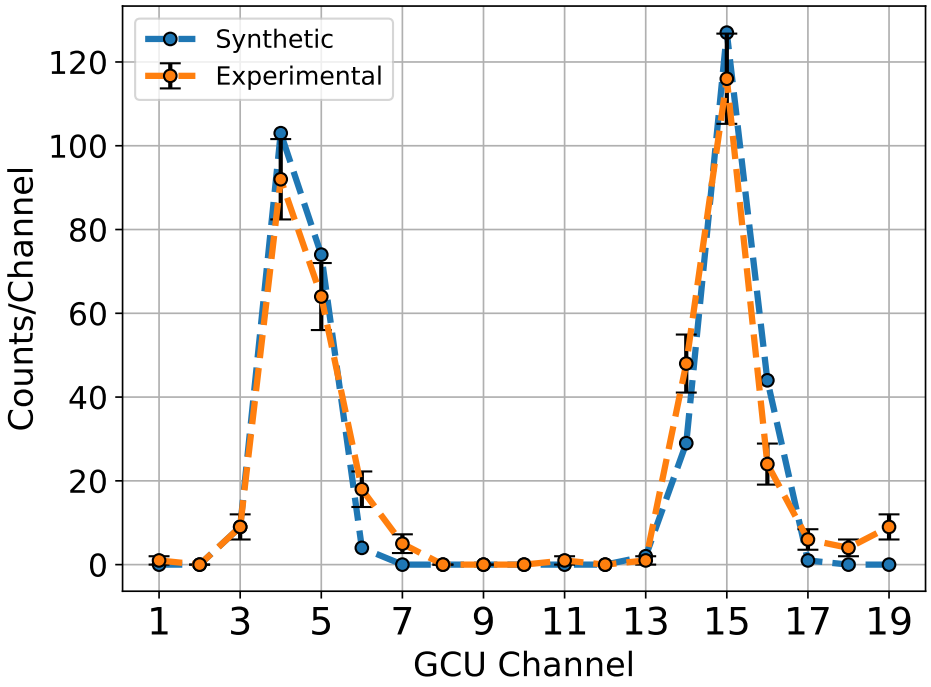

Figure 3.16: Comparison between experimental (orange) and synthetic (blue) Gamma Camera profiles. The synthetic profile is normalised to the total experimental Gamma Camera counts, for direct comparison (and also because the detectors are not absolutely calibrated). Error bars correspond to Poisson statistics: $\sigma = \sqrt{N}$. Shot #95671, Simulation ID "A25", discharge time: 50.0 s, Integration time: 1.0 s.

After obtaining a GCU profile from experimental data, or from numerical calculations via GENESIS using the TRANSP FDD, a tomographic reconstruction (see Section 3.1.4) via TREVISO is performed, resulting in an emissivity 2D map (see

an example in Figure 3.7). These results, although obtained analysing gamma-rays, represent the emissivity profile of alpha particles directly born from fusion reactions.

Subsequently, the 2D pixel matrix were projected into the normalised poloidal flux coordinate (ρ) space. The aim is to visualise emissivity profiles in a 1D graph, as a function of the ρ coordinate, for direct comparison. In practice, this procedure consists of evaluating, for each pixel in the R–Z plane, the corresponding ρ coordinate and plotting the emissivity value as a function of ρ. The outcome of this process is shown in Panel 3.17a, starting from the two-dimensional map presented in Fig. 3.7. One can notice that the emissivity is very high in the centre, near the magnetic axis, and suddenly decreases as one moves farther out into the outer plasma. Subsequently, points in Panel 3.17a are binned in discretised ρ-window, calculating mean and standard deviation for each bin, finally resulting in a 1D profile (see Panel 3.17b).

Two different procedures are used to determine error bars of the 1D profiles:

- **Synthetic data:** The simulated GCU profile is directly reconstructed using TREVISO. After projection onto the ρ coordinate, pixel emissivity values are binned along the ρ axis. For each bin, the mean and standard deviation are computed, representing respectively the central value and uncertainty of the 1D profile.

- **Experimental data:** A similar procedure is applied, but over a set of one hundred GCU profiles derived from the original measurement. These profiles are generated using the Poisson statistics, which is assumed to govern the counting process. For each GCU channel, the original count N is used as the mean ($\mu = \mathrm{N}$) and the variance ($\sigma^2 = \mathrm{N}$) of the distribution. The 100 synthetic profiles are then created by sampling from a Poisson distribution defined by the previous parameters. After the tomography, 100 1D profiles are obtained, and an averaged profile, along with averaged errors, are calculated. Finally, the resulting error is combined quadratically with the reconstruction uncertainty (related to the pixel dispersion in the ρ space, as in the first point) to yield the final errors of the 1D ABP. This brute-force method allows propagation of statistical uncertainties through the tomographic reconstruction.

Finally, a comparison between either synthetic and experimental derived emissivity profiles is shown. (see Figure 3.18). This procedure is then performed for each discharge in the selected timestamp (Figure 3.19). Generally, a reasonable agreement is achieved between synthetic and experimental profiles. The better predictions are achieved for simulations 95671-A25, 95679-V36 and 95680-V07. The profile shape is very similar across all discharges, characterised by an emissivity concentrated in the plasma centre with a rapid decrease to zero for ρ less than 0.2–0.4. The only visible change is how suddenly the emissivity profile goes to zero from one profile to another. Generally, the experimental profiles are less centred peaked than the synthetic ones, probably due to the presence of noise at higher ρ values. Moreover, one can notice that errorbars for synthetic profiles are larger than experimental ones, due to the fact that the pixel emissivities calculated from the TRANSP FDD are much more widespread in the ρ space, compared to the experimental emissivities.

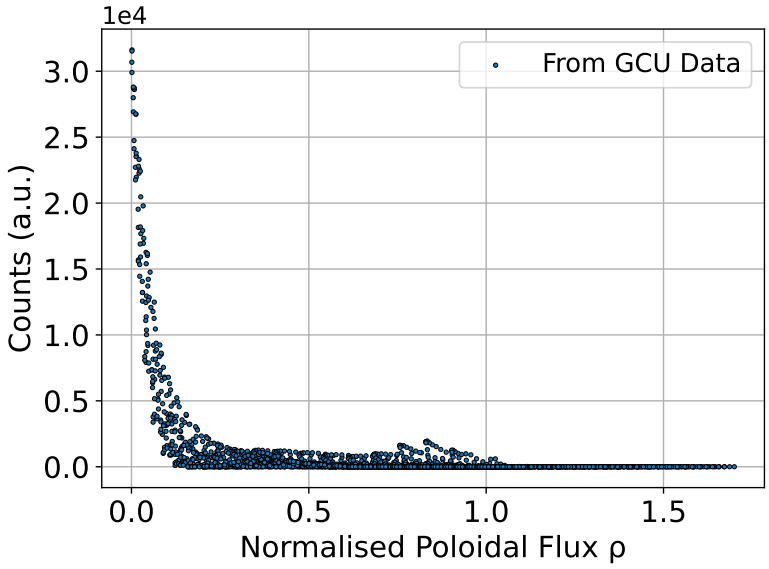

(a)

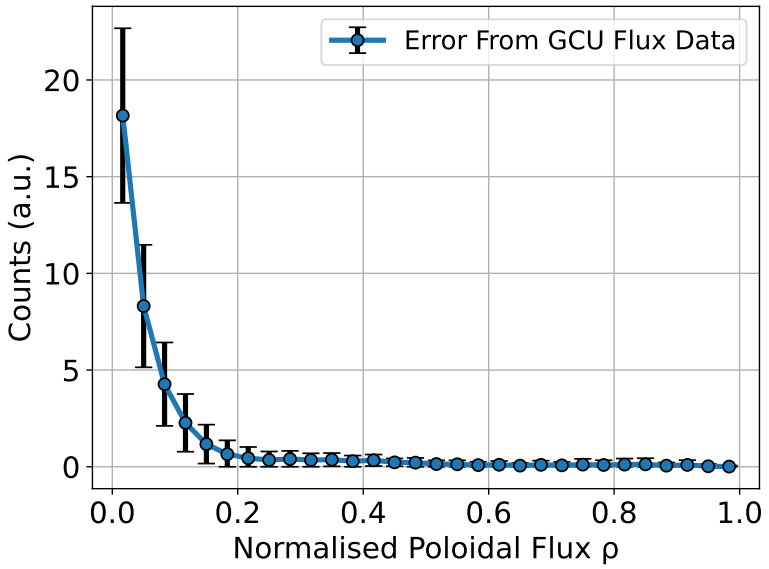

(b)

Figure 3.17: **(a)**: Counts for each pixel of Figure 3.7, plotted against each associated ρ value. Shot #95671, discharge time: 50.0 s, Integration time: 1.0 s. **(b)**: Resulting 1D profile from (a). Points and errors taken from the mean and the standard deviation of each ρ-bin.

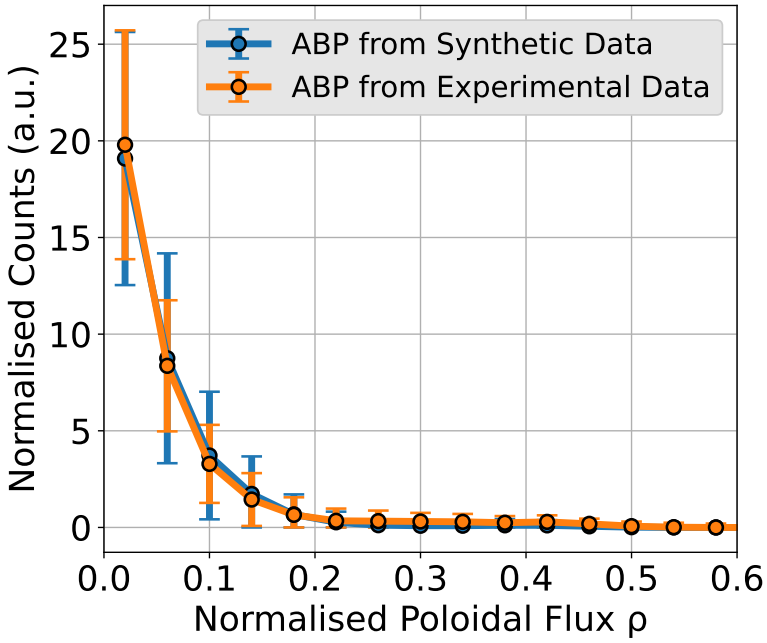

Figure 3.18: Comparison between experimental (orange) and synthetic (blue) normalized alpha emissivity profiles as a function of the normalized poloidal flux coordinate, ρ. Shot #95671, Simulation ID "A25", discharge time: 50 s.

Results suggest that, if properly configured, the TRANSP stimulations can effectively predict TIS experiments in D–^{3}He plasmas. Using TRANSP, predictions of the total neutron rate, synthetic TOFOR neutron spectra and ABPs calculations have been effectively performed.
It was observed that, in such kind of experiments, the FDD is responsible for the high neutron and gamma emission. This means that, if the control of the heating scheme is achieved, an intense source of alpha particle can be generated, providing a unique environment to study alpha particle, with lower neutron emission and without the use of tritium compared to DT scenarios. Moreover, TRANSP can be used to predict, or prepare, future TIS experiments or, more generally, to deepen our understanding of phenomena in this kind of plasmas and heating schemes.

A comparison between the Hfast density profile, as a trend of ρ, and the resulting synthetic alpha birth profiles has been made. In Figure 3.20 it is clearly shown the dependence between the Hfast-FDD and the resulting synthetic ABP, indicating that the main contribution to the emissivity could be due to the high energy part (> 100-1000 keV) of the FDD, related to the ICRH heating. The Lfast component, instead, seem to not be particularly correlated to the final ABP.

Finally, connecting with Chapter 2, it is possible to obtain quantitative information about alpha emissivity during TIS experiments. Fusion power measurements relative to aneutronic fusion reactions may be performed (similarly to the DT case from Ref. [29] and [30, 31]) only thanks to the secondary gamma-ray emission.

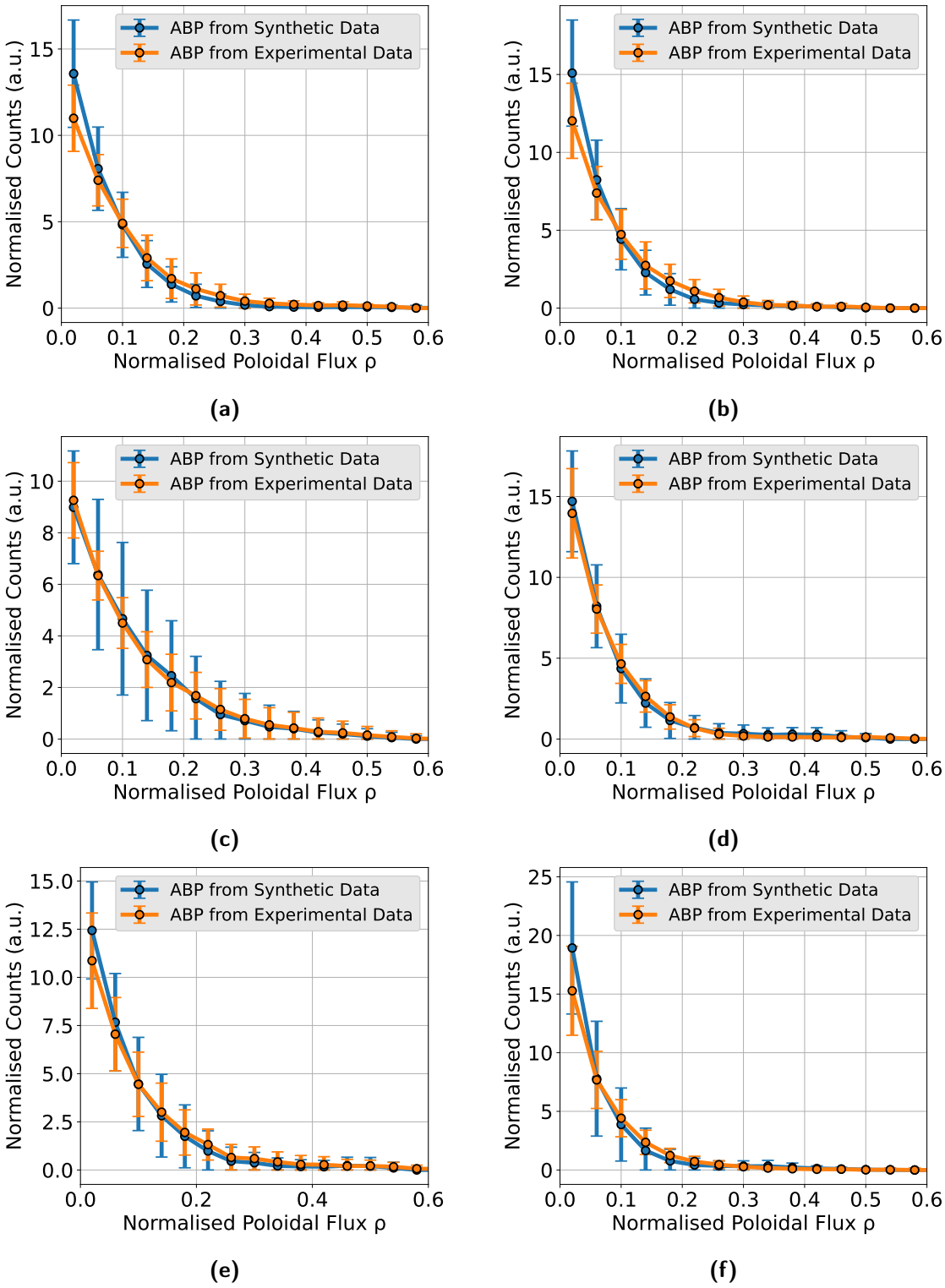

Figure 3.19: Comparisons between experimental (orange) and synthetic (blue) normalised alpha emissivity profiles as a function of the normalised poloidal flux coordinate ρ, for all the remaining analysed discharges. **(a)**: 95672-A25; **(b)**: 95673-A26; **(c)**:95679-V36; **(d)**: 95680-V07; **(e)**: 95683-V07; **(f)**: 95684-A24

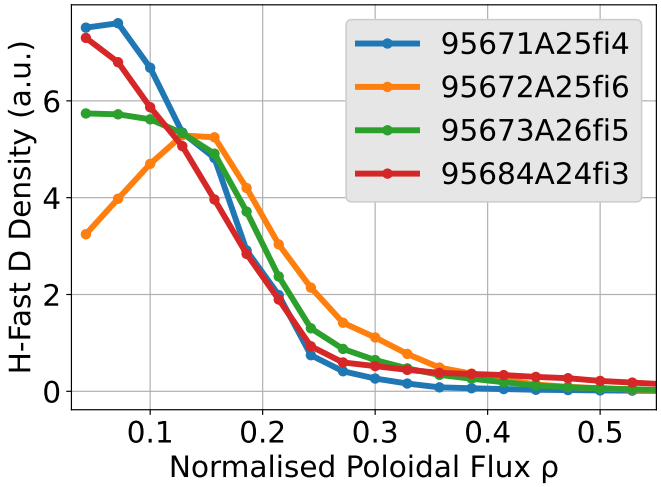

(a)

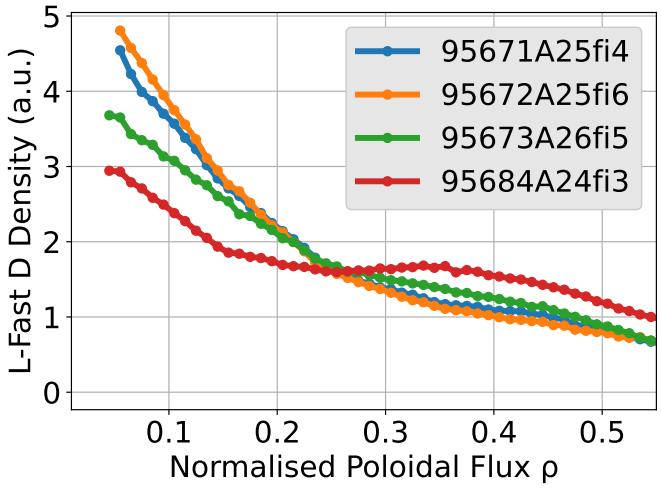

(b)

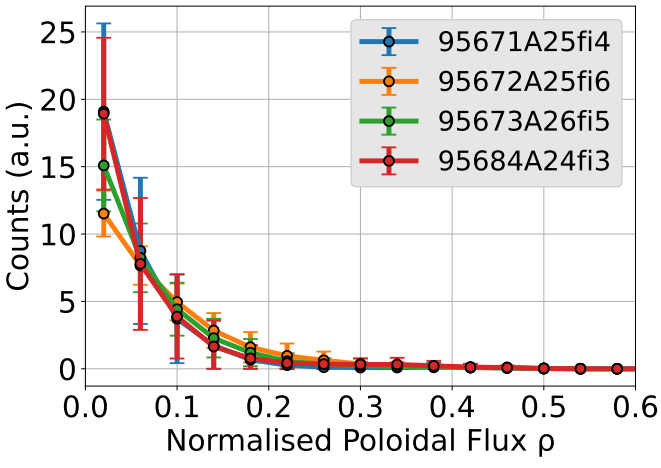

(c)

Figure 3.20: Comparison between Hfast density, Lfast density and Alpha Birth Profile shapes (Simulation type: "A"). **(a)** Normalized Hfast density profiles as functions of the ρ coordinate. **(b)** same as in (a), but for the Lfast component. **(c)** Normalized synthetic Alpha Birth Profile as functions of the ρ coordinate.

Chapter 4

Runaway Electrons Studies:

Investigating Bremsstrahlung spectral features using multiple lines of sight

Runaway Electrons (REs) represent a critical population in tokamak plasmas, requiring careful control and thorough understanding due to their potential to inflict severe damage on plasma-facing components. REs can strike the first wall of the tokamak with substantial energy, threatening its structural integrity. While plasma disruptions represent one of the most critical and widely studied sources of REs, these particles can also be generated in non-disruptive scenarios whenever sufficiently strong electric fields are present, such as during current ramp-up phases or in low-density, cold flattop plasmas. In next-generation fusion devices, operations will require either complete avoidance of disruptions and highly reliable mitigation strategies. Disruptions are characterised by a sudden loss of plasma confinement, often leading to the generation of strong electric fields capable of accelerating electrons into the *runaway regime*, where collisional friction is insufficient to counterbalance the electric force.
The first section provides an overview of RE physics and the disruption process. The second section focuses on Bremsstrahlung emission in RE discharges, analysing the features of the hard X-ray to soft gamma-ray spectra as observed from multiple lines of sight.

4.1 Disruptions and runaway electrons

RE beams impacting plasma-facing components can cause severe localised damage, depositing large amounts of energy in just a few millimetres of material [109, 110, 111, 112, 113, 114]. Their energies can range from a few keV to several tens of MeV. If this population is not adequately controlled and its physics properly understood, the operation of future machines such as ITER [115] or SPARC [116] could be seriously compromised. Particularly in large-size tokamaks, RE currents may reach several mega-amperes, releasing tens of megajoules of energy onto the tokamak wall. Such damage may take months to repair, hindering operation and increasing delays and costs.

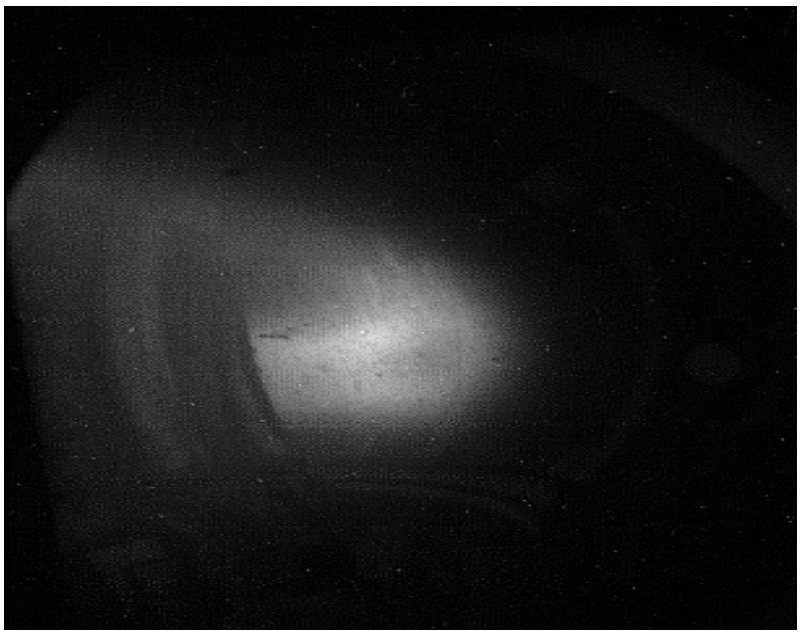

Figure 4.1: Example of a runaway-electron experiment at JET during discharge #103061. Data retrieved from the Visible Camera KL8 at 48.125 s, with an integration time Δt = 0.5 ms.

Electrons, like all charged particles, undergo Coulomb collisions with other plasma particles, resulting in a friction force [109, 117]. This slowing-down force, described by Fokker–Planck theory, depends on the electron velocity v_e and is always opposite to the direction of motion (an illustration is shown in Figure 4.2 for the case of an electron in air).

Define v_{th} as the electron thermal velocity. At low speeds ($v_e \ll v_{th}$), the friction force increases almost linearly with velocity ($\propto v_e$), reaching a maximum value at $v_e \sim v_{th}$, and then decreases as $\propto v_e^{-2}$ for $v_e \gg v_{th}$. The minimum is reached when the kinetic energy reaches the value $E_e = m_e c^2$, after which radiative losses, due to synchrotron and bremsstrahlung radiation, dominate.
If a constant electric field is applied, its ability to accelerate electrons depends on its magnitude relative to the friction force. When the resulting electric force is below the minimum friction value at $E_e \sim m_e c^2$, electrons cannot be accelerated indefinitely. This threshold is known as the *critical electric field* E_C:

$$E_C = \frac{1}{4\pi\epsilon_0}\frac{e^3 n_e \ln\Lambda}{m_e c^2} \approx 0.075 n_{20}\ [\mathrm{V/m}] \tag{4.1}$$

where $\ln\Lambda$ is the Coulomb logarithm, typically $\gg 1$, and n_{20} is the electron density in units of $10^{20}\ m^{-3}$.
If the electric field exceeds another threshold, the *Dreicer field* E_D:

$$E_D = \frac{1}{4\pi\epsilon_0}\frac{e^3 n_e \ln\Lambda}{m_e v_{th}^2} \tag{4.2}$$

then even thermal electrons ($v_e \approx v_{th}$) can enter the runaway regime.
For $E_C < E < E_D$, only electrons already above a certain velocity v_{lim} (the point

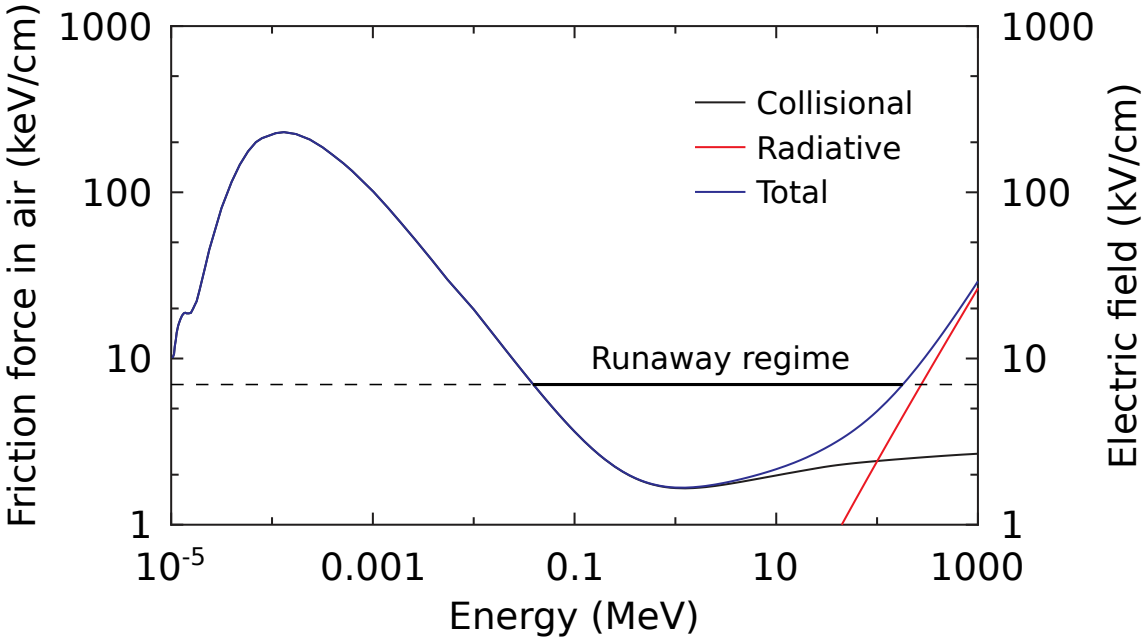

Figure 4.2: Dynamic friction on a free electron in air as a function of energy, compared to an applied electric field. [118]

where the electric force equals the friction force in the region $v_e \gg v_{th}$) will run away, while slower electrons remain collisional. Electrons in the runaway regime experience ever-decreasing friction with increasing velocity, enabling acceleration to relativistic energies until confinement is lost. The only radiative losses are due to synchrotron and bremsstrahlung radiation.

4.1.1 Disruptions

Runaway Electrons can be generated during various discharge phases, including startup, flattop, and especially during disruptions. In the latter case, the plasma thermal and magnetic energy can be suddenly released to the vessel. A disruption begins with the *thermal quench*, caused by growing magnetohydrodynamic instabilities or impurity influx, which rapidly dissipates the plasma thermal energy and reduces the temperature within hundreds of microseconds to about 1 ms.
The resulting increase in plasma resistivity leads to the *current quench*, lasting several milliseconds. As the plasma current drops, the changing poloidal flux induces strong electric fields proportional to the decay rate. If this field exceeds E_C, a fraction of electrons enter the runaway regime. The RE current can grow exponentially until it reduces the induced electric field below the critical value, after which a plateau phase lasting tens of milliseconds may follow. In this phase, the plasma consists of cold ions and highly energetic electrons, concentrated in a narrow beam that may lose confinement and strike the wall. Coulomb collisions with plasma ions are not sufficient to slow them down, and the acceleration is mainly limited by relativistic radiative losses.
The resulting damage to first-wall material can be severe, with potential risks also for components located behind it, such as coolant pipes or structural supports. Damage

may include metal vaporisation, thermal-shock cracking, recrystallisation, and crack formation.

Two types of RE generation processes can be distinguished:

- **Primary generation:** for an electric field $E_C < E < E_D$, only a fraction of the electron population is accelerated, forming a suprathermal component ($v_e \gg v_{lim}$). Subsequently, through collisions, additional electrons can be pushed into the runaway regime (Dreicer mechanism). Other RE sources include tritium beta decay and Compton scattering with gamma rays from activated wall materials. Finally, the hot-tail mechanism occurs during a rapid thermal quench, when low-energy electrons thermalise quickly while high-energy electrons survive and can run away. This effect becomes particularly important during gas injection, which produces a cold electron population from ionisation of the injected gas itself, while hot plasma electrons remain, responsible for runaway generation.

- **Secondary generation:** this is the most dangerous mechanism of RE generation in large-scale tokamaks. Existing REs from primary generation can transfer energy via collisions to slower electrons in the thermal region, pushing them into the runaway regime in an avalanche process, resulting in a fast exponential growth of the RE population.

Mitigation strategies

Future tokamaks must both avoid disruptions and mitigate them effectively when they occur [119, 120, 121, 122]. Several mitigation strategies have been developed:

- **Massive Gas Injection (MGI):** a large quantity of noble gas is injected into post-disruption plasma. The resulting density increase raises plasma resistivity, enhancing collisional dissipation of the RE beam and increasing E_C, thereby reducing the runaway fraction [123]. High-Z gases (argon, neon, krypton) also enhance bremsstrahlung radiation, further dissipating RE energy. However, MGI has limited penetration into the plasma core, reducing its effectiveness in large devices. Moreover, complete removal of these gases can be difficult and stressful for the vacuum system. For this reason, low-Z gases such as deuterium are being investigated [124].

- **Shattered Pellet Injection (SPI):** cryogenic noble-gas pellets penetrate deeper into the plasma core than MGI gas clouds, improving efficiency in larger devices. This method will be used in ITER as the primary mitigation system [125].

- **Resonant Magnetic Perturbations (RMPs):** magnetic perturbations distort and break the remaining closed flux surfaces, degrading RE confinement and reducing avalanche multiplication [126]. Moreover, this scheme limits the energy gained by REs after each toroidal loop.

Dedicated experiments at JET and ASDEX have deliberately triggered disruptions, often via argon (Ar) injection, to study RE dynamics and test mitigation techniques.

4.1.2 Bremsstrahlung from runaway electrons

The ultimate goal of RE research is to enable predictive modelling for avoidance and mitigation. However, using diagnostics during RE events is challenging due to the nature of the phenomenon. Despite these difficulties, REs interact with plasma particles, generating radiation that can escape the plasma and be detected.
During disruptions, REs emit both synchrotron and Bremsstrahlung radiation [127]. Synchrotron emission, typically in the infrared-to-visible range, is observed by cameras (see Figure 4.1). Bremsstrahlung, emitted from a few keV to several tens of MeV, results from Coulomb collisions between REs and other charged particles, where the electron trajectory is deflected and hard X-rays and gamma rays are produced (see Figure 4.3). Thus, a fraction of the electron kinetic energy is converted into radiation. Strong emissivities are expected, with fluxes reaching up to 10^6 photons/(s cm^2) several metres away from the tokamak.

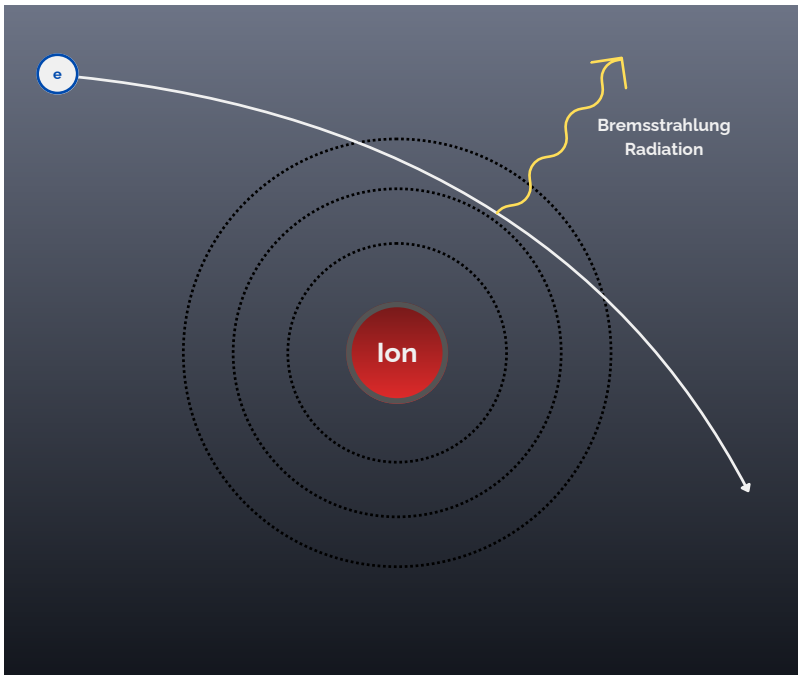

Figure 4.3: Schematic of the Bremsstrahlung emission process.

As previously mentioned, high-Z impurities lead to more intense Bremsstrahlung emission. These impurities can be deliberately introduced to trigger the thermal quench (e.g. argon injection) or to mitigate the RE beam. Alternatively, they may originate from first-wall materials (such as tungsten) and pose a threat to plasma operations.
Due to the nature of Bremsstrahlung emission, the maximum photon energy can reach the kinetic energy of the RE itself: the resulting energy spectrum is continuous, extending up to several tens of MeV.
The emission is strongly anisotropic in the typical energy range of RE events in tokamaks (E $>$ 1 MeV). Most of the radiation is emitted along the same direction as the RE, due to relativistic effects (see Figure 4.4) [128].

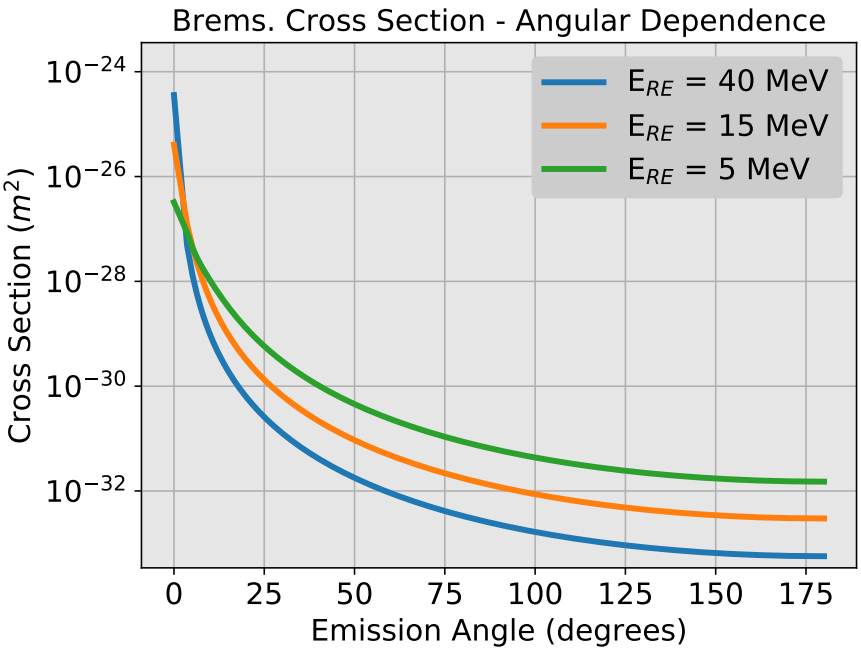

Figure 4.4: Bremsstrahlung cross section as a function of the RE emission angle (with respect to the observation direction), for different RE energy values. The strong anisotropy is evident, typical of energies above 1 MeV. One can notice that the maximum emissivity is obtained along the RE direction at zero degrees.

4.2 Analysis of Bremsstrahlung emission

Runaway Electrons (REs) can be indirectly detected through gamma-ray diagnostics. In particular, Bremsstrahlung (Bs) radiation is produced when REs interact with background plasma ions, generating intense Hard X-Ray (HXR) emission across a broad energy range, from a few keV up to several tens of MeV.
At JET, Bs emission has been systematically measured during dedicated RE experiments using several diagnostics, such as the Gamma Camera Upgrade, the tangential gamma-ray spectrometer (TGRS), and the vertical gamma-ray spectrometers (VGRS), all equipped with $LaBr_3$:Ce scintillators (see Figure 4.5). These systems provide insight into both the RE energy distribution and the spatial emissivity profile.

This work investigates how the spectral features of Bs vary depending on the line of sight used during RE events. Previous analyses often assumed a RE population strictly aligned with the magnetic field, i.e., purely co-passing electrons [128, 96, 129]. By contrast, the approach presented in this thesis considers more general pitch-angle distributions. From theoretical considerations, it can be shown that the overall shape of the HXR spectrum depends on the orientation of the line of sight with respect to the magnetic field only if the RE population includes a significant fraction of electrons at non-zero pitch angles. This provides a possible explanation for experimental evidence at JET, where diagnostics with different observation angles measure spectra with different slopes. Figure 4.6 illustrates this effect: during

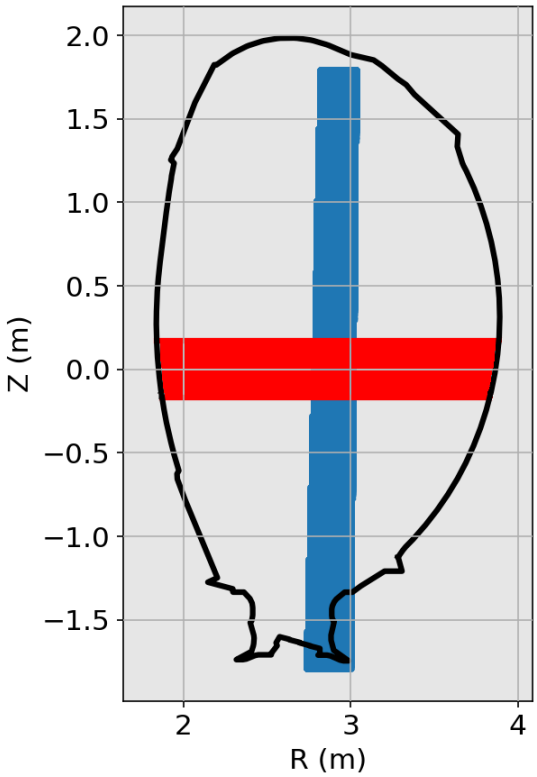

Figure 4.5: Lines of sight of the two gamma-ray spectrometers installed at JET: TGRS (red) and VGRS (blue).

a dedicated RE discharge (#103061), the spectra obtained with TGRS and VGRS display markedly different slopes.
Several factors may contribute to this behaviour. However, this thesis focuses on demonstrating that such differences may come from a non-single valued RE pitch-angle distribution.

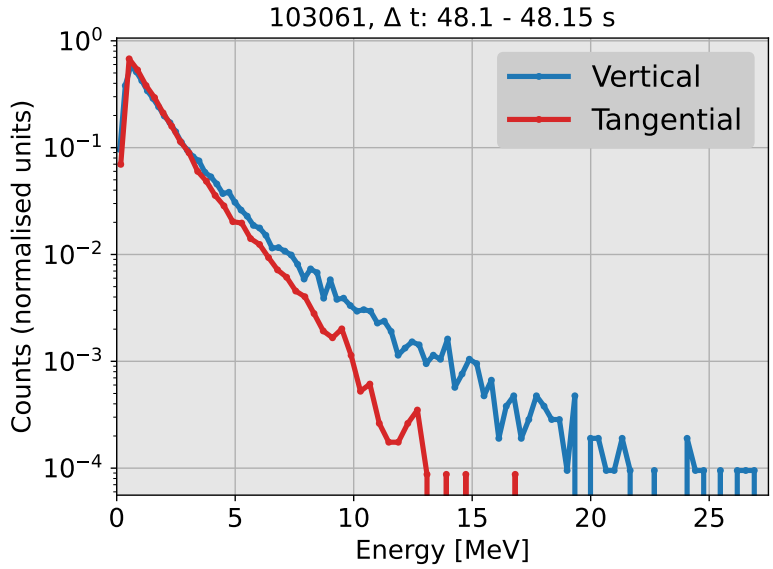

Figure 4.6: Experimental HXR spectra obtained with TGRS (red) and VGRS (blue) during a RE experiment at JET (discharge #103061, time window [48.10, 48.15] s). The spectra exhibit different slopes depending on the diagnostic used.

The analysis developed in this chapter shows that the HXR spectrum can be represented as a sum of contributions, each of which can be separated into two distinct terms: the first controlling the intensity, and the second controlling the spectral shape.
Furthermore, it is shown that a semi-analytical code can be implemented to simulate Bs spectra without relying on MonteCarlo methods, thus significantly reducing computational costs.

4.2.1 The weight function

Consider a tokamak plasma composed of pure deuterium ($Z = 1$), and focus on a specific spatial position $\vec{x}_0$ located on the magnetic axis at the fixed time t_0. A detector is assumed to intercept $\vec{x}_0$ along a line of sight forming a fixed angle α with the magnetic axis.
The quantity $S_{\epsilon_1,\epsilon_2}$ is defined as the Bremsstrahlung emissivity (with dimension photons/(s·m^3)) corresponding to photon energies between ϵ_1 and ϵ_2, where $\epsilon_1 < \epsilon_2$. For instance, ϵ_1 and ϵ_2 may represent the lower and upper limits of an energy bin in a discretised spectrum. $S_{\epsilon_1,\epsilon_2}$ is related to the RE distribution function F_{RE} through:

$$S_{\epsilon_1,\epsilon_2}(\alpha,\phi) = \int_0^{\infty} dE_{RE} \int_{-1}^{+1} dP_{RE}\, W_{\epsilon_1,\epsilon_2}(E_{RE}, P_{RE}, \alpha, \phi)\, F_{RE}(E_{RE}, P_{RE}) \quad (4.3)$$

Here, $F_{RE}(E_{RE}, P_{RE})$ denotes the RE distribution in energy–pitch space, where the pitch is defined as $P_{RE} = V_{RE,\parallel}/V_{RE} = \cos(\varphi_P)$, with φ_P being the pitch angle. V_{RE} is the RE velocity and $V_{RE,\parallel}$ its component parallel to the magnetic field. The angle ϕ is the RE gyro-angle.
$W_{\epsilon_1,\epsilon_2}$ is the Bremsstrahlung weight function, representing the sensitivity in the RE energy–pitch space for the photon energy range ϵ_1–ϵ_2 of a given spectrum. By integrating the product of the weight function and a given RE distribution function, the emissivity $S_{\epsilon_1,\epsilon_2}$ can be obtained. In the discretised case, performing this operation over a set of energy bins yields the corresponding spectrum, using the appropriate weight function for each bin. Examples of weight matrices (i.e. the discretised version of the weight functions) as functions of E_{RE} and P_{RE} for fixed α and ϵ are shown in Figure 4.7.

In earlier work, F_{RE} was often assumed to peak at $P_{RE} = 0$, corresponding to co-passing electrons, which allowed the development of inversion methods for reconstructing F_{RE} from experimental spectra [96, 128].

For clarity, now consider a monoenergetic and mono-pitch RE distribution:

$$F_{RE}(E_{RE}, P_{RE}) = \delta(E_{RE} - E_0)\,\delta(P_{RE} - P_0) \tag{4.4}$$

so that Equation 4.3 reduces to:

$$S_{\epsilon_1,\epsilon_2}(\alpha, \phi) = W_{\epsilon_1,\epsilon_2}(E_0, P_0, \alpha, \phi) \tag{4.5}$$

Since ϕ is uniformly distributed, the gyro-averaged quantities $\overline{S}_{\epsilon_1,\epsilon_2}$ and $\overline{W}_{\epsilon_1,\epsilon_2}$ can be expressed as:

$$\overline{S}_{\epsilon_1,\epsilon_2}(\alpha) = \frac{1}{2\pi}\int_0^{2\pi} S_{\epsilon_1,\epsilon_2}(\alpha, \phi)\,d\phi = \frac{1}{2\pi}\int_0^{2\pi} W_{\epsilon_1,\epsilon_2}(E_0, P_0, \alpha, \phi)\,d\phi = \overline{W}_{\epsilon_1,\epsilon_2}(E_0, P_0, \alpha) \tag{4.6}$$

Physically, $\overline{W}_{\epsilon_1,\epsilon_2}(E_0, P_0, \alpha)$ represents the Bremsstrahlung emissivity (for photon energies between ϵ_1 and ϵ_2) produced by a monoenergetic RE population with fixed pitch and observed at a given angle α, averaged over all possible gyro-angles.

Weight function separation

The aim of this section is to derive an expression for the weight function $W_{\epsilon_1,\epsilon_2}$, decomposed into two terms:

$$W_{\epsilon_1,\epsilon_2}(E_{RE}, P_{RE}, \alpha, \phi) \coloneqq R(E_{RE}, P_{RE}, \alpha, \phi) \cdot \mathcal{P}_{\epsilon_1,\epsilon_2}(E_{RE}) \tag{4.7}$$

The first term, R, is associated with the intensity of Bremsstrahlung radiation ($[R] = \mathrm{s}^{-1}\,\mathrm{m}^{-3}$) and is independent of photon energy. It is referred to as the *Rate Function*, $R(E_{RE}, P_{RE}, \alpha, \phi)$. The second term, $\mathcal{P}_{\epsilon_1,\epsilon_2}(E_{RE})$, represents the probability of emitting a photon with energy between ϵ_1 and ϵ_2, and depends solely on the RE energy.
Once E_{RE}, P_{RE}, and α are fixed, and ϵ_1, ϵ_2 are defined, the first term depends

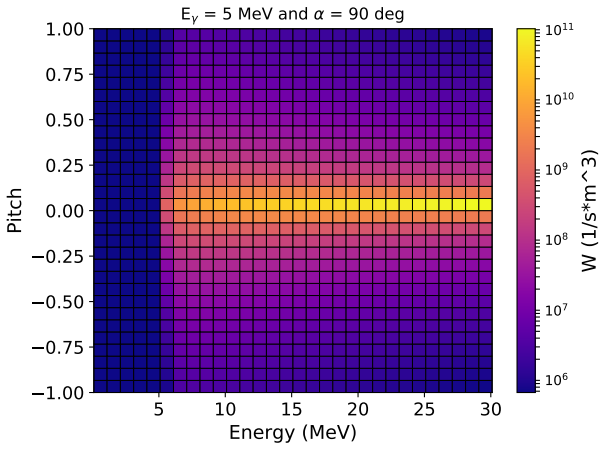

(a)

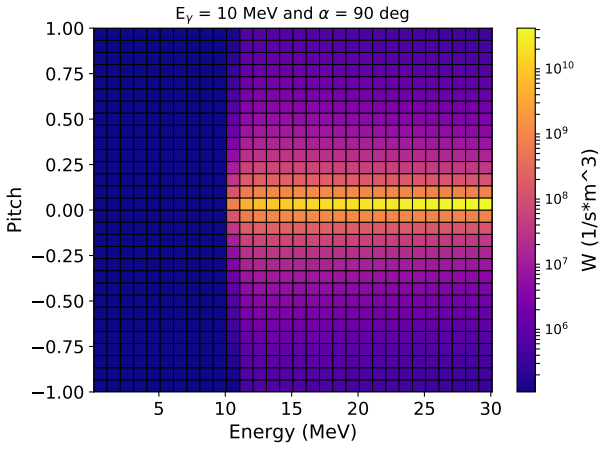

(b)

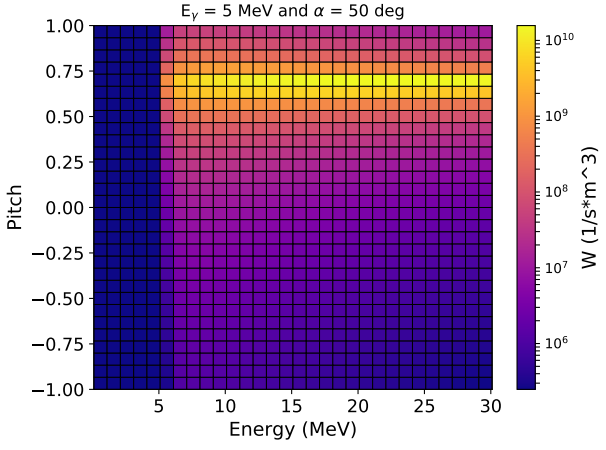

(c)

Figure 4.7: **(a)** Weight matrix calculated for a fixed photon energy $\epsilon = 5$ MeV and observation angle $\alpha = 90°$ (gyro-averaged values). **(b)** Same as (a), but for $\epsilon = 10$ MeV. **(c)** Same as (a), but for $\alpha = 50°$.

only on the RE gyro-angle ϕ, while the second has no dependence. Moreover, the dependence on the Larmor phase vanishes once $W_{\epsilon_1,\epsilon_2}$ (and therefore R) is averaged over all gyro-angles.

Equation 4.5 shows that $W_{\epsilon_1,\epsilon_2}$ corresponds to the Bremsstrahlung emissivity integrated over the energy interval ϵ_1–ϵ_2, when E_{RE}, P_{RE} are fixed. The emissivity is expressed in units of $\mathrm{s}^{-1}\,\mathrm{m}^{-3}$, representing the number of photons emitted per second per unit volume. Accordingly, $W_{\epsilon_1,\epsilon_2}$ can be calculated using:

$$W_{\epsilon_1,\epsilon_2}(E_{RE}, P_{RE}, \alpha, \phi) = \delta\Omega\, n_{ion} n_{RE} \langle \sigma v \rangle_{\epsilon_1,\epsilon_2} \tag{4.8}$$

Here, n_{ion} and n_{RE} are the background ion and runaway electron densities, respectively, at the observation point $\vec{x}_0$, while $\delta\Omega$ is the solid-angle fraction subtended by the detector. The term $\langle \sigma v \rangle_{\epsilon_1,\epsilon_2}$ denotes the Bremsstrahlung reactivity for photons with energies between ϵ_1 and ϵ_2, defined as:

$$\langle \sigma v \rangle_{\epsilon_1,\epsilon_2} = \iint d\vec{V}_{ion}\, d\vec{V}_{RE}\, v_{rel} \left.\frac{d^2\sigma}{d\epsilon\, d\Omega}\right|_{\epsilon_1<\epsilon<\epsilon_2} f(\vec{V}_{RE})\, f(\vec{V}_{ion}) \tag{4.9}$$

The relative velocity $v_{rel} = |\vec{V}_{RE} - \vec{V}_{ion}|$ can be approximated by the RE velocity V_{RE}, as the thermal ion velocity V_{ion} is negligible compared with the typical RE speed. The terms $f(\vec{V}_{RE})$ and $f(\vec{V}_{ion})$ represent the velocity distribution functions of the REs and ions, respectively.

The reactivity in Equation 4.9 includes the Bremsstrahlung Cross Section (BCS), for which a semi-empirical expression is available. Following Refs. [130, 131], the BCS can be written as:

$$\frac{d^2\sigma}{d\epsilon\, d\Omega} = \frac{1}{2\pi} P_{dipole}(E_{RE}, \theta) \frac{d\sigma}{d\epsilon}(\epsilon, E_{RE}) \tag{4.10}$$

The term $P_{dipole}(E_{RE}, \theta)/2\pi$, known as the *dipole function*, describes the anisotropy of the BCS. An explicit form is given in Ref. [60]:

$$P_{dipole}(E_{RE}, \theta) = \frac{3}{8}\left[1 + \left(\frac{\cos\theta - \beta}{1 - \beta\cos\theta}\right)^2\right] \frac{1}{\gamma^2(1 - \beta\cos\theta)^2} \tag{4.11}$$

where $\beta = V_{RE}/c$ and $\gamma = 1/\sqrt{1-\beta^2}$. The *emission angle* θ is defined as the angle between the RE velocity vector $\vec{V}_{RE}$ and the line of sight direction $\hat{u}_{los}$. It can be expressed as a function of P_{RE}, α, and the gyro-angle ϕ, as demonstrated in the next subsection.

The gyro-averaged dipole function, $\overline{P}_{\mathrm{dipole}}$, is obtained by averaging P_{dipole} over all gyro-angles. This is achieved by expressing P_{dipole} as a function of the gyro-angle ϕ (see Equation 4.17 in the next subsection) and integrating over a uniform distribution in the interval $[0, 2\pi]$. In practice, this integral is evaluated as a discrete sum over a large number of equally spaced ϕ values and normalised by 2π. Figures 4.8a and 4.8b show the behaviour of $\overline{P}_{\mathrm{dipole}}$ as a function of the pitch angle φ_P for observation angles $\alpha = 50°$ and $\alpha = 90°$, respectively, and for different RE energies.

The term $d\sigma/d\epsilon\,(\epsilon, E_{RE})$ represents the energy-dependent component of the BCS, where ϵ is the energy of the emitted Bremsstrahlung photon. Figure 4.8c shows its

dependence on ϵ for different RE energies. For a given spectral energy interval ($\epsilon_1 < \epsilon < \epsilon_2$), the energy-dependent part of the cross section becomes:

$$\left.\frac{d\sigma}{d\epsilon}\right|_{\epsilon_1<\epsilon<\epsilon_2}(E_{RE}) = \int_{\epsilon_1}^{\epsilon_2} d\epsilon \, \frac{d\sigma}{d\epsilon}(\epsilon, E_{RE}) \tag{4.12}$$

The BCS in Equation 4.10 has significant implications for the weight function $W_{\epsilon_1,\epsilon_2}$, as will be discussed later. It also strongly influences the shape of the Bremsstrahlung spectrum: a monoenergetic RE distribution, for instance, produces a continuous spectrum extending from 0 to E_{RE} due to the energy-dependent term. Furthermore, the observation angle and the RE pitch distribution have a marked impact on the spectral intensity through the P_{dipole} term.

Angle dependence

In Equation 4.10, the Bremsstrahlung cross section depends on the emission angle θ, defined as the angle between the RE velocity vector $\hat{V}_{RE}$ and the observation line of sight $\hat{u}_{los}$.
It is often more convenient to express the emission angle in terms of three other angles: the pitch angle $\varphi_P = \arccos(P_{RE})$, which is the angle between the RE direction and the magnetic field; the observation angle α, defined between the magnetic axis and the line of sight; and the RE gyro-angle ϕ, which describes the Larmor phase of the particle around the magnetic field. These quantities are generally easier to use in analysis than θ itself.
An explicit relation between θ and these three angles can be derived. Consider a line of sight that intersects the magnetic axis and lies in the same plane as the unit vector $\hat{x}$, which is perpendicular to the magnetic field direction $\hat{B} = \hat{z}$. This defines a Cartesian coordinate system (x,y,z). The unit vector along the observation line of sight is then given by:

$$\hat{u}_{los} = \cos(\alpha)\hat{z} + \sin(\alpha)\hat{x} \tag{4.13}$$

The RE velocity vector can be written as:

$$\vec{V}_{RE} = V_{RE}\cos(\varphi_P)\hat{z} + V_{RE}\sin(\varphi_P)\hat{B}_\perp \tag{4.14}$$

where $\hat{B}_\perp$ is the unit vector perpendicular to the magnetic field and can be expressed as a linear combination of $\hat{x}$ and $\hat{y}$:

$$\hat{B}_\perp = \cos(\phi)\hat{x} - \sin(\phi)\hat{y} \tag{4.15}$$

By combining these expressions, we obtain the following relation for the emission angle:

$$\begin{gathered}\cos(\theta) = \hat{u}_{los} \cdot \hat{V}_{RE} = \\ (\cos(\alpha)\hat{z} + \sin(\alpha)\hat{x}) \cdot [\cos(\varphi_P)\hat{z} + \sin(\varphi_P)\,(\cos(\phi)\hat{x} - \sin(\phi)\hat{y})] \\ = \cos(\alpha)\cos(\varphi_P) + \sin(\alpha)\sin(\varphi_P)\cos(\phi)\end{gathered} \tag{4.16}$$

Equivalently, it can be expressed as a function of the pitch P_{RE}:

$$\cos(\theta) = \cos(\alpha)P_{RE} + \sin(\alpha)\cos(\phi)\sqrt{1 - P_{RE}^2} \tag{4.17}$$

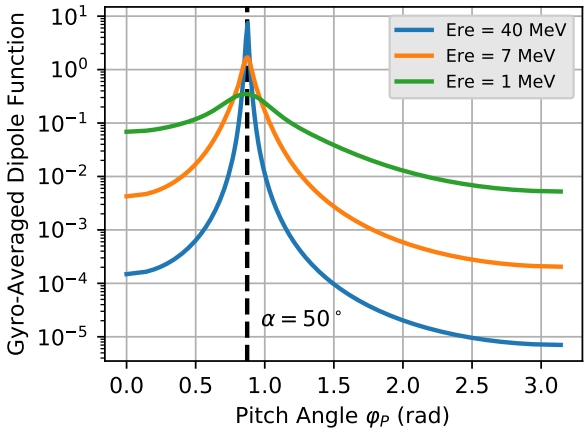

(a)

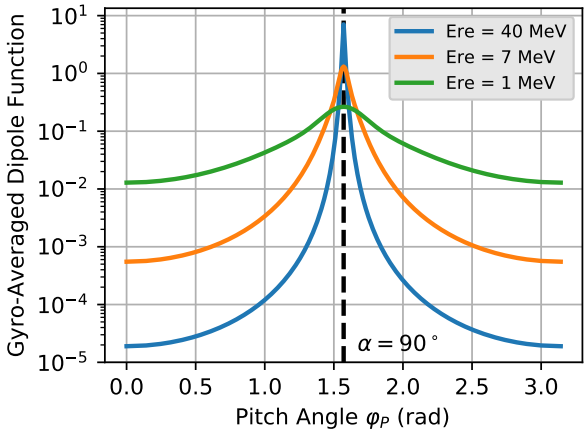

(b)

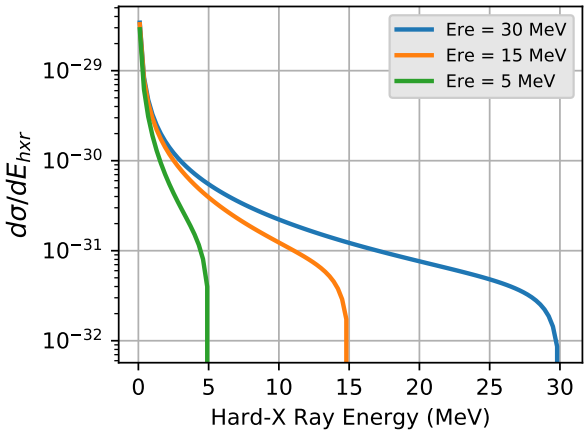

(c)

Figure 4.8: **(a)** Gyro-averaged dipole function as a function of the pitch angle φ_P for different RE energies and observation angle α = 50°. **(b)** Same as (a), for α = 90°. **(c)** Energy-dependent part of the BCS as a function of ϵ, for different RE energies.

Thus, the Bremsstrahlung cross section can be expressed as a function of the gyro-angle ϕ, the observation angle α, and the pitch angle φ_P. The direct consequence is that $W_{\epsilon_1,\epsilon_2}$ can be expressed as a function of the three angles instead of θ.

In Figure 4.9 a schematic of the reference system used in this treatment is shown.

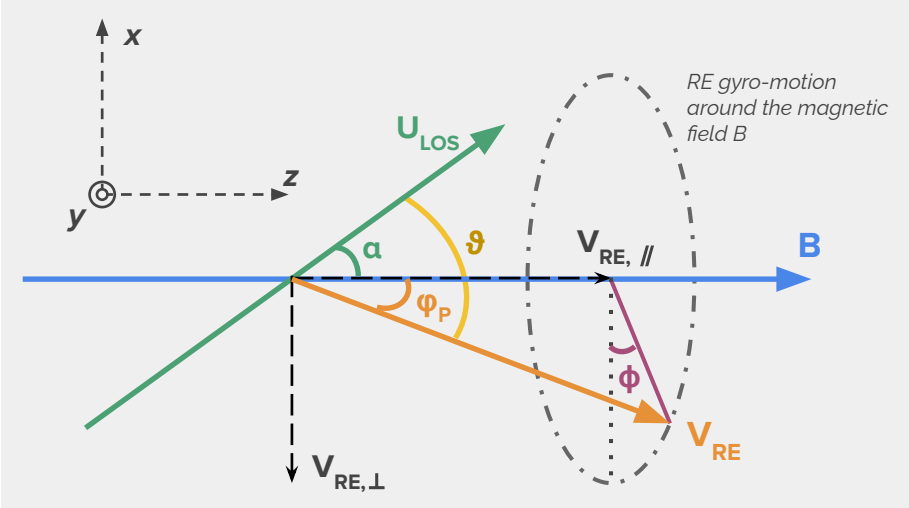

Figure 4.9: Schematic of the reference system used for the spectral calculation. Angle α denotes the angle between the magnetic field direction (denoted by $\vec{B}$) and the observation LoS ($\vec{u}_{los}$) direction. Angle ϕ is the gyro-angle of the RE, showing off when the pitch angle φ_P is different from zero. Angle φ_P is the pitch angle of the RE i.e., the angle between the RE direction (determined by the RE velocity $\vec{V}_{RE}$) and the magnetic field. Finally, θ represents the emission angle between the observation direction $\vec{B}$ and the RE direction $\vec{V}_{RE}$.

4.2.2 Calculations

Now, the reactivity for a RE beam with fixed energy and pitch can be computed, such that $V_{RE} = V_0$, $E_{RE} = E_0$, and $P_{RE} = P_0$:

$$\begin{aligned}\langle\sigma v\rangle_{\epsilon_1,\epsilon_2} &= \iint d\vec{V}_{ion}\, d\vec{V}_{RE}\, v_{rel}\, \frac{d^2\sigma}{d\epsilon\, d\Omega}\bigg|_{\epsilon_1<\epsilon<\epsilon_2} \delta(V_{RE}-V_0)\,\delta(V_{ion}-0) \\ &= V_0\, \frac{d^2\sigma}{d\epsilon\, d\Omega}\bigg|_{\epsilon_1<\epsilon<\epsilon_2}(E_0,P_0,\alpha,\phi) = \frac{V_0}{2\pi}\,\frac{d\sigma}{d\epsilon}\bigg|_{\epsilon_1<\epsilon<\epsilon_2}(E_0)\;\; P_{dipole}(E_0,P_0,\alpha,\phi) \end{aligned} \tag{4.18}$$

where Equation 4.10 has been used. The relative velocity v_{rel} equals the RE velocity V_0, since ion velocities are negligible compared with typical RE velocities.

The weight function $W_{\epsilon_1,\epsilon_2}$ from Equation 4.8 can be written as:

$$W_{\epsilon_1,\epsilon_2}(E_0,P_0,\alpha,\phi) = \delta\Omega\, n_{ion} n_{RE} V_0 \frac{1}{2\pi} P_{dipole}(E_0,P_0,\alpha,\phi)\, \frac{d\sigma}{d\epsilon}\bigg|_{\epsilon_1<\epsilon<\epsilon_2}(E_0) \tag{4.19}$$

Next, the total energy cross-section Σ is defined as the energy-dependent part of the cross-section integrated over all photon energies ϵ:

$$\Sigma(E_{RE}) \coloneqq \int_{\epsilon_{min}}^{\epsilon_{max}} d\epsilon\, \frac{d\sigma}{d\epsilon}(\epsilon, E_{RE}) \tag{4.20}$$

(with units m^2) which depends solely on the RE energy E_{RE}. The integration bounds are chosen such that ϵ_{max} is sufficiently large to include E_{RE}, while ϵ_{min} is set to a small but finite value.
Once $E_{RE} = E_0$ is fixed, one can denote $\Sigma = \Sigma_0$. Using this, Equation 4.19 can be rewritten as:

$$W_{\epsilon_1,\epsilon_2}(E_0, P_0, \alpha, \phi) = \delta\Omega\, n_{ion} n_{RE} V_0 \frac{1}{2\pi} P_{dipole}(E_0, P_0, \alpha, \phi)\, \Sigma_0 \cdot \left.\frac{d\sigma}{d\epsilon}\right|_{\epsilon_1<\epsilon<\epsilon_2}(E_0)\, \frac{1}{\Sigma_0} \quad (4.21)$$

The first part of the right-hand side of Equation 4.21 (before the dot) corresponds to a rate. The rate function R is defined as:

$$R(E_0, P_0, \alpha, \phi) = \delta\Omega\, n_{ion} n_{RE} V_0 \frac{1}{2\pi} P_{dipole}(E_0, P_0, \alpha, \phi)\, \Sigma_0 \quad (4.22)$$

which depends on E_0, P_0, α, and ϕ, but is independent of the photon energy. The rate function determines the total emission intensity, irrespective of photon energy. The gyro-averaged rate function is expressed as:

$$\overline{R}(E_0, P_0, \alpha) = \delta\Omega\, n_{ion} n_{RE} V_0 \frac{1}{2\pi} \Sigma_0\, \overline{P}_{dipole}(E_0, P_0, \alpha) \quad (4.23)$$

The gyro-averaged rate function depends on both RE energy (through V_{RE} and Σ) and the RE pitch and observation angles. This dependence is illustrated in Figures 4.8a and 4.8b, showing how the dipole function—and consequently the rate function—varies with pitch for different energies and observation angles.

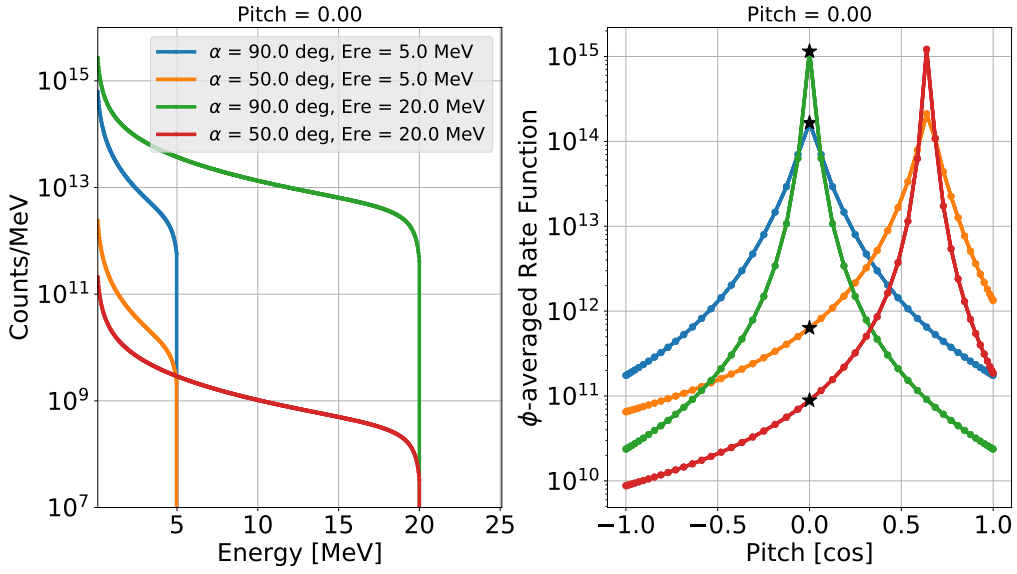

Figure 4.10: Effect of the gyro-averaged rate function on Bremsstrahlung spectra. Right: gyro-averaged rate function as a function of pitch angle for $E = 5$ and 20 MeV and observation angles $\alpha = 90°$ and 50°. Left: corresponding Bremsstrahlung spectra at pitch angle $\varphi_P = 90°$.

Figures 4.10 and 4.11 show that the maximum of the rate function (and thus of the emission intensity) occurs when the pitch angle matches the observation angle.

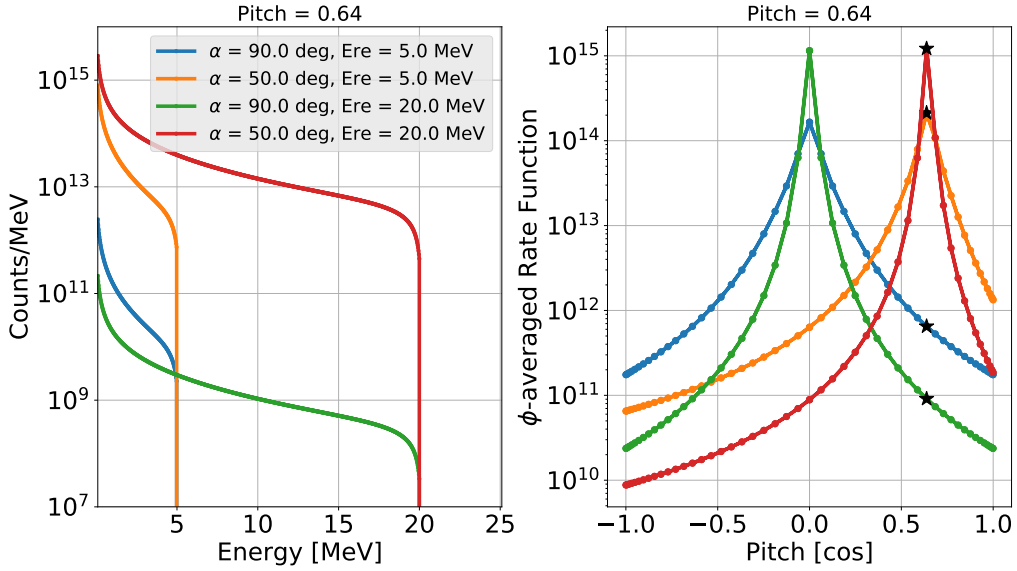

Figure 4.11: Effect of the gyro-averaged rate function on Bremsstrahlung spectra. Right: gyro-averaged rate function as a function of pitch angle for $E = 5$ and 20 MeV and observation angles $\alpha = 90°$ and 50°. Left: corresponding Bremsstrahlung spectra at pitch angle $\varphi_P = 50°$.

As the pitch deviates from the observation angle, the intensity decreases. If two detectors with different observation angles are used simultaneously, and the RE pitch and energy are fixed, they will record different photon intensities–one higher and one lower–depending on their alignment with the pitch direction, as shown in the figures.
The RE energy dependence of the dipole function enhances this directional sensitivity: at higher RE energies, the emission becomes more strongly peaked along the RE direction of motion (see Figures 4.8a and 4.8b). This behaviour is also reflected in the rate function. Finally, the factor $V_{RE}\,\Sigma$ in Eq. 4.23 scales the overall intensity but does not alter its angular dependence.

The second part of the right-hand side of Equation 4.21 (after the dot) represents a probability. Define $\mathcal{P}_{\epsilon_1,\epsilon_2}$ as:

$$\mathcal{P}_{\epsilon_1,\epsilon_2}(E_0) = \frac{1}{\Sigma_0}\frac{d\sigma}{d\epsilon}\bigg|_{\epsilon_1<\epsilon<\epsilon_2}(E_0) \tag{4.24}$$

This quantity represents the probability of detecting a photon with energy $\epsilon_1 < \epsilon < \epsilon_2$ following a Bremsstrahlung event, depending on E_{RE}. Since the energy-dependent term $\frac{d\sigma}{d\epsilon}$ is integrated between ϵ_1 and ϵ_2, $\mathcal{P}_{\epsilon_1,\epsilon_2}$ is dimensionless, whereas

$$\mathcal{P}(\epsilon, E_0) = \frac{1}{\Sigma_0}\frac{d\sigma}{d\epsilon}(\epsilon, E_0) \tag{4.25}$$

is a probability distribution function with units of [MeV^{-1}], representing the probability density of emitting a Bremsstrahlung photon with energy ϵ from a RE with energy E_0. The qualitative shape of $\mathcal{P}$ mirrors that of the energy-dependent term of the Bremsstrahlung cross-section (see Figure 4.8c), normalised by $1/\Sigma_0$. As the RE

energy increases, the high-energy tail of the distribution extends to larger photon energies, up to $\epsilon_{max} = E_0$. Consequently, the spectrum becomes flatter (i.e. less steep) at higher RE energies and steeper at lower ones.

Finally, the weight function $W_{\epsilon_1,\epsilon_2}$ can be written as:

$$W_{\epsilon_1,\epsilon_2}(E_0, P_0, \alpha, \phi) = R(E_0, P_0, \alpha, \phi) \cdot \mathcal{P}_{\epsilon_1,\epsilon_2}(E_0) \tag{4.26}$$

Averaging over all gyroangles, Equation 4.26 becomes:

$$\overline{W}_{\epsilon_1,\epsilon_2}(E_0, P_0, \alpha) = \overline{R}(E_0, P_0, \alpha) \cdot \mathcal{P}_{\epsilon_1,\epsilon_2}(E_0) \tag{4.27}$$

4.2.3 Implementation in a code

The results presented above show the possibility of implementing semi-analytical calculations in a code to simulate Bremsstrahlung spectra from RE experiments.
In general, a monochromatic or mono-pitch RE distribution is not expected; rather, a broad range of energies and pitch angles is considered. Nevertheless, the RE distribution can be discretised into energy and pitch bins, and a weighted sum over all possible combinations of E_{RE} and P_{RE} can be performed. Equation 4.3 then becomes:

$$\overline{S}_{\epsilon_k}(\alpha) = \sum_{i,j} \overline{W}_{\epsilon_k}(E_i, P_j, \alpha) \cdot w_{i,j} \tag{4.28}$$

where the average over all gyroangles has been taken. The bin-intensity $\overline{S}_{\epsilon_k}$ and the discretised weight function $\overline{W}_{\epsilon_k}$ are calculated for the photon energy bin ϵ_k. The weights $w_{i,j}$ are extracted directly from the discretised RE distribution F_{RE} and represent the relative population of each 2D bin in the E–P space. In practice, this task is carried out by computing Equation 4.27 for a finite set of iterations, discretising the E_{RE}–P_{RE} space and applying the corresponding weights $w_{i,j}$. Finally, the whole procedure is performed for each k-th spectral bin.
Moreover, the calculation can be extended to different spatial locations within the plasma by discretising it into "voxels", each characterised by different ion and RE densities, optical transport factor, observation angle, and RE distribution function (hence different $w_{i,j}$). Finally, this procedure can also be repeated at different time steps, taking in account the time evolution of the magnetic equilibrium.

The calculation is referred to as "semi-analytical" for several reasons. The weight function $\overline{W}_{\epsilon_k}$ is primarily determined by the Rate function and the energy probability. Each of these components depends on the Bremsstrahlung cross section, which can itself be decomposed into two parts: the dipole function and the energy-dependent part of the cross section. Solutions for these terms are already available: the former is analytical, given by Equation 4.11, while the latter is semi-empirical, as presented in Ref. [131]. Finally, the average over all gyroangles is performed by summing the dipole functions over a large, finite set of equally spaced ϕ values, with equal weights due to the uniform distribution of the ϕ angles.
The two components of the cross section can thus be efficiently calculated in a routine over a finely discretised space, making the overall approach computationally feasible. Both terms are already implemented in the GENESIS libraries, and a simple Python script can be written to leverage the GENESIS routines.

4.2.4 A simple case study

Consider a runaway electron (RE) distribution consisting of two distinct monochromatic and mono-pitch beams:

- b_1 with energy $E_1 = 15\,\mathrm{MeV}$ and pitch $P_1 = 1.0$
- b_2 with energy $E_2 = 25\,\mathrm{MeV}$ and pitch $P_2 = -0.5$

In this simple scenario, n_{RE} and n_i are fixed, and both beams have equal populations. The RE source is observed by two diagnostics (A and B), placed at different observation angles relative to the magnetic field: $\alpha = 90°$ and $\beta = 50°$, respectively. Using Equation 4.27, the spectra seen by each diagnostic can be calculated with a semi-analytical approach, as shown in Figure 4.12. It is clear that the two spectra share similar features but also show distinct differences. Both diagnostics observe the same source but from different angles, resulting in different spectral features.

- Both diagnostics observe b_1, but diagnostic B has a smaller average angle (over all gyro-angles) between its line of sight and the beam velocity than diagnostic A.
- Both diagnostics observe b_2 but diagnostic A has a smaller average angle relative to the beam velocity than diagnostic B.
- Both spectra include contributions from E_1 and E_2, but diagnostic A, compared to diagnostic B, records a higher count rate at high energies and a lower one at low energies.
- The overall spectral slopes differ between the two diagnostics.

These differences arise from the combined effects of the probability distribution function $\mathcal{P}$ and the rate function $\overline{R}$. The former is the same for both diagnostics and differ only from the two beams. The latter varies with the observation angle, producing four components in total. Diagnostic B is "more aligned" with b_2 than diagnostic A, whereas diagnostic A is "more aligned" with b_1 than diagnostic B. This angular sensitivity causes distinct spectral features, especially when non-zero pitch angles are present in the RE distribution

The resulting intensities for the bin ϵ_k for the two diagnostics are:

$$S_{\epsilon_k}(\alpha) = \overline{W}_{\epsilon_k}(E_1, P_1, \alpha) + \overline{W}_{\epsilon_k}(E_2, P_2, \alpha) \tag{4.29}$$

$$S_{\epsilon_k}(\beta) = \overline{W}_{\epsilon_k}(E_1, P_1, \beta) + \overline{W}_{\epsilon_k}(E_2, P_2, \beta) \tag{4.30}$$

where each weight function is defined as:

$$\overline{W}_{\epsilon_k}(E_1, P_1, \alpha) = \overline{R}(E_1, P_1, \alpha) \cdot \mathcal{P}_{\epsilon_k}(E_1) \tag{4.31}$$

$$\overline{W}_{\epsilon_k}(E_2, P_2, \alpha) = \overline{R}(E_2, P_2, \alpha) \cdot \mathcal{P}_{\epsilon_k}(E_2) \tag{4.32}$$

$$\overline{W}_{\epsilon_k}(E_1, P_1, \beta) = \overline{R}(E_1, P_1, \beta) \cdot \mathcal{P}_{\epsilon_k}(E_1) \tag{4.33}$$

$$\overline{W}_{\epsilon_k}(E_2, P_2, \beta) = \overline{R}(E_2, P_2, \beta) \cdot \mathcal{P}_{\epsilon_k}(E_2) \tag{4.34}$$

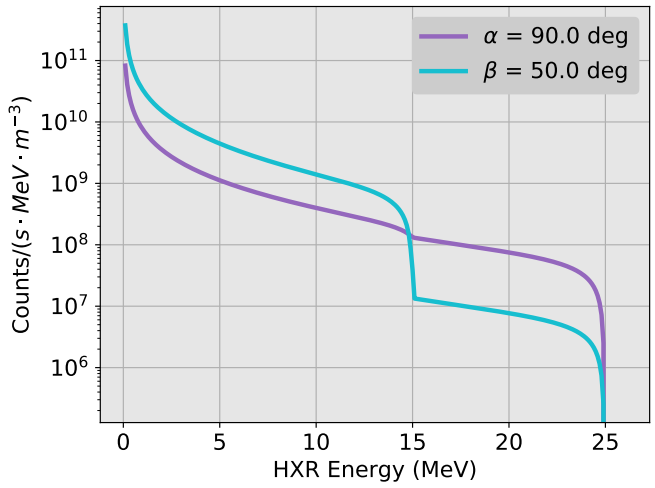

(a)

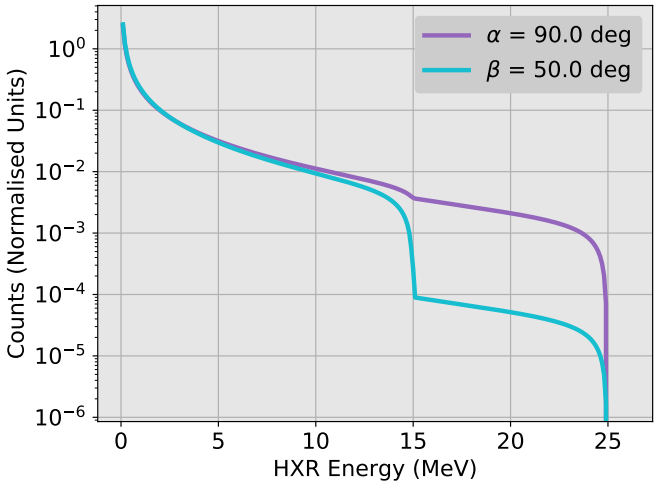

(b)

Figure 4.12: Energy spectra observed from two different angles. The RE distribution consists of two beams: b_1 (E_1 = 15 MeV, P_1 = 1) and b_2 (E_2 = 25 MeV, P_2 = −0.5). Original (a) and normalised (b) counts.

Finally, calculating the intensities for each bin ϵ_k, we obtain two different spectra from the two diagnostics.
Figure 4.13 shows the four weight functions defined above, calculated for all energy bins ϵ_k. The trends discussed are clearly visible: diagnostic B is more sensitive to b_1, while diagnostic A is more sensitive to b_2. As a result, the spectrum seen by diagnostic B is dominated by the lower-energy beam (b_1), while the spectrum from diagnostic A is dominated by the higher-energy beam (b_2).

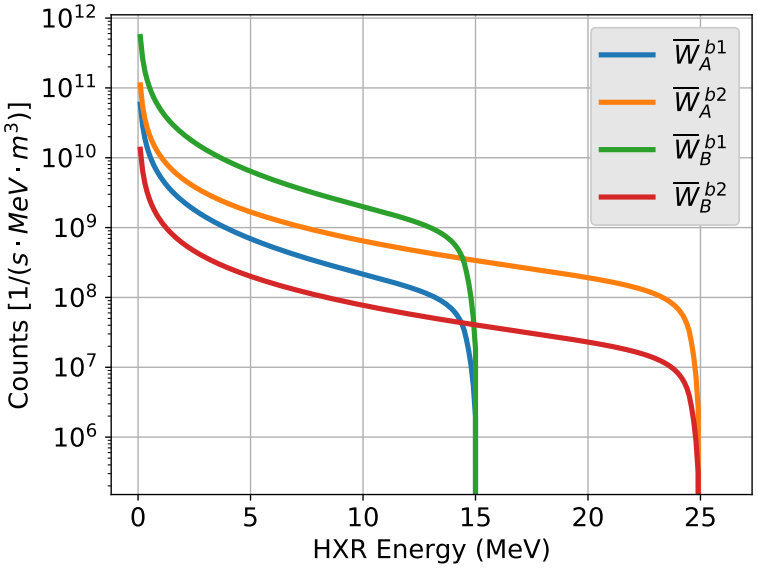

Figure 4.13: Weight functions corresponding to Equations 4.31–4.34. Diagnostic A is more sensitive to beam b_2, while diagnostic B is more sensitive to beam b_1.

A more complex case

Now, consider a more complex energy-pitch distribution. As shown in Figure 4.14, a series of equally populated bins forms a "triangular" shape, with the majority of bins aligned along the $P_{RE} = 1$ axis (co-passing electrons). Moving farther from the magnetic axis, the maximum RE energy decreases.

Figure 4.15 shows the resulting bremsstrahlung spectra observed by two diagnostics at 90° and 50°. This example demonstrates how even more complex distributions can affect the measured spectra and highlights the impact of the RE pitch-angle distribution. One can notice that the simulated spectra in Figure 4.15 better mimic the experimental ones seen in Figure 4.6. This is a proof of concept: it shows that pitch-angle distributions can influence spectral measurements when multiple lines of sight are used, without asserting that this is the actual cause of any experimental observation.

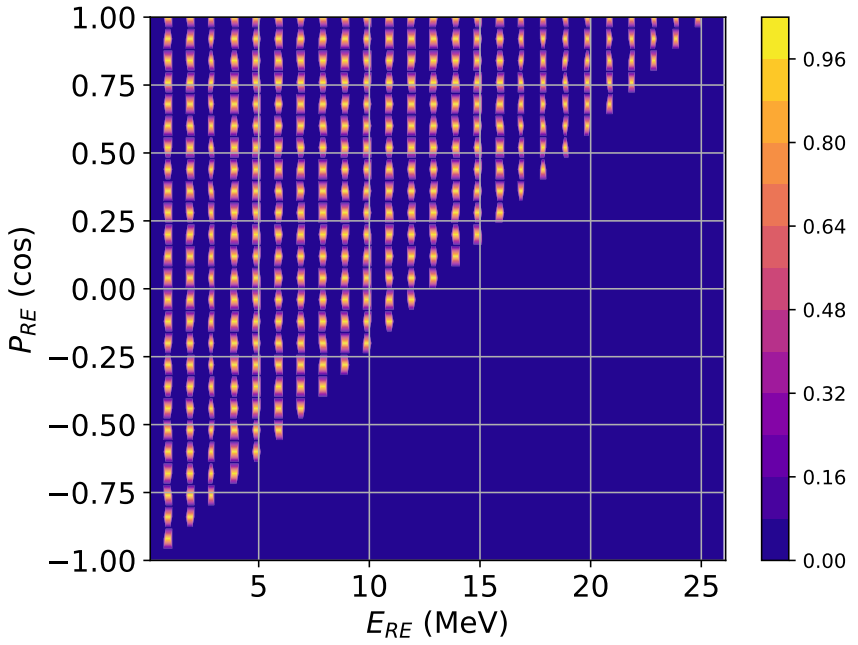

Figure 4.14: Tentative energy-pitch distribution of a RE population. Each bin is equally populated. Most of the RE population has zero pitch angle.

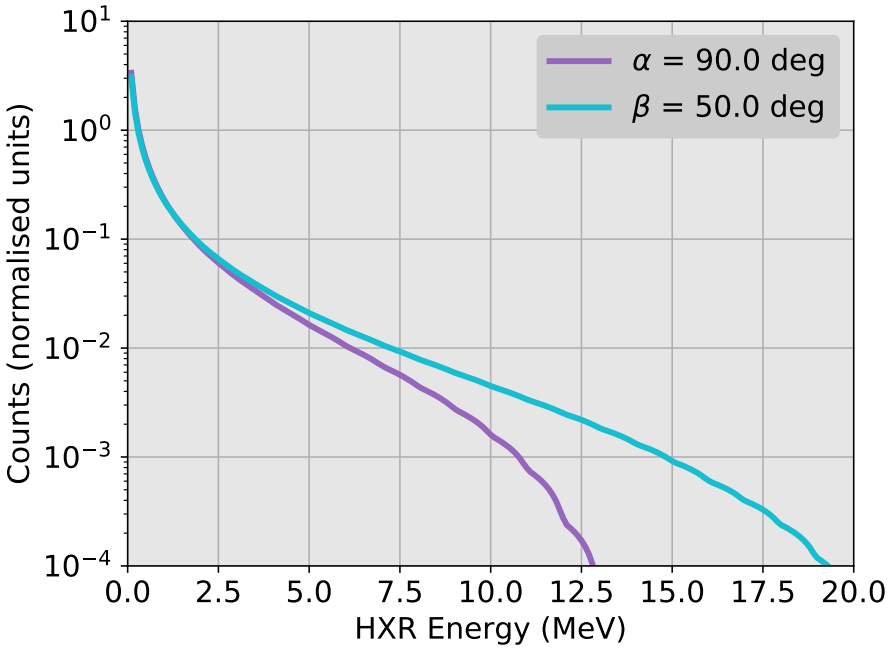

Figure 4.15: Resulting bremsstrahlung spectra from the RE distribution in Figure 4.14, as observed by two diagnostics at 90° and 50°.

Conclusions and Outlooks

In this thesis, applications of gamma-ray diagnostics in tokamaks have been presented. These include fusion power measurements, reconstructions of the alpha particle birth profile and the analysis of Bremsstrahlung emission from runaway electrons using multiple lines of sight.
The Cerium-activated Lanthanum Bromide ($LaBr_3$:Ce) crystal has been key to perform these studies. It is an inorganic scintillator representing the state of the art for gamma-ray measurements in magnetic confinement reactors, thanks to its high performance at intense radiation rates and robustness in harsh environments.

In Chapter 2, a feasibility study of a detector based on the $LaBr_3$:Ce scintillator has been presented for the SPARC tokamak, aiming to perform fusion power evaluations by measuring gamma-rays from the DT reaction. This study strongly relies on the experience gained at the JET tokamak, where gamma-ray emission from DT fusion reactions has been observed and used to determine the γ/n branching ratio of the emission. In particular, by employing a detector similar to the one used at JET, it has been found in this work that gamma-ray-based fusion power measurements at SPARC are possible within the range from 0.2 MW up to the maximum expected fusion power scenario at 140 MW. A Lithium Hydride neutron attenuator, analogous to the one used at JET, is mandatory for gamma-ray measurements due to the very high neutron flux expected at SPARC. The gamma-ray background is also expected to be very intense, based on the observations at JET. Without a gamma-ray attenuator, the measurable fusion power range along the horizontal channel is limited to [0.2, 13.2] MW (assuming a JET-like background). By using Tungsten as the attenuating material and varying the attenuator length, the overall operational range can be extended to [0.2, 140] MW. For the channel adjacent to the horizontal one, the measurable fusion power range is [9.7, 140] MW, indicating that this configuration could serve as an alternative if the horizontal channel is not accessible to the proposed diagnostic, although it would be restricted to high-performance fusion scenarios.
To proceed with the engineering design of the diagnostics, a detailed engineering model of the SPARC tokamak is required in order to calculate a more realistic gamma-ray background spectrum using MonteCarlo simulations of neutron and gamma-ray transport, for example with the MCNP code. Furthermore, the choice of attenuators represents a critical factor, due to secondary issues associated with Lithium Hydride and Tungsten. The former may pose serious safety concerns in experimental facilities, while the latter affects the width of the operational range, as it attenuates gamma-rays from the signal region ($12 < E_\gamma < 17$ MeV) more strongly

than those from the background ($E_\gamma < 10$ MeV). The evaluation of alternative materials is therefore recommended to avoid these shortcomings.

In Chapter 3, the possibility of performing studies of the alpha birth profile using gamma-ray measurements is discussed. In particular, the Gamma Camera Upgrade at JET, consisting of 19 lines of sight – 10 radial and 9 vertical – collects data from a $LaBr_3$:Ce detector installed on each channel. D–^{3}He plasmas represent a source of alpha particles from the $^3\mathrm{He}(\mathrm{D},\mathrm{p})\alpha$ reaction. By observing the gamma-ray emission from the rarer ^{3}He(D,γ)^{5}Li branch, a tomographic reconstruction of the two-dimensional gamma profile – and consequently, of the alpha birth profile – can be performed.
The focus of this work is on the validation of TRANSP simulations performed at JET, related to D–^{3}He plasmas from Three-Ion Scheme experiments. For a selected discharge set, some TRANSP outputs have been retrieved to create synthetic versions of the alpha birth profile, which are then compared with those obtained from experimental data. Before completing this task, two validation steps were carried out. First, the time evolution of the total neutron rate from TRANSP was compared with experimental data from fission chambers, showing an overall acceptable agreement in the quiescent phase of the discharge, before the sawtooth crash. Then, the TRANSP simulation of the fast deuterium beam distribution was retrieved at the timestamp corresponding to the best agreement in the total neutron rate. The second validation step concerns the numerical calculation of a synthetic TOFOR neutron spectrum due to D(D,n)^{3}He reactions, using the previously retrieved fast D distribution. After comparison with experimental data, and after introducing the exact particle orbits to account for the Finite Larmor Radius effects, an overall good agreement is found across the discharge set. Finally, data from the Gamma Camera are analysed and an alpha birth profile is obtained through tomographic reconstruction using the TREVISO code. A synthetic version calculated using the fast D distribution simulated by TRANSP is also produced and compared with the experimental one. An overall good, or at least reasonable, agreement is found across the discharge set.
The results presented suggest that TRANSP simulations, if properly configured, can reliably predict gamma and neutron emission when applied to D–^{3}He plasmas from Three-Ion Scheme experiments at JET. Moreover, TRANSP may support the optimisation of heating scenarios in future tokamaks with the aim of generating alpha particles. Finally, this study opens the possibility of evaluating quantitatively the D–^{3}He gamma-ray and alpha particle emissions. In particular, the experimental evaluation of fusion power in D–^{3}He plasmas may be achieved by observing the gamma-ray emission from the ^{3}He(D,γ)^{5}Li reaction.

In Chapter 4, another application of gamma-ray spectroscopy has been investigated, concerning Bremsstrahlung radiation from runaway electron events. Experimental observations at JET have shown different spectral features in Bremsstrahlung spectra obtained using distinct lines of sight with different observation angles, where $LaBr_3$:Ce-based detectors were installed. This is a peculiar phenomenon, since the spectral shape is usually observed to be approximately the same. In this thesis, it has been found that, based on theoretical considerations, the spectral shape may vary when observing the same event from different lines of sight. When runaway

electrons are emitted at large pitch angles, significantly different from zero, two detectors may experience different sensitivities to co-passing (pitch angle ≈ 0) electrons compared to electrons with large pitch angles. This represents a proof of concept rather than a demonstration that the experimental spectral differences observed at JET may indeed be due to the presence of runaway electrons with large pitch angles. This finding can be used to improve the understanding of runaway electron physics and their distribution in tokamaks, by applying multiple lines of sight to investigate the pitch angle distribution of runaway electrons.

Bibliography

[1] Kenneth S. Krane. *Introductory Nuclear Physics*. en. John Wiley & Sons, Jan. 1991. ISBN: 978-0-471-80553-3.

[2] John Wesson and D. J. Campbell. *Tokamaks*. en. Clarendon Press, 2004. ISBN: 978-0-19-850922-6.

[3] Fastfission. *A graph displaying the average binding energy per nucleon for a varied number of neutrons*. Public Domain. 2008. URL: https://upload.wikimedia.org/wikipedia/commons/5/53/Binding_energy_curve_-_common_isotopes.svg.

[4] S. E. Caldwell et al. «Observation of d–t Fusion Gamma Rays (Invited)». In: *Review of Scientific Instruments* 74.3 (Mar. 2003), pp. 1837–1841. ISSN: 0034-6748, 1089-7623. DOI: 10.1063/1.1534932.

[5] J. P. Riley and M. Tongudai. «The Lithium Content of Sea Water». In: *Deep Sea Research and Oceanographic Abstracts* 11.4 (Aug. 1964), pp. 563–568. ISSN: 0011-7471. DOI: 10.1016/0011-7471(64)90002-6.

[6] Qunying Huang et al. «Activation Analysis of Structural Materials Irradiated by Fusion and Fission Neutrons». In: *Journal of Nuclear Materials* 307–311 (Dec. 2002), pp. 1031–1036. ISSN: 0022-3115. DOI: 10.1016/S0022-3115(02)01306-5.

[7] WikiHelper2221. *Cross Section of DT, DD, D-He3, P-B11 and Helium3 nuclear fusion reaction. These rates are measured in cross section (m^2)*. CC BY-SA 4.0, via Wikimedia Commons. 2021. URL: https://upload.wikimedia.org/wikipedia/commons/d/db/Cross_Section_for_Fusion_reactions.png.

[8] Francis F. Chen. *Introduction to Plasma Physics and Controlled Fusion: Volume 1: Plasma Physics*. Springer Science & Business Media, Mar. 2013. ISBN: 978-1-4757-5595-4.

[9] Thomas James Dolan. *Fusion Research: Principles*. Elsevier, Oct. 2013. ISBN: 978-1-4831-5299-8.

[10] MikeRun. *Schematic of a tokamak chamber and magnetic profile.* CC BY 4.0 &lt, via Wikimedia Commons. 2021. URL: https://upload.wikimedia.org/wikipedia/commons/e/ed/Schematic-of-a-tokamak-chamber-and-magnetic-profile.png.

[11] Dstrozzi. *Plot of the fusion reactivity (average of cross-section times relative speed of reacting nuclei) vs. temperature for three common reactions. The average is over Maxwellian ion distributions with the appropriate temperature.* CC BY 2.5, via Wikimedia Commons. 2006. URL: https://upload.wikimedia.org/wikipedia/commons/d/d0/Fusion_rxnrate.svg.

[12] Glenn F. Knoll. *Radiation Detection and Measurement*. en. John Wiley & Sons, Aug. 2010. ISBN: 978-0-470-13148-0.

[13] H. Bethe. «Zur Theorie Des Durchgangs Schneller Korpuskularstrahlen Durch Materie». In: *Annalen der Physik* 397.3 (1930), pp. 325–400. ISSN: 1521-3889. DOI: 10.1002/andp.19303970303.

[14] Д.Ильин. *The Klein-Nishina distribution of photon scattering angles over a range of energies.* CC0, via Wikimedia Commons. 2023. URL: https://upload.wikimedia.org/wikipedia/commons/8/8a/Klein-Nishina_distribution-en.svg.

[15] Joshua hykes. *Plot of the gamma macroscopic cross section of lead.* CC BY-SA 3.0, via Wikimedia Commons. 2011. URL: https://upload.wikimedia.org/wikipedia/commons/e/e2/Pb-gamma-xs.svg.

[16] Berklas. *Main attenuation effects of x-rays depending on energy and atomic number.* CC BY-SA 3.0, via Wikimedia Commons. 2010. URL: https://upload.wikimedia.org/wikipedia/commons/9/96/Xray-shielding.svg.

[17] G. Marcer et al. «Detailed Analysis of a Previously Uninvestigated Feature in Lanthanum Bromide Scintillation Crystals Intrinsic Background». In: *Nuclear Instruments and Methods in Physics Research Section A: Accelerators, Spectrometers, Detectors and Associated Equipment* 1047 (Feb. 2023), p. 167796. ISSN: 0168-9002. DOI: 10.1016/j.nima.2022.167796.

[18] Qwerty123uiop. *Schematic view of a photomultiplier coupled to a scintillator, illustrating detection of gamma rays.* CC BY-SA 3.0, via Wikimedia Commons. 2013. URL: https://upload.wikimedia.org/wikipedia/commons/e/e8/PhotoMultiplierTubeAndScintillator.svg.

[19] AllenMcC. *Neutron capture gamma spectrum of a radioactive Am-Be-source, measured with a scintillation detector.* CC BY-SA 3.0, via Wikimedia Commons. 2007. URL: https://upload.wikimedia.org/wikipedia/commons/f/f2/Am-Be-SourceSpectrum.jpg.

[20] M. Nocente et al. «Energy resolution of gamma-ray spectroscopy of JET plasmas with a $LaBr_3$ scintillator detector and digital data acquisition». In: *Review of Scientific Instruments* 81.10 (Oct. 2010), p. 10D321. ISSN: 0034-6748. DOI: 10.1063/1.3501386.

[21] M. Nocente et al. «Gamma-Ray Spectroscopy at MHz Counting Rates with a Compact LaBr3 Detector and Silicon Photomultipliers for Fusion Plasma Applications». In: *Review of Scientific Instruments* 87.11 (Aug. 2016), 11E714. ISSN: 0034-6748. DOI: 10.1063/1.4961073.

[22] M. Nocente et al. «High Resolution Gamma Ray Spectroscopy at MHz Counting Rates With $LaBr_3$ Scintillators for Fusion Plasma Applications». In: *IEEE Transactions on Nuclear Science* 60.2 (Apr. 2013), pp. 1408–1415. ISSN: 1558-1578. DOI: 10.1109/TNS.2013.2252189.

[23] E. V. D van Loef et al. «Scintillation properties of $LaBr_3$:Ce3+ crystals: fast, efficient and high-energy-resolution scintillators». In: *Nuclear Instruments and Methods in Physics Research Section A: Accelerators, Spectrometers, Detectors and Associated Equipment*. Proceedings of the 6th International Conference on Inorganic Scin tillators and their Use in Scientific and Industrial Applications 486.1 (June 21, 2002), pp. 254–258. ISSN: 0168-9002. DOI: 10.1016/S0168-9002(02)00712-X.

[24] D. Rigamonti et al. «Performance of the Prototype LaBr3 Spectrometer Developed for the JET Gamma-Ray Camera Upgrade». In: *The Review of Scientific Instruments* 87.11 (Nov. 2016), 11E717. ISSN: 1089-7623. DOI: 10.1063/1.4961060.

[25] M. Nocente et al. «A New Tangential Gamma-Ray Spectrometer for Fast Ion Measurements in Deuterium and Deuterium–Tritium Plasmas of the Joint European Torus». In: *Review of Scientific Instruments* 92.4 (Apr. 2021), p. 043537. ISSN: 0034-6748. DOI: 10.1063/5.0043806.

[26] A. Dal Molin et al. «A New Hard X-Ray Spectrometer for Runaway Electron Measurements in Tokamaks». In: *Measurement Science and Technology* 34.8 (May 2023), p. 085501. ISSN: 0957-0233. DOI: 10.1088/1361-6501/acd46c.

[27] C. Cazzaniga et al. «Response of LaBr3(Ce) scintillators to 2.5 MeV fusion neutrons». In: *Review of Scientific Instruments* 84.12 (Dec. 2013), p. 123505. ISSN: 0034-6748. DOI: 10.1063/1.4847056.

[28] C. Cazzaniga et al. «Response of LaBr3(Ce) scintillators to 14 MeV fusion neutrons». In: *Nuclear Instruments and Methods in Physics Research Section A: Accelerators, Spectrometers, Detectors and Associated Equipment* 778 (Apr. 2015), pp. 20–25. ISSN: 0168-9002. DOI: 10.1016/j.nima.2015.01.002.

[29] A. Dal Molin et al. «Measurement of the Gamma-Ray-to-Neutron Branching Ratio for the Deuterium-Tritium Reaction in Magnetic Confinement Fusion Plasmas». In: *Physical Review Letters* 133.5 (July 2024). Publisher: American Physical Society, p. 055102. DOI: 10.1103/PhysRevLett.133.055102.

[30] M. Rebai et al. «First direct measurement of the spectrum emitted by the $^3H(^2H,\gamma)^5He$ reaction and assessment of the relative yield γ_1 to γ_0». In: *Physical Review C* 110.1 (July 2024). Publisher: American Physical Society, p. 014625. DOI: 10.1103/PhysRevC.110.014625.

[31] G. Marcer et al. «Absolute measurement of the deuterium-tritium reaction gamma-ray emission in magnetic confinement fusion plasmas». In: *Nuclear Fusion* (2025). ISSN: 0029-5515. DOI: 10.1088/1741-4326/adeea7.

[32] J. Bielecki and A. Kurowski. «Neutron Diagnostics for Tokamak Plasma: From a Plasma Diagnostician Perspective». In: *Journal of Fusion Energy* 38.3 (Aug. 2019), pp. 386–393. ISSN: 1572-9591. DOI: 10.1007/s10894-018-0195-9.

[33] L. Bertalot et al. «Fusion Neutron Diagnostics on ITER Tokamak». In: *Journal of Instrumentation* 7.04 (Apr. 2012), p. C04012. ISSN: 1748-0221. DOI: 10.1088/1748-0221/7/04/C04012.

[34] D. B. Syme et al. «Fusion Yield Measurements on JET and Their Calibration». In: *Fusion Engineering and Design* 89.11 (Nov. 2014), pp. 2766–2775. ISSN: 0920-3796. DOI: 10.1016/j.fusengdes.2014.07.019.

[35] H. W. Hendel et al. «In Situ Calibration of TFTR Neutron Detectors». In: *Review of Scientific Instruments* 61.7 (July 1990), pp. 1900–1914. ISSN: 0034-6748. DOI: 10.1063/1.1141115.

[36] L. C. Johnson et al. «Cross Calibration of Neutron Detectors for Deuterium-tritium Operation in TFTR». In: *Review of Scientific Instruments* 66.1 (Jan. 1995), pp. 894–896. ISSN: 0034-6748. DOI: 10.1063/1.1146197.

[37] T. Nishitani et al. «Absolute Calibration of the JT-60U Neutron Monitors Using a 252Cf Neutron Source». In: *Review of Scientific Instruments* 63.11 (Nov. 1992), pp. 5270–5278. ISSN: 0034-6748. DOI: 10.1063/1.1143439.

[38] P. Batistoni et al. «14 MeV Calibration of JET Neutron Detectors—Phase 1: Calibration and Characterization of the Neutron Source». In: *Nuclear Fusion* 58.2 (Dec. 2017), p. 026012. ISSN: 0029-5515. DOI: 10.1088/1741-4326/aa98f6.

[39] L. Bertalot et al. «Calibration of the JET Neutron Activation System for DT Operation». In: *Review of Scientific Instruments* 70.1 (Jan. 1999), pp. 1137–1140. ISSN: 0034-6748. DOI: 10.1063/1.1149332.

[40] M. Hoek et al. «Neutron Yield Measurements by Use of Foil Activation at JT-60U». In: *Review of Scientific Instruments* 66.1 (Jan. 1995), pp. 885–887. ISSN: 0034-6748. DOI: 10.1063/1.1146527.

[41] O. N. Jarvis et al. «In-vessel Calibration of the JET Neutron Monitors Using a 252Cf Neutron Source: Difficulties Experienced». In: *Review of Scientific Instruments* 61.10 (Oct. 1990), pp. 3172–3174. ISSN: 0034-6748. DOI: 10.1063/1.1141677.

[42] P. Batistoni et al. «14 MeV Calibration of JET Neutron Detectors—Phase 2: In-Vessel Calibration». In: *Nuclear Fusion* 58.10 (Aug. 2018), p. 106016. ISSN: 0029-5515. DOI: 10.1088/1741-4326/aad4c1.

[43] H. Sjöstrand et al. «Fusion Power Measurement Using a Combined Neutron Spectrometer-Camera System at ITER». In: *AIP Conference Proceedings* 988.1 (Mar. 2008), pp. 319–322. ISSN: 0094-243X. DOI: 10.1063/1.2905090.

[44] J. E. Kammeraad et al. «Measurement of the Cross-Section Ratio $^{3}\mathrm{H}(\mathrm{d},\gamma)^{5}\mathrm{He}/^{3}\mathrm{H}(\mathrm{d},\alpha)\mathrm{n}$ at 100 keV». In: *Physical Review C* 47.1 (Jan. 1993), pp. 29–35. DOI: 10.1103/PhysRevC.47.29.

[45] Y. Kim et al. «D-T Gamma-to-Neutron Branching Ratio Determined from Inertial Confinement Fusion Plasmas». In: *Physics of Plasmas* 19.5 (May 2012), p. 056313. ISSN: 1070-664X, 1089-7674. DOI: 10.1063/1.4718291.

[46] F. Ajzenberg-Selove. «Energy levels of light nuclei A = 5-10». In: *Nuclear Physics A* 490.1 (Dec. 1988), pp. 1–225. ISSN: 0375-9474. DOI: 10.1016/0375-9474(88)90124-8.

[47] D. R. Tilley et al. «Energy Levels of Light Nuclei A=5, 6, 7». In: *Nuclear Physics A* 708.1 (Sept. 2002), pp. 3–163. ISSN: 0375-9474. DOI: 10.1016/S0375-9474(02)00597-3.

[48] A. M. Lane and R. G. Thomas. «R-Matrix Theory of Nuclear Reactions». In: *Reviews of Modern Physics* 30.2 (Apr. 1958). Publisher: American Physical Society, pp. 257–353. DOI: 10.1103/RevModPhys.30.257.

[49] A. Zohar et al. «Validation of realistic Monte Carlo plasma gamma-ray source on JET discharges». In: *Nuclear Fusion* 62.6 (Apr. 2022). Publisher: IOP Publishing, p. 066004. ISSN: 0029-5515. DOI: 10.1088/1741-4326/ac50c0.

[50] M. Nocente et al. «Fusion product measurements by nuclear diagnostics in the Joint European Torus deuterium–tritium 2 campaign (invited)». In: *Review of Scientific Instruments* 93.9 (Sept. 2022), p. 093520. ISSN: 0034-6748. DOI: 10.1063/5.0101767.

[51] D. Rigamonti et al. «Role of neutron attenuators for gamma-ray measurements in deuterium–tritium magnetic confinement plasmas». In: *Review of Scientific Instruments* 93.9 (Sept. 2022), p. 093515. ISSN: 0034-6748. DOI: 10.1063/5.0101783.

[52] A. J. Creely et al. «Overview of the SPARC tokamak». In: *Journal of Plasma Physics* 86.5 (Oct. 2020), p. 865860502. ISSN: 0022-3778, 1469-7807. DOI: 10.1017/S0022377820001257.

[53] P. Rodriguez-Fernandez et al. «Overview of the SPARC physics basis towards the exploration of burning-plasma regimes in high-field, compact tokamaks». In: *Nuclear Fusion* 62.4 (Mar. 2022). Publisher: IOP Publishing, p. 042003. ISSN: 0029-5515. DOI: 10.1088/1741-4326/ac1654.

[54] P. Raj et al. «Overview of the neutron diagnostic systems for the SPARC tokamak». In: *Review of Scientific Instruments* 95.10 (Oct. 2024), p. 103507. ISSN: 0034-6748. DOI: 10.1063/5.0219538.

[55] E. Andersson Sundén et al. «The Thin-Foil Magnetic Proton Recoil Neutron Spectrometer MPRu at JET». In: *Nuclear Instruments and Methods in Physics Research Section A: Accelerators, Spectrometers, Detectors and Associated Equipment* 610.3 (Nov. 2009), pp. 682–699. ISSN: 0168-9002. DOI: 10.1016/j.nima.2009.09.025.

[56] M. Tardocchi et al. «Ion Temperature and Plasma Rotation Profile Effects in the Neutron Emission Spectrum». In: *Review of Scientific Instruments* 75.3 (Mar. 2004), pp. 661–668. ISSN: 0034-6748, 1089-7623. DOI: 10.1063/1.1646733.

[57] M. Nocente et al. «High resolution gamma-ray spectrometer with MHz capabilities for runaway electron studies at ASDEX Upgrade». In: *Review of Scientific Instruments* 89.10 (Oct. 2018), p. 10I124. ISSN: 0034-6748. DOI: 10.1063/1.5036658.

[58] D. Rigamonti et al. «The upgraded JET gamma-ray cameras based on high resolution/high count rate compact spectrometers». In: *Review of Scientific Instruments* 89.10 (Oct. 2018), p. 10I116. ISSN: 0034-6748. DOI: 10.1063/1.5038839.

[59] M. Nocente. «Neutron and gamma-ray emission spectroscopy as fast ion diagnostics in fusion plasmas». eng. PhD thesis. Milano-Bicocca, Jan. 2012. URL: https://boa.unimib.it/handle/10281/28397 (visited on 10/16/2024).

[60] M. Nocente et al. «Conceptual design of the radial gamma ray spectrometers system for α particle and runaway electron measurements at ITER». In: *Nuclear Fusion* 57.7 (May 2017). Publisher: IOP Publishing, p. 076016. ISSN: 0029-5515. DOI: 10.1088/1741-4326/aa6f7d.

[61] A. Celora et al. «A multipurpose numerical method for imaging studies and tomographic reconstruction». In: *Journal of Instrumentation* 19.3 (Mar. 2024). Publisher: IOP Publishing, p. C03032. ISSN: 1748-0221. DOI: 10.1088/1748-0221/19/03/C03032.

[62] *cfs-energy/SPARCPublic*. Accessed on Oct 16, 2024. 2022. URL: https://github.com/cfs-energy/SPARCPublic.

[63] *FreeGS: Free Gyrokinetic Simulator*. https://github.com/freegs-plasma/freegs. Accessed: 2025-09-17. 2025.

[64] P. Rodriguez-Fernandez et al. «Predictions of core plasma performance for the SPARC tokamak». In: *Journal of Plasma Physics* 86.5 (Oct. 2020), p. 865860503. ISSN: 0022-3778, 1469-7807. DOI: 10.1017/S0022377820001075.

[65] G. Marcer. «A novel method for DT fusion power measurement in magnetic confinement plasmas based on the gamma ray emission from the $\mathrm{D(T,He)}\gamma$ reaction». Accepted: 2025-02-26T16:33:49Z, Publisher: Italy. PhD thesis. University of Milano-Bicocca, Feb. 2025. URL: https://boa.unimib.it/handle/10281/543003.

[66] I. N. Chugunov et al. «Testing the neutron attenuator based on ^6LiH for γ-ray diagnostics of plasmas in the JET tokamak». In: *Instruments and Experimental Techniques* 51.2 (Mar. 2008), pp. 166–170. ISSN: 1608-3180. DOI: 10.1134/S0020441208020024.

[67] *Monte Carlo N-particle*. URL: https://mcnp.lanl.gov/.

[68] A. Zohar et al. «Modelling of plasma gamma ray sources in large tokamaks». In: *Fusion Engineering and Design* 163 (Feb. 2021), p. 112158. ISSN: 0920-3796. DOI: 10.1016/j.fusengdes.2020.112158.

[69] G. Marcer et al. «Study of a single line of sight gamma ray diagnostics for measurements of the absolute gamma ray emission from JET». In: *Journal of Instrumentation* 16.12 (Dec. 2021), p. C12019. ISSN: 1748-0221. DOI: 10.1088/1748-0221/16/12/C12019.

[70] «X-Ray Mass Attenuation Coefficients». In: *NIST* (Sept. 2009). URL: https://www.nist.gov/pml/x-ray-mass-attenuation-coefficients.

[71] M. Nocente et al. «MeV range particle physics studies in tokamak plasmas using gamma-ray spectroscopy». In: *Plasma Physics and Controlled Fusion* 62.1 (Nov. 2019). Publisher: IOP Publishing, p. 014015. ISSN: 0741-3335. DOI: 10.1088/1361-6587/ab4f32.

[72] M. Nocente et al. «Generation and observation of fast deuterium ions and fusion-born alpha particles in JET D-^{3}He plasmas with the 3-ion radio-frequency heating scenario». In: *Nuclear Fusion* 60.12 (Oct. 2020). Publisher: IOP Publishing, p. 124006. ISSN: 0029-5515. DOI: 10.1088/1741-4326/abb95d.

[73] A. Shevelev et al. «Study of runaway electron dynamics at the ASDEX Upgrade tokamak during impurity injection using fast hard x-ray spectrometry». In: *Nuclear Fusion* 61.11 (Sept. 2021). Publisher: IOP Publishing, p. 116024. ISSN: 0029-5515. DOI: 10.1088/1741-4326/ac2638.

[74] T. Gray et al. *Divertor Component Testing*. Tech. rep. ORNL/SPR–2022/2536, 1993696, NFE-20-08060. July 2022, ORNL/SPR–2022/2536, 1993696, NFE–20–08060. DOI: 10.2172/1993696.

[75] G. L. Jackson et al. «Boronization in DIII-D». In: *Journal of Nuclear Materials*. Plasma-Surface Interactions in Controlled Fusion Devices 196-198 (Dec. 1992), pp. 236–240. ISSN: 0022-3115. DOI: 10.1016/S0022-3115(06)80038-3.

[76] U. Schneider et al. «Boronization of ASDEX». In: *Journal of Nuclear Materials* 176-177 (Dec. 1990), pp. 350–356. ISSN: 0022-3115. DOI: 10.1016/0022-3115(90)90071-T.

[77] Federico Scioscioli et al. «Design and Development Status of the ITER Radial Gamma Ray Spectrometer». In: *Fusion Engineering and Design* 221 (Dec. 2025), p. 115376. ISSN: 0920-3796. DOI: 10.1016/j.fusengdes.2025.115376.

[78] V. G. Kiptily. «Gamma-Ray Measurements of 10B(α,Pγ)13C Reaction for Alpha-Particle Diagnostics in Fusion Plasmas». In: *Fusion Engineering and Design* 215 (June 2025), p. 114959. ISSN: 0920-3796. DOI: 10.1016/j.fusengdes.2025.114959.

[79] V.G. Kiptily et al. «Escaping alpha-particle monitor for burning plasmas». In: *Nuclear Fusion* 58.8 (Aug. 2018), p. 082009. ISSN: 0029-5515, 1741-4326. DOI: 10.1088/1741-4326/aab676.

[80] Clemente Angioni. «Impurity Transport in Tokamak Plasmas, Theory, Modelling and Comparison with Experiments». In: *Plasma Physics and Controlled Fusion* 63.7 (May 2021), p. 073001. ISSN: 0741-3335. DOI: 10.1088/1361-6587/abfc9a.

[81] M. Salewski et al. «Energetic Particle Physics: Chapter 7 of the Special Issue: On the Path to Tokamak Burning Plasma Operation». In: *Nuclear Fusion* 65.4 (Mar. 2025), p. 043002. ISSN: 0029-5515. DOI: 10.1088/1741-4326/adb763.

[82] Ye. O. Kazakov et al. «Physics and applications of three-ion ICRF scenarios for fusion research». In: *Physics of Plasmas* 28.2 (Feb. 19, 2021), p. 020501. ISSN: 1070-664X. DOI: 10.1063/5.0021818.

[83] Ye.O. Kazakov et al. «Plasma Heating and Generation of Energetic D Ions with the 3-Ion ICRF + NBI Scenario in Mixed H-D Plasmas at JET-ILW». In: *Nuclear Fusion* 60.11 (Sept. 2020), p. 112013. ISSN: 0029-5515. DOI: 10.1088/1741-4326/ab9256.

[84] B.C.G. Reman et al. «Velocity-Space Tomography of an MeV Fast-Ion Tail Generated by Three-Ion Scheme ICRF Heating at JET». In: *Nuclear Fusion* 65.7 (June 2025), p. 076007. ISSN: 0029-5515. DOI: 10.1088/1741-4326/addb60.

[85] K. K. Kirov et al. «Synergistic ICRH and NBI heating for fast ion generation and maximising fusion rate in mixed plasmas at JET». In: *AIP Conference Proceedings* 2254.1 (Sept. 16, 2020), p. 030011. ISSN: 0094-243X. DOI: 10.1063/5.0014235.

[86] E. Panontin et al. «First spatially resolved measurements of the D–^{3}He α-particle source with the upgraded JET gamma-ray camera». en. In: *Review of Scientific Instruments* 92.5 (May 2021), p. 053529. ISSN: 0034-6748, 1089-7623. DOI: 10.1063/5.0043776.

[87] R. Felton et al. «Real-Time Measurement and Control at JET Experiment Control». In: *Fusion Engineering and Design*. Proceedings of the 23rd Symposium of Fusion Technology 74.1 (Nov. 2005), pp. 561–566. ISSN: 0920-3796. DOI: 10.1016/j.fusengdes.2005.06.286.

[88] G. Ericsson. «Advanced Neutron Spectroscopy in Fusion Research». en. In: *Journal of Fusion Energy* 38.3 (Aug. 2019), pp. 330–355. ISSN: 1572-9591. DOI: 10.1007/s10894-019-00213-9.

[89] M. Gatu Johnson et al. «The 2.5-MeV neutron time-of-flight spectrometer TOFOR for experiments at JET». In: *Nuclear Instruments and Methods in Physics Research Section A: Accelerators, Spectrometers, Detectors and Associated Equipment* 591.2 (June 2008), pp. 417–430. ISSN: 0168-9002. DOI: 10.1016/j.nima.2008.03.010.

[90] M. Gatu Johnson et al. «The TOFOR neutron spectrometer and its first use at JET». In: *Review of Scientific Instruments* 77.10 (Sept. 2006), 10E702. ISSN: 0034-6748. DOI: 10.1063/1.2219422.

[91] L. Giacomelli et al. «Advanced Neutron Diagnostics for JET and ITER Fusion Experiments». In: *Nuclear Fusion* 45.9 (Sept. 2005), p. 1191. ISSN: 0029-5515. DOI: 10.1088/0029-5515/45/9/019.

[92] A. S. Jacobsen et al. «Velocity-Space Sensitivities of Neutron Emission Spectrometers at the Tokamaks JET and ASDEX Upgrade in Deuterium Plasmas». In: *Review of Scientific Instruments* 88.7 (July 2017), p. 073506. ISSN: 0034-6748. DOI: 10.1063/1.4991651.

[93] M. Iliasova et al. «Gamma-Ray Measurements in D 3 He Fusion Plasma Experiments on JET». In: *Nuclear Instruments and Methods in Physics Research Section A: Accelerators, Spectrometers, Detectors and Associated Equipment* 1031 (May 2022), p. 166586. ISSN: 01689002. DOI: 10.1016/j.nima.2022.166586.

[94] V. Zoita et al. «Design of the JET Upgraded Gamma-Ray Cameras». In: *Fusion Engineering and Design*. Proceeding of the 25th Symposium on Fusion Technology 84.7 (June 2009), pp. 2052–2057. ISSN: 0920-3796. DOI: 10.1016/j.fusengdes.2008.11.026.

[95] V. G. Kiptily et al. «γ-ray diagnostics of energetic ions in JET». In: *Nuclear Fusion* 42.8 (Aug. 2002), p. 999. ISSN: 0029-5515. DOI: 10.1088/0029-5515/42/8/308.

[96] E Panontin. «Development of Nuclear Radiation Based Tomography Methods for Runaway Electrons and Fast Ions in Fusion Plasmas». PhD thesis. Milano: Milano-Bicocca, 2020. URL: https://boa.unimib.it/handle/10281/383194.

[97] Jan Mlynar et al. «Current Research into Applications of Tomography for Fusion Diagnostics». In: *Journal of Fusion Energy* 38.3 (Aug. 2019), pp. 458–466. ISSN: 1572-9591. DOI: 10.1007/s10894-018-0178-x.

[98] M. Salewski et al. «High-Definition Velocity-Space Tomography of Fast-Ion Dynamics». In: *Nuclear Fusion* 56.10 (Aug. 2016), p. 106024. ISSN: 0029-5515. DOI: 10.1088/0029-5515/56/10/106024.

[99] N. Belcari, M. G. Bisogni, and A. Del Guerra. «Positron Emission Tomography: Its 65 Years and Beyond». In: *La Rivista del Nuovo Cimento* 46.11 (Dec. 2023), pp. 693–785. ISSN: 1826-9850. DOI: 10.1007/s40766-024-00050-3.

[100] Thomas C. Kwee, Drew A. Torigian, and Abass Alavi. «Overview of Positron Emission Tomography, Hybrid Positron Emission Tomography Instrumentation, and Positron Emission Tomography Quantification». In: *Journal of Thoracic Imaging* 28.1 (Jan. 2013), p. 4. ISSN: 0883-5993. DOI: 10.1097/RTI.0b013e31827882d9.

[101] B. A. Grierson et al. «Orchestrating TRANSP Simulations for Interpretative and Predictive Tokamak Modeling with OMFIT». In: *Fusion Science and Technology* 73.2018 (Feb. 2018). ISSN: 1536-1055. DOI: 10.1080/15361055.2017.1398585.

[102] A. Y. Pankin et al. «TRANSP Integrated Modeling Code for Interpretive and Predictive Analysis of Tokamak Plasmas». In: *Computer Physics Communications* 312 (July 2025), p. 109611. ISSN: 0010-4655. DOI: 10.1016/j.cpc.2025.109611.

[103] PPPL. *TRANSP*. URL: https://transp.pppl.gov/.

[104] Ž. Štancar et al. «Overview of Interpretive Modelling of Fusion Performance in JET DTE2 Discharges with TRANSP». In: *Nuclear Fusion* 63.12 (Nov. 2023), p. 126058. ISSN: 0029-5515. DOI: 10.1088/1741-4326/ad0310.

[105] D. K. Yang et al. «Simulations of Neutral Beam Injection and Ion Cyclotron Resonance Heating Synergy in High Power EAST Scenarios». In: *Review of Scientific Instruments* 93.11 (Nov. 2022), p. 113501. ISSN: 0034-6748. DOI: 10.1063/5.0101645.

[106] L. Hägg et al. «Estimating the Neutron Yield in a Deuterium Plasma with the JET Neutron Camera». In: *Review of Scientific Instruments* 94.7 (July 2023), p. 073502. ISSN: 0034-6748. DOI: 10.1063/5.0144654.

[107] J Eriksson et al. «Finite Larmor radii effects in fast ion measurements with neutron emission spectrometry». In: *Plasma Physics and Controlled Fusion* 55.1 (Dec. 2012). Publisher: IOP Publishing, p. 015008. ISSN: 0741-3335. DOI: 10.1088/0741-3335/55/1/015008.

[108] M. Dalla Rosa. «Development of nuclear techniques for gamma-ray spectroscopy in thermonuclear plasmas». Master's thesis. Milano-Bicocca, 2023.

[109] Boris N. Breizman et al. «Physics of Runaway Electrons in Tokamaks». In: *Nuclear Fusion* 59.8 (June 2019), p. 083001. ISSN: 0029-5515. DOI: 10.1088/1741-4326/ab1822.

[110] B.N. Breizman and P.B. Aleynikov. «Kinetics of Relativistic Runaway Electrons». In: *Nuclear Fusion* 57.12 (Oct. 2017), p. 125002. ISSN: 0029-5515. DOI: 10.1088/1741-4326/aa8c3f.

[111] Laleh Ataeiseresht et al. «Runaway Electrons and Their Interaction with Tungsten Wall: A Comprehensive Study of Effects». In: *Scientific Reports* 13.1 (Dec. 2023), p. 21760. ISSN: 2045-2322. DOI: 10.1038/s41598-023-48672-7.

[112] H. -W. Bartels. «Impact of Runaway Electrons». In: *Fusion Engineering and Design* 23.4 (Jan. 1994), pp. 323–328. ISSN: 0920-3796. DOI: 10.1016/0920-3796(94)90016-7.

[113] T. Kawamura, H. Obayashi, and A. Miyahara. «On the Generation of Runaway Electrons and Their Impact to Plasma Facing Components». In: *Fusion Engineering and Design* 9 (Jan. 1989), pp. 39–44. ISSN: 0920-3796. DOI: 10.1016/S0920-3796(89)80007-9.

[114] T. Kunugi. «Effects of Runaway Electrons on Plasma Facing Components». In: *Fusion Engineering and Design* 23.4 (Jan. 1994), pp. 329–339. ISSN: 0920-3796. DOI: 10.1016/0920-3796(94)90017-5.

[115] Allen H. Boozer. «Runaway Electrons and ITER». In: *Nuclear Fusion* 57.5 (Mar. 2017), p. 056018. ISSN: 0029-5515. DOI: 10.1088/1741-4326/aa6355.

[116] R. Datta et al. «Coupled 2D MHD and Runaway Electron Fluid Simulations of SPARC Disruptions». In: *Physics of Plasmas* 32.8 (Aug. 2025), p. 082505. ISSN: 1070-664X. DOI: 10.1063/5.0272430.

[117] C. Liu. «Runaway Electrons in Tokamaks». PhD thesis. 2017. URL: https://dataspace.princeton.edu/handle/88435/dsp01ks65hf712.

[118] Becarlson. *Dynamic friction on a free electron in air as a function of energy, compared to an applied electric field. The runaway relativistic electron energy range is shown.* CC BY-SA 3.0, via Wikimedia Commons. 2011. URL: https://upload.wikimedia.org/wikipedia/commons/5/5d/Runaway_electron_dynamic_friction_in_air.svg.

[119] A. Fil et al. «Disruption Runaway Electron Generation and Mitigation in the Spherical Tokamak for Energy Production (STEP)». In: *Nuclear Fusion* 64 (Sept. 2024). DOI: 10.1088/1741-4326/ad73e9.

[120] V.A. Izzo et al. «Boundary Condition Effects on Runaway Electron Mitigation Coil Modeling for the SPARC and DIII-D Tokamaks». In: *Nuclear Fusion* 64.6 (Apr. 2024), p. 066003. ISSN: 0029-5515. DOI: 10.1088/1741-4326/ad3c52.

[121] F. Saint-Laurent et al. «Overview of Runaway Electron Control and Mitigation Experiments on Tore Supra and Lessons Learned in View of ITER». In: *Fusion Science and Technology* 64.4 (Nov. 2013), pp. 711–718. ISSN: 1536-1055. DOI: 10.13182/FST13-A24090.

[122] O. Vallhagen et al. «Runaway Electron Dynamics in ITER Disruptions with Shattered Pellet Injections». In: *Nuclear Fusion* 64.8 (June 2024), p. 086033. ISSN: 0029-5515. DOI: 10.1088/1741-4326/ad54d7.

[123] G Pautasso et al. «Disruption Mitigation by Injection of Small Quantities of Noble Gas in ASDEX Upgrade». In: *Plasma Physics and Controlled Fusion* 59.1 (Nov. 2016), p. 014046. ISSN: 0741-3335. DOI: 10.1088/0741-3335/59/1/014046.

[124] N. Commaux et al. «Demonstration of Rapid Shutdown Using Large Shattered Deuterium Pellet Injection in DIII-D». In: *Nuclear Fusion* 50.11 (Sept. 2010), p. 112001. ISSN: 0029-5515. DOI: 10.1088/0029-5515/50/11/112001.

[125] L.R. Baylor et al. «Disruption Mitigation System Developments and Design for ITER». In: *Fusion Science and Technology* 68.2 (Sept. 2015), pp. 211–215. ISSN: 1536-1055. DOI: 10.13182/FST14-926.

[126] M Gobbin et al. «Runaway Electron Mitigation by 3D Fields in the ASDEX-Upgrade Experiment». In: *Plasma Physics and Controlled Fusion* 60.1 (Nov. 2017), p. 014036. ISSN: 0741-3335. DOI: 10.1088/1361-6587/aa90c4.

[127] H. Bethe and W. Heitler. «On the stopping of fast particles and on the creation of positive electrons». In: *Proceedings of the Royal Society of London. Series A, Containing Papers of a Mathematical and Physical Character* 146.856 (Jan. 1997). Publisher: Royal Society, pp. 83–112. DOI: 10.1098/rspa.1934.0140.

[128] A. Dal Molin. «Reconstruction of the velocity space of runaway electrons by spectral measurements of the hard x-ray emission in tokamaks». eng. Accepted: 2021-02-23T11:46:39Z Publisher: Italy. PhD thesis. Milano-Bicocca, Feb. 2021. URL: https://boa.unimib.it/handle/10281/304289.

[129] E. Panontin et al. «Comparison of unfolding methods for the inference of runaway electron energy distribution from gamma-ray spectroscopic measurements». en. In: *Journal of Instrumentation* 16.12 (Dec. 2021). Publisher: IOP Publishing, p. C12005. ISSN: 1748-0221. DOI: 10.1088/1748-0221/16/12/C12005.

[130] F. Salvat et al. «Monte Carlo Simulation of Bremsstrahlung Emission by Electrons». In: *Radiation Physics and Chemistry*. Bremsstrahlung: Theory and Experiment 75.10 (Oct. 2006), pp. 1201–1219. ISSN: 0969-806X. DOI: 10.1016/j.radphyschem.2005.05.008.

[131] F. Salvat and J. M. Fernández-Varea. «Semiempirical Cross Sections for the Simulation of the Energy Loss of Electrons and Positrons in Matter». In: *Nuclear Instruments and Methods in Physics Research Section B: Beam Interactions with Materials and Atoms* 63.3 (Feb. 1992), pp. 255–269. ISSN: 0168-583X. DOI: 10.1016/0168-583X(92)95108-4.

Acknowledgements

I would like to express my sincere gratitude to my supervisor Massimo for his scientific guidance and continuous support throughout the PhD programme, and to Marco, as tutor, for his contribution to the development of this work.

I also acknowledge the colleagues of the Department of Physics at the University of Milano-Bicocca and of CNR–ISTP for their support, assistance, and for the stimulating scientific environment.

I gratefully acknowledge Eni and its representatives for funding my PhD fellowship, which made this research activity possible.

Finally, I thank all those who, directly or indirectly, contributed to the completion of this doctoral work through scientific collaborations, discussions, or personal support.

Fusion Engineering and Design 222 (2026) 115403

Contents lists available at ScienceDirect

Fusion Engineering and Design

journal homepage: www.elsevier.com/locate/fusengdes

Feasibility study of gamma-ray spectroscopy for the determination of the fusion power at the SPARC tokamak☆

Simone Lorenzo Fugazza [a], Giulia Marcer [b], Massimo Nocente [a,*], Alessandro Ciurlino [a], Gabriele Croci [a], Marco Dalla Rosa [a], Andrea Dal Molin [a], Erik Gallo [c], Giuseppe Gorini [a,b], Miriam Parisi [c], Prasoon Raj [d], Marica Rebai [b], Matthew Reinke [d], Davide Rigamonti [b], Federico Scioscioli [a,b], Marco Tardocchi [b], JET Contributors[1]

[a] Department of Physics - University of Milano Bicocca, Piazza della Scienza 3, Milan, 20126, Italy
[b] Institute for Plasma Science and Technology - National Research Council, Via Roberto Cozzi 53, Milan, 20125, Italy
[c] Eni S.p.A., Piazzale Enrico Mattei 1, Rome, 00144, Italy
[d] Commonwealth Fusion Systems, 117 Hospital Rd, Devens, 01434, MA, USA

ARTICLE INFO

Keywords:
Nuclear fusion
Tokamak
Gamma ray
Neutron
Diagnostics
SPARC
Fusion power

ABSTRACT

SPARC is a high-field, compact tokamak aiming to obtain a fusion gain Q>1 in Deuterium-Tritium (DT) plasmas for the first time in a magnetic confinement fusion reactor. Fusion power measurement is a key diagnostic requirement. In this work we present a scoping study of a gamma-ray spectrometer for the determination of the fusion power at SPARC. Measurements are based on the detection of the 16.7 MeV and ~ 14 MeV gamma-rays produced by the weak secondary channel $T(D,\gamma)^5He$ of the DT fusion reaction, whose branching ratio has been recently measured at the JET tokamak. Starting from the numerical calculation of the DT gamma source and a first evaluation of the sources of background radiation, we determine the fusion power range where measurements are possible at SPARC. We find that the fusion power can be determined in the broad range of 0.2 MW to 140 MW, when different neutron and gamma-ray attenuators are employed depending on the operational conditions. Potential additional applications of the gamma-ray detector scoped in this work are also briefly discussed.

1. Introduction

One of the primary objectives of nuclear fusion research is achieving a fusion gain Q > 1 in Deuterium-Tritium (DT) plasmas. This means that the fusion power produced exceeds the input power required to keep the plasma sufficiently hot. Tokamaks like ITER and SPARC must achieve this milestone to advance nuclear fusion commercialization.

A key factor in calculating Q is measuring the fusion power. In DT plasmas, absolute measurements of neutron yield are obtained using flux monitors cross-calibrated with activation foils. Although this method is well-established, it comes with challenges: significant MonteCarlo (MC) modelling of the machine is necessary, followed by extensive in-situ calibration campaigns. These procedures need to be repeated whenever modifications to the machine vessel are made [1].

An alternative method to measure the fusion power can leverage on measurements of the gamma-rays produced by the weak secondary channel $T(D,\gamma)^5He$ of the DT fusion reaction. When this occurs, the ^5He nucleus born from D+T fusion, rather than splitting into a neutron and an alpha particle, decays either to its ground or first excited state, leading to the emission of a gamma-ray with average energy 16.75 MeV (γ_0) or ~14 MeV (γ_1), respectively [2]. The feasibility of the method in a tokamak environment has been recently proven in DT experiments at the JET tokamak [3], where a value of $(2.4 \pm 0.5) \cdot 10^{-5}$ γ/n has been determined for the branching ratio of the de-excitation of the ^5He nucleus by gamma-ray emission with respect to the more common disintegration in a neutron and an alpha particle [4].

Although complicated by the need to handle the significant neutron and gamma-ray background that is produced together with the γ_0 and γ_1 emissions, one main advantage of the method is that it relies on modelling of gamma-ray (rather than neutron) transport in the tokamak, which is a comparatively much simpler task. Moreover, even in machines where the determination of the fusion power by neutron

☆ This article is part of a Special issue entitled: 'SOFT 2024' published in Fusion Engineering and Design.

* Corresponding author.
E-mail address: massimo.nocente@unimib.it (M. Nocente).

[1] See the author list of "C.F. Maggi et al 2024 Nucl. Fusion 64 112012 https://doi.org/10.1088/1741-4326/ad3e16"

https://doi.org/10.1016/j.fusengdes.2025.115403
Received 27 November 2024; Received in revised form 27 June 2025; Accepted 23 August 2025
Available online 12 September 2025

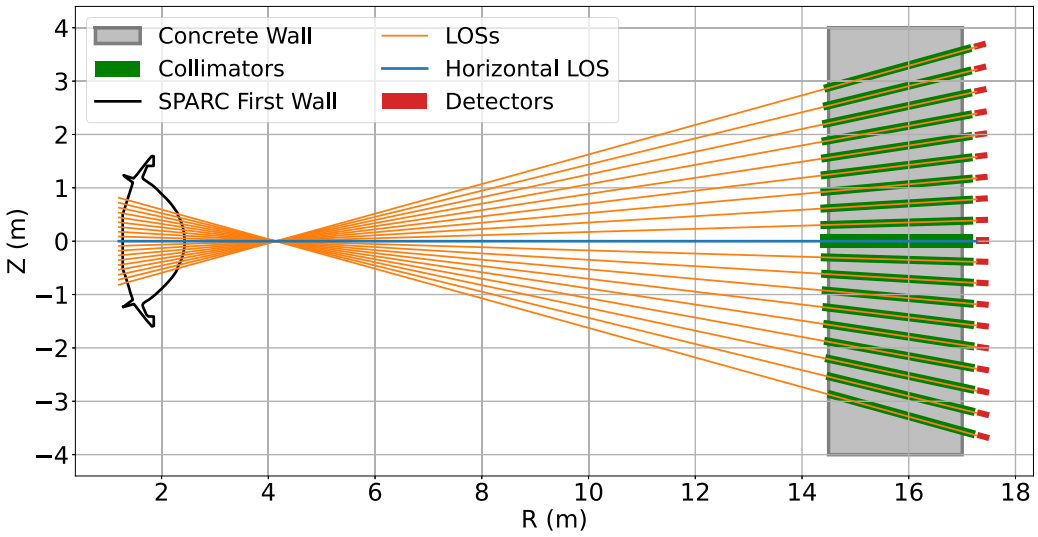

Fig. 1. A schematic of the SPARC neutron camera. A 2.4 m thick wall separates the Diagnostic Hall from the Tokamak Hall. 19 lines of sight (labelled "LOSs" in the figure) observe the plasma from a radial field of view. R and Z are the radial and vertical cylindrical coordinates, respectively, with the origin at the torus centre.

measurements remains the main method, measurements of the γ_0 and γ_1 emission are still valuable as an independent way to validate fusion power measurements by neutron diagnostics.

Building on the recent experimental progress described above, in this paper we present the scoping study of a gamma-ray detector designed for fusion power measurements at SPARC. SPARC is a compact ($R_0 = 1.85$ m) and high magnetic field ($B_0 \sim 12$ T) tokamak [5] currently being developed by Commonwealth Fusion Systems (CFS) which aims to demonstrate DT plasmas with Q > 1 for the first time in a tokamak.

The paper is organized as it follows. After the detector specification provided in Section 2, we describe the numerical evaluation of the signal and background sources in Section 3. The results are used to identify the fusion power range where measurements are feasible, depending on the set of neutron and gamma-ray attenuators that is used. We finally discuss the limitations of our method and briefly mention some other diagnostic applications [6] that the detector could contribute to, leaving their detailed exploration to future work.

2. A gamma ray detector for SPARC

We base our scoping study on the $LaBr_3$:Ce scintillator spectrometer, as this has been successfully used for the DT gamma measurements at the JET tokamak [7,8], and adopt the same dimensions (a cylinder of 3″ × 6″, diameter × length). The detector still represents the state of the art for gamma-ray spectroscopy in fusion plasmas, thanks to its short decay time (30 ns), enabling gamma-ray measurements at MHz counting rates [9,10], high photon yield (61/keV) [11], and energy resolution (3.8% at 662 keV) [12,13].

The SPARC facility will have a dedicated area for nuclear diagnostics, referred to as the Diagnostic Hall. This will be separated from the Tokamak Hall by a thick concrete wall, approximately 2.4 m thick. A Neutron CAMera (NCAM) with up to 19 channels is being designed, providing a set of radial views in the poloidal cross section. The separation distance between adjacent channels is about 40 cm at the detectors position ($R \gtrsim 17.0$ m, from the centre of the SPARC torus) and about 7 cm inside the plasma ($R = 1.85$ m).

In this scoping study, we assume that the gamma diagnostic can be placed along one of the NCAM lines of sight, at a distance $R > 17$ m. For example, the gamma diagnostics could be integrated with one of the planned NCAM spectrometers for neutron measurements along the NCAM channels, by placing the diagnostics behind the diamond detector. In this study we assume that collimators with a diameter $D = 1$ cm are expected for all channels, except for the central one, which has a diameter $D = 3$ cm [14]. Indeed, to compensate for the low efficiency of the magnetic proton recoil spectrometer planned for the central channel, a wider collimator is employed to ensure a sufficiently high neutron flux. Fig. 1 shows a schematic view of the NCAM.

3. Fusion power measurements at SPARC

3.1. Signal evaluation

To determine whether gamma-based fusion power measurements will be feasible in SPARC, we must first estimate the DT-gamma signal counting rate at the detector. We require that the fusion power is measured with at least 10% accuracy over a time scale of 1 s. Considering the Poisson statical nature of the measurement, this implies a minimum counting rate at the detector of 100 Hz. For comparison, a statistical accuracy of 1% would correspond to a counting rate of 10 kHz at the detector, which may be desired to counteract additional systematic uncertainties that may affect the measurement (see later).

In order to assess the feasibility of the measurement, we have evaluated the counting rate expected when the detector is positioned at the end of each channel of the NCAM. This was done by using the REVOLT [15] MC code for the numerical description of each line of sight in combination with GENESIS [16] for the evaluation of the neutron and gamma-ray radiation source due to the fusion reactions. Based on the geometrical input parameters for each line of sight, REVOLT determines the plasma region seen by the detector, dividing it into smaller volume pixels (voxels). For each voxel, the code evaluates the emission direction that the radiation must have to reach the detector, as well as the transport factor, which is proportional to the fraction of solid angle where the radiation must be emitted to reach the detector.

The evaluation of the DT-gamma emissivity source has been made with GENESIS, which makes use of the line of sight information provided by REVOLT to evaluate the radiation intensity (gamma/second) that reaches the front surface of the detector. Input parameters for GENESIS are the SPARC magnetic equilibrium (flux surfaces) and plasma profiles (temperature and density). It is further assumed that the fuel ions are in local thermal equilibrium, so that their distribution functions are described by a Maxwellian. In our calculations we have used magnetic and kinetic profiles for the Q = 11 scenario (corresponding to an expected fusion power of 140 MW) available in the paper [17]

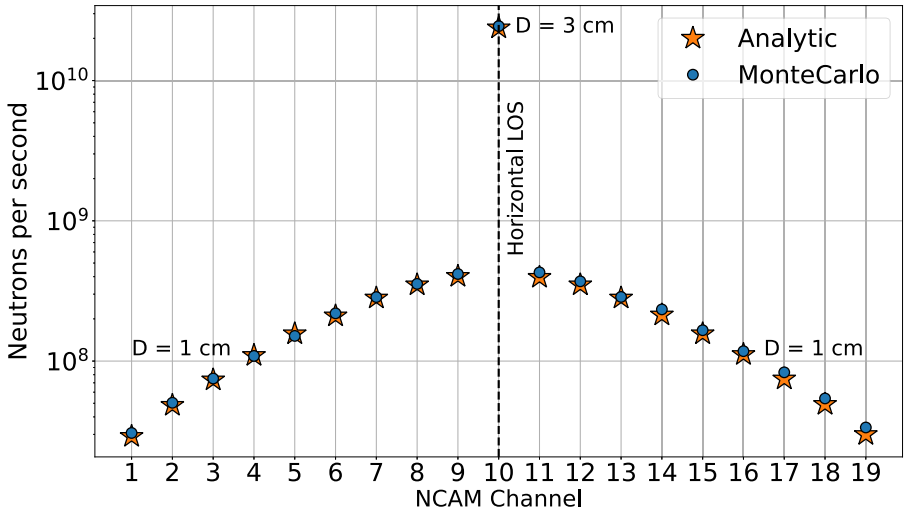

Fig. 2. MC (GENESIS+REVOLT) and semi-analytical results (Lynalitic) of the expected DT direct neutron rate for each detector in the NCAM. Notice that the highest rates are observed along the central horizontal channel (Channel #10), which views the plasma core and is equipped with a larger collimator. Channels from #1 to #19 have a collimator diameter D = 1 cm, except for Channel #10 with D = 3 cm.

Table 1
DT neutrons and gammas per second at the detector front surface calculated via GENESIS for SPARC NCAM Channel #9 (D = 1 cm) and #10 (D = 3 cm).

NCAM channel	DT-Neutrons (Hz)	DT-Gammas (Hz)
Channel#9	4.2 10^{8}	1.0 10^{4}
Channel#10	2.4 10^{10}	5.8 10^{5}

and in the SPARC GitHub open repository [18]. Signals for lower fusion power scenarios are obtained from those corresponding to 140 MW by linear down scaling.

Fig. 2 shows results on the neutron signal (neutron/s) expected at the front surface of each channel of the NCAM. Note that, primarily as a result of the collimator size, the intensity of the signal along the central channel (3 cm diameter) is rather different from that along all the others (1 cm diameter). As expressed in the following equation, adapted from [19]:

$$r_{n,\gamma} = \epsilon_{n,\gamma} \frac{\pi}{64} \left(\frac{d_D \, d_C}{L} \right)^2 \int_{\lambda} y_{n,\gamma}(s) \, ds \tag{1}$$

the neutron and gamma-ray rates are proportional to the square of both the detector diameter (d_D) and the collimator diameter (d_C). When the two diameters are approximately equal ($d = d_C \approx d_D$), the resulting signal scales as $\propto d^4$. The other terms in Eq. (1) include: $\epsilon_{n,\gamma}$, the full-energy peak efficiency of the detector; L, the length of the collimator; λ, the line of sight (assuming a narrow field of view); and $y(s)$, the neutron or gamma-ray emissivity along λ.

The corresponding gamma-ray signal is obtained by multiplying the neutron signal with the branching ratio and is reported in Table 1 for the most central channels.

The numerical calculations based on coupling GENESIS and REVOLT (indicated by circles in Fig. 2) have been bench-marked by independent semi-analytical calculations (stars). These have been based on the Linalytic code, as described in [20]. Linalytic, unlike GENESIS and REVOLT, combines analytical and numerical methods to calculate the transport factors. The two methods agree within 5% for the most peripheral channels and better than 1% for the central channel, which provides confidence on the validity of the calculations of the signal, particularly for the central channels.

3.2. Background sources

We now address the background sources that affect fusion power measurements using gamma spectrometry. One source comes from the direct neutrons produced by the main fusion reaction and which will reach the detector with the intensities shown in Fig. 2 and Table 1 if no dedicated neutron attenuator is used. Another source is due to prompt gamma-rays born from the interaction between the direct neutrons and the tokamak structures. This turns out to be the main limiting factor for fusion power measurements using gamma spectrometry, but it can be addressed by the use of dedicated gamma-ray attenuators of different length, determined depending on the operational range.

3.2.1. Direct neutron background

The $LaBr_3$:Ce detector is highly sensitive (efficiency ~1) to neutrons [21,22] implying that, without neutron attenuators, the detector would experience counting rates well in excess of 10 MHz. For comparison, fusion power measurements at the JET tokamak were shown to be possible for total counting rates <500 kHz [4], with pile-up and detector stability being the main limiting factors above this experimental counting rate threshold.

To counteract the background contribution from direct neutrons, we have to include a neutron attenuator in the SPARC detector application. Based on the experience at JET and successful tests at nuclear accelerators [23,24], this is a cylindrical sample of LiH with 1.2 m length and a diameter that matches that of the $LaBr_3$:Ce scintillator. Based on previous calculations [19], which have been recently benchmarked by measurements at JET, 1.2 m of LiH can attenuate 14.1 MeV neutrons by a factor of 10^6 and the high energy gamma-rays of interest for fusion power measurements by a factor 8 only.

Table 2 lists the neutron and gamma-ray intensities that may be observed at Channels #9 and #10 of the NCAM with and without the 1.2 m LiH attenuator for the Q = 11 scenario. We find that the intensity due to direct neutrons would always lead to a counting rate well in excess of 500 kHz if no LiH attenuator is used. Acceptable measurement conditions (statistical uncertainty in the range 1% to 10%) can be achieved both on channel #9 and #10 (central), although statistical uncertainties better than 1% can be achieved using channel #10 only. However, we here stress that these considerations do not take into account additional sources of background, such as that arising from prompt gamma-rays, as discussed in the next section. As far as the background contribution of scattered neutrons is concerned, based on the JET measurements this can be reduced to a few % by a well collimated line of sight, such as that designed for the SPARC NCAM, and it is therefore neglected in this scoping study.

Table 2
Intensities at the detector front surface for direct DT neutrons and DT gamma-rays with and without 1.2 m of LiH, calculated along Channels #9 and #10. In the "Comment" columns, intensities are marked as "Not acceptable" when in excess of 500 kHz; "Desired" when they lead to a statistical uncertainty better than 1%; "Acceptable" when leading to an uncertainty between 1% and 10%.

DT-Particle and attenuator	Intensities (Hz) at Ch#9	Comment (Ch#9)	Intensities (Hz) at Ch#10	Comment (Ch#10)
Neutron (no LiH)	4.2 10^{8}	Not acceptable	2.4 10^{10}	Not acceptable
Gamma (no LiH)	1.0 10^{4}	Desired	5.8 10^{5}	Not acceptable
Neutron + LiH	4.2 10^{2}	Acceptable	2.4 10^{4}	Acceptable
Gamma + LiH	1.0 10^{3}	Acceptable	5.8 10^{4}	Desired

3.2.2. Neutron-induced prompt gamma-ray background

Another important source of background comes from the prompt gamma-rays that originate from the interaction of neutrons with the tokamak structures, as observed at JET. The origin of this further contribution is due to the fact that the footprint of the line of sight intercepts the machine inboard first wall and the vacuum vessel. These structures are constantly impacted by the intense neutron emission from the plasma, leading to the production of prompt gamma-rays, with a fraction of them reaching the detector through the line of sight, as also verified by comprehensive MCNP [25] simulations for the JET case [26,27]. In absence of detailed Monte Carlo models of SPARC, we have developed an empirical method to estimate the prompt gamma-ray background at SPARC based on the JET data, as described below.

Assuming a known neutron flux F_n^{in} on the tokamak first wall, the outgoing F_γ^{out} prompt gamma-ray flux can be expressed as the product of a prompt gamma-ray emission probability P and F_n^{in}, i.e.

$$P = F_\gamma^{out} / F_n^{in} \tag{2}$$

Unlike F_γ^{out}, as fusion neutrons are all born with an energy of 14 MeV irrespective of the device, we surmise that P is independent of the intensity of the neutron source, but may have a dependence on the material composition of the tokamak structures.

For the JET case, we can use the data collected in fusion power measurement experiments by the Tangential Gamma Ray Spectrometer (TGRS) [7,20,28] diagnostic to evaluate P. The TGRS system [28] consists of a 3" × 6" $LaBr_3$:Ce detector with a LiH attenuator, characterized by a line of sight tangential to the inner wall and lying on the JET equatorial plane. The $LaBr_3$:Ce detector observes two sections of the wall (one at the inner and one at the outer wall) while passing twice through the plasma core.

From the JET experience with TGRS, we can establish that the majority of the gamma ray background is concentrated below 10 MeV. This fact suggests that, while prompt gamma-rays constitute an important radiation load for the detector, they interfere little within the spectral region associated with the γ_0 and γ_1 signals. If we interpret all the events in the spectral region below 10 MeV as primarily due to prompt gamma-rays, also considering that direct and scattered neutrons are almost fully suppressed by the use of LiH for the TGRS, we can estimate the gamma-ray flux at the locations of the first wall that are intersected by the line of sight, assuming only geometrical transport through the line of sight. This, combined with the evaluation of the neutron flux on the first wall from the known total neutron emission, leads to a prompt gamma-ray emission probability P.

The value of P was recently estimated from the analysis of 96 discharges of the DTE2 campaign at JET, resulting in $P = 4.7\%$ [20].

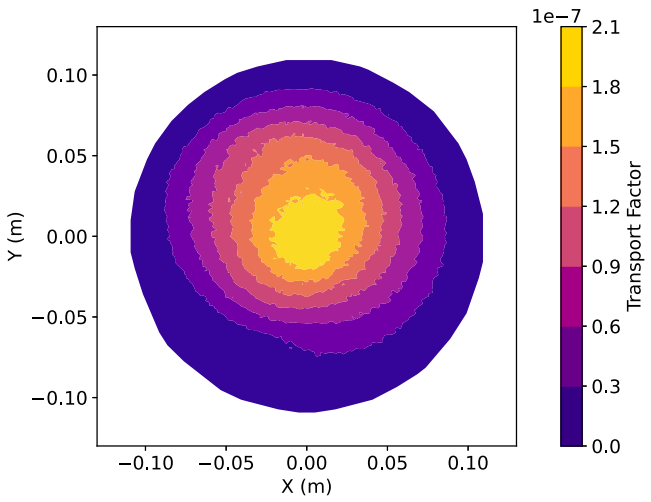

Fig. 3. Contour plot of the SPARC wall section observed frontally by the detector along the Channel #10 horizontal line of sight. The brightness corresponds to the transport factor of each pixel.

3.3. Gamma-ray spectrometer operational range

To determine the operational range for fusion power measurement using gamma spectrometry at SPARC, we must now evaluate the background that will be present together with the signal of Fig. 2. To do this, we assume that the detector is placed at a distance of 1.3 m behind the central channel of the NCAM to allow for some space that may be needed in an actual implementation of the diagnostics. Similar results in terms of fusion power operational range are obtained if the detector is placed right behind the central channel, although the background due to prompt gamma-ray emission is found to be roughly 2 times larger in such case. In order to evaluate the contribution of prompt gamma-rays to the background at the detector, we have used REVOLT to model the transport factors of the prompt gamma-rays emitted by the area of the first wall that is intercepted by the detector line of sight, with the results shown in Fig. 3.

The prompt gamma-ray source to which the transport factors of Fig. 3 are applied has been evaluated by multiplying the neutron flux on the first wall for the Q > 11 scenario of SPARC with the probability P obtained from the JET data. While P may be different in SPARC with respect to JET (and cannot currently be evaluated as we lack both a MCNP model and experimental data for SPARC) only an increase of P by more than an order of magnitude, which we deem unlikely, would eliminate the scope for fusion power measurements at SPARC. Calculation of background fluxes due to prompt gamma-rays have been made for all channels and added to those from the direct neutrons. The final result on the operational range for fusion power measurements is shown for channel #10 in Fig. 4. In this figure, the two horizontal lines represent the practical requirements for good measurements based on the JET experience, namely that the signal leads to a counting rate of at least 100 Hz and that the overall counting rate on the detector (signal+background) is below 500 kHz. The oblique lines show the expected signal and background level for different fusion power levels where, as noted above, calculations have been made using the kinetic and magnetic equilibrium profiles of the Q > 11 scenario and linearly down-scaled for lower fusion power levels. We find that, without additional gamma-ray attenuators, there is a fusion power window of about 1.8 orders of magnitudes, between 0.2 MW and up to 13.2 MW, where measurements are possible. We also note that, once the LiH neutron attenuator is in place, the prompt gamma-ray background becomes the main factor that sets the upper bound of the window for fusion power measurements by gamma-ray spectroscopy. For channels

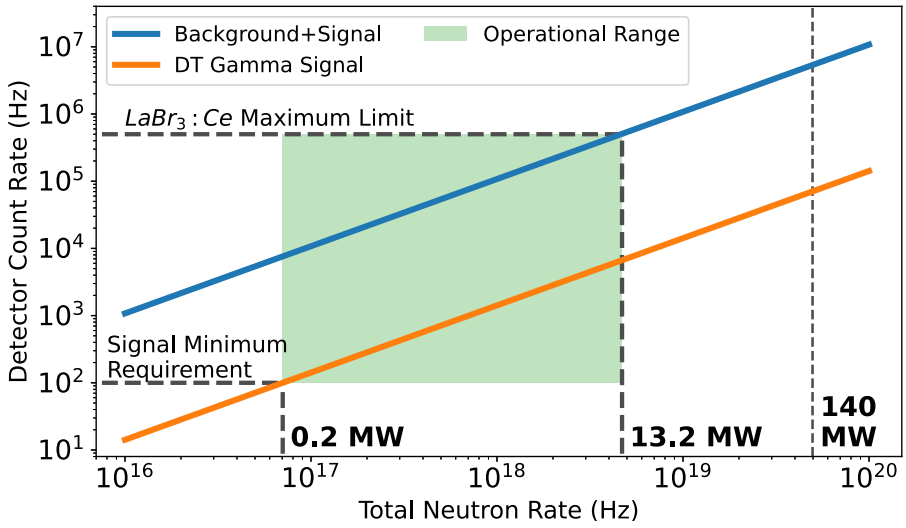

Fig. 4. Expected count rate at the $LaBr_3$:Ce detector (with a LiH attenuator) when placed along Channel #10 of the SPARC-NCAM. The horizontal lines indicate the practical requirements for good measurements, namely that the signal counting rate is at least 100 Hz and the overall counting rate does not exceed 500 kHz. The operational range for fusion power measurements is indicated by the green shaded area.

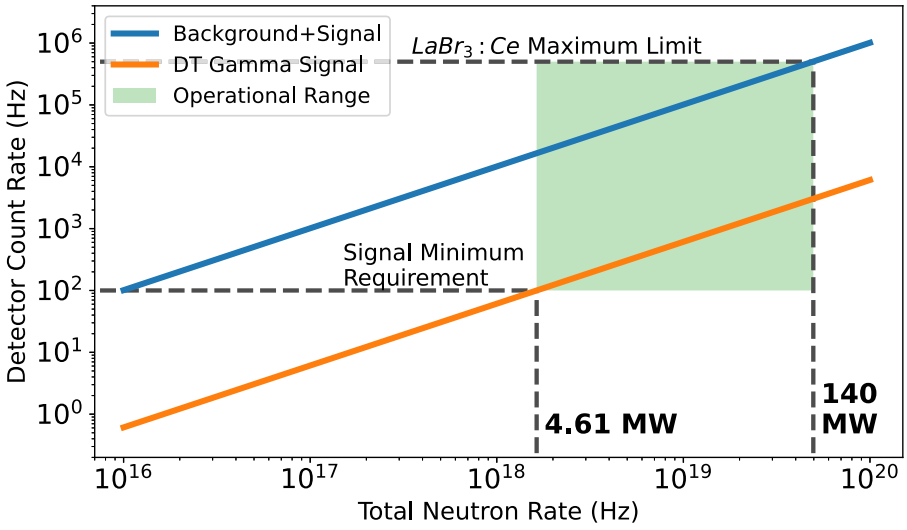

Fig. 5. Expected count rate at the $LaBr_3$:Ce detector (with a LiH neutron attenuator and a 3.0 cm tungsten attenuator) when placed along Channel #10 of the SPARC-NCAM. The horizontal lines indicate the practical requirements for good measurements, namely that the signal counting rate is at least 100 Hz and the overall counting rate does not exceed 500 kHz. The operational range for fusion power measurements is indicated by the green shaded area.

other than #10, due to their smaller diameter of 1 cm in the currently assumed NCAM design, the window for fusion power measurements has an extent that is less than a factor 2, which makes these channels impractical for this application.

While the results of Fig. 4 suggest that there is a relatively large window where fusion power measurements are possible at SPARC, provided that a sufficiently large collimator and a LiH neutron attenuator are used, it would be desirable to find ways to centre the fusion power measurement window at higher powers. This is possible by adding gamma-ray attenuators to the setup, such as tungsten.

Based on the Lambert–Beer law, the gamma-ray intensity $I(x)$, after travelling a distance x, is attenuated according to

$$I(x) = I_0 \exp(-\mu x) \tag{3}$$

where I_0 is the initial intensity and μ is an attenuation coefficient depending on both the material and the gamma ray energy. We have used the NIST database [29] to find the length l required for the tungsten attenuator to enable an upper boundary of 140 MW for the fusion power range, leading to $l = 3.0$ cm.

Fig. 5 illustrates the operational range of the $LaBr_3$:Ce detector for SPARC when a 3.0 cm tungsten attenuator is added to the 1.2 m LiH neutron attenuator. There is now a new measurement range that extends from ~5 MW up to the maximum projected fusion power, 140 MW. We note that, in the 140 MW scenario, DT-gamma count rates of about 3.04 kHz are expected, corresponding to a statistical uncertainty of 1.8%.

4. Discussion

The calculations presented in this paper suggest that there is scope for the development of a gamma-ray spectrometer for fusion power measurements at the SPARC tokamak. Their accuracy level is however not yet sufficient to proceed towards the actual development of the detector, as our findings are subject to some assumptions and limitations, which are discussed here.

One main limitation comes from the evaluation of the prompt gamma-ray background at SPARC. For this contribution, as described

in Section 3.2.2, we have used JET data to infer the emission probability P and used that for SPARC. As the exact value of P depends on the mix of materials used for the SPARC tokamak, which may be different than those of JET, it is likely that our evaluation of P comes with some systematic uncertainty, perhaps of a factor 2 or 3. The uncertainty on P for SPARC ultimately impacts the extent of the operational range where fusion power measurements are possible (see Fig. 5). For example, if P were larger by a factor of 2, the operational range would correspondingly be reduced by the same factor. However, as Figs. 4 and 5 show, fusion power measurements at SPARC seem to be possible over more than an order of magnitude. This suggests that the operational window would be null only if P were larger by more than a factor 10 than assumed here, which we deem unlikely. More generally, there is a need to better understand the neutron-induced reactions that lead to the background observed for the measurements at JET, for example by attempting to reproduce the observed spectral shape and intensity of the background using an MC model. In this way, materials that contribute the most to the background could be identified and a more detailed evaluation of the background at SPARC could be made, which is required to enable the actual development of the gamma-ray detector. Ultimately, the accurate evaluation of the background at SPARC would have to rely on an MCNP model, once sufficient knowledge on the most relevant processes that affected the background in the measurements at JET is gained.

Other aspects that require further study towards the development of an actual detector for SPARC are the neutron and gamma-ray attenuators. Concerning neutrons, our study has been based on the use of LiH, which has been tested at JET. However, there are some safety concerns which make LiH not ideal for use in a high performance tokamak. LiH is a hazardous material which undergoes violent exothermic reactions with water, even in the form of moist air. Additionally, even if properly sealed, it can release hydrogen at high temperature, leading to detonation. For this reason, we are presently seeking alternative attenuators that provide a similar, excellent neutron abatement factor, but pose less challenging safety hazards and are thus easier to integrate in a tokamak such as SPARC.

Concerning the gamma-ray attenuator, our evaluations have been based on the use of tungsten, as it can be easily manufactured and is widely available. The gamma-ray attenuation of tungsten is however higher for the signal ($I_0/I(l) \approx 23$ at the energies corresponding γ_0 and γ_1 emissions) than the background, which has an average energy of 4 MeV ($I_0/I(l) \approx 11$ at this energy). This is the reason why the operational window of Fig. 5 is reduced by about 2.5 with respect to that of Fig. 4. Ideally, one would like to find a gamma-ray attenuator that has a larger abatement factor at the gamma-ray energies of the background, which may be possible by studying the attenuation properties of other high Z materials than tungsten.

We further note that this study does not consider other factors that require a detailed evaluation for the actual development of the diagnostics, such as the detailed (i.e. not just geometrical) transport of both the signal and background gamma rays through ports and collimators.

The main motivation of this work has been to scope a gamma-ray spectrometer for fusion power measurements at SPARC, as this is a key parameter for a machine than aims at reliably producing plasmas with $Q > 1$ up to $Q > 11$. We however note that the same instrument could contribute to a broader range of physics studies, as demonstrated at JET [6]. Examples are the diagnostics of ions accelerated to the MeV range by radio-frequency [30,31], for example ^{3}He and protons in the planned hydrogen and ^{3}He minority scenarios [17,32], or the diagnostics of the runaway electron energies during the startup of the discharge or in dedicated experiments [10,33]. A highly desired capability for a gamma-ray detector in DT plasmas is the diagnostics of the fusion born alpha particles. Unlike JET, where alpha particle diagnostics by gamma-ray spectroscopy have been relying on reactions between the alpha particles and ^{9}Be impurities naturally present in the plasma due to the beryllium first wall, in SPARC, where the first wall will primarily be made of tungsten [32,34], different reactions would have to be relied on. A possibility could be to exploit the $^{10}\mathrm{B}(\alpha, \mathrm{p}\,\gamma)^{13}\mathrm{C}$ reaction [35], which leads to the generation of gamma-rays at the energies 3.09, 3.68 and 3.85 MeV. The boron impurities required for the reaction could either be injected on purpose using pellets, or could be available in the plasma as a legacy of the conditioning of the first wall using boron ("boronization") [36,37]. Unlike reactions with beryllium, the cross sections of $^{10}\mathrm{B}(\alpha, \mathrm{p}\,\gamma)^{13}\mathrm{C}$ are however not as well measured and there is currently no experimental demonstration on the use of such reactions to measure properties of the alpha particles. For example, the minimum amount of boron impurities required to measure a statistically meaningful signal is not known, as well as the overall spectral shape due to the combination of the three emission lines at 3.09, 3.68 and 3.85 MeV, convolved with the instrument response function. While we are currently performing first studies to establish the experimental basis for alpha particle measurements via the $^{10}\mathrm{B}(\alpha, \mathrm{p}\,\gamma)^{13}\mathrm{C}$ reaction in SPARC and elsewhere, we anticipate that the prompt gamma-ray background analysed in Section 3.2.2 will be a limiting factor. Such background may even have a more severe impact for this application, as the $^{10}\mathrm{B}(\alpha, \mathrm{p}\,\gamma)^{13}\mathrm{C}$ signal falls in the same spectral region of the background, which requires a careful evaluation.

5. Conclusion

A scoping study of a gamma ray detector to determine the fusion power at the SPARC tokamak has been made. Measurements are based on the detection of the 16.7 MeV and ≈14 MeV gamma-rays produced by the weak secondary channel $\mathrm{T(D,\gamma)^5He}$ of the DT fusion reaction, whose branching ratio has been recently measured at the JET tokamak. Based on the numerical calculation of the DT gamma source, and an estimation of the sources of background radiation due to neutrons and prompt gamma-rays, we find that there is an operational window of more than an order of magnitude where the fusion power can be determined, in the range of 0.2 MW to 13.2 MW if a 1.2 m LiH is used as the neutron attenuator, without gamma-ray attenuators. By the addition of tungsten attenuators with a variable length up to 3.0 cm, measurements over the full operational range 0.2 MW to 140 MW are deemed possible with a statistical accuracy of at least 10%, when the fusion power is provided every second. The background due to the emission of prompt gamma-rays that enter the line of sight and are due to neutrons interacting with the tokamak structures is identified as the main limiting factor for the measurement and needs to be better evaluated. Besides fusion power measurements, the detector could serve additional scopes, such as the diagnostics of runaway electrons, fast ions generated by radio-frequency heating or alpha particles born from the fusion reactions, which will be the subject of future studies.

CRediT authorship contribution statement

Simone Lorenzo Fugazza: Writing – review & editing, Writing – original draft, Visualization, Validation, Software, Formal analysis, Conceptualization. **Giulia Marcer:** Writing – review & editing, Visualization, Validation, Software, Formal analysis, Conceptualization. **Massimo Nocente:** Writing – review & editing, Writing – original draft, Visualization, Supervision, Methodology, Conceptualization. **Alessandro Ciurlino:** Formal analysis. **Gabriele Croci:** Conceptualization. **Marco Dalla Rosa:** Formal analysis. **Andrea Dal Molin:** Conceptualization. **Erik Gallo:** Funding acquisition, Conceptualization. **Giuseppe Gorini:** Supervision, Conceptualization. **Miriam Parisi:** Funding acquisition, Conceptualization. **Prasoon Raj:** Conceptualization. **Marica Rebai:** Conceptualization. **Matthew Reinke:** Conceptualization. **Davide Rigamonti:** Conceptualization. **Federico Scioscioli:** Conceptualization. **Marco Tardocchi:** Supervision, Project administration, Conceptualization.

Declaration of competing interest

The authors declare the following financial interests/personal relationships which may be considered as potential competing interests: Simone Lorenzo Fugazza reports financial support was provided by Eni SpA Marco Dalla Rosa reports financial support was provided by Eni SpA. If there are other authors, they declare that they have no known competing financial interests or personal relationships that could have appeared to influence the work reported in this paper.

Acknowledgements

This research was made possible through the support of Commonwealth Fusion Systems, USA and the funding provided by Eni SpA, Italy, which also supports the PhD scholarships of Simone Lorenzo Fugazza and Marco Dalla Rosa, Italy.

This work has been carried out within the framework of the EUROfusion Consortium, funded by the European Union via the Euratom Research and Training Programme (Grant Agreement No 101052200 - EUROfusion). Views and opinions expressed are however those of the author(s) only and do not necessarily reflect those of the European Union or the European Commission. Neither the European Union nor the European Commission can be held responsible for them.

Data availability

Data will be made available on request.

References

[1] D.B. Syme, et al., Fusion yield measurements on JET and their calibration, in: Nuclear Engineering and Design, Selected and Expanded Papers from International Conference Nuclear Energy for New Europe 2010, Portorož, Slovenia, September 6-9, 2010, vol. 246, (ISSN: 0029-5493) 2012, pp. 185–190, http://dx.doi.org/10.1016/j.nucengdes.2011.08.003.

[2] F. Ajzenberg-Selove, Energy levels of light nuclei A = 5–10, Nucl. Phys. A (ISSN: 0375-9474) 490 (1) (1988) 1–225, http://dx.doi.org/10.1016/0375-9474(88)90124-8.

[3] M. Rebai, et al., First direct measurement of the spectrum emitted by the ^{3}H(^{2}H, γ)^{5}He reaction and assessment of the relative yield γ_1 to γ_0, Phys. Rev. C 110 (1) (2024) 014625, http://dx.doi.org/10.1103/PhysRevC.110.014625, Publisher: American Physical Society.

[4] A. Dal Molin, et al., Measurement of the Gamma-Ray-to-Neutron branching ratio for the Deuterium-Tritium Reaction in magnetic confinement fusion plasmas, Phys. Rev. Lett. 133 (5) (2024) 055102, http://dx.doi.org/10.1103/PhysRevLett.133.055102, Publisher: American Physical Society.

[5] A.J. Creely, et al., Overview of the SPARC tokamak, J. Plasma Phys. 86 (5) (2020) 865860502, http://dx.doi.org/10.1017/S0022377820001257, ISSN: (1469) 0022-3778-7807.

[6] M. Nocente, et al., MeV range particle physics studies in tokamak plasmas using gamma-ray spectroscopy, Plasma Phys. Control. Fusion (ISSN: 0741-3335) 62 (1) (2019) 014015, http://dx.doi.org/10.1088/1361-6587/ab4f32, Publisher: IOP Publishing.

[7] M. Nocente, et al., A new tangential gamma-ray spectrometer for fast ion measurements in deuterium and deuterium–tritium plasmas of the joint european torus, Rev. Sci. Instrum. 92 (4) (2021).

[8] M. Nocente, et al., Fusion product measurements by nuclear diagnostics in the joint european torus deuterium–tritium 2 campaign, Rev. Sci. Instrum. 93 (9) (2022).

[9] M. Nocente, et al., High resolution gamma ray spectroscopy at MHz counting rates with $LaBr_3$ scintillators for fusion plasma applications, IEEE Trans. Nucl. Sci. 60 (2) (2013) 1408–1415.

[10] M. Nocente, et al., High resolution gamma-ray spectrometer with MHz capabilities for runaway electron studies at asdex upgrade, Rev. Sci. Instrum. 89 (10) (2018).

[11] E.V.D. van Loef, et al., Scintillation properties of $LaBr_3$:Ce3+ crystals: Fast, efficient and high energy-resolution scintillators, Nucl. Instrum. Methods Phys. Res. Sect. A: Accel. Spectrometers Detect. Assoc. Equip. (ISSN: 0168-9002) 486 (1) (2002) 254–258, http://dx.doi.org/10.1016/S0168-9002(02)00712-X, Proceedings of the 6th International Conference on Inorganic Scintillators and their Use in Scientific and Industrial Applications.

[12] M. Nocente, et al., Energy resolution of gamma-ray spectroscopy of JET plasmas with a $LaBr_3$ scintillator detector and digital data acquisition, Rev. Sci. Instrum. (ISSN: 0034-6748) 81 (10) (2010) 10D321, http://dx.doi.org/10.1063/1.3501386.

[13] D. Rigamonti, et al., The upgraded JET gamma-ray cameras based on high resolution/high count rate compact spectrometers, Rev. Sci. Instrum. (ISSN: 0034-6748) 89 (10) (2018) 10I116, http://dx.doi.org/10.1063/1.5038839.

[14] P. Raj, et al., Overview of the neutron diagnostic systems for the SPARC tokamak, Rev. Sci. Instrum. (ISSN: 0034-6748) 95 (10) (2024) 103507, http://dx.doi.org/10.1063/5.0219538.

[15] A. Celora, et al., A multipurpose numerical method for imaging studies and tomographic reconstruction, J. Inst. 19 (03) (2024) C03032, http://dx.doi.org/10.1088/1748-0221/19/03/C03032.

[16] M. Nocente, Neutron and Gamma-Ray Emission Spectroscopy As Fast Ion Diagnostics in Fusion Plasmas (Ph.D. dissertation), University of Milano-Bicocca, 2012, Available: https://boa.unimib.it/handle/10281/28397.

[17] P. Rodriguez-Fernandez, et al., Predictions of core plasma performance for the SPARC tokamak, J. Plasma Phys. 86 (5) (2020) 865860503, http://dx.doi.org/10.1017/S0022377820001075, ISSN: (1469) 0022-3778-7807.

[18] Cfs-energy/SPARCPublic, 2022, [Online]. Available: https://github.com/cfs-energy/SPARCPublic. (Accessed 16 October 2024).

[19] M. Nocente, et al., Conceptual design of the radial gamma ray spectrometers system for α particle and runaway electron measurements at ITER, Nucl. Fusion (ISSN: 0029-5515) 57 (7) (2017) 076016, http://dx.doi.org/10.1088/1741-4326/aa6f7d, Publisher: IOP Publishing.

[20] G. Marcer, A Novel Method for DT Fusion Power Measurement in Magnetic Confinement Plasmas Based on the Gamma Ray Emission from the D(T, ^{5}He)γ Reaction, University of Milano-Bicocca, 2025, Available: https://boa.unimib.it/handle/10281/543003.

[21] C. Cazzaniga, et al., Response of LaBr3(Ce) scintillators to 14 MeV fusion neutrons, Nucl. Instrum. Methods Phys. Res. Sect. A: Accel. Spectrometers Detect. Assoc. Equip. (ISSN: 0168-9002) 778 (2015) 20–25, http://dx.doi.org/10.1016/j.nima.2015.01.002.

[22] C. Cazzaniga, et al., Response of LaBr3(Ce) scintillators to 2.5 MeV fusion neutrons, Rev. Sci. Instrum. (ISSN: 0034-6748) 84 (12) (2013) 123505, http://dx.doi.org/10.1063/1.4847056.

[23] I.N. Chugunov, et al., Testing the neutron attenuator based on ^{6}LiH for γ-ray diagnostics of plasmas in the JET tokamak, Instrum. Exp. Tech. (ISSN: 1608-3180) 51 (2) (2008) 166–170, http://dx.doi.org/10.1134/S0020441208020024.

[24] D. Rigamonti, et al., Role of neutron attenuators for gamma-ray measurements in deuterium–tritium magnetic confinement plasmas, Rev. Sci. Instrum. (ISSN: 0034-6748) 93 (9) (2022) 093515, http://dx.doi.org/10.1063/5.0101783.

[25] Monte carlo n-particle, Online. Available: https://mcnp.lanl.gov/.

[26] A. Zohar, et al., Validation of realistic Monte Carlo plasma gamma-ray source on JET discharges, Nucl. Fusion (ISSN: 0029-5515) 62 (6) (2022) 066004, http://dx.doi.org/10.1088/1741-4326/ac50c0, Publisher: IOP Publishing.

[27] A. Zohar, et al., Modelling of plasma gamma ray sources in large tokamaks, Fusion Eng. Des. (ISSN: 0920-3796) 163 (2021) 112158, http://dx.doi.org/10.1016/j.fusengdes.2020.112158.

[28] G. Marcer, et al., Study of a single line of sight gamma ray diagnostics for measurements of the absolute gamma ray emission from JET, J. Instrum. (ISSN: 1748-0221) 16 (12) (2021) 012019, http://dx.doi.org/10.1088/1748-0221/16/12/C12019.

[29] X-Ray Mass Attenuation Coefficients, NIST, 2009, [Online]. Available: https://www.nist.gov/pml/x-ray-mass-attenuation-coefficients. (Last Modified: 2022-02-17T15:37-05:00).

[30] M. Nocente, et al., High-resolution gamma ray spectroscopy measurements of the fast ion energy distribution in JET 4 He plasmas, Nucl. Fusion (ISSN: 0029-5515) 52 (6) (2012) 063009, http://dx.doi.org/10.1088/0029-5515/52/6/063009, Publisher: IOP Publishing and International Atomic Energy Agency.

[31] M. Nocente, et al., Generation and observation of fast deuterium ions and fusion-born alpha particles in jet plasmas with the 3-ion radio-frequency heating scenario, Nucl. Fusion 60 (12) (2020) 124006.

[32] P. Rodriguez-Fernandez, et al., Overview of the SPARC physics basis towards the exploration of burning-plasma regimes in high-field, compact tokamaks, Nucl. Fusion (ISSN: 0029-5515) 62 (4) (2022) 042003, http://dx.doi.org/10.1088/1741-4326/ac1654, Publisher: IOP Publishing.

[33] A. Shevelev, et al., Study of runaway electron dynamics at the asdex upgrade tokamak during impurity injection using fast hard x-ray spectrometry, Nucl. Fusion 61 (11) (2021) 116024.

[34] T. Gray, et al., Divertor Component Testing, Tech. Rep. ORNL/SPR–2022/2536, 1993696, NFE-20-08060, 2022, http://dx.doi.org/10.2172/1993696, ORNL/SPR–2022/2536, 1993696, NFE–20–08 060.

[35] V. Kiptily, et al., Escaping alpha-particle monitor for burning plasmas, Nucl. Fusion 58 (8) (2018) 082009, http://dx.doi.org/10.1088/1741-4326/aab676, ISSN: (1741) 0029-5515-4326.

[36] G.L. Jackson, et al., Boronization in DIII-d, J. Nucl. Mater. Plasma-Surface Interact. Control. Fusion Devices (ISSN: 0022-3115) 196–198 (1992) 236–240, http://dx.doi.org/10.1016/S0022-3115(06)80038-3.

[37] U. Schneider, et al., Boronization of ASDEX, J. Nucl. Mater. (ISSN: 0022-3115) 176–177 (1990) 350–356, http://dx.doi.org/10.1016/0022-3115(90)90071-T.

Plasma Physics and Controlled Fusion

Crossmark

RECEIVED
22 Oct 2025

REVISED
8 Dec 2025

PAPER

Validation of TRANSP simulations of the fast deuterium beam distribution in D–^{3}He plasmas from (D)–(D_{NBI})–(^{3}He) three–ion scheme experiments at JET

Simone Lorenzo Fugazza[1,*], Marco Dalla Rosa[1], Enrico Panontin[2], Andrea Dal Molin[3], Jacob Eriksson[4], Giuseppe Gorini[1,3], Yevgen Kazakov[5], Vasily Kiptily[6], Michal Poradzinski[7], John Rice[2], Davide Rigamonti[3], Mirko Salewski[8], Žiga Štancar[6], Marco Tardocchi[3], Massimo Nocente[1], JET Contributors[a] and EUROfusion Tokamak Exploitation Team[b]

[1]University of Milano Bicocca, Department of Physics, Milan, Italy [2]Massachusetts Institute of Technology, Plasma Science and Fusion Center, Cambridge MA, USA [3]National Research Council, Institute for Plasma Science and Technology, Milan, Italy [4]Uppsala University, Department of Physics and Astronomy, Uppsala, Sweden [5]Laboratory for Plasma Physics – ERM/KMS, Brussels, Belgium [6]United Kingdom Atomic Energy Authority, Culham Science Centre, Abingdon, UK [7]Institute of Plasma Physics and Laser Microfusion, Warsaw, Poland [8]Technical University of Denmark, Department of Physics, Lyngby, Denmark [a]See the author list of "C.F. Maggi et al 2024 Nucl. Fusion 64 112012 https://doi.org/10.1088/1741-4326/ad3e16" [b]See the author list of "E. Joffrin et al 2024 Nucl. Fusion 64 112019 https://doi.org/10.1088/1741-4326/ad2be4" *Author to whom any correspondence should be addressed.

E-mail: s.fugazza2@campus.unimib.it

Keywords: JET Tokamak, Gamma-ray, Diagnostics, TRANSP simulations, Alpha particles, Deuterium–Helium-3, Three-ion scheme

Abstract

At JET, Deuterium–Helium-3 (D–^{3}He) experiments using ion cyclotron resonance heating (ICRH) with the three–ion scheme were conducted, involving thermal Deuterium (D), thermal Helium-3 (^{3}He), and a fast D beam injected via Neutral Beam Injection (NBI) and further heated using ICRH.

In these plasmas, intense neutron emission at the level of $\approx 10^{16}$ n/s was observed, and a non-thermal neutron spectrum was measured with the JET time of flight neutron spectrometer. Furthermore, the spatial profile of ≈ 16.4 MeV gamma rays originating from the ^{3}He(D,γ)^{5}Li reaction was observed. This is a weak branch ($\approx 10^{-5}$ relative probability) of the more common ^{3}He(D,p)α reaction and it can be used to assess the production of alpha particles in these experiments.

In this work we analyse a set of data from nuclear diagnostics in D–D_{NBI}–^{3}He experiments at JET and compare them with synthetic diagnostics based on TRANSP simulations of the fast deuterium distribution function, using the so-called "kick operator" to model power transfer from the wave to the beam fast deuterons. The neutron rate predicted by the TRANSP simulations broadly agrees with data measured with fission chambers. The shape of the neutron emission spectrum is also well understood, once finite Larmor radius effects are introduced into calculations.

Data from the gamma ray camera are used to infer the alpha birth profile through tomographic reconstructions based on the TREVISO code. These were compared with corresponding calculations starting from TRANSP results and showing an overall good agreement with the experimental tomographies. The validated TRANSP results are finally used to discuss the modifications of the fast deuterium distribution function and of the alpha birth profile in a set of discharges.

1 Introduction

The investigation of alpha particles represents one of the most challenging aspects of diagnostics in tokamaks. [1] For energy production, the most promising fusion reaction is the Deuterium-Tritium (DT) reaction, where an alpha particle (in addition to a neutron) is produced, which is anticipated

to be the dominant source of heating in burning plasma. [2, 3] Due to their positive charge, alpha particles are confined by strong magnetic fields and cannot escape the plasma. The detection of confined alpha particles is particularly difficult, as opposed to the lost alpha particles, which can be detected outside the plasma. In addition, alpha measurements in DT plasmas are particularly challenging due to the intense neutron background. [4] This fact suggests the need to look for another method to study alphas.

An important source of alpha particles has been achieved at JET through Deuterium—Helium-3 (D–^{3}He) plasmas, during dedicated experiments known as the "Three-Ion Scheme" [5, 6, 7, 8]. In the scheme analysed in the present manuscript, the plasma is made of deuterium and ^{3}He, at relative concentrations of 50% and 25%, respectively. The fast ion source comes from Neutral Beam Injection (NBI) of deuterium that absorbs most of the power injected by Ion Cyclotron Resonance Heating (ICRH) when the wave frequency is set to match the Doppler shifted ion cyclotron frequency of the deuterium beam in the plasma core. [9] These conditions result in a strong alpha and neutron emission produced by ^{3}He(D,p)α and D(D,n)^{3}He reactions, respectively, with total neutron rates in the range of $\sim 1 \cdot 10^{16}$ n/s. This emission is expected to be localised in the plasma core and to be significantly lower in the outer regions. [10] This localised and intense alpha source provides a unique opportunity to test alpha diagnostics.

Experimental evidence of the interaction among the three ion species (thermal Deuterium, thermal Helium-3 and the fast Deuterium population) has been obtained at JET. The Gamma Camera Upgrade [11, 12], equipped with $LaBr_3$:Ce scintillators [13, 14, 15], detects the 16.4 MeV gamma emission from the ^{3}He(D,γ)^{5}Li reaction. [16, 17, 18] Information about alpha particles born from ^{3}He(D,p)α reactions can be inferred from the 16.4 MeV gamma-ray measurements, as previously performed in Ref. [10]. Simultaneously, the TOFOR neutron spectrometer measures neutrons from the D(D,n)^{3}He reaction.[19, 20] In both diagnostics, the fast deuterium plays a key role in determining the shape and features of gamma and neutron spectra.

These diagnostics provide experimental data from which information on the spatial and energy distribution of alpha particles can be extracted. In parallel, simulations with the TRANSP code [21, 22, 23] can be used to predict emission spectra in three–ion scheme scenarios, thereby enhancing our understanding of the underlying physics processes and thus of the alpha emissivity.

The aim of this work was to validate the TRANSP simulations against experimental TOFOR neutron spectra and Gamma Camera data, from a set of discharges during three–ion scheme experiments. First, we compared the time evolution of the total neutron rate predicted by TRANSP with experimental measurements. Second, we compared neutron time-of-flight spectra measured using TOFOR with synthetic spectra computed from the fast deuterium distribution retrieved by TRANSP. Third, we analysed the spatial poloidal profiles of alpha emissivity, both experimental (reconstructed from Gamma Camera data) and synthetic (calculated from TRANSP outputs). A tomographic reconstruction was then performed using the TREVISO code [24], which implements an iterative inversion algorithm based on the Maximum Likelihood–Expectation Maximization method.

The paper is organized as follows. Section 2 describes the JET instruments (TOFOR and Gamma Camera) used to collect the experimental data. Section 3 presents the three-ion scheme discharges. The analysis method is outlined in Section 4, including the TRANSP simulations under investigation, the procedure to generate synthetic TOFOR neutron spectra, the approach used to derive Gamma Camera profiles from both experimental and simulated data, and the tomographic method for reconstructing the alpha birth profile. The results are presented in Section 5, while their discussion is provided in Section 6.

2 Instrumentation

2.1 The Time-of-Flight Neutron Spectrometer at JET

In three-ions scheme experiments, a significant amount of deuterium is present in the plasma, enabling D(D,n)^{3}He fusion reactions. These produce neutrons with a characteristic energy of approximately 2.5 MeV. In the idealized case of cold deuterium (i.e. negligible kinetic energy), the neutron emission spectrum would be monoenergetic. However, heating mechanisms such as Thermal, NBI, and ICRH introduce distinctive features in the neutron spectrum, which can be detected by dedicated diagnostics [25, 26, 27].

TOFOR is a neutron time-of-flight (TOF) spectrometer at JET, optimized for the detection of DD neutrons with energies around 2.5 MeV [19, 20]. It measures the neutron TOF across a known distance, which is related to the neutron energy via the instrumental response function [28]. For

TOFOR, the most likely response is described by:

$$E_n = \frac{2m_n R^2}{\mathrm{TOF}^2} \tag{1}$$

where E_n is the neutron energy, m_n is the neutron mass, and $R = 705$ mm is the radius of the constant-TOF sphere (a fixed geometric parameter of TOFOR). Longer TOF values correspond to lower neutron energies, and vice versa.

TOFOR was designed to achieve an optimal compromise among performance parameters for DD neutron measurements: an energy resolution of $\Delta E_n/E_n = 5.8\%$, a geometrical efficiency $\epsilon = 0.12$ cm^2, and a count rate $C_n = 300$ kHz, corresponding to a maximum neutron flux of 3×10^6 n s^{-1} cm^{-2} incident on the entrance detector.

In TOF space, the DD neutron peak (2.5 MeV) typically appears around 65 ns. A narrow peak indicates monoenergetic or thermal emission, while broader spectra are observed when ~ 100 keV NBI ions dominate. In three-ion scheme experiments, spectra are significantly broader and have a non-trivial shape, suggesting a strong contribution to the neutron emission from the fast deuterium population, which dominates both the spectral structure and intensity.

2.2 The Gamma Camera Upgrade at JET

Figure 1 shows a schematic of the Gamma Camera Upgrade at JET [11, 12]. The system comprises 19 channels, 10 horizontal and 9 vertical lines of sight, intersecting in a poloidal plane near the first octant of the JET vessel. Each line of sight is equipped with a 1"×2/3" $LaBr_3$:Ce scintillator [29], enabling gamma-ray spectroscopy.

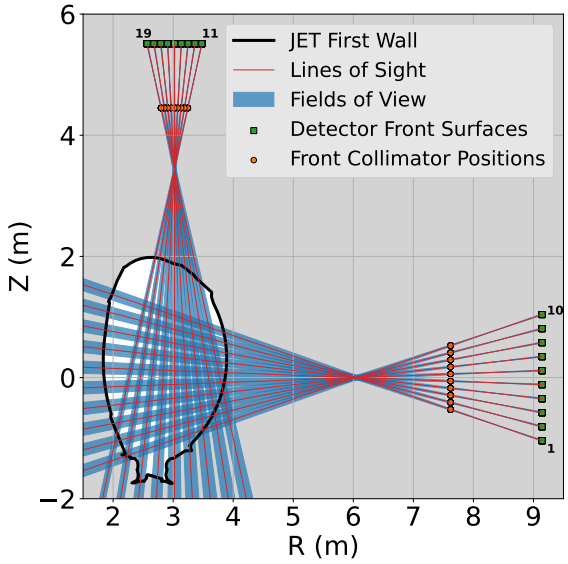

Figure 1: The Gamma Camera Upgrade at JET. The diagnostic consists of 19 channels (9 vertical and 10 horizontal intersecting lines of sight) viewing a poloidal cross-section of the plasma near the first octant. Each channel is equipped with a 1"×2/3" $LaBr_3$:Ce detector, providing spectroscopic capabilities.

The Gamma Camera diagnostic system can be used to detect gamma-ray emission from the ^{3}He(D,γ)^{5}Li reaction [17, 10]. This is a rare branch of the D–^{3}He fusion reaction that emits a 16.4 MeV photon instead of an alpha particle, with a branching ratio BR $\sim 10^{-5}$ γ/α. [30]

Observing the spatial distribution of this emission allows us to infer the birth profile of fusion-born alpha particles, and a substantial contribution from fast deuterium is expected in determining this profile. As already stated, the 16.4 MeV gamma-ray emission originates from the D–^{3}He reaction, which also produces alpha particles. If the gamma-per-alpha branching ratio of the D–^{3}He reaction is assumed to remain approximately constant, then the gamma-ray spatial profile directly reflects the alpha-particle birth profile. A similar approach was previously adopted in Ref. [10]. Ref. [17] indeed reports that the gamma-per-alpha branching ratio remains nearly constant at $\sim 2.5\ 10^{-5}$ for deuteron energies between 300 and 600 keV, and there is then an almost linear increase up to $\sim 4.5\ 10^{-5}$ at 900 keV. For the discharges analysed in this paper, we have evaluated that the mean energy of the deuterons that contribute to alpha particle production,

weighted by the fusion reactivity, is below 600 keV in most cases and up to 650 keV in all cases. Hence, it is expected that the increase of the branching ratio reported in Ref. [17] will have little impact on the reconstruction of the alpha particle profile from gamma-ray measurements, which is the focus of this paper. There may be some impact on the determination of the overall absolute alpha particle production rate from measurements, which is however out of the scope of this paper and will be addressed in a separate study.

3 Description of discharges

This study analyses seven JET discharges (95671, 95672, 95673, 95679, 95680, 95683, 95684) performed under similar experimental conditions. These shots are part of the three–ion scheme experiments, characterised by the presence of three ion species in the plasma: thermal deuterium, thermal helium-3, and a fast deuterium population [5, 6]. The fast deuterium is initially injected via NBI at approximately 100 keV and subsequently accelerated through ICRH, reaching energies up to 1–2 MeV. A schematic overview of the heating scheme is shown in Figure 2.

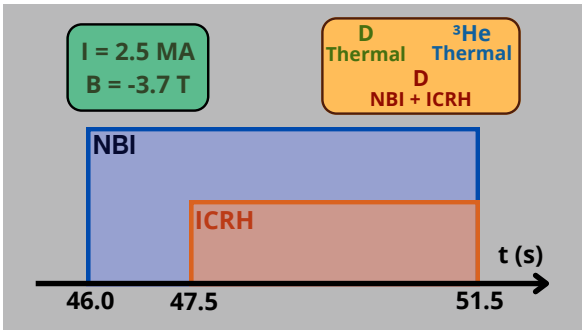

Figure 2: Schematic of the auxiliary heating waveforms in a typical three-ions scheme discharge.

All discharges were operated with a plasma current of 2.5 MA and a toroidal magnetic field of -3.7 T. The electron density at the plasma core is around 1.0×10^{20} m^{-3}, and the ^{3}He concentration varies between 18% and 28%, according to data from the real-time experiment central control (RTCC) system [31]. The electron temperature typically ranges from 1 to 10 keV. The discharge is initially heated by NBI and there is a phase of a few seconds where ICRH is also applied. This is when the three–ion scheme is established and most of neutron and gamma-ray emission is observed. In most cases, the NBI power exceeds the ICRH power by a factor of 2–3, except for discharges 95673 and 95684. NBI power ranges from 3.1 to 18.6 MW, while ICRH power varies from 2.1 to 6.1 MW. Across all discharges, the neutron rate reaches values of the order of some 10^{15} n/s, up to about 10^{16} n/s.

An example of the actual waveforms for discharge #95671 is shown in Figure 3.

4 Analysis Method

4.1 TRANSP simulations

The TRANSP code [21, 22, 23] has been developed to simulate particle and energy transport in tokamak plasmas. In this study, it is used to model the time evolution of the total neutron rate and the fast deuterium distribution during each discharge.

For each pulse, a TRANSP simulation was performed in an iterative manner. Measured plasma parameters, such as the magnetic equilibrium, the profiles of density, temperature, effective ion charge and bolometry, where used as input. The simulations further used the actual heating profile of NBI and ICRH. As in other analyses of radio-frequency heating scenario, the TORIC code was used within TRANSP to simulate wave absorption. A "kick operator" [32] was active to calculate the power transfer from the wave to the beam ions and their acceleration to higher energies. The exact impurity content at JET, mainly Beryllium and Nickel, is uncertain, as is the value of ^{3}He concentration, which is estimated at about 20% of the ion density in these discharges. For this reason, these parameters were varied in a number of iterations (namely, TRANSP runs) until a reasonable agreement between the measured and simulated neutron rate and plasma stored energy was achieved. In the discharges analysed here, neutron emission is due to reaction among thermal ions (thermal component), fast ions and thermal ions (beam-target component) and fast ions among themselves (beam-beam component).

For each discharge, the timestamp at which the simulated neutron rate best matches the experimental measurement is identified. The corresponding fast deuterium distribution is then

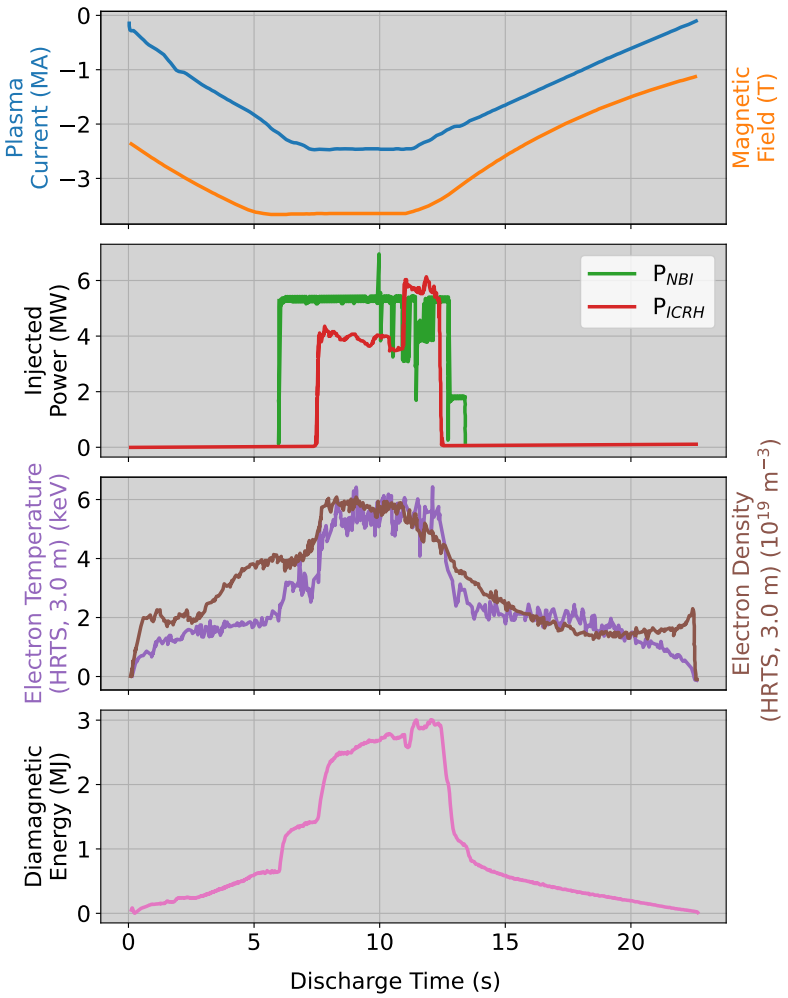

Figure 3: Time traces measured at the plasma core for Discharge #95671, showing: plasma current and magnetic field; NBI and ICRH power; electron temperature (HRTS, 3.0m) and density (HRTS, 3.0m); diamagnetic energy. Time offset of 40 s.

Table 1: Discharges and associated TRANSP simulations, together with the selected timestamps for fast deuterium distribution analysis.

Shot #	95671	95672	95673	95679	95680	95683	95684
Simulation ID	A25	A25	A26	V36	V07	V07	A24
Time (s)	10.0	12.0	11.0	9.95	9.95	9.20	9.00

extracted at the selected time (see timestamps in Table 1).

TRANSP computes the fast distribution over the full phase space, resolving it in space, time, energy, and pitch. An example for discharge #95671 is shown in Figure 4. Panel 4a presents the spatial density of fast deuterium (integrated over energy and pitch), while Panel 4b shows the energy-pitch distribution (integrated over space). A high-energy tail is visible in the positive pitch area, extending from 100 keV to 1–2 MeV.

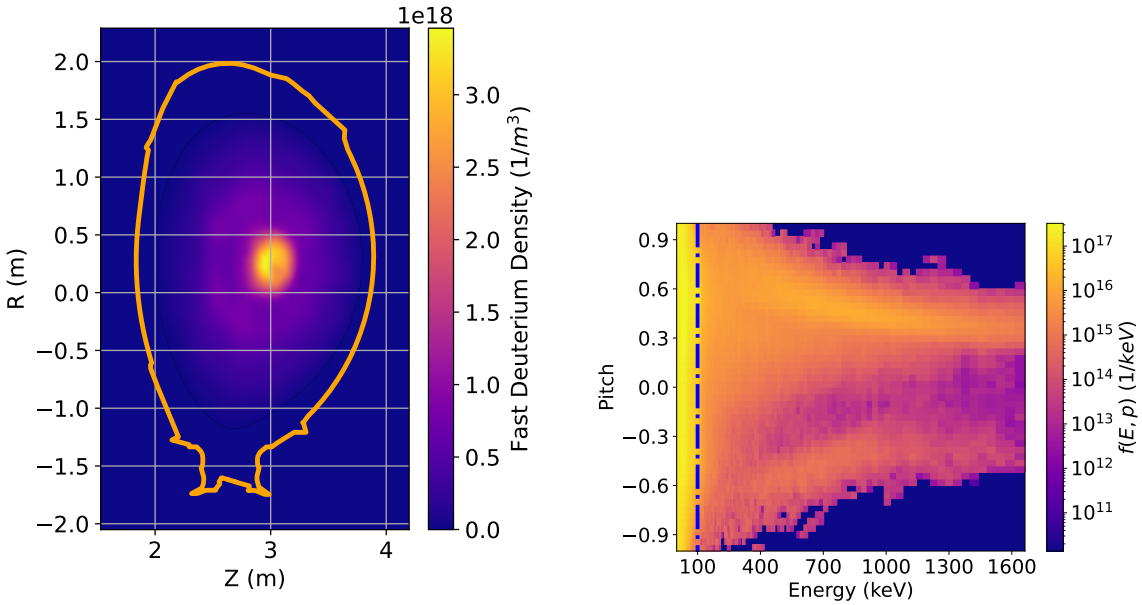

(a) (b)

Figure 4: **(a)** Poloidal fast deuterium density profile from TRANSP. Shot #95671, sim. ID A25, time = 10.0 s. **(b)** Full space-integrated energy–pitch distribution for the same case as in (a).

The errors of the TRANSP outputs are likely underestimated as they originate in part from the interpolation of data affected by significant experimental uncertainties. However, for the purposes of this work, we deemed it appropriate to regard them as not reliably assessable using only the estimation method previously described and, instead, focused on building a functional framework. One of the next planned upgrades will be to evaluate the impact of these errors on the performed simulations.

4.1.1 Synthetic neutron spectra The fast deuterium distribution (see Figure 4) is extracted at the selected timestamp (see Table 1) for each simulation and it is used to calculate the expected time of flight spectrum along the line of sight of the TOFOR neutron spectrometer and for comparison with data obtained with this instrument.

The validation process begins by extracting TOFOR neutron energy spectra at each timestamp, using a time window of 0.8 s centred around the selected time point. Synthetic spectra are then generated using the GENESIS Monte Carlo code [33] and convolved with the TOFOR response function for comparison with experiment. Thermal deuterium profiles (density and temperature), magnetic equilibria and the fast deuterium distribution are taken from TRANSP outputs, while the TOFOR line of sight file was calculated using the LINE2.1 code. [34]

To accurately model the TOFOR spectrum, all relevant neutron-producing interactions must be included. Reactions involving fast deuterons dominate due to their higher energies and larger cross sections compared to thermal reactions. The fast deuteron population is artificially divided into two components: a low-energy (Lfast) and a high-energy (Hfast) group, identified based on whether their energies are higher or lower than a 100 keV threshold (see the dashed blue line in Figure 4b). The Lfast population is attributed mainly to NBI, while Hfast originates from ICRH heating and reaches energies up to 1–2 MeV.

Six interaction channels contribute to the total spectrum:

- Thermal–Thermal (ThTh)
- Thermal–Lfast (ThLf)

- Thermal–Hfast (ThHf)
- Lfast–Lfast (LfLf)
- Hfast–Lfast (HfLf)
- Hfast–Hfast (HfHf)

Among these, Hfast-related channels are expected to dominate both the spectral shape and neutron yield.

TRANSP fast distribution simulations can track either the exact particle orbit or the particle's gyro-centre. In this study, for performance reasons, TRANSP records the gyro-centres of fast deuterons. When Larmor orbits are sufficiently small, approximating the particle motion by its gyro-centre is generally acceptable. However, as the Larmor radius increases, Finite Larmor Radius effects may become significant. [35]

In such cases, the TOFOR neutron spectra can be affected, since some fast deuterons may exhibit Larmor radii of several centimetres. Specifically, the finite plasma volume observed by the TOFOR line of sight may not fully encompass the orbit of the fast deuterons around their gyro-centres. Due to the system geometry, some fast deuterons are effectively within the TOFOR line of sight when moving towards the detector, but move outside the field of view when moving away from it. If a fast deuteron undergoes a D(D,n)^{3}He reaction while moving towards the detector, the resulting neutron can be detected and will appear with an increased energy (due to energy and momentum conservation). Conversely, if the reaction occurs while the particle is moving away, the resulting neutron would be shifted to a lower energy, but is likely not observed because the particle has moved outside the line of sight. This asymmetry reduces the neutron yield in the low-energy region of the spectrum. Therefore, an orbit correction must be included in the calculations, where the full particle orbit is taken into account rather than just the gyro-centre.

The correction itself is relatively straightforward and was first introduced in Ref. [35]. Only the toroidal magnetic field B is considered and its value at each fast-deuteron gyrocentre is computed using

$$B = B_0 \frac{R_0}{R} \tag{2}$$

where B_0 is the magnetic field on the magnetic axis, R_0 the radial position of the magnetic axis, and R the radial position of the gyrocentre. The corresponding Larmor radius r_L was then obtained from

$$r_L = \frac{m_D\, v_\perp}{e\, B} \tag{3}$$

where $v_\perp$ is the perpendicular velocity of the gyrocentre, e the proton charge, and m_D the deuteron mass. Knowing the Larmor radius, the particle position in the R–Z plane can be computed by uniformly sampling the gyroangle.

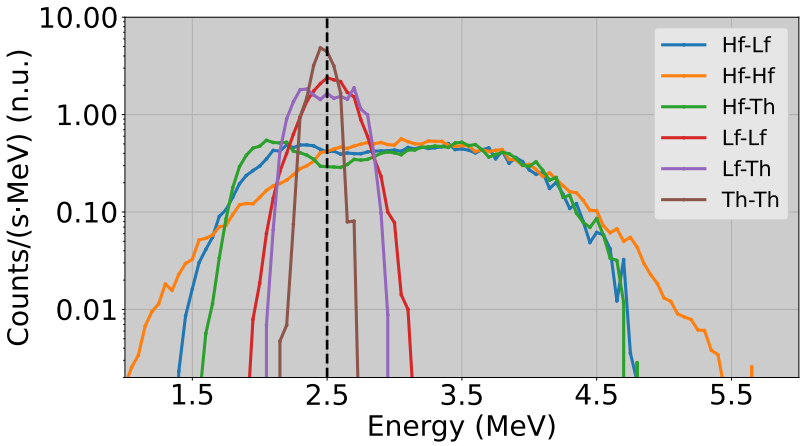

Figure 5: Normalised neutron spectral components from orbit-corrected simulations (TOFOR diagnostic, energy-resolved). Shot #95671, simulation ID A25, discharge time = 10 s.

Figure 5 shows the synthetic neutron energy spectra obtained from the orbit-corrected simulation of shot #95671 (ID A25) at 10 s. The Hfast-related components (blue, orange, and green lines) clearly dominate the spectral shape in both the high-energy ($E_n > 3$ MeV) and

low-energy ($E_n < 2$ MeV) regions. This trend is consistent across the full discharge set, as expected from the enhanced fusion cross sections at energies above 100 keV.

4.2 Alpha particle source

To reconstruct the alpha birth profile, it is necessary to model the alpha particle source in three–ions scheme experiments. The goal is to derive the alpha birth profile both from experimental observations and from TRANSP-based simulations, enabling a direct comparison to evaluate the spatial predictive accuracy of the simulation.

In D–^{3}He plasmas, alpha particles are produced via the ^{3}He(D,p)α fusion reaction. A less frequent branch of this reaction leads to the emission of a 16.4 MeV gamma ray through the ^{3}He(D,γ)^{5}Li channel [30]. This gamma-ray emission, whose spatial profile provides a good approximation of that of fusion-born alpha particles from ^{3}He(D,p)α, can escape the plasma and be detected by the Gamma Camera at JET during three–ion scheme experiments, providing a means to assess the alpha birth profile.

Our analysis begins with the extraction of experimental Gamma Camera profiles. These are then processed using the TREVISO code [24] to obtain a tomographic reconstruction of the alpha birth profile. The methods for deriving both experimental and synthetic Gamma Camera profiles are described in Section 4.2.1, while the tomographic approach is presented in Section 4.3.

4.2.1 Processing Experimental Gamma Camera Data Gamma Camera data consist of a set of waveforms and the corresponding time stamps. When a gamma-ray is detected, its pulse shape is digitised in a waveform and the time of detection is stored in a time stamp. By analysing individual waveforms, using one of the algorithms described in [36], we can reconstruct the energy spectrum deposited in the crystal in any arbitrary time interval. In the discharges considered in this work the capability to resolve super-imposed pulses (pile-up) was particularly relevant to correctly reconstruct the shape of the spectrum in the high energy region of interest for alpha particle studies. A pile-up recovery algorithm has been recently implemented in a software named GetAGRaSp (Get A Gamma-Ray Spectrum) and used also to process the data analysed here. [18]

For all discharges listed in Table 1, Gamma Camera binary files were retrieved and processed with GetAGRaSp to obtain reliable energy spectra for each Gamma Camera channel. Figure 6 shows an example of the gamma-ray spectrum measured by channel #4 in discharge #95671 and time integrated over the whole duration of the discharge. The spectrum comprises both high (say, $E_\gamma > 10$ MeV) and low energy events, where the latter arise from the gamma-ray background induced by neutron interactions with the materials that surround the detectors. In order to eliminate such neutron induced background for our analysis, we have proceeded as it follows.

Each discharge follows a consistent heating sequence: NBI is activated at 6 s, followed by ICRH between 7.5 s and 12.5 s (see Figure 2). The interval from 6 to 7.5 s, during which only NBI is active, is used to estimate the background. No significant 16.4 MeV gamma-ray emission is expected in this phase due to the lower deuteron energies involved, as also confirmed by our data. For each channel, a background spectrum is obtained by integrating over the NBI-only time window and averaging across the discharge set. The resulting spectrum is then normalised to the neutron yield of the pulse under analysis (obtained by the JET fission chambers), as shown by the orange line in Figure 6, and subtracted from the corresponding signal spectrum during the ICRH phase, integrated over the desired time window.

The high-energy residual structure (green line in Figure 6) reflects the interaction of 16.4 MeV gamma rays within the 1"×2/3" $LaBr_3$:Ce detector [5, 10]. By integrating the background-subtracted spectrum above a 9 MeV threshold, the total gamma count per channel is obtained, providing the experimental Gamma Camera profile (an example is shown in Figure 10).

4.2.2 Synthetic Gamma Camera Profiles As indicated earlier, one way to validate TRANSP simulations of the deuterium distribution function and its spatial profile is to use this input to calculate synthetic Gamma Camera signal and to compare them with actual measurements.

To compute a synthetic Gamma Camera profile for comparison with experimental data, the fast deuterium distribution from TRANSP is used as input to the GENESIS code. This enables the numerical calculation of the gamma-ray emission expected from the ^{3}He(D,γ)^{5}Li reaction in each Gamma Camera channel. As with the synthetic TOFOR spectra, the calculation of the gamma yield for each line of sight is performed in GENESIS, using the TRANSP fast deuterium distribution as input, along with the magnetic equilibria and helium-3 kinetic profiles. The 19 Gamma Camera line-of-sight files were calculated via the LINE 2.1 code [34].

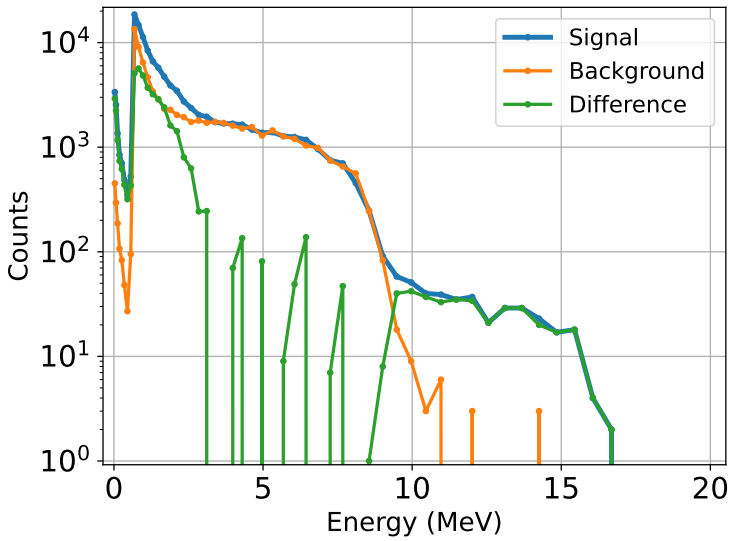

Figure 6: Difference (green line) between the signal spectrum (blue) and the background spectrum (orange). Shot #95671, full discharge integration, Gamma Camera Channel #4.

4.3 Tomographic method

Starting from the actual Gamma Camera data, or corresponding synthetic signals evaluated from TRANSP results, we can determine the two-dimensional map of the gamma-ray emission in the poloidal plane by tomographic inversion.

To reconstruct a 2D poloidal map of the gamma-ray emissivity, and thus the alpha birth profile, we use the TREVISO code [24]. Specifically developed for Gamma Camera data at JET, TREVISO implements an iterative algorithm based on the Maximum Likelihood–Expectation Maximisation method to invert the line-integrated Gamma Camera signals into a pixel-based emissivity distribution. Magnetic equilibrium information is used to smooth the reconstructed emissivity along flux surfaces, enhancing the physical consistency of the results. This procedure is applied to both experimental and synthetic Gamma Camera profiles. An example is shown in Figure 7.

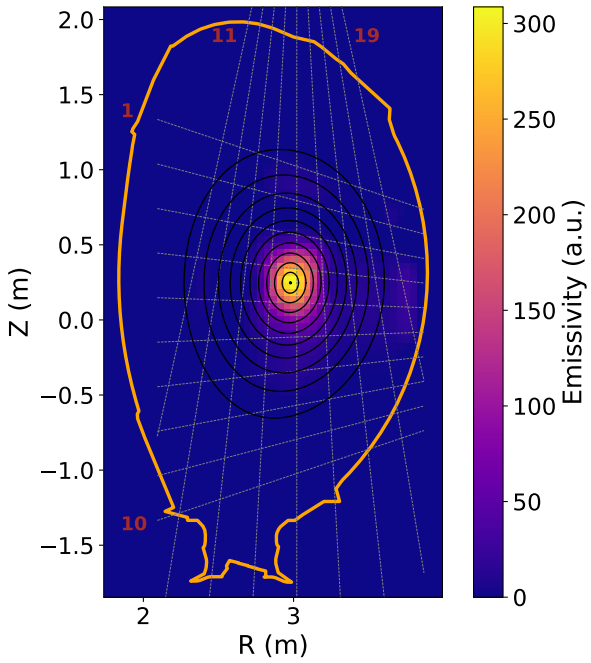

Figure 7: Tomographic reconstruction of the Gamma Camera profile using TREVISO. Emission is strongly localized near the magnetic axis. Black curves: magnetic flux surfaces; white dashed lines: Gamma Camera lines of sight. Shot #95671, experimental data, discharge time: 10 s.

For comparison purposes, the 2D emissivity maps are projected onto the normalized poloidal

flux coordinate ρ. A ρ value is assigned to each pixel, and the emissivity values are then binned to produce a 1D emissivity profile. Two different procedures are used to derive the 1D profiles:

- **Synthetic data:** The simulated Gamma Camera profile is directly reconstructed using TREVISO. After projection onto the ρ coordinate, pixel emissivity values are binned along the ρ axis. For each bin, the mean and standard deviation are computed, representing respectively the central value and uncertainty of the 1D profile.
- **Experimental data:** A similar procedure is applied, but over a set of one hundred Gamma Camera profiles derived from the original measurement. These profiles are generated using Poisson statistics, which govern counting processes. For each Gamma Camera channel, the original count N is used as the mean ($\mu = N$) and the variance ($\sigma^2 = N$) of the distribution. 100 synthetic profiles are then created by sampling from a Poisson distribution characterised by the previous parameters. This brute-force method allows propagation of statistical uncertainties through the tomographic reconstruction. The resulting error is combined quadratically with the reconstruction uncertainty to yield the final uncertainty of the 1D alpha birth profile.

5 Results

5.1 Total Neutron Rate Time Evolution

A comparison between the TRANSP-simulated and experimentally measured total neutron rate is used as an initial validation step for each simulation. A representative example is shown in Figure 8.

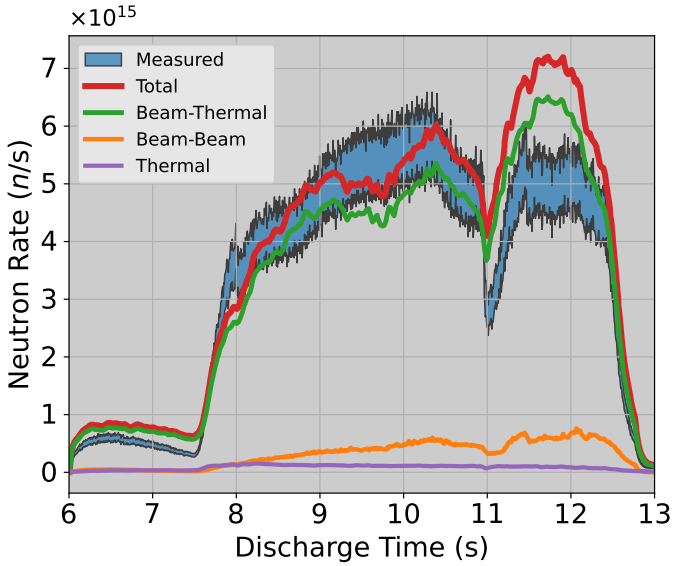

Figure 8: Comparison between TRANSP-simulated and experimentally measured total neutron rate for discharge 95671 at JET.
Blue: experimental measurement bounds. Red: TRANSP-predicted total neutron rate. Green: D beam–thermal D contribution. Orange: beam–beam contribution. Purple: thermal–thermal contribution.
Simulation ID: "A25". Experimental data from fission chambers at JET. Time offset of 40 s.

As shown in Figure 8, simulation 95671A25 exhibits reasonable agreement with the experimental data up to the major sawtooth crash occurring at approximately $t \approx 11$ s. A similar trend is observed across all discharges in the dataset, with a large sawtooth event occurring toward the end of each shot.

We do not expect the simulated and measured data after the sawtooth crash to agree since sawteeth eject fast ions with a velocity-space selective pattern [37]. We did not use a sawtooth crash model depleting the fast-ion population in the plasma centre in the TRANSP simulation. For this reason, the comparison between predictions and nuclear diagnostics data is limited to time intervals before the crash in all the discharges.

The overall good agreement between the measured and modelled neutron rate before the sawtooth crash indicates that, when properly set up, TRANSP is capable of quantitatively

reproducing the neutron rate time evolution with reasonable accuracy. For each discharge, we select the fast deuterium distribution calculated at the time points showing the best agreement with the measured neutron rate, as summarized in Table 1.

5.2 Fast Deuterium Distribution and TOFOR Spectra

Experimental neutron spectra from the TOFOR diagnostic were retrieved, and synthetic spectra were generated using the GENESIS code based on the TRANSP-calculated fast deuterium distribution, both with and without the application of the orbit correction procedure.

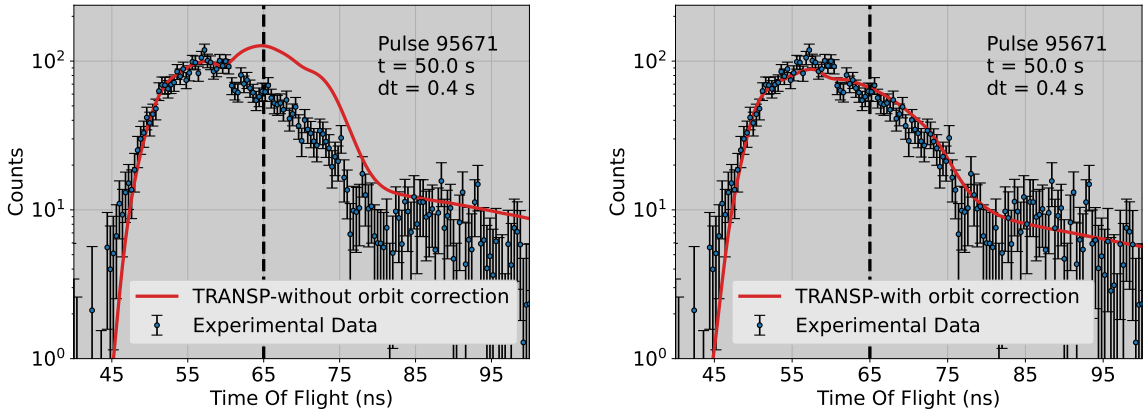

(a) (b)

Figure 9: Comparison between experimental and synthetic TOFOR spectra for discharge #95671, simulation ID "A25", at $t = 10$ s. **(a)** Spectrum computed without orbit correction. **(b)** Spectrum computed with orbit correction applied.

As shown in Figure 9a, the uncorrected synthetic spectrum exhibits good agreement with experimental data at low time-of-flight (TOF) values, corresponding to high neutron energies. However, a notable overestimation is observed at higher TOF values (lower energies).

Figure 9b displays the corresponding spectrum after applying orbit correction. In this case, a significantly improved match with the experimental data is obtained across the full TOF range. Similar results were observed for all analysed discharges, supporting the validity of the fast deuterium distribution from the selected TRANSP simulations in terms of spatial localization, energy distribution, and pitch-angle dependence.

5.3 Alpha Birth Profiles

Experimental Gamma Camera profiles were extracted and compared with synthetic profiles generated using GENESIS, with the TRANSP-derived fast deuterium distribution as input. Both profiles refer to the same time window. For direct comparison – and also because the Gamma Camera detectors are not absolutely calibrated – the synthetic profile was normalised to match the total gamma-ray counts of the experimental one.

As shown in Figure 10, a good general agreement is observed between the experimental and synthetic profiles, consistently across all analysed discharges. The central channels (3–6 and 14–16), which intersect the plasma core, exhibit the strongest gamma-ray signals, indicating that the emission is concentrated near the plasma centre. Discrepancies in peripheral channels may result from localised vessel emissions or from background components not fully removed during processing.

Subsequently, the synthetic Gamma Camera profiles were reconstructed tomographically using the TREVISO code. With the aid of magnetic equilibrium data, the resulting 2D emissivity maps were projected onto the normalised poloidal flux coordinate, ρ, to obtain 1D radial profiles, following the method described in Section 4.3.

As illustrated in Figure 11, the reconstructed emissivity profiles exhibit good consistency between experiment and simulation. In all cases, the alpha emission is strongly peaked at the plasma centre ($\rho < 0.2$) and rapidly decreases, with the exact profile shape depending on the specific discharge. These results suggest that the simulation accurately represents the spatial distribution of alpha birth within the plasma core.

It can be observed that the alpha birth profile derived from synthetic data in Figure 11 generally exhibits larger error bars compared to the one obtained from experimental data. This is

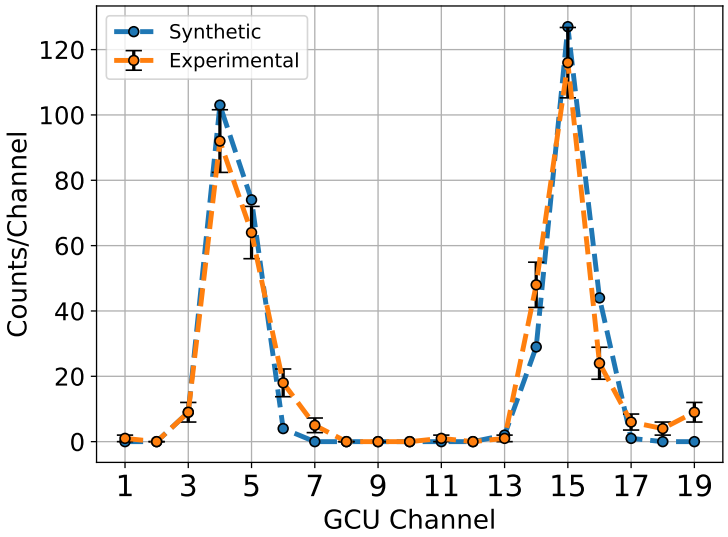

Figure 10: Comparison between experimental (orange) and synthetic (blue) Gamma Camera profiles. The synthetic profile is normalized to the total experimental Gamma Camera counts, for direct comparison. Error bars correspond to Poisson statistics (see Section 4.3): $\sigma = \sqrt{N}$. Shot #95671, Simulation ID "A25", discharge time: 10 s, Integration time: ± 0.5 s.

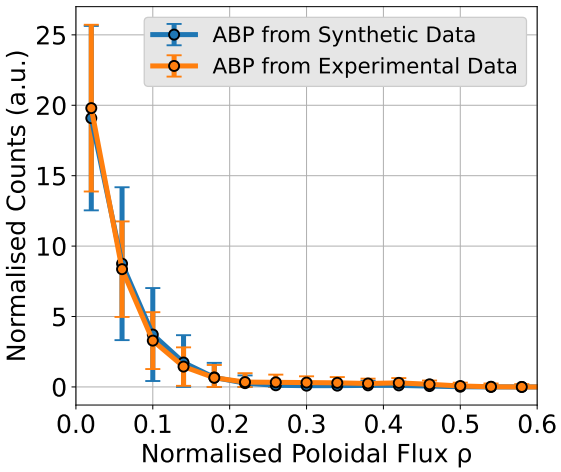

Figure 11: Comparison between experimental (orange) and synthetic (blue) normalized alpha emissivity profiles as a function of the normalized poloidal flux coordinate, ρ. See section 4.3 for error bar information. Shot #95671, Simulation ID "A25", discharge time: 10 s.

due to the greater spread in ρ-space of the pixels involved in the reconstruction of the synthetic Gamma Camera profile, compared to those contributing to the experimental profile.

6 Discussion

The results presented in this work indicate that, if properly configured (see Section 4.1), TRANSP simulations at JET can effectively predict gamma and neutron emission from D–^{3}He plasmas in three–ion scheme experiments. In particular, TRANSP provides time, space, energy and pitch-resolved distributions of the fast deuterium density, originating from NBI injection and further heated via ICRH. This fast component is primarily responsible for the localized and intense sources of gamma rays, neutrons, and alpha particles through fusion reactions. Based on the TRANSP fast D distribution, both emission spectra and synthetic diagnostic profiles can be computed, enabling predictions for this class of experiments and deepening our understanding of three–ion scheme scenarios.

The neutron rate predicted by TRANSP is in acceptable agreement with experimental measurements, especially during the early phase of the discharge, prior to the major sawtooth crash occurring at ~ 11 s in all analysed discharges. For this reason, timestamps for extracting the fast D distribution were selected in this early phase, where both the qualitative and quantitative behaviour of the neutron rate is in better agreement with fission chamber data at JET. The simulations confirm that neutron production is primarily driven by the interaction between thermal deuterium and the fast deuterium population. This highlights the importance of accurately modelling the fast D distribution, as it plays a central role in interpreting three–ion scheme experiments. To produce a properly configured TRANSP simulation, ^{3}He concentration variations, explored by incremental changes of about 5%, were used to identify the parameters required. In this three-ion heating scheme, due to the underlying physics mechanisms that determine the polarisation of the electric field, the neutron rate is very sensitive to the ^{3}He concentration and variations of 5-10% of the ^{3}He concentration typically result in significant changes of the simulated neutron rate with respect to that measured.

TOFOR measurements offered an opportunity to test the TRANSP fast D distribution. Spectral features observed in the TOFOR data reflect corresponding structures in the simulated fast D distribution. By including finite Larmor radius effects in the synthetic spectra, a good agreement was obtained between TRANSP-based simulations and TOFOR data. In most discharges, the broad peak centred around 65 ns, typically attributed to thermal and NBI components, is not observed, suggesting a dominant contribution from the Hfast population (i.e., NBI deuterons effectively heated by ICRH). This component exhibits a broad and non-trivial spectral structure. Conversely, for discharge #95683, the peak associated with unheated NBI deuterons (with energies $\lesssim 100$ keV) interacting with thermal deuterium is clearly visible. This may indicate reduced ICRH heating effectiveness or comparatively lower ICRH power relative to NBI. Overall, TRANSP simulations facilitate the interpretation of the distinct components contributing to the neutron emission.

Gamma Camera measurements offer a complementary spatial diagnostic for validating the fast D distribution. Using the TRANSP-derived fast D distribution as input, the poloidal distribution of alpha birth profiles can be numerically reconstructed and compared with tomographically inverted alpha birth profiles obtained from experimental Gamma Camera data. Across all analysed discharges, synthetic alpha birth profiles from TRANSP show reasonable agreement with the experimental reconstructions (Figures 11 and 12). All cases exhibit a pronounced central peaking of emissivity near the magnetic axis, with a sharp drop-off at larger ρ values. Synthetic alpha birth profiles show a larger error due to the greater dispersion of the pixel into the ρ-space. The primary variation between discharges lies in the degree of central peaking relative to the outer plasma. TRANSP-derived fast D distributions help elucidate the connection between heating schemes and the resulting alpha birth profile shape.

A cross-analysis of normalized Hfast density profiles and synthetic alpha birth profiles as functions of the normalized poloidal flux ρ reveals a qualitative correlation (see Figure 13). The sharper the Hfast density is peaked near the magnetic axis, the more pronounced the central peaking of the emissivity profile. In contrast, the Lfast component appears to have no significant impact on the alpha birth profile structure.

These observations suggest that TRANSP can be used not only for post-analysis but also for predictive purposes. In particular, controlling the heating scheme, especially the efficiency and spatial localization of ICRH, may allow shaping of the final alpha emissivity profile. This capability offers a pathway toward improved understanding and control of three–ions scheme experiments at JET and in future devices operating with D–^{3}He plasmas.

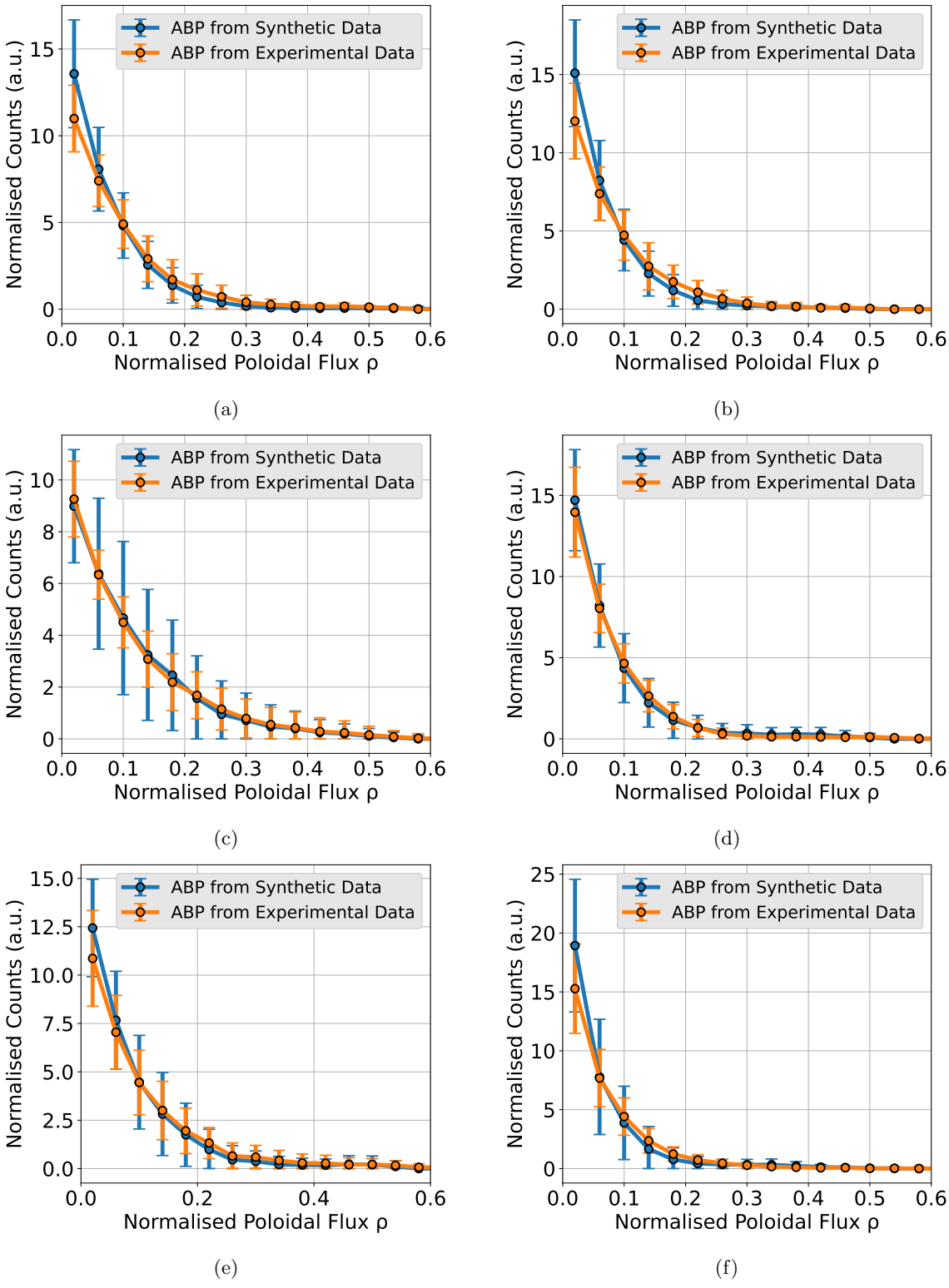

Figure 12: Comparisons between experimental (orange) and synthetic (blue) normalized alpha emissivity profiles as a function of the normalized poloidal flux coordinate ρ, for all the remaining analysed discharges.
(a): 95672-A25; **(b)**: 95673-A26; **(c)**: 95679-V36; **(d)**: 95680-V07; **(e)**: 95683-V07; **(f)**: 95684-A24

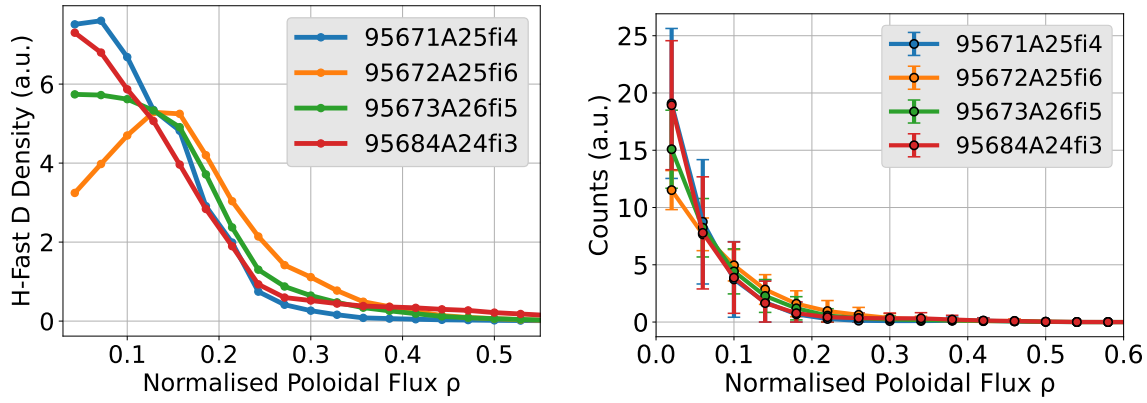

(a) (b)

Figure 13: Correlation between Hfast density and synthetic alpha birth profile shape (Simulation type: "A"). **(a)** Normalized Hfast density profiles as functions of the ρ coordinate. **(b)** Normalized synthetic alpha birth profiles as functions of the ρ coordinate.

Further investigations can include the quantitative evaluation in absolute units of the alpha particle intensity. Although beyond the scope of this work, this could be assessed in a similar manner to fusion power measurements performed at JET using DT gamma-ray detection via the TGRS system. [13, 38, 39, 40] As shown in Section 4.2.1, 16.4 MeV gamma-rays from ^{3}He(D,γ)^{5}Li reaction are easily observed in D–^{3}He plasmas and, in principle, the corresponding fusion power (and, hence, the absolute intensity of the alpha particle source) can be determined from this emission. This is the only method to measure fusion power in D–^{3}He plasmas because the D–^{3}He reaction is aneutronic.

7 Conclusion

In this work, a set of D–^{3}He discharges during Three–Ion Scheme experiments at JET has been analysed. For each discharge a TRANSP simulation has been performed, and outputs like the time evolution of the total neutron rate and the fast deuterium distribution have been retrieved and analysed. The aim was to validate the TRANSP outputs by producing synthetic neutron spectra and alpha particle birth profiles, comparing them against experimental results obtained from diagnostics like TOFOR and the Gamma Camera Upgrade at JET.

The time evolution of the total neutron rate predicted by TRANSP showed reasonable agreement with experimental data from the JET fission chambers. Synthetic spectra generated with GENESIS, based on the TRANSP-derived fast deuterium distribution, also showed good agreement with TOFOR measurements, especially when finite Larmor radius effects were included. Finally, the synthetic alpha birth profile, computed from the TRANSP fast deuterium distribution and reconstructed tomographically using the TREVISO code, was compared with the experimental alpha emissivity profile, showing acceptable agreement.

Moreover, the broader utility of TRANSP simulations has been discussed, highlighting their potential as a tool for improving the understanding of three-ions scheme experiments. In particular, TRANSP may help to optimise the heating scenarios, ultimately contributing to the development of efficient alpha particle sources based on the three–ion scheme for studies of alpha particles in plasmas without tritium and for tests of the diagnostics.

Acknowledgments

This work has been carried out within the framework of the EUROfusion Consortium, funded by the European Union via the Euratom Research and Training Programme (Grant Agreement No 101052200 - EUROfusion). Views and opinions expressed are however those of the author(s) only and do not necessarily reflect those of the European Union or the European Commission. Neither the European Union nor the European Commission can be held responsible for them.
This scientific paper has been published as part of the international project co-financed by the Polish Ministry of Science and Higher Education within the programme called "PMW".

Funding
Eni SpA, Italy, provides support for this work through the PhD scholarships of Simone Lorenzo Fugazza and Marco Dalla Rosa.

Author contributions
Simone Lorenzo Fugazza: Writing–original draft, Data Curation, Methodology, Visualization, Validation, Software, Formal analysis, Conceptualization. **Marco Dalla Rosa**: Writing – review & editing, Software, Data Curation, Investigation, Formal analysis. **Enrico Panontin**: Software, Formal Analysis, Methodology. **Andrea Dal Molin**: Conceptualization. **Jacob Eriksson**: Data Curation, Resources, Software. **Giuseppe Gorini**: Supervision, Project Administration. **Yevgen Kazakov**: Conceptualization. **Vasily Kiptily**: Conceptualization. **Michal Poradzinski**: Writing – Review & Editing, Software, Resources. **John Rice**: Conceptualization. **Davide Rigamonti**: Conceptualization. **Mirko Salewski**: Writing – Review & Editing, Conceptualization. **Žiga Štancar**: Software, Resources. **Marco Tardocchi**: Supervision, Project Administration. **Massimo Nocente**: Writing – Review & Editing, Conceptualization, Software, Project Administration, Resources, Supervision, Validation, Funding Acquisition, Methodology.

Data availability
Data will be made available on request.

References
[1] M. Salewski et al., 'Energetic particle physics: Chapter 7 of the special issue: on the path to tokamak burning plasma operation', Nucl. Fusion, vol. 65, no. 4, p. 043002, Mar. 2025, doi: 10.1088/1741-4326/adb763.

[2] P. Mantica et al., 'Detection of alpha heating in JET-ILW DT plasmas by a study of the electron temperature response to ICRH modulation', Nucl. Fusion, vol. 64, no. 8, p. 086001, Jun. 2024, doi: 10.1088/1741-4326/ad52aa.

[3] V. G. Kiptily et al., 'Evidence of Electron Heating by Alpha Particles in JET Deuterium-Tritium Plasmas', Phys. Rev. Lett., vol. 131, no. 7, p. 075101, Aug. 2023, doi: 10.1103/PhysRevLett.131.075101.

[4] M. Nocente et al., 'Fusion product measurements by nuclear diagnostics in the Joint European Torus deuterium–tritium 2 campaign (invited)', Rev. Sci. Instrum., vol. 93, no. 9, p. 093520, Sep. 2022, doi: 10.1063/5.0101767.

[5] M. Nocente et al., 'Generation and observation of fast deuterium ions and fusion-born alpha particles in JET D-^{3}He plasmas with the 3-ion radio-frequency heating scenario', Nucl. Fusion, vol. 60, no. 12, p. 124006, Oct. 2020, doi: 10.1088/1741-4326/abb95d.

[6] Ye. O. Kazakov et al., 'Physics and applications of three-ion ICRF scenarios for fusion research', Physics of Plasmas, vol. 28, no. 2, p. 020501, Feb. 2021, doi: 10.1063/5.0021818.

[7] Ye. O. Kazakov et al., 'Plasma heating and generation of energetic D ions with the 3-ion ICRF + NBI scenario in mixed H-D plasmas at JET-ILW', Nucl. Fusion, vol. 60, no. 11, p. 112013, Sep. 2020, doi: 10.1088/1741-4326/ab9256.

[8] B. C. G. Reman et al., 'Velocity-space tomography of an MeV fast-ion tail generated by three-ion scheme ICRF heating at JET', Nucl. Fusion, vol. 65, no. 7, p. 076007, Jun. 2025, doi: 10.1088/1741-4326/addb60.

[9] K. K. Kirov et al., 'Synergistic ICRH and NBI heating for fast ion generation and maximising fusion rate in mixed plasmas at JET', AIP Conference Proceedings, vol. 2254, no. 1, p. 030011, Sep. 2020, doi: 10.1063/5.0014235.

[10] E. Panontin et al., 'First spatially resolved measurements of the D–^{3}He α-particle source with the upgraded JET gamma-ray camera', Review of Scientific Instruments, vol. 92, no. 5, p. 053529, May 2021, doi: 10.1063/5.0043776.

[11] D. Rigamonti et al., 'The upgraded JET gamma-ray cameras based on high resolution/high count rate compact spectrometers', Review of Scientific Instruments, vol. 89, no. 10, p. 10I116, Oct. 2018, doi: 10.1063/1.5038839.

[12] V. Zoita et al., 'Design of the JET upgraded gamma-ray cameras', Fusion Engineering and Design, vol. 84, no. 7, pp. 2052–2057, Jun. 2009, doi: 10.1016/j.fusengdes.2008.11.026.

[13] M. Nocente et al., 'A new tangential gamma-ray spectrometer for fast ion measurements in deuterium and deuterium–tritium plasmas of the Joint European Torus', Rev. Sci. Instrum., vol. 92, no. 4, p. 043537, Apr. 2021, doi: 10.1063/5.0043806.

[14] M. Nocente et al., 'High Resolution Gamma Ray Spectroscopy at MHz Counting Rates With $LaBr_3$ Scintillators for Fusion Plasma Applications', IEEE Transactions on Nuclear Science, vol. 60, no. 2, pp. 1408–1415, Apr. 2013, doi: 10.1109/TNS.2013.2252189.

[15] M. Nocente et al., 'Energy resolution of gamma-ray spectroscopy of JET plasmas with a LaBr3 scintillator detector and digital data acquisitiona)', Rev. Sci. Instrum., vol. 81, no. 10, p. 10D321, Oct. 2010, doi: 10.1063/1.3501386.

[16] V. G. Kiptily et al., 'γ-ray diagnostics of energetic ions in JET', Nucl. Fusion, vol. 42, no. 8, p. 999, Aug. 2002, doi: 10.1088/0029-5515/42/8/308.

[17] M. Iliasova et al., 'Gamma-ray measurements in D^3He fusion plasma experiments on JET', Nuclear Instruments and Methods in Physics Research Section A: Accelerators, Spectrometers, Detectors and Associated Equipment, vol. 1031, p. 166586, May 2022, doi: 10.1016/j.nima.2022.166586.

[18] M. Nocente et al., 'MeV range particle physics studies in tokamak plasmas using gamma-ray spectroscopy', Plasma Phys. Control. Fusion, vol. 62, no. 1, p. 014015, Jan. 2020, doi: 10.1088/1361-6587/ab4f32.

[19] M. Gatu Johnson et al., 'The TOFOR neutron spectrometer and its first use at JET', Review of Scientific Instruments, vol. 77, no. 10, p. 10E702, Sep. 2006, doi: 10.1063/1.2219422.

[20] M. Gatu Johnson et al., 'The 2.5-MeV neutron time-of-flight spectrometer TOFOR for experiments at JET', Nuclear Instruments and Methods in Physics Research Section A: Accelerators, Spectrometers, Detectors and Associated Equipment, vol. 591, no. 2, pp. 417–430, Jun. 2008, doi: 10.1016/j.nima.2008.03.010.

[21] A. Y. Pankin et al., 'TRANSP integrated modeling code for interpretive and predictive analysis of tokamak plasmas', Computer Physics Communications, vol. 312, p. 109611, Jul. 2025, doi: 10.1016/j.cpc.2025.109611.

[22] B. A. Grierson et al., 'Orchestrating TRANSP Simulations for Interpretative and Predictive Tokamak Modeling with OMFIT', Fusion Science and Technology, vol. 73, no. 2018, Feb. 2018, doi: 10.1080/15361055.2017.1398585.

[23] Ž. Štancar et al., 'Overview of interpretive modelling of fusion performance in JET DTE2 discharges with TRANSP', Nucl. Fusion, vol. 63, no. 12, p. 126058, Nov. 2023, doi: 10.1088/1741-4326/ad0310.

[24] E. Panontin, 'Development of Nuclear Radiation Based Tomography Methods for Runaway Electrons and Fast Ions in Fusion Plasmas', Milano-Bicocca, Milano, 2020. Available: https://boa.unimib.it/handle/10281/383194

[25] C. Hellesen, L. Giacomelli, and M. Gatu Johnson, 'Measurement and analysis of the neutron emission from ICRH and NB heated JET D plasmas using the TOFOR spectrometer', Aug. 2007, Available: https://www.osti.gov/etdeweb/biblio/20956169

[26] A. Valentini et al., 'A model for analytical calculations of synthetic neutron energy spectra from beam-target reactions', Nucl. Fusion, vol. 65, no. 2, p. 026001, Dec. 2024, doi: 10.1088/1741-4326/ad9bc8.

[27] A. Valentini et al., 'Relativistic calculations of neutron and gamma-ray spectra from beam–target reactions in magnetized plasmas', Rev. Sci. Instrum., vol. 95, no. 8, p. 083551, Aug. 2024, doi: 10.1063/5.0216680.

[28] A. S. Jacobsen et al., 'Velocity-space sensitivities of neutron emission spectrometers at the tokamaks JET and ASDEX Upgrade in deuterium plasmas', Rev. Sci. Instrum., vol. 88, no. 7, p. 073506, Jul. 2017, doi: 10.1063/1.4991651.

[29] M. Nocente et al., 'Gamma-ray spectroscopy at MHz counting rates with a compact LaBr3 detector and silicon photomultipliers for fusion plasma applications', Rev. Sci. Instrum., vol. 87, no. 11, p. 11E714, Aug. 2016, doi: 10.1063/1.4961073.

[30] D. R. Tilley et al., 'Energy levels of light nuclei A=5, 6, 7', Nuclear Physics A, vol. 708, no. 1, pp. 3–163, Sep. 2002, doi: 10.1016/S0375-9474(02)00597-3.

[31] R. Felton et al., 'Real-time measurement and control at JET experiment control', Fusion Engineering and Design, vol. 74, no. 1, pp. 561–566, Nov. 2005, doi: 10.1016/j.fusengdes.2005.06.286.

[32] D. K. Yang et al., 'Simulations of neutral beam injection and ion cyclotron resonance heating synergy in high power EAST scenarios', Rev. Sci. Instrum., vol. 93, no. 11, p. 113501, Nov. 2022, doi: 10.1063/5.0101645.

[33] M. Nocente, 'Neutron and gamma-ray emission spectroscopy as fast ion diagnostics in fusion plasmas', Milano-Bicocca, 2012. Available: https://boa.unimib.it/handle/10281/28397

[34] L. Hägg et al., 'Estimating the neutron yield in a deuterium plasma with the JET neutron camera', Rev. Sci. Instrum., vol. 94, no. 7, p. 073502, Jul. 2023, doi: 10.1063/5.0144654.

[35] J. Eriksson et al., 'Finite Larmor radii effects in fast ion measurements with neutron emission spectrometry', Plasma Phys. Control. Fusion, vol. 55, no. 1, p. 015008, Dec. 2012, doi: 10.1088/0741-3335/55/1/015008.

[36] M. Dalla Rosa, 'Development of nuclear techniques for gamma-ray spectroscopy in thermonuclear plasmas', Master's thesis, Milano-Bicocca, 2023.

[37] M. Salewski et al., 'High-definition velocity-space tomography of fast-ion dynamics', Nucl. Fusion, vol. 56, no. 10, p. 106024, Aug. 2016, doi: 10.1088/0029-5515/56/10/106024.

[38] M. Rebai et al., 'First direct measurement of the spectrum emitted by the ^{3}H(^{2}H,γ)^{5}He reaction and assessment of the relative yield γ_1 to γ_0', Phys. Rev. C, vol. 110, no. 1, p. 014625, Jul. 2024, doi: 10.1103/PhysRevC.110.014625.

[39] A. Dal Molin et al., 'Measurement of the Gamma-Ray-to-Neutron Branching Ratio for the Deuterium-Tritium Reaction in Magnetic Confinement Fusion Plasmas', Phys. Rev. Lett., vol. 133, no. 5, p. 055102, Jul. 2024, doi: 10.1103/PhysRevLett.133.055102.

[40] G. Marcer et al., 'Absolute measurement of the deuterium-tritium reaction gamma-ray emission in magnetic confinement fusion plasmas', Nucl. Fusion, 2025, doi: 10.1088/1741-4326/adeea7.